Mengxing Huang
Yan Zhang
Weipeng Jing
Amjad Mehmood (Eds.)


214

LNICST

# Wireless Internet

9th International Conference, WICON 2016
Haikou, China, December 19–20, 2016
Proceedings


# Lecture Notes of the Institute for Computer Sciences, Social Informatics and Telecommunications Engineering 214

More information about this series at http://www.springer.com/series/8197

Mengxing Huang · Yan Zhang
Weipeng Jing · Amjad Mehmood (Eds.)

# Wireless Internet

9th International Conference, WICON 2016
Haikou, China, December 19–20, 2016
Proceedings

Springer

*Editors*
Mengxing Huang
Hainan University
Hainan
China

Yan Zhang
Simula Research Laboratory
Fornebu
Norway

Weipeng Jing
Northeast Forestry University
Harbin, Heilongjiang
China

Amjad Mehmood
Guangdong University
of Petrochemical Technology
Maoming Shi
China

ISSN 1867-8211 ISSN 1867-822X (electronic)
Lecture Notes of the Institute for Computer Sciences, Social Informatics and Telecommunications Engineering
ISBN 978-3-319-72997-8 ISBN 978-3-319-72998-5 (eBook)
https://doi.org/10.1007/978-3-319-72998-5

Library of Congress Control Number: 2017962873



Printed on acid-free paper

This Springer imprint is published by Springer Nature
The registered company is Springer International Publishing AG
The registered company address is: Gewerbestrasse 11, 6330 Cham, Switzerland

# Preface

We are delighted to introduce the proceedings of the 9th EAI International Wireless Internet Conference. The conference brings together technical experts and researchers from academia, industry, and government from all around the world to discuss novel research results related to the future wireless Internet.

WICON 2016 was held during December 19–20, 2016, in Haikou, China. The conference is organized by the EAI (European Alliance for Innovation). The Program Committee received over 60 submissions and each paper was reviewed by at least three expert reviewers. We chose 30 papers after intensive discussions held among the Program Committee members.

The conference tracks were: Track 1, Seamless Integration of Heterogeneous Networks; Track 2, Cross-Layer Design and Optimization; Track 3, Wireless Access Technologies; Track 4, Multi-hop Wireless Networks; Track 5, Emerging Technologies and Applications; Track 6, Network Security; Track 7, Wireless Internet Platforms and Software; Track 8, Green Communications.

The two keynote speeches were by Prof. Michael Pecht from the University of Maryland, USA, and Prof. Huiping Xu from Sanya Institue of Deep-Sea Science and Engineering, Chinese Academy of Sciences, China. The invited talk was presented by Prof. Rong Yu from Guangdong University of Technology, China, and Dr. Zhibo Pang, from ABB AB, Corporate Research, Sweden.

We strongly believe that WICON 2016 provided a good forum for all researchers, developers, and practitioners to discuss science and technology aspects that are relevant to smart grids. The conference was successful and stimulating, as indicated by the contributions presented in this volume.

November 2017

Lei Shu
Mengxing Huang
Yan Zhang
Weipeng Jing

# Organization

## Steering Committee

### Steering Committee Chair

| | |
|---|---|
| Imrich Chlamtac | Create-Net |

### Steering Committee Members

| | |
|---|---|
| Athanasios Vasilakos | Kuwait University, Kuwait |
| Xudong Wang | Shanghai Jiao Tong University, China |
| Hsiao-Hwa Chen | National Cheng Kung University, Taiwan |

## Organizing Committee

### General Chair

| | |
|---|---|
| Mengxing Huang | Hainan University, China |

### General Co-chair

| | |
|---|---|
| Yan Zhang | University of Oslo, Norway |

### Technical Program Committee Chair

| | |
|---|---|
| Lei Shu | University of Lincoln, UK/Guangdong University of Petrochemical Technology, China/EAI China Office, EAI |

### Technical Program Committee Co-chair

| | |
|---|---|
| Yong Bai | Hainan University, China |

### Track Chairs

**PHY**

| | |
|---|---|
| Hui Gao | Beijing University of Post and Telecommunications, China |

**MAC**

| | |
|---|---|
| Xianfu Chen | VTT, Finland |
| Zheng Chang | University of Jyväskylä, Finland |

**Network**

| | |
|---|---|
| Celimuge Wu | University of Electro-Communications, Japan |
| Xing Zhou | Hainan University, China |
| Soufiene Djahel | Manchester Metropolitan University, UK |

**Security**

| | |
|---|---|
| Genge Bela | Petru Maior University of Tirgu Mures, Romania |
| Rongxing Lu | Nanyang Technological University, Singapore |

**Cloud and Big Data**

| | |
|---|---|
| Chau Yuen | Singapore University of Technology and Design, Singapore |
| Hao Wang | Norwegian University of Science Technology, Aalesund, Norway |
| Sabita Maharjan | Simula Research Laboratory, Norway |

**Emerging IoT Systems**

| | |
|---|---|
| Rong Yu | Guangdong University of Technology, China |
| Meng Wang | Ericsson Research, Sweden |

**Local Chair**

| | |
|---|---|
| Jingbing Li | Hainan University, China |

**Workshops Chairs**

| | |
|---|---|
| Kun Wang | NJUPT, China |
| Deze Zeng | China University of Geosciences, China |

**Demos Chairs**

| | |
|---|---|
| Xiaoling Wu | Guangzhou Institute of Advanced Technology, Chinese Academy of Sciences |
| Yu Zhang | University of Lincoln, UK |

**Posters and PhD Track Chairs**

| | |
|---|---|
| Mithun Mukherjee | Guangdong University of Petrochemical Technology, China |
| Gerhard Hancke | City University of Hong Kong, Hong Kong, SAR China |

**Industrial Exhibition Co-chairs**

| | |
|---|---|
| Chaoxing Su | Zhongke Industrial Park of Western Guangdong Province (Director) |
| Jun Feng | Zhongke Industrial Park of Western Guangdong Province (Deputy Director) |
| Meiquan Ou | Zhongke Industrial Park of Western Guangdong Province |
| Tianping Chen | Zhongke Industrial Park of Western Guangdong Province |

**Publicity and Social Media Chair**

| | |
|---|---|
| Chunsheng Zhu | UBC, Canada |

**Publications Chairs**

| | |
|---|---|
| Weipeng Jing | Northeast Forestry University, China |
| Amjad Mehmood | Guangdong University of Petrochemical Technology, China |

**Website Chairs**

| | |
|---|---|
| Yuanfang Chen | Guangdong University of Petrochemical Technology, China |
| Minxiang Zhang | Guangdong University of Petrochemical Technology, China |

**Conference Manager**

| | |
|---|---|
| Barbara Fertalova | EAI (European Alliance for Innovation) |

## Technical Program Committee

| | |
|---|---|
| Xianfu Chen | VTT, Finland |
| Zheng Chang | University of Jyvaskyla, Finland |
| Celimuge Wu | University of Electro-Communications, Japan |
| Xing Zhou | Hainan University, China |
| Soufiene Djahel | Manchester Metropolitan University, UK |
| Genge Bela | Petru Maior University of Tirgu Mures, Romania |
| Rongxing Lu | Nanyang Technological University, Singapore |
| Chau Yuen | Singapore University of Technology and Design, Singapore |
| Hao Wang | Norwegian University of Science Technology, Aalesund, Norway |
| Sabita Maharjan | Simula Research Laboratory, Norway |
| Rong Yu | Guangdong University of Technology, China |
| Meng Wang | Ericsson Research, Sweden |
| Chunsheng Zhu | UBC, Canada |
| Yuanfang Chen | Guangdong University of Petrochemical Technology, China |

| | |
|---|---|
| Weipeng Jing | Northeast Forestry University, China |
| Amjad Mehmood | Guangdong University of Petrochemical Technology, China |
| Kun Wang | NJUPT, China |
| Deze Zeng | China University of Geosciences, China |
| Xiaoling Wu | Guangzhou Institute of Advanced Technology, Chinese Academy of Sciences |
| Yu Zhang | University of Lincoln, UK |
| Mithun Mukherjee | Guangdong University of Petrochemical Technology, China |
| Gerhard Hancke | City University of Hong Kong, Hong Kong, SAR China |

**Security Track**

| | |
|---|---|
| Piroska Haller | Petru Maior University of Tirgu Mures, Romania |
| Bogdan Crainicu | Petru Maior University of Tirgu Mures, Romania |
| Marina Krotofil | Honeywell |
| Georgios Karopoulos | University of Athens, Greece |
| Al-Sakib Khan Pathan | Southeast University, Bangladesh and Islamic University in Madinah, Saudi Arabia |
| Urko Zurutuza | Mondragon Unibersitatea, Spain |
| Alvaro Cardenas | The University of Texas at Dallas, USA |

**PHY Track**

| | |
|---|---|
| Xiaoming Chen | Nanjing University of Aeronautics and Astronautics, China |
| Jun Zhang | Nanjing University of Posts and Telecommunications, China |
| Jue Wang | Singapore University of Technology and Design |
| Jie Zeng | Tsinghua University, China |

**Network Track**

| | |
|---|---|
| Imane Horiya Brahmi | University College Dublin, Ireland |
| Bo Gu | Kogakuin University, Japan |
| Yassine Hadjadj-Aoul | IRISA, France |
| Pingguo Huang | Tokyo University of Science, Japan |
| Nafaa Jabeur | German University of Technology in Oman |
| Zhi Liu | Waseda University, Japan |
| Farid Nait-Abdesselam | Paris Descartes University, France |
| Razvan Stanica | INSA Lyon, France |
| Suhua Tang | The University of Electro-Communications, Japan |
| Xiaoyan Wang | Ibaraki University, Japan |
| Lei Zhong | National Institute of Informatics, Japan |
| Hao Zhou | University of Science and Technology of China |

# Contents

**Sensor Networks**

Joint Asynchronous Time and Localization of an Unknown Node in Wireless Sensor Networks . . . . . 3
*Junhui Zhao, Lei Li, and Yi Gong*

Distributed Beacon Synchronization Mechanism for 802.15.4 Cluster-Tree Topology . . . . . 10
*Nikumani Choudhury, Rakesh Matam, Mithun Mukherjee, and Lei Shu*

A Short Survey on Fault Diagnosis in Wireless Sensor Networks . . . . . 21
*Zeyu Zhang, Lei Shu, Amjad Mehmood, Li Yan, and Yu Zhang*

Research on Data Storage Scheme Under Sink Failures in Wireless Sensor Networks . . . . . 27
*Yue Wang and Jun Wang*

Impact of Irregular Radio and Faulty Nodes on Localization in Industrial WSNs . . . . . 36
*Xiaoman Ran, Lei Shu, Mithun Mukherjee, Yuntao Wu, Yuanfang Chen, and Zhihong Sun*

**Security**

A SDN Proactive Defense Scheme Based on IP and MAC Address Mutation . . . . . 51
*Liancheng Zhang, Zhenxing Wang, Jiabao Fang, and Yi Guo*

An Attribute Based Encryption Middleware with Rank Revocation for Mobile Cloud Storage . . . . . 61
*Qinghe Dong, Qian He, Mengfei Cai, and Peng Liu*

High Capacity Embedding Methods of QR Code Error Correction . . . . . 70
*Song Wan, Yuliang Lu, Xuehu Yan, Wanmeng Ding, and Hanlin Liu*

Perceptual Secret Sharing Scheme Based on Boolean Operations and Random Grids . . . . . 80
*Xuehu Yan, Yuliang Lu, Lintao Liu, Song Wan, Wanmeng Ding, and Hanlin Liu*

Security-Aware Distributed Service Composition for Wireless Sensor Networks Based Smart Metering in Smart Grid Using Software Defined Networks . . . . . 91
*Gaolei Li, Yang Wu, Jun Wu, Jianhua Li, and Chengcheng Zhao*

**Wireless Networks**

A Simplified Interference Model for Outdoor Millimeter Wave Networks . . . 101
*Xiaolin Jiang, Hossein Shokri-Ghadikolaei, Carlo Fischione, and Zhibo Pang*

A CWMN Spectrum Allocation Based on Multi-strategy Fusion Glowworm Swarm Optimization Algorithm. . . . . 109
*Zhuhua Hu, Yugui Han, Lu Cao, Yong Bai, and Yaochi Zhao*

Decode-and-Forward Full-Duplex Relay Selection Under Rayleigh Fading Environment . . . . . 121
*Qinghai Ou, Qingsu He, Lingkang Zeng, Wenjing Li, Xiao Liao, Shaofeng Fang, Fang Liu, Yuanan Liu, and Xinjing Hou*

Parameter Control Scheme Among Multi-cell for Mobility Load Balancing in Ultra-dense Network . . . . . 131
*Xin Su, Qi Zhang, Jie Zeng, and Liping Rong*

Spectrum Sensing Based on Modulated Wideband Converter with CoSaMP Reconstruction Algorithm. . . . . 139
*Minglei Tong and Yong Bai*

Joint Partial Relay and Antenna Selection for Full-Duplex Amplify-and-Forward Relay Networks. . . . . 149
*Qinghai Ou, Xinjing Hou, Fang Liu, Yuanan Liu, and Shaofeng Fang*

A Low-Complexity Power Allocation Method in Ultra-dense Network. . . . . 155
*Xin Su, Bei Liu, Jie Zeng, Jing Wang, and Xibin Xu*

QRD Architecture Using the Modified ILMGS Algorithm for MIMO Systems . . . . . 164
*Cang Liu, Chuan Tang, Zuocheng Xing, Luechao Yuan, Yu Wang, Lirui Chen, Yang Zhang, Suncheng Xiang, Wangfeng Zhao, Xing Hu, and Jinsong Xu*

Simulating and Analyzing the Effect of Timeliness on the Accuracy Rate of Central Path Planning . . . . . 179
*Dayong Song, Yanheng Liu, Jian Wang, Shaoqing Xu, and Lin Li*

An Optimization of DBN/GPU Speech Recognition on Wireless Network Applications . . . . . 189
*Weipeng Jing, Tao Jiang, and Yaqiu Liu*

Estimating End-to-End Available Bandwidth for Cyber-Physical Applications in Hybrid Networks . . . . . 197
*Hui Zhou, Chunyang Ye, Yucong Duan, Qi Qi, and Yu Zhang*

Delay Aware Resource Allocation for Device-to-Device Communication Underlaying Cellular Networks . . . . . 207
*Heli Zhang, Wang Yang, Hong Ji, Xi Li, Victor C. M. Leung, and Lichao Yang*

An Improved Dynamic Clustering Algorithm Based on Uplink Capacity Analysis in Ultra-Dense Network System . . . . . 218
*Jie Zeng, Qi Zhang, Xin Su, and Liping Rong*

Wideband Spectrum Sensing by Multi-step Sample Autocorrelation Detection . . . . . 228
*Lu Chen, Xiaoqin Wu, and Yong Bai*

Noncoherent Joint Multiple Symbol Differential Detection and Channel Decoding in Massive MIMO System . . . . . 240
*Jing Feng, Hui Gao, Taotao Wang, Tiejun Lv, and Weibin Guo*

Downlink PDMA in the Heterogeneous Network . . . . . 250
*Jie Zeng, Xiaofeng Lin, Liping Rong, and Xin Su*

**Internet of Things**

Edge Caching to Deliver Mobile Content in Vehicular Ad Hoc Networks . . . 263
*Zhou Su, Qichao Xu, and Yilong Hui*

Enhanced IoT Data Acquisition in Information Centric Networks . . . . . 272
*Lijun Dong*

Horizontal Slicing Clustering Based Movement Detection Method for IoTs . . . . . 279
*Xiaoyu Li, Xiaoling Wu, Daoping Huang, and Lei Shu*

Using Wireless Vibration Sensors to Study the Impact of Fouling on Fluid-Conveying Pipelines . . . . . 288
*Pengfei Wen, Jianfeng Huang, Yuanfang Chen, and Lei Shu*

**Poster and Demo**

Research on Spectrum Detection Technology in Cognitive Radio . . . . . 295
*Xiaoyu Tang and Baodan Chen*

Video Quality Assessment by Decoupling Distortions on Primary Visual Information . . . . . 299
*Yang Li, Xu Wang, Feng Li, Qingrui Guo, Qiang Fan, Qiwei Peng, Wang Luo, Min Feng, Yuan Xia, and Shaowei Liu*

Faster-Than-Nyquist Transmission in SC-FDE System over Frequency Selective Channel with One Equalizer . . . . . 308
*Zhifeng Wang and Yong Bai*

An Ensemble Method Based on SVC and Euclidean Distance for Classification Binary Imbalanced Data . . . . . 312
*Lei Zhao, Lei Wang, and Guan Gui*

**Author Index** . . . . . 321

# Sensor Networks

# Joint Asynchronous Time and Localization of an Unknown Node in Wireless Sensor Networks

Junhui Zhao[1,2(✉)], Lei Li[2], and Yi Gong[3]

[1] East China Jiaotong University, Nanchang 330013, China
eeejhzhao@163.com
[2] Beijing Jiaotong University, Beijing 100044, China
14120084@bjtu.edu.cn
[3] South University of Science and Technology of China, Shenzhen 518055, China
sustc.gy@gmail.com

**Abstract.** This paper considers the location of an unknown source node with asynchronous anchor nodes in Wireless Sensor Networks (WSN). In this paper, a joint synchronization and localization framework is considered and examined. Firstly, the proposed algorithm obtains algebraic solutions of the source location and the clock skew by improved Taylor series based on regularization theory. Then the clock offset is estimated. The Cramer-Rao lower bound is derived for the considered problem. Simulations show that the proposed algorithm is robust to the inaccurate initial value and better accuracy than the closed-form methods. This proposed algorithm can be widely applied in practice.

**Keywords:** Localization · Clock offset · Clock skew · WSN

## 1 Introduction

There has been much research on localization techniques and asynchronous time in Wireless sensor networks. Different measurement techniques used in source localization include time of arrival (TOA) [1], time difference of arrival (TDOA) and frequency difference of arrival (FDOA) [2] and hybrid algorithm with two or three techniques [1]. In [3,4], the authors proposed a close-form algorithms to solve the synchronization and localization parameters at the same time. [5] only considered the client location and clock offset of access points, ignored the clock skews. [6,7] provided two estimators which jointly estimate the position of the target node as well as the unknown clock-skews and clock offsets.

The main contribution of this paper is driving an estimator for determining the source node location, the anchor nodes skews and offsets. Asynchronous

This work was supported by the National Natural Science Foundation of China (61471031), the Fundamental Research Funds for the Central Universities, Beijing Jiaotong University (2013JBZ001), Guangdong Science and Technology Program under Grant No. 2016A010101003.


M. Huang et al. (Eds.): WICON 2016, LNICST 214, pp. 3–9, 2018.
https://doi.org/10.1007/978-3-319-72998-5_1

TDOA-based source localization using improved Taylor series to obtain the three parameters is studied. The paper introduces the Regularization theory to modify the Taylor series to ensure the iteration convergence. The simulation results show that the proposed approach offer better robustness and accuracy.

## 2 System Model

The localization system consists of $M$ sensors which have known position and they are separated into $N$ groups according to [8]. Group $j$, $j = 1, 2, ..., N$, has the same clock skew $\omega_j$ and clock offset $\theta_j$. And there is 1 anchor node in group 1 for reference. The localization system is used to determine the position of one source node which has unknown transmission time $t_s$. The internal time is modeled as a function of the reference as (1). $t_i$ and $t$ are the internal time of the $i$th ($i = 1, 2, ...M$) node and the reference time, respectively.

$$t_i = \omega_j t + \theta_j \tag{1}$$

$\mathbf{s}_i = [x_i, y_i]$ denote the location of the $i$th anchor, where $\mathbf{x} = [x, y]$ denotes the location of the source node. $d_i$ is determined by the Euclidean distance: $d_i = \|\mathbf{x} - \mathbf{s}_i\|$. Then, the packet arrival time vector is represented as follows:

$$t_i = \omega_j(t_s + \frac{1}{c}d_i + n_{ti}) + \theta_j \tag{2}$$

Here $c = 3 \times 10^8$ (m/s). $n_{ti}$ is a random measurement error with zero mean and a standard deviation of $\sigma_t$.

The transmit time will be abandoned, TDOA based localization is more appropriate than TOA based localization. The clock skew and offset of group 1 is $\omega_1 = 1$ and $\theta_1 = 0$. Then the TDOA vector is obtained by subtracting the packet arrival times from that of the representative as follows:

$$\frac{t_i}{\omega_j} - t_1 = \frac{d_i}{c} - \frac{d_1}{c} + n_{ti} - n_{t1} + \frac{\theta_j}{\omega_j} \tag{3}$$

## 3 Proposed Algorithm Based on Taylor Series Method

### 3.1 Improved Taylor Series Method

To progress, an approximation need be applied to the model. The clock skew of the anchor node can be expressed as $\omega_j = 1 + \delta_j$, where $\delta_j \ll 1$ is relatively small value. For sufficiently small $\delta_j$, we have [4] $\frac{1}{\omega_i} = 1 - \delta_i$. Consider Eq. (3), we take $j = 2$, $i = 2$ and $i = 3$ as example. $c(t_2 - t_3) = \frac{1}{c}(d_2 - d_3) + n_{23} + c(t_2 - t_3)\delta_2$, where $r_{23} = c(t_2 - t_3)$ can be regarded as the TDOA measurement. And $n_{23}$ is the additive noise of distance. Extend the situation to N groups, in vector form,

$$\mathbf{r_A} = \mathbf{d_A} + \mathbf{F}\delta_\mathbf{A} + \mathbf{n_A} \tag{4}$$

where $\mathbf{r_A} = [r_{m_1+2,m_1+1}, r_{m_1+3,m_1+1}, \cdots, r_{m_N,m_N-1}]$ is the TDOA vector. $\mathbf{n_A}$ is the noise vector which is zero-mean Gaussian random variables. $\mathbf{d_A}$ is the true distance vector. $\delta_\mathbf{A} = [\delta_2, \delta_3, \cdots, \delta_N]$ is the clock skew after the approximation in (8). And the $(M-N-1)\times(N-1)$ matrix $\mathbf{F}$ is

$$\mathbf{F} = \begin{bmatrix} r_{32}, r_{42} \ldots, r_{m_2 2}, 0 & . & . & . & 0, 0, & . & . & . & 0 \\ 0 \quad \cdots & 0, r_{m_2+2,m_2+1}, \ldots, r_{m_3,m_2+1}, 0, & 0, & & . & . & . & 0 \\ \vdots & & & & & & & & \\ 0 \quad \cdots & 0, 0 & . & . & . & 0, r_{m_{N-1}+2,m_{N-1}+1} \ldots, r_{m_N,m_{N-1}+1} & & & \end{bmatrix}^T \tag{5}$$

The parameter vector is $\mathbf{z}^T = \left[\mathbf{x}^T, \delta_\mathbf{A}^T\right]$. The target function is:

$$f(\mathbf{r};\mathbf{p}) = k - \frac{1}{2}(\mathbf{r_A} - \mathbf{d_A} - \mathbf{F}\delta_\mathbf{A})^T \mathbf{Q}_{\mathbf{r_A}}^{-1}(\mathbf{r_A} - \mathbf{d_A} - \mathbf{F}\delta_\mathbf{A}) \tag{6}$$

And the partial differentiations in (5) are formulated as follows:

$$\frac{\partial f}{\partial \mathbf{x}} = \frac{\mathbf{x} - \mathbf{s}_i}{\|\mathbf{x} - \mathbf{s}_i\|} - \frac{\mathbf{x} - \mathbf{s}_{m_j+1}}{\left\|\mathbf{x} - \mathbf{s}_{m_j+1}\right\|} \quad \frac{\partial f}{\partial \delta_\mathbf{A}} = \mathbf{F} \tag{7}$$

Taylor series method requires initial guess. Because the measurements are independent, we assume that the $\mathbf{Q}_{\mathbf{r_A}} = 2c^2\sigma_t^2\mathbf{I}$, it is a diagonal matrix. Then the $k$th iterative change is

$$\Delta\mathbf{z}_k = ({\mathbf{B}_k}^T\mathbf{B}_k)^{-1}{\mathbf{B}_k}^T\mathbf{p}_k \tag{8}$$

where

$$\mathbf{B}_k = \left[\frac{\partial f}{\partial \mathbf{x}}|_{\mathbf{x}_k}, \mathbf{F}\right] \quad \mathbf{p}_k = \mathbf{r_A} - \mathbf{d_A}|_{\mathbf{x}_k} - \mathbf{F}\delta_\mathbf{A}|_{\delta_{\mathbf{A}_k}} \tag{9}$$

And after every iteration, the parameter vector becomes $\mathbf{z}_{k+1} = \mathbf{z}_k + \Delta\mathbf{z}_k$. Taylor series method requires a good initial value, and a bad initial value can cause an ill-posed Jacobian matrix which leads to the iteration divergence. According to (8), We set $\mathbf{A} = \mathbf{B}^T\mathbf{B}$, $\mathbf{b} = \mathbf{B}^T\mathbf{p}$. Jacobian matrix is symmetric matrix. So the SVD of $\mathbf{A}$ is given by $\mathbf{A} = \mathbf{U}\sum\mathbf{U}^T = \sum_{i=1}^{n}\mathbf{u}_i\sigma_i\mathbf{u}_i^T$. Then the Iterative change is $\Delta\mathbf{z} = \mathbf{A}^{-1}\mathbf{b} = \sum_{i=1}^{n}\frac{\mathbf{u}_i^T\mathbf{b}}{\sigma_i}\mathbf{u}_i$.

From the equation, $\Delta\mathbf{z}$ is affected by smaller singular value obviously. As a result, $\Delta\mathbf{z}$ will be sign changed and rand. Then based on Regularization theory, the problem turns into (10) to modify the iterative change.

$$\min \quad \|\mathbf{A}\Delta\mathbf{z} - \mathbf{b}\|_2^2 + \lambda\|\Delta\mathbf{z}\|_2^2 \tag{10}$$

The DSVD method is used to modify the change as:

$$\Delta\mathbf{z}_{dsvd} = (A + \lambda I)^{-1}b = \sum_{i=1}^{n}\frac{\sigma_i}{\sigma_i+\lambda}\frac{\mathbf{u}_i^T\mathbf{b}}{\sigma_i}\mathbf{u}_i \tag{11}$$

From the modification, the cond of matrix becomes lower, and the sign change and rand situation will be decreased. The $\lambda$ is a regularization parameter controlling the tradeoff between the first and second terms. The L-curve criterion [8] is adopted to determine $\lambda$.

The procedure is as follows: the unknown parameter is $\mathbf{z}^T = \left[\mathbf{x}^T, \delta_{\mathbf{A}}^T\right]$. First we assume $\delta_{\mathbf{A}} = 0$, the initial guess $\mathbf{x}_k$. The tradeoff is $\|\Delta\mathbf{z}\| < \varepsilon$. Do $\mathbf{z}_{k+1} = \mathbf{z}_k + \Delta\mathbf{z}_{dsvdk}$ until the tradeoff is satisfied. Then we can get $\hat{\mathbf{z}} = [\mathbf{x}, \delta_{\mathbf{A}}]$.

### 3.2 Estimation of Clock Offset

Since the $d_1$ and $d_i$ are not known, we shall replace it by the reconstructed value using Euclidean distance, with $\hat{\mathbf{x}}$ substituted by $\mathbf{x}$ by final result. Let us denote the resulted vector be $\mathbf{R}(\mathbf{x}, \delta_{\mathbf{A}})$. Then the solution of $\theta$ is

$$\theta = (\mathbf{H}^T\mathbf{Q}_r^{-1}\mathbf{H})^{-1}\mathbf{H}^T\mathbf{Q}_r^{-1}(\mathbf{R} - \mathbf{R}(\mathbf{x}, \delta_{\mathbf{A}})) \tag{12}$$

where

$$\begin{aligned} \mathbf{H} &= \left[\tfrac{1}{\omega_2}, \tfrac{1}{\omega_2} \cdots \tfrac{1}{\omega_N}\right]^T \\ \mathbf{R} &= [t_2 - t_1, t_3 - t_1, ..., t_M - t_1]^T \\ \mathbf{R}(\mathbf{x}, \delta_{\mathbf{A}}) &= \left[\tfrac{d_2 - d_1}{c} + t_2\delta_2, ..., \tfrac{d_M - d_1}{c} + t_M\delta_N\right] \end{aligned} \tag{13}$$

## 4 Simulation Results and Discussion

As tabulated in Table 1, $M = 8$, $N = 3$. They are used to locate a source whose actual position is [0, 0]m. The time skew is randomly drawn from [0.95 1.05], and the time offset is randomly drawn from [1 10] ns. The RMSEs of the location, clock skew and clock offset estimation are defined as $\sqrt{(\hat{x} - x)^2 - (\hat{y} - y)^2}$, $\sum_{j=2}^{N} \sqrt{(\omega_j - \omega)^2}/(N-1)$ and $\sum_{j=2}^{N} \sqrt{(\theta_j - \theta)^2}/(N-1)$, respectively. Two estimators given in [3,6] are selected for comparisons.

**Table 1.** Sensor positions [m]

| | Set 1 | Set 2 | | | | Set 3 | | |
|---|---|---|---|---|---|---|---|---|
| $x_i$ | −80 | 0 | 60 | 20 | 100 | 50 | −65 | −20 |
| $y_i$ | 50 | −100 | −10 | 90 | 100 | 100 | 90 | 80 |

The first figure depicts the comparison of proposed algorithm and traditional Taylor series method with different initial guess. The measurement noise is set $\sigma_d^2 = 1\,\mathrm{m}^2$. With good initial guess, the proposed algorithm needs more iterations. But with the bad initial guess, the traditional Taylor method diverges to unexpected result. The amount of calculation of proposed algorithm is larger

than traditional Taylor method because of the revise of ill-posed matrix. But the proposed algorithm is robust and accurate.

The rest figures illustrate the estimation accuracy of location root-mean-square error (RMSE), clock skews and offsets with the log function of distance variance deviation changes from −30 to 15. The proposed algorithm is more accurate than LS and the separate approach. When the measurement error is small, the performance gap between Proposed algorithm and CRLB is not significant. The clock offsets rely on the previous estimations. If the localization and clock skews are biased, the clock offsets accuracy will be affected seriously (Fig. 1).

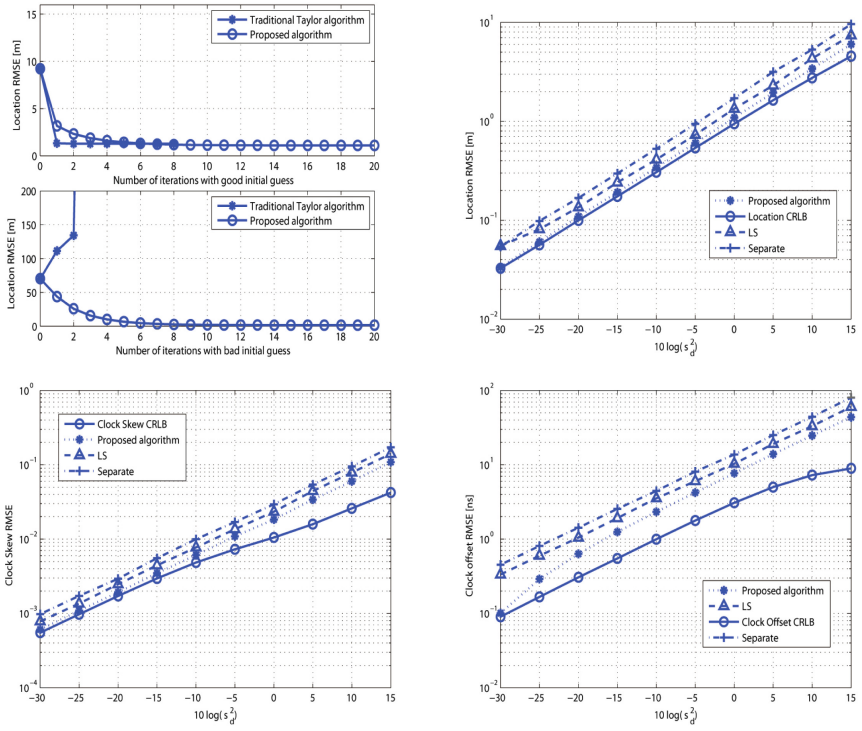


**Fig. 1.** Simulation of robustness and accuracy of the proposed algorithm

## 5 Cramer-Rao Lower Bound

$$\text{FIM} = \begin{bmatrix} \mathbf{X}_{11} & \mathbf{X}_{12} & \mathbf{X}_{13} \\ \mathbf{X}_{12}^T & \mathbf{X}_{22} & \mathbf{X}_{23} \\ \mathbf{X}_{13}^T & \mathbf{X}_{23}^T & \mathbf{X}_{33} \end{bmatrix} \tag{14}$$

We have used the $\nabla$ symbol to denote partial derivative:

$$\nabla_{\mathbf{a},\mathbf{b}} = \frac{\partial \mathbf{a}}{\partial \mathbf{b}^T} \tag{15}$$

$$\begin{aligned}
\mathbf{X}_{11} &= -E\left[\frac{\partial \ln p}{\partial \mathbf{x}^0 \partial \mathbf{x}^{0T}}\right] = \left(\frac{\partial \zeta}{\partial \mathbf{x}^0}\right)^T Q_r^{-1}\left(\frac{\partial \zeta}{\partial \mathbf{x}^0}\right) \\
\mathbf{X}_{12} &= \nabla^T_{\zeta,\mathbf{x}^0} Q_r^{-1} \nabla_{\zeta,\omega^0} \\
\mathbf{X}_{13} &= \nabla^T_{\zeta,\mathbf{x}^0} Q_r^{-1} \nabla_{\zeta,\theta^0} \\
\mathbf{X}_{22} &= \nabla^T_{\zeta,\omega^0} Q_r^{-1} \nabla_{\zeta,\omega^0} + Q_\omega^{-1} \\
\mathbf{X}_{23} &= \nabla^T_{\zeta,\omega^0} Q_r^{-1} \nabla_{\zeta,\theta^0} \\
\mathbf{X}_{33} &= \nabla^T_{\zeta,\theta^0} Q_r^{-1} \nabla_{\zeta,\theta^0} + Q_\theta^{-1}
\end{aligned} \tag{16}$$

where the $Q_r$, $Q_\omega$ and $Q_\theta$ are the covariance matrix of measurement error, anchor node clock skew and offsets error. The partial derivatives are obtained using (1), (3) and (7),

$$\frac{\partial \zeta}{\partial \mathbf{x}^0} = \left[\rho_2^0 - \rho_1^0, \rho_3^0 - \rho_1^0, ..., \rho_M^0 - \rho_1^0\right]^T \quad \rho_i^0 = \frac{\left(\mathbf{x}^0 - \mathbf{s}_i^0\right)}{\|\mathbf{x}^0 - \mathbf{s}_i^0\|} \tag{17}$$

$$\nabla_{\zeta,\omega^0} = \frac{\mathbf{d}}{{\omega^0}^2} \otimes \mathbf{1}_M - \frac{c\theta}{{\omega^0}^2} \otimes \mathbf{1}_M \quad \nabla_{\zeta,\theta^0} = \frac{c}{\omega^0} \otimes \mathbf{1}_M \tag{18}$$

The CRLB for location estimation is given by

$$\mathrm{CRLB}(\mathbf{x}^0) = \mathbf{X}_{11}^{-1} + \mathbf{X}_{11}^{-1}\mathbf{S}_1\left(\mathbf{S}_2 - {\mathbf{S}_1}^T\mathbf{X}_{11}^{-1}\mathbf{S}_1\right){\mathbf{S}_1}^T\mathbf{X}_{11}^{-1} \tag{19}$$

where

$$\mathbf{S}_1 = \begin{bmatrix}\mathbf{X}_{12}\ \mathbf{X}_{13}\end{bmatrix} \quad \mathbf{S}_2 = \begin{bmatrix}\mathbf{X}_{22} & \mathbf{X}_{23} \\ \mathbf{X}_{23}^T & \mathbf{X}_{33}\end{bmatrix} \tag{20}$$

By arranging the matrix blocks in (20) properly, the CRLB for the clock skews and offsets can be determined using the same method.

## 6 Conclusion

This paper investigates the problem of source localization in the presence of sensor clock skews and offsets. A sequential estimation method is developed that obtains the source position and clock skews first, the sensor node clock offset finally. Simulations show that the proposed algorithm can converge with bad initial guess. Compared with the close-formed approaches, the performance of proposed algorithm is closer to the CRLB.

## References

1. Zhang, Y., Ren, J., Chen, W.: A ToA-based location algorithm reducing the NLoS error under location-aware networks. In: WiCOM, pp. 1–4, September 2011
2. Fang, J.Q., Feng, D.Z., Li, J.: A robustly convergent algorithm for source localization using time difference of arrival and frequency difference of arrival. J. Electron. Inf. Technol. **37**, 798–803 (2015)
3. Zheng, J., Wu, Y.C.: Joint time synchronization and localization of an unknown node in wireless sensor networks. IEEE Trans. Signal Process. **58**, 1309–1320 (2010)

4. Vaghefi, R.M., Buehrer, R.M.: A linear estimator for joint synchronization and localization in wireless sensor networks. In: GLOBECOM, pp. 505–510, June 2014
5. Kim, R., Ha, T., Lim, H., et al.: TDoA localization for wireless networks with imperfect clock synchronization. In: IEEE International Conference on Information Networking, pp. 417–421 (2014)
6. Chepuri, S.P., Leus, G., van der Veen, A.J.: Joint localization and clock synchronization for wireless sensor networks. In: ASILOMAR, pp. 1432–1436 (2012)
7. Naseri, H., Koivunen, V.: Cooperative joint synchronization and localization using time delay measurements. In: IEEE International Conference on Acoustics, Speech and Signal Processing (ICASSP), pp. 3146–3150 (2016)
8. Hansen, P.C., Jensen, T.K., Rodriguez, G.: An adaptive pruning algorithm for the discrete L-curve criterion. J. Comput. Appl. Math. **198**, 483–492 (2007)

# Distributed Beacon Synchronization Mechanism for 802.15.4 Cluster-Tree Topology

Nikumani Choudhury[1(✉)], Rakesh Matam[1], Mithun Mukherjee[2], and Lei Shu[2]

[1] Indian Institute of Information Technology Guwahati, Guwahati, India
nikumani.choudhury.2014@ieee.org, rakesh@iiitg.ac.in
[2] Guangdong Provincial Key Laboratory of Petrochemical Equipment Fault Diagnosis, Guangdong University of Petrochemical Technology, Maoming, China
{m.mukherjee,lei.shu}@ieee.org

**Abstract.** Lack of synchronization mechanism in IEEE 802.15.4 standard for cluster-tree topology has restricted its use to non-beacon mode. Initial works in this direction are more centralized in nature whereas more recent works follow the distributed way. The former way of achieving synchronization have performance limitations in terms of scalability and overhead. In this paper, we propose a distributed beacon synchronization scheme that requires lesser transmissions and results in improved channel utilization. Apart from that, the proposed scheme also minimizes the number of collisions during beacon transmissions thus lowering the number of orphan nodes. Analytical and simulation studies corroborate our findings.

## 1 Introduction

The IEEE 802.15.4 standard [1] has emerged as a de facto standard for low-power wireless personal area networks (WPAN). It defines multiple physical layer (PHY) technologies and medium access control sub-layer for such low data-rate devices. IEEE 802.15.4 networks support both star and cluster-tree topologies. They can operate in either beacon-enabled (BEM) or non beacon-enabled (NBE) modes. In BEM, beacon synchronization allows attached devices to detect any pending messages or to track the beacon. In addition, as the structure of superframe is described in beacon, synchronization becomes important. In BEM, medium access control is achieved through slotted CSMA/CA. In addition, a guaranteed time slot (GTS) can be obtained for transmission that are assigned by a coordinator using an optional superframe. In presence of multiple end-devices and multiple coordinators, synchronization among coordinators reduces collisions.

In a star network, achieving synchronization is straight forward as all nodes are within communication range of central PAN coordinator (PANC). All communications are through the central coordinator. On the other hand, devices in a cluster-tree network can communicate with any other node provided they are within range of each other. This allows the network to scale whereby other


M. Huang et al. (Eds.): WICON 2016, LNICST 214, pp. 10–20, 2018.
https://doi.org/10.1007/978-3-319-72998-5_2

devices can also act as coordinators by providing services to its attached devices. Many commercial and industrial applications need such a topology. However, the operation of such a network comes with its own set of challenges. Synchronization is difficult as multiple coordinators are involved and overlapping beacon schedules result in frequent collisions and orphan nodes.

This problem has been addressed in [2–13]. But, majority of them are centralized in nature where a central coordinator computes beacon schedules and transmits to each coordinator with the help of a routing protocol. Nodes that actively participate in message relay run out of battery power resulting in network disconnections. Furthermore, distributed schemes like [9,10,14] are constrained by their own set of limitations like the need to shift between radio channels and maintaining tree routes. This motivated us to design a beacon scheduling scheme with low-overhead for a cluster-tree network. The main contributions of this paper are summarized as follows.

- We propose a distributed beacon synchronization scheme for a cluster-tree network that uses available channel slots effectively, incurs fewer transmissions and in turn consumes less energy.
- We present the collision probability analysis of the proposed synchronization mechanism.

A preliminary version of this work has been published in [15]. The rest of the paper is organized as follows. Section 2 provides brief overview of IEEE 802.15.4 MAC superframe as the proposed work uses beacon order (BO) and superframe order (SO) parameters. The proposed synchronization mechanism and its analytical evaluation is presented in Sect. 3. Simulation results are presented in Sect. 4. Finally, conclusion and future scope is presented in Sect. 5.

## 2 Overview of Superframe in 802.15.4 MAC

The superframe is bounded by two successive beacons that are separated by beacon interval (BI). It consists of an active period (contention access period and contention free period) followed by an optional inactive period. The superframe structure is divided into 16 equal duration slots. Slots in the contention access period (CAP) are accessed through slotted CSMA/CA, whereas, dedicated access is possible in contention free period (CFP) through GTSs. The active period of the superframe beginning from the beacon transmission is called superframe duration (SD). Nodes sleep during the inactive period and wakes up marking the beginning of the next superframe cycle. Two parameters namely `macBeaconOrder` (BO) and `macSuperframeOrder` (SO) together defines the structure of superframe as,

$$BI = \texttt{aBaseSuperframeDuration}.2^{\mathrm{BO}}$$

$$SD = \texttt{aBaseSuperframeDuration}.2^{\mathrm{SO}}$$

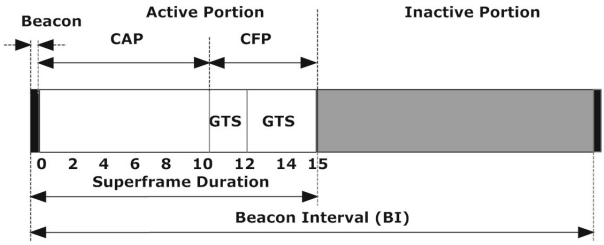


**Fig. 1.** IEEE 802.15.4 superframe structure.

where, SO and BO refer to the duration of active period along with beacon transmission time and the cyclic time period when the coordinator communicates using beacons, respectively. The structure of the superframe is shown in Fig. 1. The `aBaseSuperframeDuration` is the number of symbols constituting a superframe when the SO is set to zero. It gives us the time period between two beacon frame transmission. With $0 \leq \text{SO} \leq \text{BO} \leq 14$ and $\text{BO} = 15$ implies non-beacon mode.

## 3 Proposed Distributed Beacon Synchronization Scheme

### 3.1 Network Model

We consider a cluster-tree network, comprised of coordinators and end devices, as shown in Fig. 2. One of the selected coordinators acts as overall network coordinator. Coordinators are entrusted with additional functionality of synchronizing associated nodes with the help of periodic beacons. An end device associates with a coordinator and all data is routed via the parent. Clusters are formed among a group of coordinators and end devices, that executes a common function. A cluster head is chosen among the coordinators in each cluster for operational simplicity. The main notations in this paper are summarized in Table 1.

### 3.2 2-hop Distributed Beacon Synchronization (2-hop DBS)

The proposed scheme emphasizes on reducing the number of transmissions required to achieve beacon synchronization in a network and to restrict beacon collisions between neighboring coordinators. We focus on striking a balance between reducing the number of orphaned devices when beacons of multiple coordinators collide, and the synchronization simplicity. The proposed mechanism is presented below.

**2-hop Distributed Beacon Synchronization:** Following the designed synchronization scheme, a coordinator that aims to compute a synchronized schedule needs the *BO* and *SO* values of the parent coordinator (i.e. the coordinator to which it is associated) and all its (parent's) relatives. The first part of the information can be retrieved from the beacon frame received from the parent.

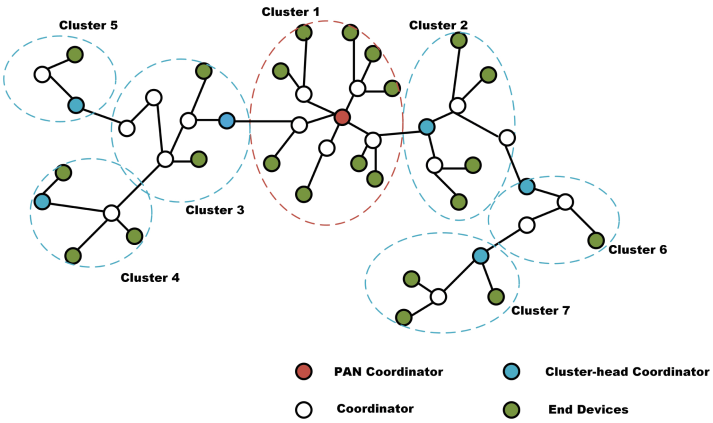


**Fig. 2.** Cluster-tree topology.

**Table 1.** Main notation definition

| Symbols | Definition |
|---|---|
| $N$ | Total number of coordinators in neighbor list (both 1-hop and 2-hop) |
| $n$ | Number of coordinators in transmission range + $N$ |
| $\rho_N$ | The probability of $n = N$ |
| $\rho_n$ | The probability that $n > N$ |
| $p_t$ | The probability that a node chooses a slot $t_l$ that do not overlap with any of the coordinators in its neighbor list |
| $P_c$ | The collision probability |

The relatives information is provided by the parent coordinator in the form of a neighbor list. To simply put, a node requires information about its parent and all the coordinators associated to it, which may include all the coordinators grand parent and peers if any. The payload part of the beacon carries this additional information comprising of short addresses of respective coordinators followed by their *BO* and *SO*, and an association field that is of two bits. The association field allows a coordinator to determine the relative ranking which are by default *0* for a grand parent, *1* for the parent and {2, 3 or 4} for the peers sorted based on their association time. These values are set by a coordinator (read parent) in accordance to their association times. This allows a coordinator to schedule accordingly based on its priority with respect its peers.

Algorithm 1 lists the steps involved in computing a synchronized schedule. First, a coordinator awaits the reception of a beacon frame from its parent that contains all the required *BO* and *SO* information. Based on this, it determines the respective *BI* and *SD* for each neighboring coordinator. For an agreed *BO* and *SO*, the coordinator also calculates its *BI* and *SD*. The goal is to estimate neighboring coordinators schedules and synchronize with them. Based on the

information realized in the first part, a coordinator sorts all $BI$ based on the order of association and selects the maximum $BI$ ($BI_{\max}$) to fix a time cycle. This time cycle is divided into slots, where each slot equals minimum $SD$. Now, the superframe duration of a coordinator $i$, given as $SD_i$, is allocated based on first empty time slot. Based on $BI_i$, the duration of $SD_i$ is set until $BI_{\max}$ is reached. This allows a coordinator to recreate a map of beacon transmissions of all its neighbors and thus synchronize its own transmissions avoiding collisions. The gathered two hop neighborhood information prevents collisions between coordinators whose transmission ranges overlap. The probability of such an occurrence is estimated in the following sub-section.

**Algorithm 1.** Distributed beacon synchronization algorithm

1: From parent beacon, obtain $BO$, $SO$, and association order.
2: Compute $BI$ for all received $BO$, $SO$, represented by set $B$, for all $BI_i$.
3: Compute $BI_{\min} = 2^{BO_{\min}}$ and $BI_{\max} = 2^{BO_{\max}}$.
4: Sort $B$ based on association order for each $BI$.
5: Set $time - line = BI_{\max}$, where slot $= \min(SD_i), 1 \leq i \leq N$
6: **for** each $i$ in $B$ **do**
7: find the first available consecutive time slots $\geq SD_i$
8: fix $(i)$ of $SD_i$ in consecutive time slots beginning with first empty slot
9: **end for**
10: **return** The coordinators time slot.

### 3.3 Illustrative Example of 2-hop DBS

To illustrate the 2-hop DBS algorithm, assume a simple hierarchy where a coordinator c2 is associated with coordinator c1, and coordinators c3 and c4 are associated to c2. That is, c1 is parent of c2 and grand parent of c3 and c4. Let {c1, c2, c3} be already synchronized and transmitting beacons. Now, node c4 that needs to compute its schedule, retrieves the required $BO$, $SO$ and association order parameters from its parent (c2's) beacon payload. Table 2 shows the configuration of c4. Based on received parameters, c4 computes corresponding $BI$ and $SD$ for each coordinator. Then, it chooses the maximum $BI$, $BI_{\max} = 16$, and minimum $BI$, $BI_{\min} = 8$, where each time slot corresponds to a base superframe duration, $SO = 0$. BI values are further arranged to form a ordered set $B = \{16(c1), 8(c2), 16(c3), 8(c4)\}$ with respect to their order of association.

Next, from the set $B$, c4 schedules each instance of $SD$ of the corresponding coordinator in the first available slot of size $SD$ time slots in such a way that it does not overlap with other superframe durations. Subsequent instances are placed at a distance equal to a multiple of $BI_{\min} = 8$ time slots from the first instance corresponding to its $BI$. We place $SD$ of c1 in first horizontal line. Then c2 is placed after the instance of c1. Afterward, c3 is placed in the third horizontal line after the c2. Finally c4 is placed after the instance of coordinator c3. The instances are repeated according to the coordinators' $BI$. The schedule is periodically repeated after a slotted timeline of 16 slots ($BI_{\max}$). The final beacon schedule computed by c4 is shown in Fig. 3 upto 32 timeslots.

**Table 2.** Configuration of c4

| Coordinator | SD | BI | Association order |
|---|---|---|---|
| c1 (grand parent) | 2 | 16 | 0 |
| c2 (parent) | 2 | 8 | 1 |
| c3 (sibling) | 1 | 16 | 2 |
| c4 | 2 | 8 | 3 |

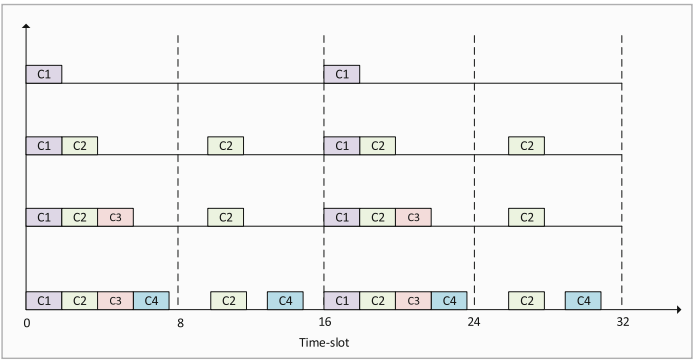


**Fig. 3.** Beacon schedule for coordinator c4.

### 3.4 Collision Probability with 2-hop Information

Consider an all probable scenario where all $n$ devices of coordinator $A$ aim for beacon transmission. Relying on $N$ (obtained from the proposed scheme), $A$ can compute a non overlapping transmission schedule. But, in case of $n > N$, a set of $k$ coordinators ($k < n$) exist that are within $A$*'s* reach but not accounted while realizing schedule. This issue can be categorized as the problem of overlapping schedules with one of $n_1, n_2, ..., n_k$ coordinators. Inherently, this can be viewed as $N \subset n$. That is, we need to account for transmission of those $(n - N)$ nodes. For simplicity, let us assume that all the devices that are within the range of $A$ are also present in the neighbor list obtained by $A$. That is $n = N$. Consider the probability of such an occurrence is $\rho_N$. Alternatively, for the case of $n > N$, the probability be $\rho_n$. Also, $\rho_N = (1 - \rho_n)$. In a given scenario of $n > N$, device $A$ determines a time slot $t_l$ with $p_t$ probability. This time line avoids collisions with all devices in the neighbor list but may still collide with unaccounted $(n - N)$ nodes. The probability of non-occurrence of such an event is given by

$$(1 - p_t)^{n-N} \tag{1}$$

This means that the remaining $(n - N)$ devices have not chosen the same time slot as $A$. It in turn means that a node $A$ has chosen a collision free time slot $t_l$ with probability $p_t(1-p_t)^{2(n-N)}$. Let $P_c$ be the collision probability with

one of $(n - N)$ if it selects same slot $t_l$. So,

$$P_c = 1 - (1 - p_t)^{2(n-N)}. \tag{2}$$

To account for a scenario of $n = N$, let a device select a time slot $t_l$ with a probability $p_t$ based on the proposed scheme. Accordingly, the rest of the $(N-1)$ nodes not selecting the same slot $t_l$ is given by $(1 - p_t)^{N-1}$. Since, the proposed scheme makes sure that no two coordinators select the same $t_l$, the probability of collision $P_c$ in this case is 0. This is achieved with the help of association order that is assigned by the coordinators parent resolving colliding beacon schedules between neighbouring coordinators.

## 4 Simulation Results and Discussion

In this section, we compare the proposed algorithm with the centralized and distributed schemes presented in [7,10], respectively. We have used the network simulator NS-2.34 [16] to evaluate the aforementioned protocols. Parameters that are used in the experiments are listed in Table 3. An 802.15.4 cluster tree network consisting of seven clusters, where 23 devices act as coordinators and another 24 devices are associated with these coordinators as end devices. Figure 2 represents the network set up. The protocols performance is distinguished in terms of number of transmissions, energy consumed and utilization of the channel. For simplicity, we do not consider any battery model and assume one unit of energy is spent per byte transmission.

To achieve synchronization, all the coordinators need to transmit messages and this forms the basis of our first experiment. In other words, we measure the transmission count that is necessary for synchronization. Each coordinator exchanges beacons with the neighboring devices to determine their respective slots of transmission. More the number of such transmissions more the network overhead. Figure 4 shows a linear increase in number of transmissions for a centralized scheme like [7], as the size of the network grows. It is due to the fact that the overall central coordinator determines the beacon schedules of all other coordinators in the network and transmits these to respective coordinators that may be located multiple hops away. To achieve this a routing protocol like ZigBee [17] can be used. On the contrary, distributed mechanism like MeshMAC achieves synchronization within fewer number of transmissions as it depends on all the neighboring coordinators. However, this is still higher compared to the proposed algorithm, as the 2-hop DBS relies only on the neighbor list from the parent coordinator thus restricting the transmission count to 2 for each coordinator. Thus, the proposed mechanism achieves synchronization with 30% lesser transmissions when compared to MeshMAC making it more scalable.

Next, we evaluate aforementioned schemes for average energy consumption with respect to the height of cluster-tree. Since, energy consumed is directly proportional to transmission count, and as SDS is shown to incur more transmissions, we mainly focus on the other two schemes. Figure 5 shows the comparison graph. The proposed scheme consumes lesser energy over MeshMAC as

**Table 3.** Simulation parameters

| Parameters | Values |
|---|---|
| Frequency of operation | 2.4 GHz |
| Total nodes | 48 |
| Tx range | 50 m |
| Tx Power | −7 dBm |
| BO | 8 |
| SO | 4 |
| BI | 245760 symbols |
| SD | 15360 symbols |

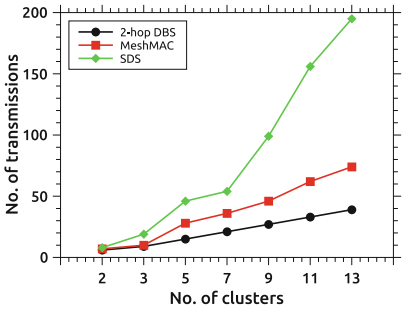


**Fig. 4.** Comparison of transmission overhead.

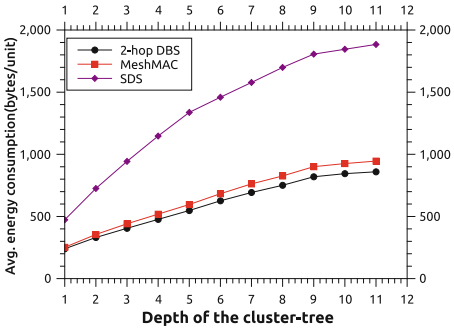


**Fig. 5.** Comparison of energy consumption.

the transmissions related to computation of beacon offset are kept to minimum. Conversely, in case of MeshMAC it varies with the degree of a coordinator. In other words, it depends on the number of neighboring coordinators that a node has to consider to compute its offset. Lesser dependencies contribute to energy efficiency in case of our scheme.

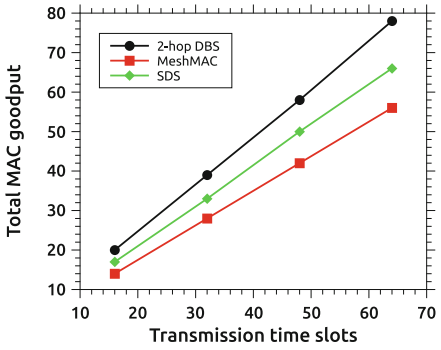


**Fig. 6.** Channel utilization of the schemes.

Beacon synchronization results in effective channel utilization in the network. This forms the basis of our final experiment that is to evaluate the channel utilization of all three synchronization mechanisms. The results are presented in Fig. 6. For a given *BO* and *SO*, the centralized scheme computes non-overlapping beacon schedules for all the coordinators in the network. This results in non optimal allocation as the central coordinator aims to assign completely non overlapping schedules even though the coordinators in contention are not in collision range of each other. Similarly, depending on superframe duration *SD* MeshMac also reports sub-optimal schedule, especially if the coordinator needs a shorter *SD*. On the other hand, the proposed scheme resolves synchronization transmission conflicts based on the cumulative information provided by the parent, it registers better channel utilization. In a dynamic network setting where different clusters may resort to different *BO* and *SO* parameter settings (based on the requirements of associated devices), the proposed mechanism has a near optimal solution. The increase in channel utilization compared to other two schemes respectively are 15% and 28%. The point to be noted is that even though the centralized scheme incurs higher transmission overhead, it offers better channel utilization.

## 5 Conclusion and Future Scope

In this paper, we presented a distributed beacon synchronization mechanism named 2-hop DBS, designed for peer-to-peer cluster-tree topologies. The proposed mechanism uses beacon information of 2-hop coordinators to compute a non-overlapping beacon schedule. The required information is provided by a parent coordinator as part of the beacon payload. This scheme is shown to perform 28% better in terms channel utilization compared to MeshMAC. Further, it does not need an active routing protocol that adheres to device constraints by minimizing the complexity of synchronization. This process may be further simplified for sparse topologies where the probability of beacon collisions is low.

**Acknowledgement.** This work is partially supported by National Natural Science Foundation of China Grant 61401107.

## References

1. IEEE Std 802.15.4: wireless medium access control (MAC) and physical layer (PHY) specifications for low-rate wireless personal area networks (WPANs). http://www.ieee.org/Standards/
2. Al Rasyid, M.U.H., Saputra, F.A., Ismar, M.R.: Performance of multi-hop networks using beacon and non-beacon scheduling in wireless sensor network (WSN). In: Proceedings of the International Electronics Symposium (IES), Surabaya, Indonesia, pp. 195–199, September 2015
3. Yeh, L.-W., Pan, M.-S.: Beacon scheduling for broadcast and convergecast in ZigBee wireless sensor networks. Comput. Commun. **38**, 1–12 (2014)
4. Zhu, C., Chen, Y., Wang, L., Shu, L., Zhang, Y.: Smac-based proportional fairness backoff scheme in wireless sensor networks. In: Proceedings of the ACM IWCMC, Caen, France, pp. 138–142, July 2010
5. Dong, X., Huo, Y., Zhu, C., Lv, S., Li, W., Wang, X.: RTC: link schedule based MAC design in multi-hop wireless network. In: QSHINE, 2015 11th International Conference on IEEE, Taipei, Taiwan, pp. 292–297, August 2015
6. Jin, X., Zhang, Q., Zeng, P., Kong, F., Xiao, Y.: Collision-free multichannel superframe scheduling for IEEE 802.15. 4 cluster-tree networks. Int. J. Sens. Netw. **15**(4), 246–258 (2014)
7. Koubâa, A., Cunha, A., Alves, M., Tovar, E.: TDBS: a time division beacon scheduling mechanism for ZigBee cluster-tree wireless sensor networks. Springer Real-Time Syst. **40**(3), 321–354 (2008)
8. Burda, R., Wietfeld, C.: A distributed and autonomous beacon scheduling algorithm for IEEE 802.15.4/ZigBee networks. In: Proceedings of the IEEE International Conference on Mobile Adhoc and Sensor System, Pisa, Italy, pp. 1–6, October 2007
9. Toscano, E., Bello, L.L.: Multichannel superframe scheduling for IEEE 802.15.4 industrial wireless sensor networks. IEEE Trans. Ind. Informat. **8**(2), 337–350 (2012)
10. Muthukumaran, P., de Paz, R., Spinar, R., Pesch, D.: MeshMAC: enabling mesh networking over IEEE 802.15.4 through distributed beacon scheduling. In: Zheng, J., Mao, S., Midkiff, S.F., Zhu, H. (eds.) ADHOCNETS 2009. LNICST, vol. 28, pp. 561–575. Springer, Heidelberg (2010). https://doi.org/10.1007/978-3-642-11723-7_38
11. Gilani, M.H.S., Sarrafi, I., Abbaspour, M.: An adaptive CSMA/TDMA hybrid MAC for energy and throughput improvement of wireless sensor networks. Elsevier Ad Hoc Netw. **11**(4), 1297–1304 (2013)
12. Jeon, H.-I., Kim, Y.: BOP (beacon-only period) and beacon scheduling for MEU (mesh-enabled USN) devices. In: Proceedings of the IEEE 9th International Conference on Advanced Communication Technology, Gangwon-Do, Korea, vol. 2, pp. 1139–1142, February 2007
13. Baseri, M., Motamedi, S.A., Maadani, M.: A load-adaptive beacon scheduling algorithm for IEEE 802.15.4 mesh topology improving throughput and qos in (WMSNs). In: Proceedings of the Computing, Communication and Networking Technologies, Hefei, China, pp. 1–5, July 2014

14. de Paz Alberola, R., Villaverde, B.C., Pesch, D.: Distributed duty cycle management (ddcm) for IEEE 802.15. 4 beacon-enabled wireless mesh sensor networks. In: Proceedings of the IEEE 8th International Conference on Mobile Ad-Hoc and Sensor System, Valencia, Spain, pp. 721–726, October 2011
15. Choudhury, N., Matam, R.: Distributed beacon scheduling for IEEE 802.15.4 cluster-tree topology. In: 2016 IEEE Annual India Conference (INDICON), pp. 1–6, December 2016
16. NS2-the network simulator. http://www.isi.edu/nsnam/ns
17. Zigbee specification, Alliance, ZigBee, and others. http://www.zigbee.org/download/standards-zigbee-specification/

# A Short Survey on Fault Diagnosis in Wireless Sensor Networks

Zeyu Zhang[1,2], Lei Shu[1,2(✉)], Amjad Mehmood[1], Li Yan[1], and Yu Zhang[2]

[1] Guangdong Provincial Key Lab of Petrochemical Equipment Fault Diagnosis, Guangdong University of Petrochemical Technology, Maoming 525000, China
zeyu-zhang@outlook.com, lei-shu@outlook.com, dramjad.mehmmood@outlook.com, li.yan0823@outlook.com

[2] School of Engineering, University of Lincoln, Lincoln, UK
YZhang@lincoln.ac.uk

**Abstract.** Fault diagnosis is one of the most important and demandable issues of the network. It makes the networks reliable and robust to operate in the normal way to handle almost all types of faults or failures. Additionally, it helps sensor nodes to work smoothly and efficiently till the end of their lifetime. This short survey paper not only presents a clear picture of the recent proposed techniques, but also draws comparisons and contrasts among them to diagnose the potential faults. In addition, it proposes some potential future-work directions which would lead to open new research directions in the field of fault diagnosis.

**Keywords:** Wireless Sensor Networks · Fault diagnosis · Reliability

## 1 Introduction

Wireless Sensor Networks (WSNs) consist of a large number of low-cost, spatially distributed, small-in size, limited computation, storage and communication power sensor nodes that are deployed across the monitoring area. These nodes perform sensing, processing, communication and coordination of information with each other to achieve the common objectives autonomously. Due to recent advancement in wireless communication and electronics, micro-electro-mechanical system (MEMS) enables the resource constrained multi-functional sensor nodes to untetheredly communicate with each other in short distances. These constraints on the network makes it different form the other existing wireless networks. In WSNs, each small sensor node is composed of the following main components such as: (a) processing (b) communication (c) computation (d) power source (e) external memory (f) one or more sensors.

## 2 Fault Diagnosis Approach

According to the architecture, fault diagnosis model in WSNs consists of the following three types of approaches to handle faults: (i) Model-based or Centralized (ii) Model-less or Distributed (iii) Model-based distributed or Hybrid


M. Huang et al. (Eds.): WICON 2016, LNICST 214, pp. 21–26, 2018.
https://doi.org/10.1007/978-3-319-72998-5_3

approaches, each one of which is explained in detail with the help of most recent relevant work available in the literature, see in Fig. 1.

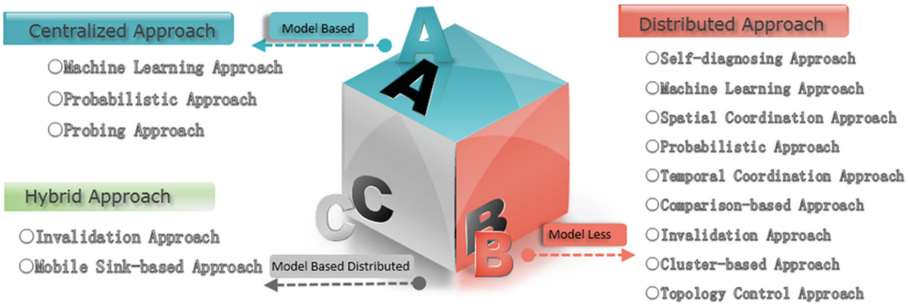


**Fig. 1.** Fault diagnosis categorization and approaches

### 2.1 Model-Based or Centralized Approach

As name indicates, an ultra-reliable centralized sensor node called sink node, with large storage, interrupted power supply and high computational power, is placed logically or geographically in the center. The base station or sink node periodically injects health requests or queries messages to determine the state of each sensor node deployed in the field. There are many techniques available in the literature of WSNs which have followed the centralized approaches for the purpose of fault detection and diagnosis.

### 2.2 Model-Less or Distributed Approach

Unlike model-based or centralized approach, each sensor node in model-less or distributed approach takes decision about their health status by gathering and analyzing diagnostic response results from the neighboring nodes. Then it updates the BS accordingly. Therefore, the model-less approaches transfer a little information to the BS that helps in prolonging the lifetime. It further reduces a lot of traffic overhead, and minimizes the end-to-end delay over the network. There are many recent techniques in the literature which have followed the distributed approaches for fault diagnosis and detection.

### 2.3 Distributed Model-Based or Hybrid Approach

It combines the advantages of both centralized (model based) and distribute approach (model-less), and avoids the limitations of both. According to literature, the model based distributed approaches are preferred in terms of reliability, robustness, energy efficiency, and minimizes traffic overhead. So these approaches

**Table 1.** Analysis with respect to different fault diagnosis parameters

| Author | Year | Diagnosis network | | | Diagnosis view | | | Fault persistence | | Fault type | | Approach |
|---|---|---|---|---|---|---|---|---|---|---|---|---|
| | | Distributed | Centralized | Hybrid | Local | Global | Permanent | Intermittent | Transient | Hard | Soft | |
| Shahram et al. [3] | 2013 | ✓ | | | ✓ | ✓ | ✓ | | ✓ | ✓ | ✓ | Self-diagnosing |
| Miao et al. [16] | 2013 | | ✓ | | | ✓ | | ✓ | ✓ | | ✓ | Machine learning |
| Kulla et al. [12] | 2013 | ✓ | | | ✓ | | | ✓ | ✓ | ✓ | ✓ | Machine learning |
| Banerjee et al. [4] | 2014 | | | ✓ | ✓ | ✓ | ✓ | ✓ | ✓ | ✓ | ✓ | Spatial-temporal coordination |
| Chanak et al. [5] | 2013 | ✓ | | | ✓ | | ✓ | | ✓ | ✓ | ✓ | Spatial coordination |
| Alessandra et al. [7] | 2013 | ✓ | | | ✓ | | | ✓ | ✓ | | ✓ | Probabilistic |
| Dima et al. [10] | 2013 | ✓ | | | ✓ | | ✓ | ✓ | ✓ | ✓ | ✓ | Spatial coordination |
| Bill et al. [13] | 2014 | | ✓ | | | ✓ | | ✓ | ✓ | | ✓ | Probabilistic |
| Arunanshu et al. [15] | 2014 | ✓ | | | ✓ | | ✓ | ✓ | | ✓ | ✓ | Comparison-based |
| Manmath et al. [21] | 2014 | ✓ | | | ✓ | | ✓ | ✓ | | ✓ | ✓ | Spatial coordination |
| Mehdi et al. [2] | 2014 | ✓ | | | ✓ | | ✓ | ✓ | ✓ | ✓ | ✓ | Cluster-based |
| Yu et al. [25] | 2014 | | ✓ | | | ✓ | ✓ | ✓ | ✓ | ✓ | ✓ | Model-based |
| Arunanshu et al. [15] | 2013 | ✓ | | | ✓ | | ✓ | ✓ | ✓ | ✓ | ✓ | Invalidation |
| M. Panda et al. [18] | 2015 | ✓ | | | ✓ | | ✓ | ✓ | ✓ | ✓ | ✓ | Self-diagnosing |
| Yuan et al. [26] | 2015 | ✓ | | | ✓ | | | ✓ | | | ✓ | Probabilistic |
| Zafar et al. [27] | 2015 | | | ✓ | ✓ | ✓ | | ✓ | ✓ | | ✓ | Invalidation |
| Dhal et al. [8] | 2015 | | ✓ | | | ✓ | | ✓ | ✓ | | ✓ | Topology control |
| Gong et al. [9] | 2015 | | ✓ | | | ✓ | | ✓ | ✓ | | ✓ | Probing |
| Meenakshi et al. [19] | 2015 | ✓ | | | ✓ | | | ✓ | ✓ | | ✓ | Majority voting |
| Lo et al. [14] | 2016 | | | ✓ | ✓ | ✓ | | ✓ | ✓ | | ✓ | Spatial coordination |
| Chafig et al. [23] | 2015 | ✓ | | | ✓ | ✓ | | ✓ | ✓ | | ✓ | Probabilistic |
| Jin et al. [11] | 2015 | | ✓ | | ✓ | ✓ | | ✓ | ✓ | | ✓ | Model-based |
| Mohammed et al. [1] | 2015 | | | ✓ | | ✓ | ✓ | ✓ | ✓ | ✓ | ✓ | Mobile sink-based |
| Christopher et al. [17] | 2016 | | ✓ | | | ✓ | | ✓ | ✓ | | ✓ | Topology control |
| Panigrahi et al. [20] | 2016 | ✓ | | | ✓ | | | ✓ | ✓ | | ✓ | Spatial coordination |
| Zhen et al. [29] | 2016 | | ✓ | | | ✓ | | ✓ | ✓ | | ✓ | Model-based |
| Hongsheng et al. [24] | 2016 | ✓ | | | ✓ | | ✓ | ✓ | ✓ | ✓ | ✓ | Spatial coordination |
| Zhang et al. [28] | 2016 | ✓ | | | ✓ | ✓ | ✓ | ✓ | ✓ | ✓ | ✓ | Spatial coordination |
| Tang et al. [22] | 2016 | ✓ | | | ✓ | ✓ | | ✓ | ✓ | | ✓ | Machine learning |
| Chanak et al. [6] | 2016 | | | ✓ | ✓ | ✓ | ✓ | ✓ | ✓ | ✓ | ✓ | Mobile sink-based |
| Chanak et al. [5] | 2016 | ✓ | | | ✓ | | ✓ | ✓ | | ✓ | ✓ | Probabilistic |

bridge the gap between the centralized, and distributed approaches. There are a few techniques available in the literature based on the subject cited above.

Table 1 presents some of the most important and recent protocols, which have been presented in the literature, are classified on the basis of different parameters of fault diagnosis. It would help the researchers to find the current trends of the protocols. It also illustrates the advantages and limitation of each. In order to contribute a more demanded-able protocol to be robust, reliable, energy-efficient for the domain.

## 3 Open Research Challenges

WSNs have steadily become a cutting edge technology of the $21^{st}$ century for the development of wireless sensor applications. It is the most important area because its applications applying to almost all walks of life. Due to its importance, a lot of work has been performed in last one decade, nevertheless the area still demands more work to be done in order to fulfill the current requirements. The followings are some challenges listed below which need be focused:

1. More intelligent algorithms are required for the purpose of fault diagnosis and detection
2. Nodes are required to be diagnosed while performing their usual task simultaneously
3. The network must be prepared for load balancing efficiently specially in the case of multi-media sensor nodes
4. It is required to be adaptive to dynamics changes occurring such as topology, transmission ranges etc.
5. Intelligent movable robot needs to be proposed for diagnosis and detection
6. QoS-based fault diagnosis needs to be concentrated on network energy consumption and link quality
7. Malicious activities and threats are required to be tracked in order to operate uninterruptedly
8. Damaged link diagnosis and detection need to be addressed in large scale WSNs
9. After diagnosing the faulty nodes, they are required to be recovered or reused as much as possible (communication, storage, computation)
10. A cross layer approach to deal with the reliability and robustness of the network

## 4 Conclusion

This short survey provides a big picture of promising techniques for fault diagnosis and detection existing till date. It also elaborates their strong and weak points. It is believed that this survey will be appreciated, helpful in proposing more robust, reliable, scalable, real-time, mobile, energy-efficient, and intelligent protocols in the near future.

**Acknowledgments.** This work is supported by International and Hong Kong, Macao & Taiwan collaborative innovation platform and major international cooperation projects of colleges in Guangdong Province (No. 2015KGJHZ026) and Guangdong University of Petrochemical Technology Internal Project 2012RC106. Lei Shu is the corresponding author.

## References

1. Abo-Zahhad, M., Ahmed, S.M., Sabor, N., Sasaki, S.: Mobile sink-based adaptive immune energy-efficient clustering protocol for improving the lifetime and stability period of wireless sensor networks. IEEE Sens. J. **15**(8), 4576–4586 (2015)
2. Afsar, M.M.: Maximizing the reliability of clustered sensor networks by a fault-tolerant service. In: 2014 IEEE 27th Canadian Conference on Electrical and Computer Engineering (CCECE), pp. 1–8. IEEE (2014)
3. Babaie, S., Khosrohosseini, A., Khadem-Zadeh, A.: A new self-diagnosing approach based on petri nets and correlation graphs for fault management in wireless sensor networks. J. Syst. Archit. **59**(8), 582–600 (2013)
4. Banerjee, I., Chanak, P., Rahaman, H., Samanta, T.: Effective fault detection and routing scheme for wireless sensor networks. Comput. Electr. Eng. **40**(2), 291–306 (2014)
5. Chanak, P., Banerjee, I.: Fuzzy rule-based faulty node classification and management scheme for large scale wireless sensor networks. Expert Syst. Appl. **45**, 307–321 (2016)
6. Chanak, P., Banerjee, I., Sherratt, R.S.: Mobile sink based fault diagnosis scheme for wireless sensor networks. J. Syst. Softw. **119**, 45–57 (2016)
7. De Paola, A., Lo Re, G., Milazzo, F., Ortolani, M.: QoS-aware fault detection in wireless sensor networks. Int. J. Distrib. Sens. Netw. (2013)
8. Dhal, R., Torres, J.A., Roy, S.: Detecting link failures in complex network processes using remote monitoring. Phys. A Stat. Mech. Appl. **437**, 36–54 (2015)
9. Gong, W., Liu, K., Liu, Y.: Directional diagnosis for wireless sensor networks. IEEE Trans. Parallel Distrib. Syst. **26**(5), 1290–1300 (2015)
10. Hamdan, D., Parissis, I., Hijazi, A., El Hassan, B., et al.: Test and diagnosis of wireless sensor networks applications. In: 2013 World Congress on Computer and Information Technology (WCCIT), pp. 1–7. IEEE (2013)
11. Jin, X., Chow, T.W., Sun, Y., Shan, J., Lau, B.C.: Kuiper test and autoregressive model-based approach for wireless sensor network fault diagnosis. Wireless Networks **21**(3), 829–839 (2015)
12. Kullaa, J.: Detection, identification, and quantification of sensor fault in a sensor network. Mech. Syst. Signal Process. **40**(1), 208–221 (2013)
13. Lau, B.C., Ma, E.W., Chow, T.W.: Probabilistic fault detector for wireless sensor network. Expert Syst. Appl. **41**(8), 3703–3711 (2014)
14. Lo, C., Lynch, J.P., Liu, M.: Distributed model-based nonlinear sensor fault diagnosis in wireless sensor networks. Mech. Syst. Signal Process. **66**, 470–484 (2016)
15. Mahapatro, A., Khilar, P.M.: Fault diagnosis in wireless sensor networks: a survey. IEEE Commun. Surv. Tutor. **15**(4), 2000–2026 (2013)
16. Miao, X., Liu, K., He, Y., Papadias, D., Ma, Q., Liu, Y.: Agnostic diagnosis: discovering silent failures in wireless sensor networks. IEEE Trans. Wirel. Commun. **12**(12), 6067–6075 (2013)
17. Oßner, C., Buchmann, E., Böhm, K.: Identifying defective nodes in wireless sensor networks. Distrib. Parallel Databases 1–20 (2016)

18. Panda, M., Khilar, P.M.: Distributed self fault diagnosis algorithm for large scale wireless sensor networks using modified three sigma edit test. Ad Hoc Netw. **25**, 170–184 (2015)
19. Panda, M., Khilar, P.: Distributed Byzantine fault detection technique in wireless sensor networks based on hypothesis testing. Comput. Electr. Eng. **48**, 270–285 (2015)
20. Panigrahi, T., Panda, M., Panda, G.: Fault tolerant distributed estimation in wireless sensor networks. J. Netw. Comput. Appl. **69**, 27–39 (2016)
21. Sahoo, M.N., Khilar, P.M.: Diagnosis of wireless sensor networks in presence of permanent and intermittent faults. Wirel. Pers. Commun. **78**(2), 1571–1591 (2014)
22. Tang, P., Chow, T.W.: Wireless sensor-networks conditions monitoring and fault diagnosis using neighborhood hidden conditional random field. IEEE Trans. Ind. Inform. **12**(3), 933–940 (2016)
23. Titouna, C., Aliouat, M., Gueroui, M.: FDS: fault detection scheme for wireless sensor networks. Wirel. Pers. Commun. **86**(2), 549–562 (2016)
24. Xu, H., Zhang, R., Lin, C., Ma, Y.: Novel approach of fault diagnosis in wireless sensor networks node based on rough set and neural network model. Int. J. Future Gener. Commun. Network. **9**(4), 1–16 (2016)
25. Yu, C.B., Hu, J.J., Li, R., Deng, S.H., Yang, R.M.: Node fault diagnosis in WSN based on RS and SVM. In: 2014 International Conference on Wireless Communication and Sensor Network (WCSN), pp. 153–156. IEEE (2014)
26. Yuan, H., Zhao, X., Yu, L.: A distributed Bayesian algorithm for data fault detection in wireless sensor networks. In: 2015 International Conference on Information Networking (ICOIN), pp. 63–68. IEEE (2015)
27. Zafar, A., Wajid, B., Akram, B.A.: A hybrid fault diagnosis architecture for wireless sensor networks. In: International Conference on Open Source Systems & Technologies (ICOSST), pp. 7–15. IEEE (2015)
28. Zhang, Y., Yuan, X.: Fault diagnosis in clustering WSN based on neighbor cooperation. In: 2016 Chinese Control and Decision Conference (CCDC), pp. 1803–1807. IEEE (2016)
29. Zhen, F., JingQi, F., Wei, S.: The gateway anomaly detection and diagnosis in WSNs. In: 2016 Chinese Control and Decision Conference (CCDC), pp. 2401–2406. IEEE (2016)

# Research on Data Storage Scheme Under Sink Failures in Wireless Sensor Networks

Yue Wang and Jun Wang(✉)

Department of Communication and Information Engineering,
Nanjing University of Posts and Telecommunications, Nanjing 210003, Jiangsu, China
980941416@qq.com, wang_jun@njupt.edu.cn

**Abstract.** In remote and inaccessible environment, sensory data must be stored inside the network in case of sink failures. Since all sensor nodes have limited storage capacity and energy, so we need to ensure that the most important and urgent data can be stored and decoded first. In this paper, we studied the data storage problem in sink-failures sensor networks. Considering that most existing algorithms mainly focus on how to maximized number of stored data, which makes the loss of the most critical data, so we design a novel network coding data storage scheme based on priority named NCSP (Network Coding Storage with Priority). In this scheme, in order to prevent the loss of the most critical information, data in the networks are divided into independent priority groups. Different network coding schemes are used in different groups. Aggressiveness mechanism is also considered in this paper. Finally, MATLAB simulations results demonstrate that NCSP outperforms than other algorithms in terms of decoding priority.

**Keywords:** Wireless sensor networks · Network Coding Storage
Priority mechanism · Fountain code · LT code · iLT code

## 1 Introduction

Many sensor network applications are deployed in hash environment (such as remote or unattended regions) and need to take a long time to monitor a large number of data, audio, video, images, etc. The network lifetime should be as long as possible until the specific monitoring tasks are completed. However some nodes including sink nodes may fail due to a variety of reasons (battery depletion, enemy attacks and challenge environment). In the case of sink nodes failure, connections between common sensor nodes and sink nodes are intermittent, therefore common sensor nodes are required to collect and store data before replacing or renewing the failed sinks. Therefore the research on the failure of nodes in wireless sensor networks has aroused people's concern and attention.[1]

[1] This work is supported by National Nature Science Foundation of China 61401234, 61271234, and PAPD Project of Jiangsu Higher Education Institutions.


M. Huang et al. (Eds.): WICON 2016, LNICST 214, pp. 27–35, 2018.
https://doi.org/10.1007/978-3-319-72998-5_4

In order to find a better solution of the data storage problem of sink-failures sensor networks in challenging environment, in this paper we propose a more applicable distributed data storage scheme. The main contribution of this work is as follows. Firstly, we study different storage schemes for wireless sensor networks (WSNs) in hostile environments and find the distributed coding scheme based on fountain codes is the most suitable scheme for data storage in wireless sensor networks. Secondly, in order to protect the most critical data, we design a network coding data storage scheme based on the data's priority, NCSP. The simulation results show it is more effective than other schemes in terms of decoding priority. Lastly, we also consider aggressiveness mechanism to subdivide the priorities of data.

The rest of this paper is organized as follows. Section 2 presents the related works. In Sect. 3, a new network coding data storage scheme based on priority is proposed. In Sect. 4, simulation results and analysis are given. Section 5 concludes the paper and gives suggestions for further study.

## 2 Related Works

In this paper, we divide different storage schemes into several classes, as shown in Fig. 1.

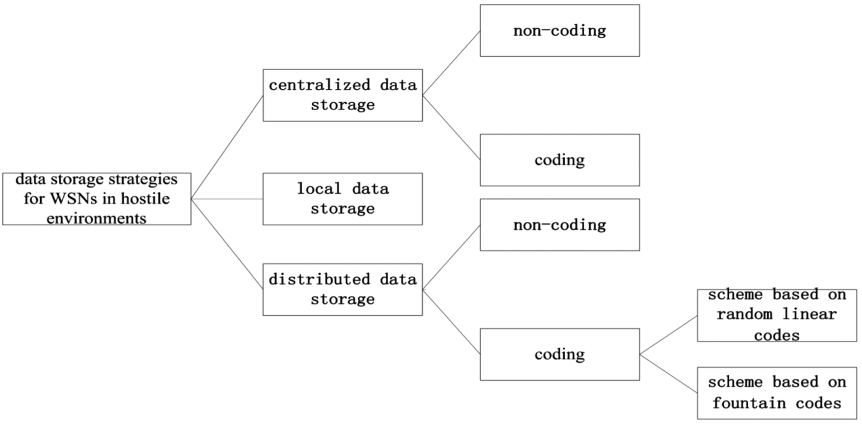


**Fig. 1.** Classification of WSNs storage schemes.

The centralized non-coding data storage scheme is controlled by the central coordinator. In [1], authors tried to assign different sensory data with different priorities and aim to maximize the preserved data priorities. Besides, data priorities were specified in advance. In reality, the data characteristics of different sensor networks are different. The priority of the data should be arranged according to the unique characteristics of the data. In the local data storage scheme, sensing data are only stored by sensor nodes in their own memories. The user will broadcast the querying request to the whole sensor network. In the distributed non-coding data storage scheme, data distribution is dependent on the cooperative communication mechanism between nodes. So, it is suitable for the scenario where the network topology is changed dynamically. Reference [2]

mainly focused on how to increase the lifetime of the data stored in the network. By redistributing data from the nodes with low energy to those with high energy, the algorithm slowed the loss of data to a certain extent. But they assumed that the sensor nodes only had a unit of storage and the source node only had one item of data. Such a network was too simple to exist in the reality.

In some cases, such as the limited resources of sensor nodes, the distributed code data storage is easier and more efficient than the centralized code data storage. According to the different coding method, the distributed coding data storage is classified into two categories: schemes based on random linear codes and schemes based on fountain codes.

The complexity of encoding and decoding is also high. Therefore, random linear codes [3, 4] are not suitable for the sensor nodes with limited energy and computing power. PRLC [3] proposed a random linear coding scheme based on priority to process data with different priorities. The main idea was to assign different coding rates for data with different priorities. That is, the lower coding rate was distributed to the data with higher priority. But in this scheme, the transmission of data packets was dependent on geographic routing. In addition, PRLC could not guarantee that all data were successfully decoded.

The retrieval of data only occurs in a small area at most time. GRLC [4] proposed a random linear code scheme based on the geographical location. According to the size of the geographic area, data in different geographic regions were stored by hierarchical coding. But GRLC was also dependent on geographic routing.

Fountain codes are easy to realize in wireless sensor networks, because the complexity of coding and decoding is relatively low. Therefore, fountain codes are very suitable for data storage in wireless sensor networks.

We show the comparison of different data storage schemes as follows (Table 1):

**Table 1.** Comparison of different data storage schemes.

| Classification | Data storage scheme | | |
|---|---|---|---|
| | *Centralized data storage* | *Local data storage* | *Distributed data storage* |
| *Advantages* | Simple structure, convenient query | Simple structure and query, no data forwarding overhead | Simple and fast query, suitable for distributed sensor networks |
| *Disadvantages* | A bottleneck, vulnerability | High communication overhead, short network lifetime, easily loss of data | Mapping to generate additional overhead |

In summary, the distributed coding scheme based on fountain codes is the most suitable scheme for data storage in wireless sensor networks. So we use different fountain codes with different characteristics in our proposed scheme. In the existing algorithms, the priority of the data was always arranged in advance. And they also assumed that the energy is infinite. But in this paper, data priorities are dynamically allocated in accordance with specific conditions. The initial energy and storage space of nodes are limited

and can't be added. In additional, it is dependent on cooperative communication between nodes instead of geographic routing.

## 3 Network Coding Data Storage Scheme Based on Priority (NCSP)

Network model: There are n sensor nodes randomly deployed in a square area of L * L, and an intermittent connection of sink node and sensor nodes. The packet size is equal in length. The number of iterations is k. The channel of the coding data packets is BEC. The packet loss rate is q = 0.05. Belief Propagation is used.

In this paper we made the following assumptions:

(1) The source data package is modeled as a sequence of data items and each data item has the same unit size.
(2) Since sensor nodes are uniformly distributed, the energy of transfer any one data between any one hop is regarded as 1 unit in the entire network. For each node, sending or receiving a data item consumes the energy of 0.50 unit. If it is the intermediate node, forwarding a data item consumes the energy of 1 unit (both receiving and sending).
(3) For an arbitrary sensor node *i*, its initial energy and storage space are limited. Due to harsh external environment, the node also has a failure ratio of 0.40.

According to the idea of the algorithm, the flow chart is constructed as shown in Fig. 2:

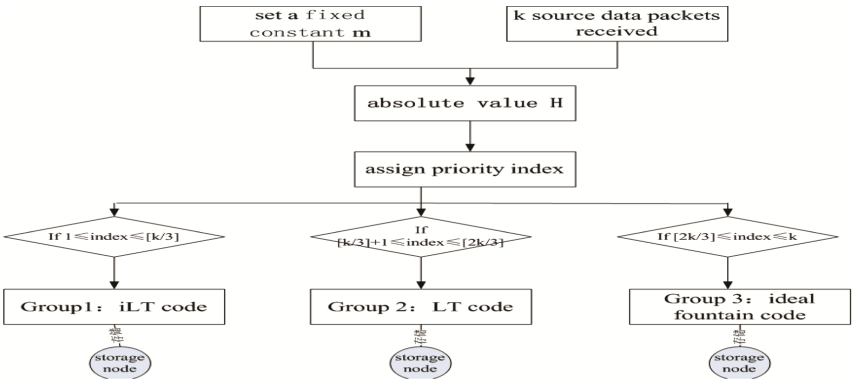


**Fig. 2.** Flow chart of the algorithm.

In this paper, in order to maximize the delivery ratio of the most important data, we propose a new data storage scheme based on both network code and data priority. We divide data into different groups according to the priority, and use different coding methods in the different group, so as to ensure the important data to be better protected.

The process of the algorithm is divided into the following stages:

### 3.1 Coding Preparation Stage

According to the different information that source data packets carried, different priorities for each packet are assigned.

According to the different quantities and values of information that each packet carried, we assign corresponding priority for each packet. The priority is stored in the head of each packet. Priority is in reverse proportion to the importance of the packet which means that the most important data will have the minimum priority and will be stored and decoded firstly.

We use the sorting method to assign the priority of data. In initial state, a fixed constant $m$ is given, which indicates the average or normal value of a certain measurement (the value is related to the specific application of the sensor networks). And the first received data's priority is set to 1 (index = 1). Then the second received data's priority is set to 2 (index = 2). The priority is related to the data's deviation from the standard value. Defining the value of $H$ is equal to the absolute value of the difference between the measurement value of each data packet and $m$. If the $H$ value of the second data packet is greater than that of the first data packet, the priorities of the data are exchanged which means the priority of the first packet is set to 2. If the $H$ of the second packet is smaller than that of the first packet, the priority of the second packet is set to 2. In the same way, we can assign corresponding priority for each packet.

### 3.2 Network Coding Stage

The priorities of the data are classified into three levels, which are coded by different coding scheme. And then they are stored in the sensor nodes in the network.

Unlike other network coding methods based on priority, we divide them into different groups according to the priority of sensor data. Encoding and decoding of important data with low decoding overhead and low error rate can ensure the success ratio of storage and retrieval of important data. According to the priority ranking, the data is divided into three groups. In different groups, we use different coding methods. Each packet is encoded and decoded in its own group, and is not affected by the other groups. We divide the data into three groups, and adopt ideal fountain code, LT [5] code and iLT [6] code respectively to encode data. For the data sets with the highest priority, the iLT code with the highest decoding rate and the lowest overhead is adopted. For the data sets with the second highest priority, the LT code with higher decoding rate and lower overhead is adopted. For the data sets with the lowest priority, the ideal fountain code with the lowest decoding rate and the highest overhead is adopted. In harsh environments, we can't completely and accurately decode all sensor data. In our scheme, it can be guaranteed that the data with highest priority will be accurately decoded with the fastest speed. It can also make the network decoding more efficiently.

### 3.3 Decoding Preparation Stage

The corresponding aggressiveness is assigned to each node.

In order to differentiate the data in the same group, and to optimize coding efficiency, the concept of "aggressiveness" is introduced in our scheme. "Aggressiveness" indicates the buffer size at the moment the node starts decoding. It is defined by the number of blocks it needs to buffer before starting to generate encoded blocks, normalized by the buffer size. By dynamically adjusting the "aggressiveness" value of higher priority data can shorten buffering latency caused by data accumulation. The aggressiveness value in our scheme is a variable. The value of priority is proportional to that of the aggressiveness. So we set the value of aggressiveness(i) as:

$$aggressiveness(i) = t \bullet index(i) \tag{1}$$

In formula (1) t is a constant (t = 2 in simulation). Since the coding data packet is always encoded by several source data packets, and each source packet carries an aggressiveness value. The total aggressiveness value follows the formula (2):

$$aggressiveness = \sum 2^{aggressiveness(i)} \tag{2}$$

The buffer size of storing the value of aggressiveness is relatively small compared with the whole storage size, so it can be neglected (Fig. 3).


**Fig. 3.** Data structure of node.

### 3.4 Decoding Stage

After processing the corresponding aggressiveness, nodes start to decode the coding packets according to their encoding method.

### 3.5 Analysis of the Algorithms

The proposed algorithm has a great performance in terms of decoding ratio of data with higher priorities. The performance can be improved by introducing the aggressiveness mechanism. Besides, as the number of nodes increases, the improvement on decoding rate becomes more obvious. Meanwhile, the promotion on decoding rate remains at a high level. It indicates when there are only several nodes in the WSNs, the contention between different priorities is not as tough as that in a large number of nodes. The results indicate that the proposed algorithm performs better in a multi-node environment.

From a theoretical analysis, different coding methods may bring some extra overhead, but the number of important data which are successfully stored and decoded will be significantly improved.

# 4 Performance Evaluation and Analysis

To verify the performance of the proposed algorithm, we conduct simulation experiments in the MATLAB environment.

The parameters are set as follows: Source data packets are generated randomly for encoding and transmission, which the length of source data packets is 500. The number of iteration is 5000, c = 0.20, $\delta = 0.80$. The channel of the coding data packets is BEC and the packet loss rate is q = 0.05. Belief Propagation is used. The node failure rate is set as 0.40.

## 4.1 Influence of the Value of Aggressiveness

Average download time is the ratio of the average decoding time to the total time. Decoding overhead is the ratio of the decoding overhead to the total overhead.

The parameters are set as follows: Source data packets are generated randomly for encoding and transmission, the length of source data packets k = 3000, constants of fountain codes c = 0.20, $\delta = 0.80$. The channel of the coding data packets is BEC channel. The packet loss rate is q = 0.05. Belief Propagation is used. The simulation result is showed in Fig. 4.

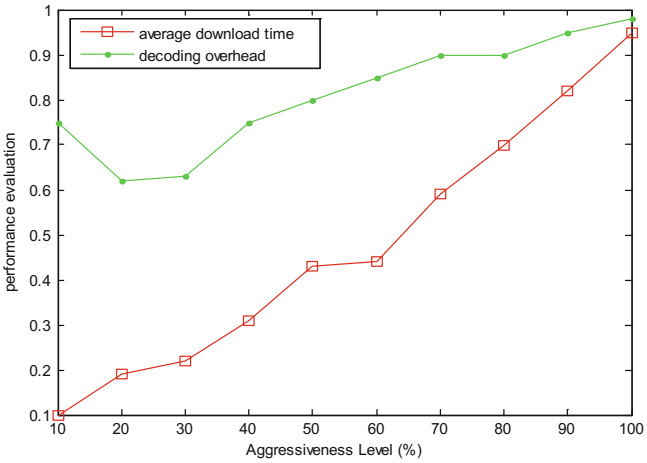


**Fig. 4.** Influence of aggressiveness.

In Fig. 4, we set aggressiveness from 10% to 100% to observe its impact to the above two parameters. As the value of aggressiveness increases, the average download time linearly increases which verified our analysis above—the nodes with smaller "aggressiveness" value will be decoded firstly. Also, decoding overhead will increase with the increase of aggressiveness. However, an extremely low aggressiveness value is also unsuitable. As shown in the graph, when the aggressiveness value is below 20%, the decoding overhead shows speed-up deterioration with the decrease of aggressiveness, which will accelerate the energy consumption. From the above analysis, we can conclude

that the system have the best performance with the aggressiveness value ranges from 20% to 50%.

### 4.2 Comparison of Different Coding Schemes

Next, we compare the performance of the following 5 schemes: only ideal fountain code (fountain), only LT code (LT), only iLT code (iLT), the coding scheme in this paper but no aggressiveness (ft+LT+iLT), the coding scheme in this paper and aggressiveness (ft +LT+iLT+aggr). The simulation result is as follows:

Shown in Fig. 5, the decoding ratio of LT code is better than that of ideal fountain code. iLT code outperforms the LT code in terms of decoding ratio. There is no obvious advantage in the decoding ratio of ft+LT+iLT when very few data packets have been transmitted. As the number of data packets sent increases, the performance on decoding ratio becomes more obvious. When more than 4000 packets have been sent, the decoding ratio is better than that of the other three methods. When the aggressiveness is introduced in the algorithm, the decoding performance can be improved.

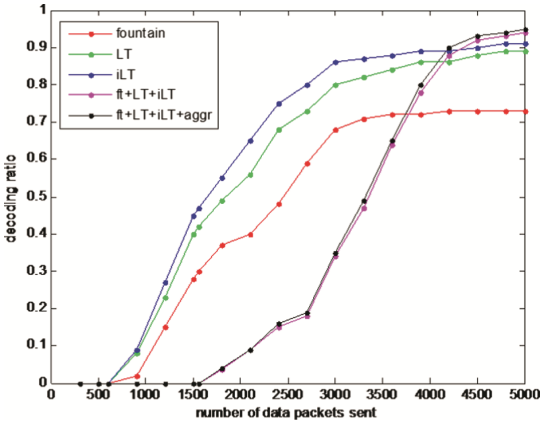


**Fig. 5.** Decoding rate of different coding schemes.

In fact, our new scheme is aim to optimize the decoding ratio of the higher priority data. Therefore, we test the decoding data packet ratio (the ratio of the data packets decoded successfully to the number of source data packets) and the decoding priority ratio (the ratio of the priorities decoded successfully to the number of total priorities) in different scenarios.

As it can be seen from Fig. 6, the proposed algorithm has a great performance on decoding ratio of higher priority data. Compared with the ideal fountain code and LT code, the total data storage capacity of iLT code is the largest. Meanwhile, the decoding ratio of the high priority data has also been increased. The proportion of high priority data which successfully decoded is significantly improved in ft+LT+iLT compared with iLT. But the total amount of data stored has decreased. When the aggressiveness is introduced, it provides more protection of the important data. When the data in the same

priority group can't be completely decoded, it adjusts the "aggressiveness" value of the important data in order to have a higher probability of successful decoding. So the successful decoding ratio of high priority data is improved further.

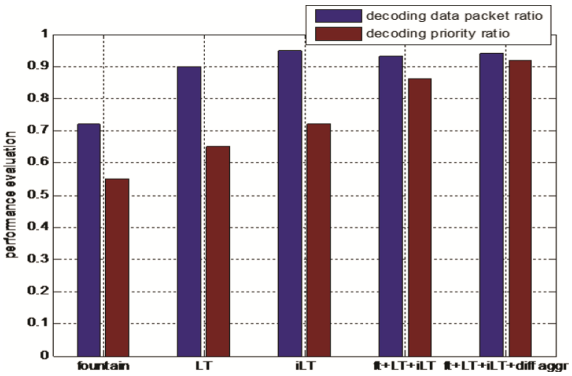


**Fig. 6.** Storage performance of different schemes.

## 5 Conclusion and Future Work

In this paper, we propose a new network coding data storage scheme based on priority to ensure the decoding ratio of the highest priority data. To a certain extent, it improves the total storage capacity, and ensures the priority storage of important data. But when the amount of data is very small, there is no obvious advantage in the decoding rate. We will explore new scheme to improve the overall decoding rate in our future work.

## References

1. Xue, X., Hou, X., Tang, B., Bagai, R.: Data preservation in intermittently connected sensor networks with data priority. In: 10th Annual IEEE Communications Society Conference on Sensor, Mesh and Ad Hoc Communications and Networks, pp. 122–130 (2013)
2. Takahashi, M., Tang, B., Jaggi, N.: Energy-efficient data preservation in intermittently connected sensor networks. In: IEEE Conference on Computer Communications Workshops, Shanghai, pp. 590–595 (2011)
3. Lin, Y., Li, B., Liang, B.: Differentiated data persistence with priority random linear code. In: Proceedings of the 27th International Conference on Distributed Computing Systems, Piscataway, NJ, pp. 47–56. IEEE (2007)
4. Lin, Y., Liang, B., Li, B.: Geometric random linear codes in sensor networks. In: Proceedings of IEEE International Conference on Communication, Piscataway, NJ, pp. 2298–2303. IEEE (2008)
5. Ye, X., Li, J., Chen, W.-T., Tang, F.: LT codes based distributed coding for efficient distributed storage in wireless sensor networks. In: 2015 IFIP (2015). ISBN 978-3-901882-68-5
6. Yang, J., Zhao, Z., Zhang, H.: Energy efficient data gathering based on distributed iLT coding. In: The 11th International Symposium on Communications & Information Technologies (ISCIT 2011) (2011)

# Impact of Irregular Radio and Faulty Nodes on Localization in Industrial WSNs

Xiaoman Ran[1,2], Lei Shu[2,3(✉)], Mithun Mukherjee[2], Yuntao Wu[1], Yuanfang Chen[2], and Zhihong Sun[1,2]

[1] School of Computer Science and Technology, Wuhan Institute of Technology, Wuhan 430205, Hubei, China
xiaoman.Ran@outlook.com, ytwu@sina.com, zhihong.sun2016@outlook.com
[2] Guangdong Provincial Key Lab of Petrochemical Equipment Fault Diagnosis, Guangdong University of Petrochemical Technology, Maoming 525000, China
{lei.shu,m.mukherjee,yuanfang_chen}@ieee.org
[3] School of Engineering, University of Lincoln, Lincoln, UK

**Abstract.** Location information of nodes is one of the basis for many applications in Wireless Sensor Networks (WSNs). In this paper, based on the implementation of the original DV-Hop localization algorithm and two variations: DV-Hop with Correction (CDV-Hop) and Improved DV-Hop (IDV-Hop), we investigate the impact of Irregular Radio and Faulty Nodes on the performance of localization. This study designs a new system model by considering Irregular Radio and random Faulty Nodes. With this new model, extensive experiments are used to conduct the investigation. From the simulation results, it is observed that both Irregular Radio and Faulty Nodes adversely affect the localization accuracy. By this investigation, the obtained conclusion can be used to direct localization algorithm design under a more realistic scenario and providing better parameter configuration for a given WSN.

**Keywords:** Industrial wireless sensor networks · Localization
Irregular radio · Faulty nodes

## 1 Introduction

Location information of sensor nodes add significant value to many applications, including military surveillance, environmental monitoring and indoor tracking [1–3]. To estimate the location of sensor nodes, a few global positioning system-equipped sensor nodes are deployed with known geographic location. These nodes are called as anchor nodes that are used to estimate the location of unknown nodes. Existing localization algorithms are broadly categorized into *range-free* [4] and *range-based* architectures [5]. An absolute point-to-point distance or angle estimation between neighbor nodes are required in range-based localization. Most of these range-based algorithms exploit received signal strength indicator (RSSI) [6], time of arrival (ToA) [7], time difference on arrival (TDoA) [8], and angle of arrival (AoA) [9]. These schemes provide


M. Huang et al. (Eds.): WICON 2016, LNICST 214, pp. 36–48, 2018.
https://doi.org/10.1007/978-3-319-72998-5_5

higher localization accuracy, however, additional hardware for distance measurement results in high cost for large-scale IWSNs. Since range-free techniques do not use signal strength, they are more robust to noise and fading. There are several range-free localization algorithms, such as Centroid [10], distance vector-hop (DV-Hop) [11], Amorphous [12] and approximate point-in triangulation test (APIT) [4]. DV-Hop is a distributed algorithm, and is easy to implement. However, the localization accuracy of DV-Hop needs to be improved. So in this paper, we focuses on the performance of DV-Hop and two variations of DV-Hop: DV-Hop with correction (CDV-Hop) [13] and improved DV-Hop (IDV-Hop) [14]. Meanwhile, none of previous schemes have considered the situation where nodes are radio irregular and random failure. The generic DV-based localization methods are not high-precision in this situation, because the connectivity of networks will be greatly affected due to nodes' radio irregular and random failure. As we can see from the Fig. 2, the communication between any pair of nodes will be affected dramatically. Therefore, the impact of irregular radio and faulty nodes on the performance of localization needs to be studied.

The rest of this paper is organized as follows: Sect. 2 briefly presents the related work on localization algorithms with irregular radio and random faulty nodes. Section 3 presents our system model. In Sect. 4, DV-Hop family-based localization algorithms are discussed. The simulation results are presented in Sect. 5. Finally, conclusions are drawn in Sect. 6.

## 2 Related Work

### 2.1 Range-Based Localization Schemes

Several range-based techniques have been proposed for WSNs, such as received signal strength indicator (RSSI) [6], time of arrival (ToA) [7], time difference on arrival (TDoA) [8], and angle of arrival (AoA) [9]. With hardware limitations and inherent energy constraints of sensor nodes, TOA-based localization methods are costly. The TDOA estimates the distance between two communicating nodes using peripheral equipment. AHLos [15] is a TDOA-based work, and it employs the TDOA technology in infrastructure-free sensor network. Like TOA, the TDOA has same problem, and further, it relies on extensive hardware which makes it less suitable for networks with low-power sensor nodes. As an augment of TDOA and TOA technologies, the AOA is proposed and it allows nodes to estimate and map relative angles between two nodes. Moreover, the AOA also requires extra hardware and this is too expensive to be used in large scale sensor networks. The RSSI technology (e.g., RADAR [16]) is used in hardware-constrained systems widely and its basic idea is to translate signal strength into distance estimation. When the environment is controllable (e.g., laboratory environment), and only when distance can be determined using signal strength, propagation patterns, and fading models, RSSI-based methods can work well.

### 2.2 Range-Free Localization Schemes

The range-free approaches do not require any distance or orientation information between nodes for localization. Network connectivity is enough for localization of unknown nodes. Although estimation accuracy is lower than range-based algorithms, the simple and cost-effective features in range-free algorithms draws significant attention in localization algorithms. Several algorithms like approximate point-in triangle test (APIT) [4], centroid [10], Amorphous [12], and distance vector-hop (DV-Hop) [11] algorithms are proposed to improve the estimation accuracy in range-free algorithms. In APIT, an unknown node is identified by the possible triangles that enclose its location, thereafter, obtaining the center of gravity of overlapping area of triangles. The localization accuracy of APIT [4] and Centroid [10] depends largely on anchor node density and transmission radius of the sensor nodes. Amorphous [12] employs more complex ways of calculating the minimum hop-counts between the sensor nodes and estimating the average hop-distance, however, requires an estimation of the average sensor node density of the WSNs.

Niculescu and Nath proposed a distributed algorithm, called DV-Hop localization [11], which is a hop-by-hop localization algorithm. In this algorithm, at first, each node counts the minimum hop number to the anchor node and then computes the distance between the anchor node and itself by multiplying minimum hop number and average hop-distance. The node finally estimates its position using either triangulation algorithm or maximum likelihood estimators (MLE) [17]. The DV-based localization algorithms are easy to implement, however, the location accuracy is one of the major challenges. To improve the estimation accuracy, Kumar and Lobiyal [18] proposed an algorithms that refines the hop-count of anchor nodes. In addition this scheme significantly reduces time and energy consumption in localization. Chen et al. [14] proposed an improved scheme to estimate hop-distance according to the number of the neighbors that belong to the same *block*. An weighted node distance was introduced to estimate the node's location.

A differential error correction scheme was proposed in [19] to improve the estimation accuracy in traditional DV-based algorithms. This scheme reduced the cumulative distance error and node location error accumulated over the multiple hops. However, high computation and communication overhead are main drawback of this scheme. Another DV-based algorithm was suggested in [20] with a correction in location estimation. Further, the estimation accuracy was improved in [14] where the anchor node broadcasts the corrected hop-distance that is the average of all anchor nodes hop-distances to the network as correction. This scheme uses 2-dimensional Hyperbolic localization algorithm instead of using the traditional triangulation to calculate the final position of a node. Gui et al. [21] discussed Checkout DV-hop algorithm that estimates the mobile node position by utilizing the nearest anchor. To improve localization accuracy, Selective 3-Anchor DV-hop algorithm was proposed to choose the best 3 anchors.

### 2.3 Irregular Radio and Faulty Nodes

**Irregular Radio.** In order to approach the real environment, we consider the irregular radio of node. In [4], He et al., for the first time, proposed an irregular radio range model: DOI model which assumes the upper bound and lower bound on the radio propagation range and three communication scenarios: (i) symmetric communication, two nodes in the communication range with each other; (ii) unidirectional & asymmetric communication, one node within another node's communication range and the another node is not in the communication range of the one node and (iii) no communication, two nodes are without the communication range of each other. However, the DOI model does not take the interacting of nodes into account. And then the paper [22] extends the DOI model considering the radio interference among sensor nodes and the new model is called as radio irregularity model (RIM) which is based on experimental results that are made with a pair of MICA2 nodes, and the RIM is used to analyze the impact of radio irregularity on MAC and routing protocols. As shown in the Fig. 1, when the DOI is zero, there is no range variation, and the communication range is a perfect circle, when we increase the value of DOI, the communication range becomes more and more irregular.

**Faulty Nodes.** The sensor nodes in the IWSNs have simple structure and limited energy, so they may go to fault due to environment interference and energy depletion, in this situation, it will brings about a direct impact on the accuracy, integrity and timeliness of the network monitoring, sometimes even lead to the collapse of the network. The research of faulty nodes has attracted people's attention and can be roughly divided into two aspects: (1) to prevent the failure of node in the beginning of network deployment, such as the use of multiple node coverage and multiple connectivity to improve network survivability, or to designing the topology control algorithm to reduce the energy loss in the data transmission [23]; (2) to detect and repair the faulty nodes, to judge the faulty node type in the process of network operation [24].

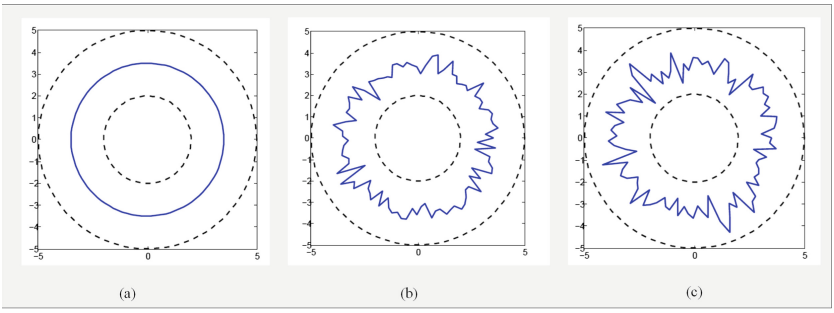


**Fig. 1.** Degree of irregularity: (a) DOI = 0, (b) DOI = 0.003, (c) DOI = 0.01

# 3 System Model

## 3.1 Network Model

We consider a multihop WSN with uniformly and randomly deployed sensor nodes in a large-scale 2-dimensional sensing field. Let $G = (S, L)$ be a network graph, where $S$ and $L = \{l(1,2), l(1,3), \ldots, l(N,N)\}$ are the set of sensor nodes with total $N$ number of sensor nodes and the set of edges between sensor nodes, respectively. The deployed sensor nodes consist of anchor nodes $S_{\text{anchor}} = \{s_{a,1}, s_{a,2}, \ldots, s_{a,N_{\text{anchor}}}\}$ and unknown nodes $S_{\text{unknown}} = \{s_{u,1}, s_{u,2}, \ldots, s_{u,N_{\text{unknown}}}\}$, where $N_{\text{anchor}}$ and $N_{\text{unknown}}$ are the number of anchor nodes and unknown nodes, respectively and $N = N_{\text{anchor}} + N_{\text{unknown}}$. In this research work, bi-directional communication between neighbors is considered. It is supposed that the industrial sensor nodes can harvest energy from environment by using additional device, e.g., solar power panel. In addition, the situation with a strong wind and the wind direction has not been taken into account in this paper.

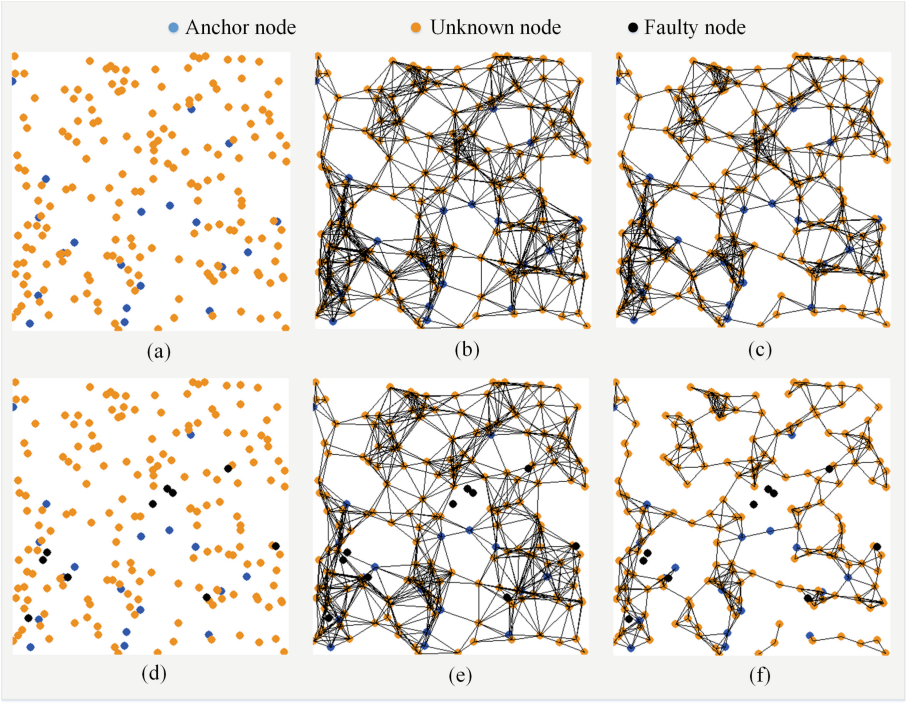


**Fig. 2.** An illustration of connectivity in an area of $600 \times 600$ m$^2$ with total 200 number of sensor nodes. (a) Ideal network, (b) Connectivity in ideal network, (c) Connectivity with irregular radio (DOI = 0.3), (d) Network with 5% faulty nodes, (e) Connectivity with 5% faulty nodes, and (f) Connectivity with irregular radio (DOI = 0.3) and 5% faulty nodes.

### 3.2 Irregular Radio and Faulty Nodes Model

**Irregular Radio.** In real environment, node's transmit power varies in different directions due to non-isotropic nature of electromagnetic transmission, path-loss, noise, and temperature. Thus, irregular radio results in link asymmetry, thereafter, affects the performance of localization in IWSNs. As shown in Fig. 2(b) and (c), it is easy to see that the connectivity of the network is reduced when the irregular radio is taken into consideration.

**Faulty Nodes.** In this paper, we have considered the case that the sensor nodes cannot work properly due to various natural (e.g., earthquakes and fires) or their own (e.g., energy depletion and hardware failure) reasons. Considering the robustness of our localization algorithm, we need to ensure that the accuracy of localization cannot be affected by random faulty nodes. Besides, we have investigated the combined influence of both random faulty nodes with irregular radio on the localization algorithms. Faulty nodes will affect the connectivity of the network. As shown in the Fig. 2(b) and (e), when the network is ideal, all sensor nodes within the transmission region $R$ can communicate with each other freely, but in the Fig. 2(d), when we take the faulty nodes into consideration, the connectivity of network will be greatly influenced.

### 3.3 Localization Error Model

A localization error is calculated as the deviation between node's actual coordinate $(x_i, y_i)$ and estimated coordinate $(x_i', y_i')$ and is expressed as $\sum_{i=1}^{N_{\text{unknown}}} \dfrac{\Delta d_i}{R \times N_{\text{unknown}}}$, where $\Delta d_i = \sqrt{(x_i - x_i')^2 + (y_i - y_i')^2}$.

## 4 DV-Hop Family-Based Localization Algorithms

### 4.1 DV-Hop Localization Algorithm

Traditional DV-Hop algorithm [11] has the following steps:

1. *Step 1: A Distance-vector Exchange:* By broadcasting the location information over the network, all anchor nodes get the distance and hops to the other anchor nodes. In addition, all unknown nodes obtain the hop-counts to the nearest anchor node.
2. *Step 2: Calculate Average Hop-distance:* To convert hop count into physical distance, the average hop-distance for any anchor node $S_{a,i}$ with coordinates $(x_i, y_i)$ is estimated by

$$\text{HopDistance}_i = \frac{\sum \sqrt{(x_i - x_j)^2 + (y_i - y_j)^2}}{\sum h_{ij}} (i \neq j), \tag{1}$$

where $h_{ij}$ is the number of hops between the anchor node $S_{a,i}$ and $S_{a,j}$. Then, the estimated average hop-distance is broadcasted over the network.

3. *Step 3: Estimation of Unknown Node's Location:* Each unknown node calculates its location $(x, y)$ using the equation-set as:

$$\begin{cases} \sqrt{(x-x_1)^2+(y-y_1)^2} = d_1 \\ \sqrt{(x-x_2)^2+(y-y_2)^2} = d_2 \\ \cdots \\ \sqrt{(x-x_n)^2+(y-y_n)^2} = d_n \end{cases}, \tag{2}$$

where $d_i = K_i \times \text{HopDistance}_i$ is the distance between the anchor nodes and the unknown nodes with hop-count $K_i$. Finally, traditional Triangulation algorithm is applied to obtain the location of unknown nodes.

### 4.2 CDV-Hop Localization Algorithm

The $d_i$ in *Step 3* of traditional DV-Hop algorithm is improved with a correction factor $c_i$ in DV-Hop with correction (CDV-Hop) [13] localization algorithm and is expressed as $d_i = K_i \times \text{HopDistance}_i + c_i$, where $c_i = \dfrac{K_i \times (R - \text{HopDistance}_i)}{R}$.

### 4.3 IDV-Hop Localization Algorithm

The estimation in localization is improved in [14], which is called improved DV-Hop (IDV-Hop) algorithm. This localization differs from *Step 2* and *Step 3* of traditional DV-Hop [11] as follows:

**Step 2 of IDV-Hop.** After obtaining the HopDistance using (2), each anchor node broadcasts its HopDistance value in a message to network. Each unknown node stores the HopDistance received from different anchor nodes. This process ends when unknown does not receive any HopDistance messages after a certain period of time. At the end of this process, each unknown node stores the HopDistance received from the anchor nodes in $S_{\text{anchor}}$.

**Step 3 of IDV-Hop.** Each unknown nodes calculate the average $\text{HopDistance}_{\text{avg}}$ by the formula:

$$\text{HopDistance}_{\text{avg}} = \frac{\sum_{i=1}^{n} \text{HopDistance}_i}{n}, \tag{3}$$

where $n$ is the number of anchor nodes it can hear. Each unknown nodes calculate the distance to the anchor nodes based on its $\text{HopDistance}_{\text{avg}}$ and hops to the anchor nodes using $d_i = K_i \times \text{HopDistance}_{\text{avg}}$. Finally, 2-D Hyperbolic location algorithm [14] is used instead of triangulation algorithm as in the traditional DV-Hop algorithm to estimate the coordinates of unknown nodes.

## 5 Simulation Results

In this section, we evaluate the impact of (a) irregular radio, (b) faulty nodes, and (c) irregular radio with faulty nodes on the performance of DV-Hop family-based localization algorithms in IWSNs. We also compare the performance of various DV-Hop family-based algorithms with irregular radio and faulty nodes.

**Table 1.** Simulation parameters

| Parameters | Values |
|---|---|
| Network size | $600 \times 600\,\mathrm{m}^2$ |
| Default anchor node density | 10% |
| Default transmission radius (R) | 60 m |
| Total number of sensor nodes | 300 to 1000 (with a step 100) |
| DOI | 0 to 0.8 (with a step 0.1) |
| Faulty node percentage | 0% to 18% (with a step 6%) |

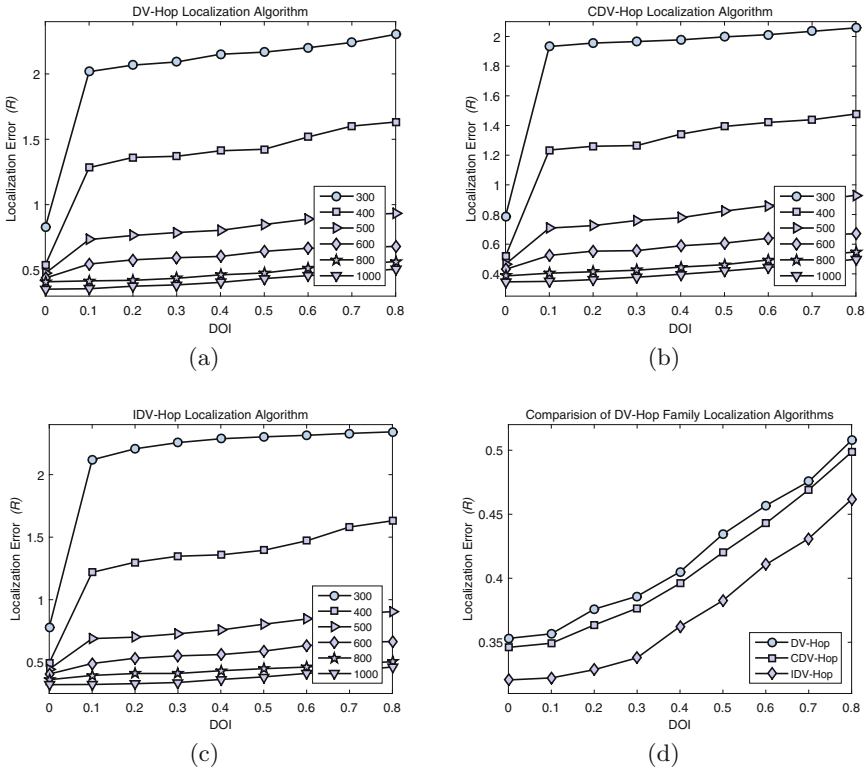


**Fig. 3.** Performance of localization error in various deployed total sensor nodes with different DOI values of irregular radio in (a) traditional DV-Hop, (b) CDV-Hop, and (c) IDV-Hop localization algorithms. (d) Performance comparison of different DV-Hop family-based localization algorithms with total 1000 nodes.

*Simulation Setup:* We conducted extensive simulations using WSN simulator NetTopo[1]. We average the localization error over 100 different network topologies. The simulation parameters are summarized in Table 1.

### 5.1 Impact of Irregular Radio

Figure 3 illustrates the impact of irregular radio on the performance of traditional DV-Hop, CDV-Hop, and IDV-Hop localization algorithms. From Fig. 3(a)–(c), we observe that the localization error increases with the increase of DOI for all three localization algorithms. The impact of irregular radio is more when the number of deployed sensor node is less than total 500 nodes. There is no significant change in estimation error beyond total 500 nodes for all localization

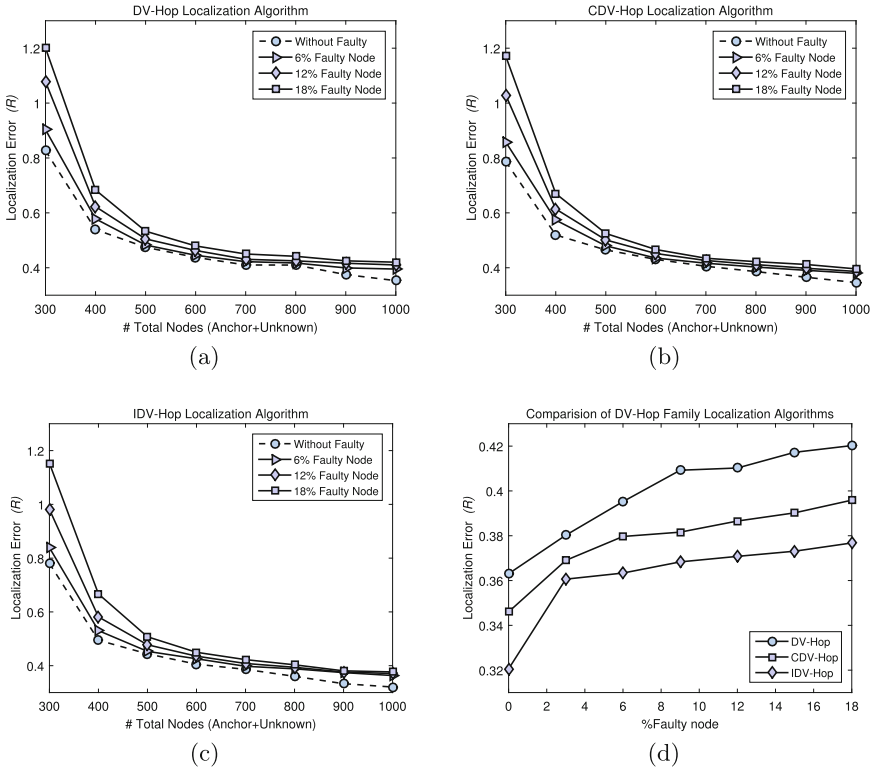


**Fig. 4.** Performance of localization error in various deployed total sensor nodes with various percentages of faulty nodes in (a) DV-Hop, (b) CDV-Hop, and (c) IDV-Hop localization algorithms. (d) Performance comparison of different DV-Hop family-based localization algorithms with total 1000 nodes.

[1] NetTopo (online at http://sourceforge.net/projects/nettopo/) is an open source software for simulating and visualizing WSNs.

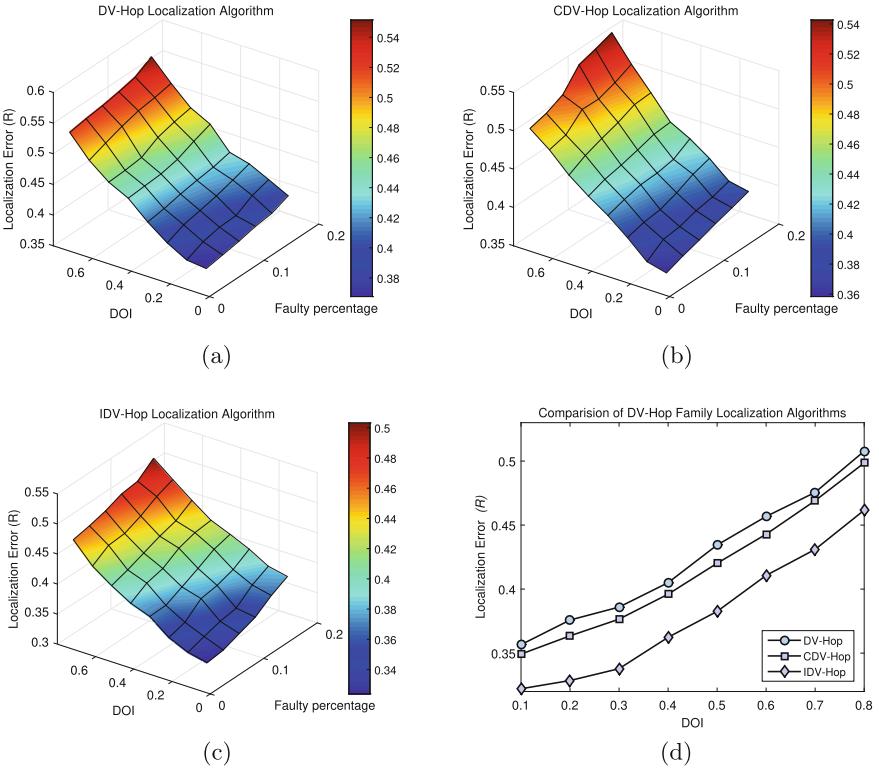


**Fig. 5.** Performance of localization error in various deployed total sensor nodes with various percentages of faulty nodes and DOI values in (a) DV-Hop, (b) CDV-Hop, and (c) IDV-Hop localization algorithms. (d) Performance comparison of different DV-Hop family-based localization algorithms with total 1000 nodes and 6% of faulty nodes.

algorithms due to sufficient number of anchor nodes. As expected, from Fig. 3(d), it is observed that IDV-Hop localization algorithm performs significantly better than both traditional DV-Hop and CDV-Hop localization algorithms in presence of radio irregularity with total 1000 sensor nodes.

### 5.2 Impact of Faulty Nodes

From Fig. 4, it is observed that increasing the faulty node percentage in DV-Hop family-based localization algorithms results in higher localization error compared to without faulty node for all of the three localization algorithms. However, the change in localization error becomes less after total 500 node deployment for the three localization algorithms. Therefore, we find the optimum deployment number as about 500 nodes without increasing the deployment cost. Furthermore, it is observed from Fig. 4(d) that CDV-Hop localization algorithm obtains lower localization error compared to traditional DV-Hop localization algorithm.

Further improvement in unknown node's location estimation is observed in IDV-Hop localization algorithm compared to CDV-Hop localization algorithm with various faulty node percentages.

### 5.3 Impact of Irregular Radio with Faulty Nodes

Finally, Fig. 5 shows the performance of localization error in DV-Hop family-based localization algorithms with both irregular radio and faulty nodes. The combined influence of irregular radio and faulty nodes results in link failure among unknown nodes as well as anchor nodes. As these DV-based localization algorithms strongly depend on hop-by-hop transmission, the estimate error dramatically increases with increasing values of faulty node percentage and DOI in all these DV-based algorithms. From Fig. 5(d), it is shown that IDV-Hop performs better than CDV-Hop and traditional DV-Hop localization algorithms in presence of both irregular radio and faulty nodes.

## 6 Conclusion

In this paper, we investigated the impact of both irregular radio and faulty nodes on DV-Hop and its two improved variations, which are called CDV-Hop and IDV-Hop localization algorithms. It has been observed that when the number of sensor nodes is less than 500, the irregular radio and faulty nodes have an adverse influence on all of three localization algorithms. However, the change in localization error is less when the deployed node is above 500. Therefore, the optimum number of sensor is found without any further deployment cost. The CDV-Hop localization algorithm provides better estimation compared to traditional DV-Hop localization algorithm in presence of irregular radio, faulty node, and combined impact of irregular radio with faulty node. Furthermore, the performance of IDV-Hop outperforms CDV-Hop localization algorithm with these realistic situations with irregular radio and faulty nodes. This study will be a useful reference to further design a new improved algorithm without losing the localization accuracy for a given deployed sensor networks under more realistic environment.

**Acknowledgments.** This work is supported by Guangdong University of Petrochemical Technology through Internal Project 2012RC106, the National Natural Science Foundation of China Grant 61401107, and the International and Hong Kong, Macao & Taiwan collaborative innovation platform and major international cooperation projects of colleges in Guangdong Province (No. 2015KGJHZ026). It is also in part supported by the program for New Century Excellent Talents in University under Grant NCET-13-0940, the Natural Science Foundation of Hubei Province under Grant 2014CFB791, and the Research Plan Project of Hubei Provincial Department of Education under Grant T201206.

## References


1. Shu, L., Wang, L., Niu, J., Zhu, C., Mukherjee, M.: Releasing network isolation problem in group-based industrial wireless sensor networks. IEEE Syst. J. **PP**(99), 1–11 (2015)
2. Sheng, Z., Mahapatra, C., Zhu, C., Leung, V.C.M.: Recent advances in industrial wireless sensor networks toward efficient management in IoT. IEEE Access **3**, 622–637 (2015)
3. Akyildiz, I.F., Su, W., Sankarasubramaniam, Y., Cayirci, E.: A survey on sensor networks. IEEE Commun. Mag. **40**(8), 102–114 (2002)
4. He, T., Huang, C., Blum, B.M., Stankovic, J.A., Abdelzaher, T.: Range-free localization schemes for large scale sensor networks. In: Proceedings of the 9th Annual International Conference on Mobile Computing and Networking, pp. 81–95. ACM, New York (2003)
5. Zhang, Y., Wu, W., Chen, Y.: A range-based localization algorithm for wireless sensor networks. J. Commun. Netw. **7**(4), 429–437 (2005)
6. Girod, L., Bychkovskiy, V., Elson, J., Estrin, D.: Locating tiny sensors in time and space: a case study. In: Proceedings of the IEEE International Conference on Computer Design: VLSI in Computers and Processors, pp. 214–219 (2002)
7. Harter, A., Hopper, A., Steggles, P., Ward, A., Webster, P.: The anatomy of a context-aware application. Wirel. Netw. **8**(2/3), 187–197 (2002)
8. Luo, C., Li, W., Fan, M., Yang, H., Fan, Q.: A collaborative positioning algorithm for mobile target using multisensor data integration in enclosed environments. Comput. Commun. **44**, 26–35 (2014)
9. Niculescu, D., Nath, B.: Ad hoc positioning system (aps) using aoa. In: IEEE INFOCOM 2003. Twenty-Second Annual Joint Conference of the IEEE Computer and Communications Societies (IEEE Cat. No. 03CH37428), vol. 3, pp. 1734–1743, March 2003
10. Bulusu, N., Heidemann, J., Estrin, D.: Gps-less low-cost outdoor localization for very small devices. IEEE Pers. Commun. **7**(5), 28–34 (2000)
11. Niculescu, D., Nath, B.: Ad hoc positioning system (aps). In: Global Telecommunications Conference, 2001. GLOBECOM 2001, vol. 5, pp. 2926–2931. IEEE (2001)
12. Nagpal, R., Shrobe, H., Bachrach, J.: Organizing a global coordinate system from local information on an ad hoc sensor network. In: Zhao, F., Guibas, L. (eds.) IPSN 2003. LNCS, vol. 2634, pp. 333–348. Springer, Heidelberg (2003). https://doi.org/10.1007/3-540-36978-3_22
13. Yu, W., Li, H.: An improved DV-Hop localization method in wireless sensor networks. In: 2012 IEEE International Conference on Computer Science and Automation Engineering (CSAE), pp. 199–202, May 2012
14. Chen, H., Sezaki, K., Deng, P., So, H.C.: An improved DV-Hop localization algorithm for wireless sensor networks. In: 2008 3rd IEEE Conference on Industrial Electronics and Applications, pp. 1557–1561, June 2008
15. Savvides, A., Park, H., Srivastava, M.B.: The bits and flops of the n-hop multilateration primitive for node localization problems. In: Proceedings of the 1st ACM International Workshop on Wireless Sensor Networks and Applications, Atlanta, Georgia, USA, pp. 112–121. ACM (2002)
16. Bahl, P., Padmanabhan, V.N.: Radar: an in-building rf-based user location and tracking system. In: Proceedings IEEE INFOCOM 2000. Conference on Computer Communications. Nineteenth Annual Joint Conference of the IEEE Computer and Communications Societies (Cat. No. 00CH37064), vol. 2, pp. 775–784 (2000)

17. Wang, X., Fu, M., Zhang, H.: Target tracking in wireless sensor networks based on the combination of kf and mle using distance measurements. IEEE Trans. Mob. Comput. **11**(4), 567–576 (2012)
18. Kumar, S., Lobiyal, D.: Improvement over DV-Hop localization algorithm for wireless sensor networks. In: World Academy of Sciences, Engineering and Technology, pp. 282–292 (2013)
19. Yi, X., Liu, Y., Deng, L., He, Y.: An improved DV-Hop positioning algorithm with modified distance error for wireless sensor network. In: 2009 Second International Symposium on Knowledge Acquisition and Modeling, pp. 216–218, November 2009
20. Ren, W., Zhao, C.: A localization algorithm based on sfla and pso for wireless sensor network. Inf. Technol. J. **12**(3), 502 (2013)
21. Gui, L., Val, T., Wei, A., Dalce, R.: Improvement of range-free localization technology by a novel DV-Hop protocol in wireless sensor networks. Ad Hoc Netw. **24**(Part B), 55–73 (2015)
22. Zhou, G., He, T., Krishnamurthy, S., Stankovic, J.A.: Impact of radio irregularity on wireless sensor networks. In: Proceedings of the 2nd International Conference on Mobile Systems, Applications, and Services, Boston, MA, USA, pp. 125–138. ACM (2004)
23. Cardei, M., Yang, S., Wu, J.: Algorithms for fault-tolerant topology in heterogeneous wireless sensor networks. IEEE Trans. Parallel Distrib. Syst. **19**(4), 545–558 (2008)
24. Zahedi, S., Szczodrak, M., Ji, P., Mylaraswamy, D., Srivastava, M., Young, R.: Tiered architecture for on-line detection, isolation and repair of faults in wireless sensor networks. In: MILCOM 2008–2008 IEEE Military Communications Conference, pp. 1–7, November 2008

# Security

# A SDN Proactive Defense Scheme Based on IP and MAC Address Mutation

Liancheng Zhang(✉), Zhenxing Wang, Jiabao Fang, and Yi Guo

China National Digital Switching System Engineering and Technological Research Center, Zhengzhou 450002, China
lianchengl7@gmail.com, {wzx05,20l4xdfjb}@sina.com, nongfu@live.cn

**Abstract.** Existing address hopping technologies are hard to be deployed and implemented, at the same time, they only randomly hop IP address information of one communication node or both communication nodes, so they can't protect their identifications on data link layer. In order to deal with these problems, a SDN proactive defense scheme based on IP and MAC address mutation is proposed, which realizes IP and MAC address mutation along the transmission path by installing corresponding address mutation flow entries to intermediate OpenFlow switches. Theoretical analysis and experimental results show that this scheme can resist network interception and analysis attack with a relatively low transmission and processing costs.

**Keywords:** Address mutation · Address hopping · Software defined network Moving target defense · Proactive defense

## 1 Introduction

Network sniffer is the key part of information collection and is a significant threat to network security. Nowadays, the costs of network defenders and network attackers are extremely unequal. Network defenders are in a very passive situation, who usually have to add layers of security protection measures for the entire network, while network attackers are relatively active, who sometimes can break the network by only one flaw or vulnerability.

With standards and products of software defined network (SDN) becoming more and more mature and deployments and applications of SDN networks becoming more and more wide (such as cloud computing, data center, etc.) [1, 2], SDN network security issues become increasingly prominent [3, 4]. However, SDN security technologies largely adopt passive network protection and defense methods, such as firewall [5], intrusion detection system [6], denial of service (DoS) detection and defense [7, 8], security policy enforcement [9, 10], etc.

In order to change this passive situation, moving target defense (MTD), a new kind of proactive defense technology, is concerned. MTD's main idea is to make every node in the network becoming a dynamic target, thus can effectively resist network attacks.

As an important component of the MTD technologies, address hopping technologies have been payed more and more attentions by scholars. Address hopping technologies


M. Huang et al. (Eds.): WICON 2016, LNICST 214, pp. 51–60, 2018.
https://doi.org/10.1007/978-3-319-72998-5_6

[11] randomly change IP address information of one or both communication parties, so as to prevent from being discovered and attacked.

As the IP address information is the unique identification of a network node and the foundation of inter-node communication, address hopping technologies face many difficulties when deployed in network environment. Firstly, in order to realize random address hopping, address hopping technologies need to change the IP address configuration of related network nodes, which will add deployment complexity and inconvenience, and limit the hopping frequency of address hopping. Secondly, existing address hopping technologies only randomly hop IP address information of one or both communication nodes, so they can't protect their identifications on data link layer, as they don't hop MAC (media access control) address information.

To enhance SDN proactive defense capability on both network layer and data link layer, this paper presents a SDN proactive defense scheme based on IP and MAC address mutation (SPD-IMAM), where address mutation means just hopping address information along the path (except communication ends) during forwarding process.

## 2 Related Works

Address hopping technologies achieve proactive security protection by randomly hopping address information of one communication side or both communication sides.

To resist the man-in-middle attack, the authors of [12] put forward dynamic network address translation (DyNAT) mechanism, which changes IP address before communication packets enter the core network or public network. To resist the hitlist worm attack, the authors of [13] propose network address space randomization (NASR) scheme, which provides a random hopping strategy to update network address in the level of local area network (LAN) based on dynamic host configuration protocol (DHCP).

The authors of [11] propose an information hiding technology based on address hopping, which provides multiple paths for data transmission in the process of communication and improves the security of data transmission through the adoption of multiple routing. The authors of [14] put forward a kind of virtual port and address hopping scheme, which utilizes false addresses and ports in the corresponding fields of message packets in the process of communication to confuse attackers.

Motivated by frequency hopping for military communication, end hopping tactic is proposed in [15], which can mitigate DoS and eavesdropping threats greatly by pseudo-randomly changing the end information of port, address, timeslot, cryptographic algorithm or even protocol during end to end transmission.

The authors of [16] put forward random host mutation (RHM) technology by frequently and unpredictably changing IP addresses, which exploits MTC (moving target controller) and MTG (moving target gateway) to implement the transformation between the actual address rIP and the virtual address vIP. Subsequently, the authors of [17] put forward the OF-RHM (OpenFlow random host mutation) technology by using NOX controller to realize the MTG and MTG function of RHM.

Existing address hopping technologies have much interaction with communication sides in hopping process, as a result, they are hard to be deployed and implemented.

Besides, existing address hopping technologies only randomly hop IP address information of one communication side or both communication sides, so they can't protect their identifications on data link layer, as they don't hop MAC addresses.

To enhance SDN proactive defense capability on both network layer and data link layer, aiming at the problem that existing address hopping technologies are difficult to be deployed and implemented, this paper presents the SPD-IMAM scheme, which is independent of the sender and the receiver.

## 3 The SPD-IMAM Scheme

The SPD-IMAM scheme implements IP and MAC address mutation along the transmission path during forwarding process, as a result, it's independent of the sender and the receiver, which can further mislead attackers.

### 3.1 SPD-IMAM Framework

Figure 1 shows the overall framework of the SPD-IMAM scheme, where path generation module generates the required path for communication, address mutation module generates the required IP and MAC address information according to specific mutation slot, flow table maintenance module is responsible for installing flow entries into all OpenFlow switches along the transmission path based on particular mutation slot and timely removing expired flow entries on OpenFlow switches along the transmission path.

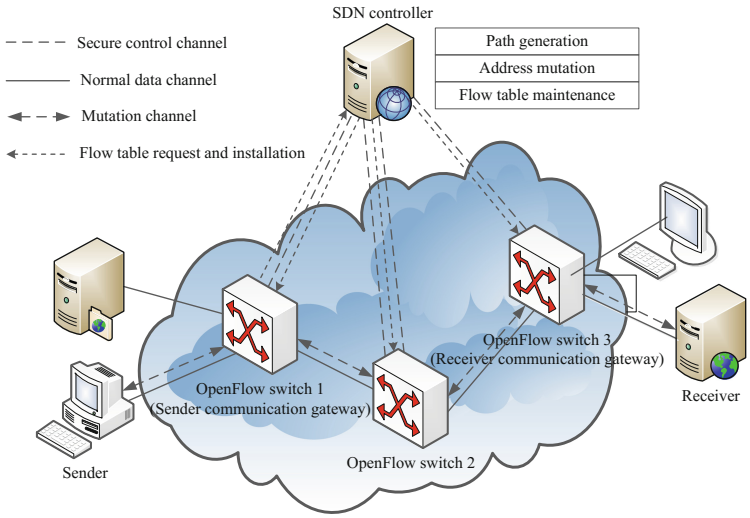


**Fig. 1.** SPD-IMAM framework.

The SPD-IMAM scheme transfers random hopping function from the sender and the receiver to the communication path, and IP and MAC addresses of every protected packet would be randomly changed by every OpenFlow switch (such as switch 1, 2 and 3 in Fig. 1) along the communication path, as a result, the hopping frequency of the SPD-IMAM scheme is much more faster than traditional address hopping schemes.

The process of address random mutation is shown as in Fig. 2, where rIPa, rIPb represent actual IP addresses, vIP1, vIP2, vIP3, vIP4, vIP5, vIP6 represent virtual IP addresses, rMACa, rMACb represent real MAC addresses, vMAC1, vMAC2, vMAC3, vMAC4 represent virtual MAC addresses.

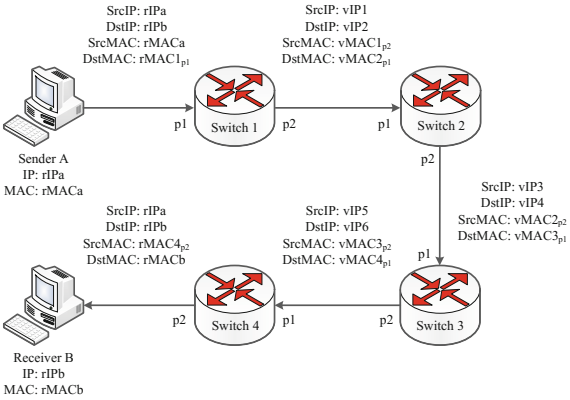


**Fig. 2.** IP and MAC address mutation.

Flow entries installed into OpenFlow switches (shown in Fig. 2) for address mutation along the transmission path is shown in Table 1.

**Table 1.** Flow entries for address mutation along the transmission path.

| Switch no | Ingress port | SrcMAC | DstMAC | SrcIP | DstIP | Actions |
|---|---|---|---|---|---|---|
| Switch 1 | p1 | rMACa | $rMAC1_{p1}$ | rIPa | rIPb | Set SrcIP=vIP1, DstIP=vIP2<br>Set SrcMAC=$vMAC1_{p2}$,<br>DstMAC=$vMAC2_{p1}$<br>Forward to Port p2 |
| Switch 2 | p1 | $vMAC1_{p2}$ | $vMAC2_{p1}$ | vIP1 | vIP2 | Set SrcIP=vIP3, DstIP=vIP4<br>Set SrcMAC=$vMAC2_{p2}$,<br>DstMAC=$vMAC3_{p1}$<br>Forward to Port p2 |
| Switch 3 | p1 | $vMAC2_{p2}$ | $vMAC3_{p1}$ | vIP3 | vIP4 | Set SrcIP=vIP5, DstIP=vIP6<br>Set SrcMAC=$vMAC3_{p2}$,<br>DstMAC=$vMAC4_{p1}$<br>Forward to Port p2 |
| Switch 4 | p1 | $vMAC3_{p2}$ | $vMAC4_{p1}$ | vIP5 | vIP6 | Set SrcIP=rIPa, DstIP=rIPb<br>Set SrcMAC=$rMAC4_{p2}$,<br>DstMAC=rMACb<br>Forward to Port p2 |

### 3.2 Process of OpenFlow Switches

To randomly mutate the IP and MAC addresses of the sender and the receiver, the SPD-IMAM scheme utilizes SDN controller to install corresponding flow entries to every OpenFlow switch on the transmission path, which is shown in Fig. 3.

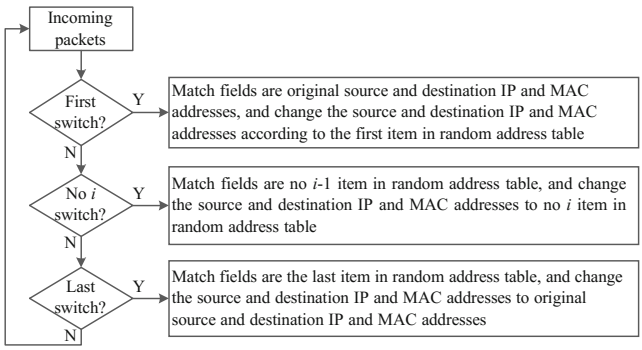


**Fig. 3.** IP and MAC address mutation process on different switches.

When a packet arrives an OpenFlow switch, the switch will try to search for a matched flow entry according to different match fields. If the switch finds one match, it will perform the actions in the matched flow entry. If the switch finds no match, it will ask SDN controller for a decision.

Before installing corresponding flow entries, SDN controller will generate a random address table, which contains a random source IP address table, a random destination IP address table, a random source MAC address table and a random destination MAC address table. According to these tables, SDN controller can then install corresponding flow entries into these OpenFlow switches along the transmission path.

## 4 Proactive Defense Ability Analysis of the SPD-IMAM Scheme

To network interception and analysis attacker, we suppose that the attacker only eavesdrop particular links or nodes in certain time and the attacker can intercept all the interactive packets in the network.

Suppose that the protected packets of the SPD-IMAM scheme are $\{p_1, p_2, p_3, \ldots, p_n\}$ and the packets intercepted by the attacker are $\{k_1, k_2, k_3, \ldots, k_m\}$ $(m > n)$. The attacker need to filter out the protected $n$ packets from all $m$ packets, and analyze their real order of the $n$ packets.

Suppose that $C_i$ is the cost of packet interception, $C_f$ is the cost of packet comparison and filtering, and $C_r$ is the cost of obtaining these real ordered packets. Then, the total cost $C_{all}$ can be expressed as $C_{all} = C_i + C_f + C_r$.

Suppose that $C_a$ is the cost for analyzing a single packet. When these compared and filtered packets contain all real ordered communication packets, the value of $C_r$ is minimum, which is:

$$C_{r_{\min}} = \sum_{i=1}^{n} C_a = nC_a = O(n) \tag{1}$$

At the same time, when these compared and filtered packets contain all communication packets and their order is reverse, the value of $C_r$ is maximum, which is:

$$C_{r_{\max}} = \sum_{i=m-n+1}^{n} iC_a = O(n^2) \tag{2}$$

Form above analysis, we can conclude that the overall cost of the attacker is $C_i + C_f + O(n) \leq C_{all} \leq C_i + C_f + O(n^2)$. In general, the value of $C_i$ and $C_f$ are relatively fixed, as a result, the overall cost of the attacker is between $\Omega(n)$ and $O(n^2)$

It is worth noting that even if the network interception and analysis attackers can capture and obtain the real IP address information of real communication nodes, but they can't find the real MAC addresses used by real communication nodes, as a result, this scheme can effectively resist data link layer based network interception and analysis.

## 5 Experimental Results and Analysis

To test the SPD-IMAM scheme, we use Mininet network simulator [18] and Open vSwitch (OVS) software switches to simulate and set up SDN test network (which is similar with Fig. 1) and utilize Floodlight as SDN controller to be responsible for address mutation function.

Mininet simulator, OVS switches, Floodlight controller, the sender, the receiver and the attacker are deployed on different computers with Intel i7-4790 quad-core 3.6 GHz CPU and 4 GB memory.

### 5.1 IP and MAC Address Mutation

When the sender pings the receiver (IP addresses of the sender and the receiver are 192.168.1.2 and 192.168.1.5 respectively, MAC addresses of them are 44:37:E6:1A:27:4A and 78:2B:CB:EB:79:D6 respectively), firstly, the sender need to know MAC address of the receiver for starting normal communication, so the sender will send ARP (address resolution protocol) broadcast packets to ask for MAC address of the receiver at first, when the sender get the ARP's reply, it will send an ICMP (Internet control message protocol) echo request packet to the receiver. At this time, flow entries in OpenFlow switches installed by SDN controller is shown in Table 2.

**Table 2.** Flow entries installed by Floodlight controller.

| Switch no | Match fields | Actions |
|---|---|---|
| Switch 1 | SrcIP: 192.168.1.2<br>DstIP: 192.168.1.5<br>SrcMAC: 44:37:E6:1A:27:4A<br>DstMAC: 78:2B:CB:EB:79:D6 | SrcIP: 219.120.169.32<br>DstIP: 36.124.113.28<br>SrcMAC: 00:13:46:65:BC:7D<br>DstMAC: 00:1E:37:52:5E:EC |
| Switch 2 | SrcIP: 219.120.169.32<br>DstIP: 36.124.113.28<br>SrcMAC: 00:13:46:65:BC:7D<br>DstMAC: 00:1E:37:52:5E:EC | SrcIP: 26.116.138.27<br>DstIP: 116.204.35.16<br>SrcMAC: 78:2B:CB:13:78:20<br>DstMAC: 00:13:46:20:EC:1B |
| Switch 3 | SrcIP: 26.116.138.27<br>DstIP: 116.204.35.16<br>SrcMAC: 78:2B:CB:13:78:20<br>DstMAC: 00:13:46:20:EC:1B | SrcIP: 119.20.108.24<br>DstIP: 29.30.104.29<br>SrcMAC: 44:37:E6:10:5C:BD<br>DstMAC: 00:1E:37:13:CE:3D |
| Switch 4 | SrcIP: 119.20.108.24<br>DstIP: 29.30.104.29<br>SrcMAC: 44:37:E6:10:5C:BD<br>DstMAC: 00:1E:37:13:CE:3D | SrcIP: 192.168.1.2<br>DstIP: 192.168.1.5<br>SrcMAC: 44:37:E6:1A:27:4A<br>DstMAC: 78:2B:CB:EB:79:D6 |

As shown in Table 2, source and destination IP and MAC addresses of the packets which are transmitted between the first and the last OpenFlow switches are random generated IP addresses and random generated MAC addresses, as a result, the SPD-IMAM scheme can realize IP and MAC address mutation to achieve the purpose of concealing real IP and MAC addresses of communication nodes, which can not only protect their address information, but also improve SDN network's proactive defense capacity of resisting network layer based and data link layer based network intercept and analysis attacks.

### 5.2 Average Transmission Delay

The average transmission delay can reflect the processing performance of the SPD-IMAM scheme. As a result, we evaluate the average transmission delay (shown in Fig. 4) within different route hops when using and not using address mutation.

From Fig. 4, we can see that the transmission delay of the SPD-IMAM scheme is higher than that of normal communication (non-mutation). But the extra delay consumed by the SPD-IMAM scheme is not heavy (approximately $10^{-6}$ s) and acceptable.

### 5.3 Overhead of Floodlight Controller's CPU Load

To test the extra processing load of Floodlight SDN controller brought from the SPD-IMAM scheme, we evaluate the influences on Floodlight controller's CPU load by utilizing packets of different length, and the results are shown in Fig. 5.

From Fig. 5, we can see that extra processing load of Floodlight controller is not heavy, which is lower than 4.8%. In order to protect communication process with address mutation, this extra overhead is in an acceptable range.

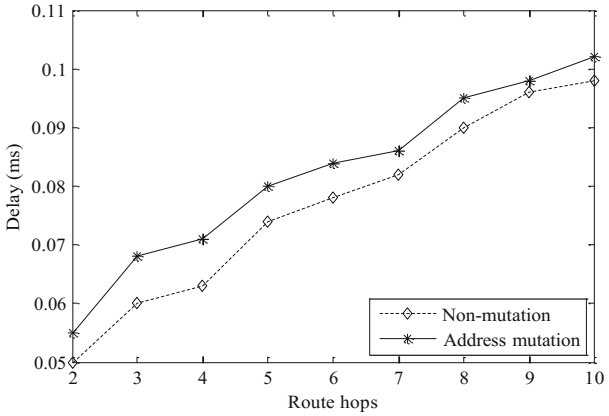


**Fig. 4.** Forwarding delay difference between address mutation and non-mutation.

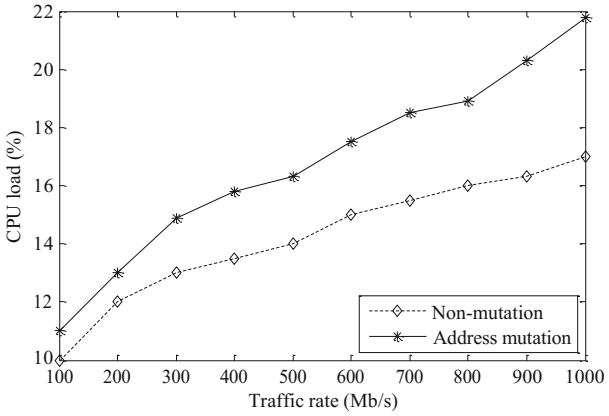


**Fig. 5.** Floodlight controller's CPU load influenced by the SPD-IMAM scheme.

## 6 Conclusions

Address hopping technology provides a new way for SDN proactive defense. On this basis, this paper puts forward an IP and MAC address mutation scheme. Based on SDN's features, such as flexible network architecture, logically centralized control and network programmable, this scheme randomly changes source and destination IP and MAC addresses of the protected flow along the communication path, so that attackers can't capture, analysis and restore the protected flow accurately. At the same time, this proposed scheme is independence of source and destination nodes, which can be easily adopted and deployed in SDN networks as well as traditional networks.

For future work, on the basis of this proposed SPD-IMAM scheme, similar idea can be applied to port hopping/mutation, end hopping/mutation, etc. In addition, multiple SDN controllers can be utilized to increase the scalability of the SPD-IMAM scheme.

**Acknowledgments.** This work was supported in part by National Natural Science Foundation of China under grant 61402526, 61402525 and 61502528, and in part by National High Technology Research and Development Program of China under grant 2012AA012902.

## References

1. Xia, W., Wen, Y., Foh, C.H., Niyato, D., Xie, H.: A survey on software-defined networking. IEEE Commun. Surv. Tutorials **17**, 27–51 (2015)
2. Farhady, H., Lee, H., Nakao, A.: Software-defined networking: a survey. Comput. Netw. **81**, 79–95 (2015)
3. Akhunzada, A., Ahmed, E., Gani, A., Khan, M.K., Imran, M., Guizani, S.: Securing software defined networks: taxonomy, requirements, and open issues. IEEE Commun. Mag. **53**, 36–44 (2015)
4. Alsmadi, I., Xu, D.: Security of software defined networks: a survey. Comput. Secur. **53,** 79–108 (2015)
5. Hu, H., Han, W., Ahn, G., Zhao, Z.: FlowGuard: building robust firewalls for software-defined networks. In: ACM SIGCOMM Workshop on Hot Topics in Software Defined Networking, pp. 97–102. ACM Press, Chicago (2014)
6. Giotis, K., Argyropoulos, C., Androulidakis, G., Kalogeras, D., Maglaris, V.: Combining openflow and sflow for an effective and scalable anomaly detection and mitigation mechanism on SDN environments. Comput. Netw. **62**, 122–136 (2014)
7. Wang, B., Zheng, Y., Lou, W., Hou, Y.T.: DDoS attack protection in the era of cloud computing and software-defined networking. Comput. Netw. **81**, 308–319 (2015)
8. Wang, H., Xu, L., Gu, G.: FloodGuard: a DoS attack prevention extension in software-defined networks. In: Proceedings of the 45th Annual IEEE/IFIP International Conference on Dependable Systems and Networks, pp. 239–250. IEEE Press, Rio de Janeiro (2015)
9. Shin, S., Yegneswaranz, V., Porrasz, P., Gu, G.: AVANT-GUARD: scalable and vigilant switch flow management in software-defined networks. In: 20th ACM Conference on Computer and Communications Security, pp. 413–424. ACM Press, Berlin (2013)
10. Kreutz, D., Ramos, F.M.V., Verissimo, P.: Towards secure and dependable software-defined networks. In: Proceedings of the 2nd ACM SIGCOMM Workshop on Hot Topics in Software Defined Networking, pp. 55–60. ACM Press, Hong Kong (2013)
11. Sifalakis, M., Schmid, S., Hutchison, D.: Network address hopping: a mechanism to enhance data protection for packet communications. In: Proceedings of 40th Annual IEEE International Conference on Communications, pp. 1518–1523. IEEE Press, Seoul (2005)
12. Kewley, D., Lowry, J., Fink, R., Dean, M.: Dynamic approaches to thwart adversary intelligence gathering. In: Proceedings of DARPA Information Survivability Conference and Exposition II, pp. 176–185. IEEE Press, Anaheim (2001)
13. Antonatos, S., Anagnostakis, K.G.: TAO: protecting against hitlist worms using transparent address obfuscation. In: Leitold, H., Markatos, E.P. (eds.) CMS 2006. LNCS, vol. 4237, pp. 12–21. Springer, Heidelberg (2006). https://doi.org/10.1007/11909033_2
14. Atighetchi, M., Pal, P., Webber, F., Jones, C.: Adaptive use of network-centric mechanisms in cyber-defense. In: 6th IEEE International Symposium on Object-Oriented Real-Time Distributed Computing, pp. 183–192. IEEE Press, Hakodate (2003)
15. Shi, L., Jia, C., Lv, S.: Research on end hopping for active network confrontation. J. Commun. **29**, 106–110 (2008)

16. Al-Shaer, E., Duan, Q., Jafarian, J.H.: Random host mutation for moving target defense. In: Keromytis, Angelos D., Di Pietro, R. (eds.) SecureComm 2012. LNICST, vol. 106, pp. 310–327. Springer, Heidelberg (2013). https://doi.org/10.1007/978-3-642-36883-7_19
17. Jafarian, J.H., Al-Shaer, E., Duan, Q.: OpenFlow random host mutation: transparent moving target defense using software defined networking. In: Proceedings of the 1st Workshop on Hot Topics in Software Defined Networks, pp. 127–132. ACM Press, Helsinki (2012)
18. Oliveira, R.L.S., Schweitzer, C.M., Shinoda, A.A., Prete, L.R.: Using mininet for emulation and prototyping software-defined networks. In: 2014 IEEE Colombian Conference on Communications and Computing, pp. 1–6. IEEE Press, Bogota (2014)

# An Attribute Based Encryption Middleware with Rank Revocation for Mobile Cloud Storage

Qinghe Dong[1], Qian He[1,2(✉)], Mengfei Cai[1], and Peng Liu[2,3]

[1] Key Laboratory of Cognitive Radio and Information Processing, Ministry of Education, Guilin University of Electronic Technology, Guilin 541004, China
treeqian@gmail.com
[2] Key Lab of Cloud Computing and Complex System, Guilin University of Electronic Technology, Guilin 541004, Guangxi, China
[3] Guangxi Key Lab of Cryptography and Information Security, Guilin University of Electronic Technology, Guilin 541004, Guangxi, China

**Abstract.** The Attribute Based Encryption (ABE) algorithm can be used to realize fine grained access control for the mobile cloud storage. In ABE, the decryption algorithm has high complexity and the rank revocation is difficult to be implemented. An ABE middleware with rank revocation is given in this paper. The ABE middleware delegate the ABE decryption operation for the resource constrained mobile device. The attribute authority can revoke the user's rank through this middleware instantly with fine-grained control and the revocation process may not affect any other users. The ABE middleware is implemented and experiment results show that the ABE middleware improves ABE decryption performance about 30 times.

**Keywords:** Attribute based encryption · Mobile cloud storage
Middleware · Rank revocation

## 1 Introduction

The mobile users increased explosively in recent years. In 2014, the mobile users reach 5.27 billion, which is beyond the personal computer (PC) users [1]. Compared with the traditional PC, the mobile device is resource constrained in the computing, storage, and battery power capacity. Therefore, the mobile device should work with the cloud to enhance its power and the mobile cloud computing becomes a new important stream.

Cloud computing is a new computing model which becomes a hot technology in recent years. Cloud computing builds a large number of computational and storage resources into a shared pool with configuration, so difference applications can be obtained different resources according to the demands [2]. In the cloud storage system, the numerous users and data storage are dispersed. Compared with the traditional software, all the data in the cloud computing are maintained by the third party, which may bring more security issues [3, 4].


M. Huang et al. (Eds.): WICON 2016, LNICST 214, pp. 61–69, 2018.
https://doi.org/10.1007/978-3-319-72998-5_7

The Attribute Based Encryption (ABE) algorithm is viewed as one solution to realize fine-grained access control in the cloud environment [5–7]. ABE has two categories: the Key Policy Attribute Based Encryption (KP-ABE) and Ciphertext Policy Attribute Based Encryption (CP-ABE). Since the pairing and exponent operation of big numbers exist in ABE, the ABE computation cost is large, which is not suitable for the resource constrained mobile device. The decryption operation should be invoked every time when the data are consumed, so it is invoked more frequently than the encryption. The attribute revocation is still a difficult problem in the ABE mechanism [8]. Pirretti etc. [9] proposed to complete attribute revocation through updating the user private key periodically, but this revocation scheme cannot be performed in real time and will produce large overhead because the users need to save the private key at each time. In the literature [10], Asim etc. realized the user name revocation by adding the revocation user name into ciphertext, but the complexity of the decryption algorithm increases with the number of users. Reference [11] constructs CP-ABE scheme supported fine-grained cancellation based on double system encryption. All above solutions require the data to be re-encrypted when the ranks are revoked, so the efficient is low.

In this paper, an ABE middleware with rank revocation is proposed. The main contributions are as follows:

1. A special ABE algorithm is proposed for the ABE middleware. The ABE middleware delegates the decryption partly, and provides the middle result for the mobile to complete the whole ABE decryption. The ABE decryption cost of the mobile device is decrease and the decryption process becomes fasten.
2. The rank revocation is provided based on the ABE middleware. If a user' rank is revoked, the process become simple and the re-encryption of data is avoided.
3. The ABE middleware based mobile storage application system is realized. The performance of the decryption and attribute revocation is verified by the experiment.

The remainder of this paper is organized as follows: Sect. 2 introduces our system architecture; Sect. 3 presents our ABE algorithms with revocation; Sect. 4 analyzes the experiment; finally, and Sect. 5 concludes this paper.

## 2 System Design of the ABE Middleware

### 2.1 System Architecture

The mobile cloud storage system based on the ABE middleware consists of five parts: Data Owner (DO), Attribute Authority (AA), ABE Middleware (ABE-M), Cloud Storage (CS) and Mobile User (MU). DO is the data owner which define the access control policy, encrypt the sensitive data with the help of ABE-M, and then upload them to the CSP; AA is responsible for the system initialization, key generation and revocation operation; ABE-M do the ABE decryption task and attribute revocation. MU is the data requestor from CS. In the whole system, the cloud host always is semi-trusted, that is to say, the cloud host will perform correctly system commands, but

at the same time it may try to steel data for his profits. The system architecture of ABE middleware application is given in Fig. 1.

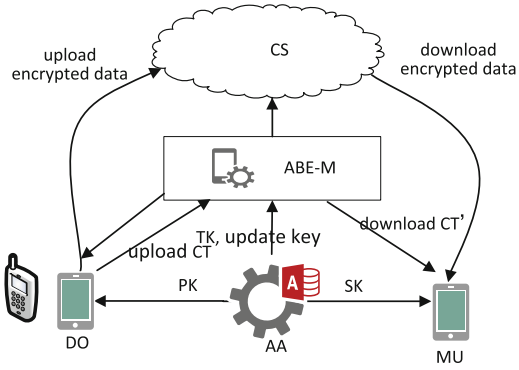


**Fig. 1.** System architecture of the ABE middleware application

In this application system architecture, two encryption algorithms including ABE and the symmetric encryption algorithm are used. ABE is used to encrypt the symmetric key and generate ciphertext *CT*, and the symmetric encryption algorithm utilizes this symmetric key to encrypt the file. The users cannot decrypt the encrypted file until the symmetric key is obtained which is decrypt with the satisfied attribute user.

## 2.2 Structure Model

The structure model of the ABE middleware is shown in Fig. 2. There exist five modules as follows.

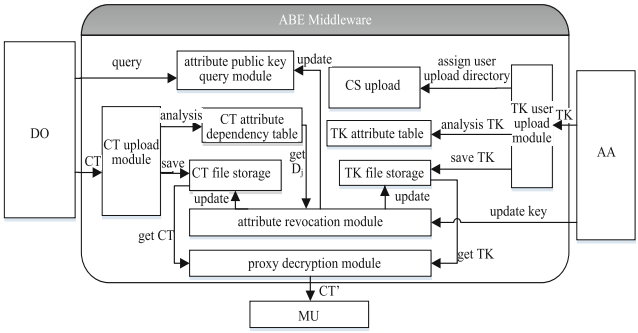


**Fig. 2.** Structure model of the ABE middleware

*TK* upload module: when *AA* releases one user's *TK* to service middleware, this module will save *TK* and assign independent upload directory to separated user.

*CS* upload module: manage directory access permission in the cloud through the access control policy. Only the satisfied user can add, delete, modify the files in the directory.

*CT* upload module: after the data sharing user uploads *CT*, the module will save *CT* and its attribute dependency according to the *CT*'s attribute dependency table. In the process of attribute revocation, *CT* needed to be uploaded can be quickly positioned through *CT* attribute dependency table.

Attribute revocation module: The module is responsible for upgrading *CT* and user conversion key generated by *AA*. If the attribute revocation user does not get the upgraded key, the key component corresponding to this attribute in *TK* become invalid.

Attribute public key query module: query whether the attribute public key changes before the data are encrypted by DO. If changed, the module upgrades the attribute public key.

Decryption delegation module: delegate and decrypt *CT* and get a middle result *CT'*, and then send to the MU who wants to access the encrypted data in the cloud storage.

## 3 ABE Algorithms

### 3.1 Construction

The reference [6] provides a basic CP-ABE, and reference [7] proposes an ABE with revocation. We combined them together and propose the ABE algorithms as follows.

**Initializing algorithm.** $Setup(\lambda, U) = \{PK, MSK, PKx\}$: is executed by attribute authority, input security parameters $\lambda$ and attribute sets $U$. Choose a group $G$ with the order $p$, and $g$ becomes the generator. The mapping function $\rho$ will map each attribute in $U$ into the element in $G$. Chooses three parameters: $\alpha, \beta, a$ from $Zp$ randomly, chooses the parameter $V_x \in Z_p$ for each attribute $x$ in $U$, and then outputs the public key $PK = \{g, e(g,g)^{\alpha}, g^a, \rho\}$, master key $MSK = \{\alpha, \beta, \{Vx\}_{x \in U}\}$, attribute public key $PK_x = \{g^{V_x}\} x \in U$.

**Encrypt algorithm.** $Encrypt(\psi, PK, PKx, A) = CT$: encrypts the input message by using *PK*, *PKx*, and access control policy *A*. According to access control policy A, the algorithm generate one LSSS matrix $M_{n,k}$, and then choose $V = [s, y_1, y_2 \ldots y_{k-1}]^{\perp}$ at random and compute $\lambda = MV$. In addition, randomly selects $r_1, r_2 \ldots r_n \in Z_p$, the ciphertext $CT = \{C = \psi \cdot e(g,g)^{\alpha s}, C' = g^s, \{C_i = g^{a\lambda_i} \cdot [g^{V_{x_i}} \cdot \rho(x_i)]^{-r_i}, \quad D_i = g^{r_i}\}_{1 \le i \le n}\}$ is gotten, where $x_i$ is attribute corresponding to the row $i$ of the matrix M.

**Key generation algorithm.** $Keygen(MSK, PK, PKx, S) = \{TK, SK\}$: is executed by *AA* by using *MSK*, *PK*, *PKx*, user's attribute set S, and output the private key SK and the conversion private key *TK*. After selecting $z \in Z_p$ randomly, $TK = \{K = g^{\alpha/z} \cdot g^{a\beta/z}, L = g^{\beta/z}, \{K_x = [g^{V_x} \cdot \rho(x)]^{\beta/z}\}_{x \in S}\}$, $SK = \{z\}$ is gotten, where *TK* is held by the service middleware, SK is held by users.

**Decryption delegation algorithm.** $Transform(CT, TK) = CT'$: is executed by the ABE middleware. First, chooses vector $W = \{w_1, w_2 \ldots w_n\}$ to make $W \cdot M = \{1, 0, 0 \ldots 0\}$. Then calculates for each line of $CT$: $e(C_i^{w_i}, L) \cdot e(D_i^{w_i}, K_i)$, where $K_i$ is the key share corresponding to the attribute. The computation result of each line is multiplied: $A = \prod_{i \in I} e(C_i^{w_i}, L) \cdot e(D_i^{w_i}, K_i) = e(g, g)^{sa\beta/z}$. Computing $R = e(C', K)/A = e(g, g)^{\alpha s/z}$, The middle result $CT' = \{C, R\}$ is send to the mobile finally.

**Decryption algorithm.** $Decrypt(CT', SK) = \psi$: is executed in the mobile. Receiving $CT'$, the mobile can decrypt and obtain the original data: $\psi = C/R^z$.

Since our ABE algorithm is based on the basic CP-ABE and the ABE given in reference [7], it has the same security properties for the decisional BDH assumption.

### 3.2 Attribute Revocation

Assuming AA hopes to revoke the attribute *attr* of one user, the procedure of attribute revocation works as follows:

1. AA chooses a new attribute parameter $V'_{attr}$ for *attr*, computes $PK_{attr} = g^{V'_{attr}}$, and sents *attr* and $PK_{attr}$ to the ABE middleware.
2. The service middleware updates attribute public key as $PK_{attr}$ of *attr* in the attribute public key query module.
3. The ABE middleware queries attribute dependency table $CT$, gets $FID$ of $CT$ using the attribute and corresponding row index. $D_{attr} = g^{r_i}$ is loaded according to FID and the row index.
4. The ABE-middleware returns $D_{attr}$ to AA.
5. AA generates the upgrade key of $CT$ based on $D_{attr}$, that is $CUK = D_{attr}^{-(V'_{attr} - V_{attr})} = g^{-r_i(V'_{attr} - V_{attr})}$, and then sends it to the service middleware.
6. The middleware upgrades $CT$ by using $CUK$: $C_{attr} = C_{attr,old} \cdot CUK$, and then get $C_{attr} = g^{a\lambda_i} \cdot [g^{V'_{attr}} \cdot \rho(attr)]^{-r_i}$.
7. AA generates the upgrading key for the mobile who has not been revoked attribute *attr*: $UUK = g^{(V'_{attr} - V_{attr}) \cdot \beta/z}$, and sents it to the ABE middleware.
8. The ABE middleware uses $UUK$ to upgrade $TK$: $K_{attr} = K_{attr,old} \cdot UUK$, and then we can obtain $K_{attr} = [g^{V'_{attr}} \rho(attr)]^{\beta/z}$.

After completing the above process, the attribute parameters of *attr* in $CT$ are upgraded from $V_{attr}$ to $V'_{attr}$. For the user who is not revoked the attribution attr, AA generates $UUK$ and upgrades the attribute attr parameter in $K_{attr}$ to $V'_{attr}$. The user who has been revoked *attr* cannot be upgraded because they don't get $UUK$. So $K_{attr}$ of the revoked users become invalid, and then the user's rank is revoked.

# 4 Experiments

## 4.1 Experiment Environment

We realize the ABE middleware and the ABE middleware based mobile client application in Java which is shown in Fig. 3, and deployed in an experiment lab. The experiment environment includes a Dawn server w5801-G10 (CPU: 2 *Intel Xeon E5-2630, Memory: 64G) and a Huawei smart phone Y635-CL00 (CPU: Snapdragon 410, Memory: 1G). The attribute authority and ABE middleware are deployed in the Dawn server as a virtual machine, and the decryption and revocation performances are evaluated.


**Fig. 3.** The ABE middleware based mobile client

## 4.2 Decryption Performance

The experiment are carried out to respectively test the server middleware and mobile equipment decryption consumed time for attribute index from 10 to 100 in the *CT*, the time consuming comparison is shown in Fig. 4.

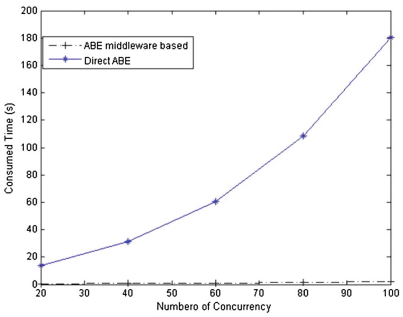


**Fig. 4.** Decryption time of the mobile

It can be seen from the experiment result that the attribute based decryption time is greatly reduced by using the middleware. When *CT* contains 10 attributes, the decryption time has been cut by 19.5 times, and with the increase of number of attributes, the advantage is more obvious. When the number of attributes is increased to 100, the decryption time is dropped by 30.7. This method using middleware proxy decryption reduce the requirement for terminal, fully reflect the advantage of cloud computing.

### 4.3 Concurrency Performance

The concurrency processing capability for server middleware is tested using the LoadRunner 9 (http://environment.yale.edu/loadrunner/). For a CT with 10 attributes, we can simulate the request decryption for 0 to 100 concurrent users. The concurrent performance is shown in Fig. 5.

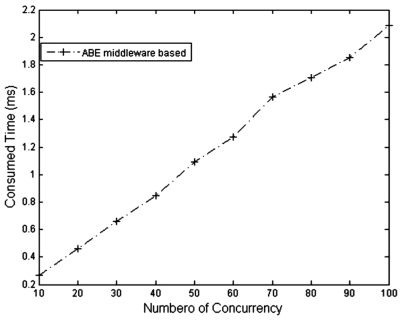


**Fig. 5.** Concurrency performance of ABE middleware

The result shows that when the system has 100 concurrent requests, the response time is 2.087 s which is shorter than directly decryption of mobile devices. With the increasing of concurrency, proxy decryption time may exceed the directly decryption time of mobile devices. But we should notice the service middleware is deployed in the cloud, cloud computing has the following features such as massive computing resources, easy expansion and easy deployment, so we can solve the high concurrency problem by extending the computing resources of service middleware.

### 4.4 Rank Revocation

The user's rank is revoked means that one or more of its attributes are changed. When revoking one attribute of users, it is needed to upgrade CT component corresponding with this attribute and other key component of no-revocation users.

Compared with the attribute revocation schemes in [9–11] require user to encrypt data again, the method in this paper has great advantage. The result shows that the attribute revocation time approximately linear increases with the increase of the number of users and CT associated with this attribute. In the experiments, when the number has

100 and the users have 400 associated with the revocation attribution, the total consumption time on attribute revocation is 17.68 s, which is 5 times of that of 1 CT and 2 users. The attribute revocation process can further improve the performance by increasing the number of middleware.

## 5 Conclusion

It is difficult to achieve the attribute based decryption because of its high complexity in the resource limited mobile device, so this paper proposes a ABE based method for the mobile to use cloud storage securely. The mobile equipment can outsource large number of computation in the ABE decryption process through the ABE middleware. The attribute authority can complete the fine grained revocation for user attribute without affecting any other users. All services in the middleware provided by the Restful interface are suitable for the mobile device to invoke. The proposed ABE middleware performance is tested in the real mobile cloud storage application. The result shows that the ABE middleware can improve the decryption performance of mobile device obviously, and the performance of concurrency and attribute revocation can satisfy the practice. In the future, we will further study the distribution integration method about the multiple ABE middle wares.

**Acknowledgment.** This work was partly supported by the National Natural Science Foundation of China (61661015), Ministry of Education Key Lab of Cognitive Radio and Information Processing Found (CRKL160101), Guangxi Collaborative Innovation Center of Cloud Computing and Big Data Found (YD16801), Guangxi Scientific and technological plan (1598008-28), High Level of Innovation Team of Colleges and Universities in Guangxi Outstanding Scholars Program Funding, and GUET Cloud Security and Cloud Service Innovation Group Project.

## References

1. The 34th accounting reports of the development situation of China Internet. China Internet, vol. 7 (2014)
2. Armbrust, M., Fox, A., Griffith, R., et al.: A view of cloud computing. Commun. ACM **53** (4), 50–58 (2010)
3. Feng, D.G., Zhang, M., Zhang, Y., Xu, Z.: Study on cloud computing security. J. Softw. **22** (1), 71–83 (2011)
4. Horváth, M.: Attribute-based encryption optimized for cloud computing. In: Italiano, G.F., Margaria-Steffen, T., Pokorný, J., Quisquater, J.-J., Wattenhofer, R. (eds.) SOFSEM 2015. LNCS, vol. 8939, pp. 566–577. Springer, Heidelberg (2015). https://doi.org/10.1007/978-3-662-46078-8_47
5. Bethencourt, J., Sahai, A., Waters, B.: Ciphertext-policy attribute-based encryption, pp. 321–334 (2007)
6. Waters, B.: Ciphertext-policy attribute-based encryption: an expressive, efficient, and provably secure realization. In: Catalano, D., Fazio, N., Gennaro, R., Nicolosi, A. (eds.) PKC 2011. LNCS, vol. 6571, pp. 53–70. Springer, Heidelberg (2011). https://doi.org/10.1007/978-3-642-19379-8_4

7. Wang, Y.D., Yang, J.H., Xu, C., Ling, X., Yang, Y.: Survey on access control technologies for cloud computing. Ruan Jian Xue Bao/J. Softw. **26**(5), 1129–1150 (2015)
8. Su, J.S., Cao, D., Wang, X.F., Sun, Y.P., Hu, Q.L.: Attribute-based encryption schemes. J. Softw. **22**(6), 1299–1315 (2011)
9. Pirretti, M., Traynor, P., Mcdaniel, P., et al.: Secure attribute-based systems, pp. 99–112 (2006)
10. Asim, M., Ibraimi, L., Petković, M.: Ciphertext-policy attribute-based broadcast encryption scheme. In: De Decker, B., Lapon, J., Naessens, V., Uhl, A. (eds.) CMS 2011. LNCS, vol. 7025, pp. 244–246. Springer, Heidelberg (2011). https://doi.org/10.1007/978-3-642-24712-5_25
11. Wang, P.P., Feng, D.G., Zhang, L.W.: CP-ABE scheme supporting fully fine-grained attribute revocation. J. Softw. **23**(10), 2805–2816 (2012)
12. Belqasmi, F., Glitho, R., Fu, C.: RESTful web services for service provisioning in next-generation networks: a survey. IEEE Commun. Mag. **49**(12), 66–73 (2011)
13. Belqasmi, F., Singh, J., Bani Melhem, S.Y., et al.: SOAP-based vs. RESTful web services: a case study for multimedia conferencing. IEEE Int. Comput. **16**(4), 54–63 (2012)
14. Li, Y., Zeng, Z.Y., Zhang, X.F.: Outsourced decryption scheme supporting attribute revocation. J. Tsinghua Univ. (Sci. Technol.) **12**, 1664–1669 (2013)

# High Capacity Embedding Methods of QR Code Error Correction

Song Wan(✉), Yuliang Lu, Xuehu Yan, Wanmeng Ding, and Hanlin Liu

Hefei Electronic Engineering Institute, Hefei 230037, China
wsong1031@163.com

**Abstract.** In this paper, two methods about how to embed message into QR code are investigated. According to different application scenarios, two different embedding ways are given. The first proposed embedding way is to modify a continuous region based on the arrangement of codewords in QR code and the mechanism of QR code error correction which can reach the maximum error correction capability as well as scan the QR code altered by a QR code reader. The second embedding way is designed to modify each column separately in coding regions which can be decoded correctly as well. Although the second embedding way couldn't reach high capacity, it can be applied in many occasions while the first embedding way couldn't. Based on the proposed two embedding methods and the analysis of the error correction mechanism, we conclude the general rules about how to embed message into QR code. The experiment results show the effectiveness of our methods.

**Keywords:** QR code · Error correction · Embedding capacity

## 1 Introduction

QR code [1] which are widely used as a means of conveying textual information, such as hyperlinks, emails, or phone numbers, through images that are interpreted using a smartphone camera are a popularly used two-dimensional barcode recently with the advantages of larger QR content and error correction capability. Even if it is dirty, we may be able to read it since it has error correcting capability. Additional to the characteristics for QR code such as high-speed reading, high-density recording (approx. 100 times higher in density than linear symbols), and large volume data (7,089 numerical characters at maximum), QR code has other superiority in both functionalities and performance aspects [2].

Recently, many researchers have proposed some schemes [3] exploiting the error correction mechanism inherent in the QR code structure to implement different applications [4]. For example, a scheme [5] which deeply integrate the error correction mechanism of QR code and the theory of Visual Secret Sharing (VSS). The scheme generates the bits corresponding to shares by VSS from a secret bit in the processing of encoding QR. Each share is a valid QR code that can be scanned and decoded by a QR code reader. The shares may not be suspected if distributed via public channels and will reduce the likelihood of attracting the


M. Huang et al. (Eds.): WICON 2016, LNICST 214, pp. 70–79, 2018.
https://doi.org/10.1007/978-3-319-72998-5_8

attention of potential attackers. Based on this, this kind of schemes has great application value. So, the applications are valuable that exploiting the error correction mechanism inherent in the QR code structure. If we want to complete the kind of schemes, the mechanism of QR codes error correction need to be understand. In addition, it is the most important that how to embed message into QR code which can reach the maximum error correction capability within the error correction level. However, there is no method to all QR code versions about how to embed message into QR code which can reach the maximum error correction capability satisfying that the QR code altered can still be decoded.

In this article, we propose two methods about how to embed message into QR code. Due to different application scenarios, two different embedding ways are given. The first embedding way modifies a continuous region of QR code which can reach the maximum error correction capability within the error correction level for all QR code versions. In addition, the output QR code can be so as to scanned correctly. The second embedding way is to modify the modules through separating columns in coding regions that the QR code altered can still be decoded for all QR code versions as well. Although this embedding way couldn't reach high capacity, it can be applied in many occasions while the first embedding way couldn't.

The remainder of the paper is organized as follows. The introduction to the QR codes are presented in Sect. 2. The proposed process described in Sect. 3. Section 4 demonstrates the simulation results and analyses. Finally, Sect. 5 concludes this paper.

## 2 Background

### 2.1 QR Code

QR code which was invented by the Denso Wave [6] Incorporated in 1994 is defined as a two-dimensional barcode. The standard [1] defines forty sizes of QR code symbol versions which range from version 1 to version 40. A QR code is divided into modules and each QR code symbol version is comprised of a different number of modules. Each version has four modules more than the previous one. For example, Version 1 is made up of $21 \times 21$ modules while version 2 is made up of $25 \times 25$ modules. The QR code structure consists of function patterns and encoding regions. The encoding region consists of error correction and data codewords, version information and format information while function patterns consist of the alignment patterns, timing, separators patterns and finder patterns. The structure of a QR code version 7 is illustrated in Fig. 1. Each QR code has three Finder Patterns which are located in the lower left, upper left and upper right corner. They are used to recognize the QR code and detect the position of the symbol. Alignment Patterns that only occur from version two up to forty permit QR code readers to compensate for image distortion and the higher the version is, the more Alignment Patterns exist. A quiet zone which is the blank area around QR code is necessary for reading the QR code. It should

have the same reflectance value as the light modules, because the QR code readers could not distinguish between the Finder Patterns and the dark background. Timing patterns are used to determine the module coordinates and the separators which are one module wide are used to separate the finder patterns from the encoding region.

The data in QR code is encoded into the binary numbers of "1" and "0" based on Reed-Solomon codes that used for error detection and correction. The bit stream which is generated by message data encoded is divided into a sequence of codewords that are 8 bits length. There are four different error correction levels (L $\sim$ 7%, M $\sim$ 15%, Q $\sim$ 25%, H $\sim$ 30%). The error correction [7–9] is used for recovering the QR code in the event that parts of the symbol are dirty or destroyed. So, the QR code can also be recognized when embed other information in it. The recovery capacity of QR code will be improved by using the higher error correction levels, but it will increase the amount of data to be encoded. It means that a larger QR code version may be required when using a higher error correction level to encode the same message.

To minimize the possibility that localized damage will cause the QR code become undecodable, the codewords from the blocks are encoded in an interleaved manner, with the error correction codewords appended to the end of the data codewords sequence. The data codewords and error correction codewords arrangement for QR code version 7, with an error correction level of H, is shown in Fig. 1.

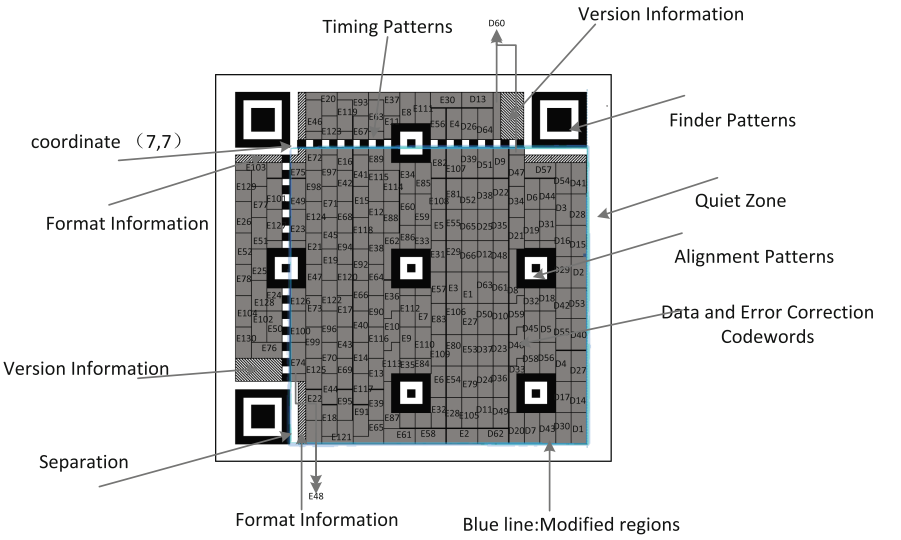


**Fig. 1.** The structure and codewords arrangement for QR code version 7 with error correction level H

## 3 Proposed High Capacity Embedding Methods

In this section, two methods about how to embed message into QR codes which can reach the maximum error correction capability are proposed. According to different application scenarios, two different embedding ways are given.

The first way about how to embed is a continuous region altered. The region altered can be a rectangle from the coordinate of $(7, p-j)$ to the lower right corner while the value of j can be determined by the error correction capacity of the QR code and the codewords altered can reach the maximum error correction capacity. The theoretical derivation is as follow.

The QR codes can be correctly decoded while the codewords altered reach the maximum that the error correction level allowed. In this paper, the methods proposed are to use the highest level of QR codes error correction.

Given a cover QR code with error correction level of H, and the embed message $S$ with $n$ bits, the length of $n$ is determined by the error correction capacity of the QR code as

$$n = \left\lfloor \frac{m-e}{2} \right\rfloor \times 8 \leq \left\lfloor \frac{m}{2} \right\rfloor \times 8 \tag{1}$$

Here, $m$ is the number of error correction codewords, $e$ is the number of error detection codewords, and a codeword equals to eight modules in the QR codes structure. The maximum number of codewords that can be altered in QR code are referred to as $l$, where $l = n/8$.

The encoded data before data mask is stored in an array module of QR codes from left to right. The coordinate of $(0, 0)$ represents the top left corner of the array module. The three identical finder patterns which are made up of $7 \times 7$ modules are used to recognize the QR code and to determine the rotational orientation of the symbol. In order to make sure that the three identical finder patterns of QR code could not be altered so that it does not affect the appearance, we define the data which is blue region as shown in Fig. 1 that could be modified is from the coordinate of $(7, 7)$ to the last. Although some bits of the format information may be altered, It couldn't affect the format information [9]. So, the region we define is possible.

Due to the characteristics and basic principles of the design of QR code, it can be seen that the arrangement of the codewords are in two modules wide starting from the symbol of the lower right corner to decorate, from right to left, and alternately from the bottom up or down. In QR code with an error correction level H, the first codeword of each block is arranged, then the second codeword, until the last one. The codewords from the blocks are encoded in an interleaved manner, with the error correction codewords appended to the end of the data codewords sequence, as shown in Fig. 1. So, the left region of QR code is error correction codewords while the right region is data codewords. It is possible that localized damage would not make the QR code undecodable.

The error correction codewords for each block is given as (c, k, r), Here, $c$ is the total number of codewords, $k$ is the number of data codewords and $r$ is the

error correction capacity which represents the maximum number of codewords that can be altered per block. It means that if more than r codewords per block contain errors, the QR code would not be decoded. So, we must make sure that the codewords altered per block can't be more than r and the total codewords altered in QR code need to be equal to or less than $l$.

When we alter the codewords including data codewords and error correction codewords, it is hard to locate the position of each block so that can't make sure that the number of codewords altered per block is smaller than r or not. In this case, although we can control the total codewords altered in QR code less than $l$, the number of codewords altered per block couldn't guarantee. As the characteristics of QR code, it can be concluded that if the codewords altered all in data region or the whole in the error correction region, we can make measurers to guarantee the codewords altered per block wouldn't more than r. So, we can ensure that the number of codewords that can be altered would be infinitely close to the maximum. In conclusion, we will altered codewords all in data region or the whole in error correction region, which can reach the maximum number of codewords that can be altered. As the blue region chosen is from the coordinate of $(7, 7)$ to the last, there are some error correction codewords and data codewords that do not be included here and that the number of error correction codewords are much more than data codewords. Based on this, we will modify the codewords all in data region.

The problem now is how to determine the coordinates of the region altered that can reach the maximum and can be scanned correctly. Due to the arrangement of data codewords, the region altered can be a rectangle from the coordinate of $(7, p - j)$ to the lower right corner. The total codewords that can be altered must be equal to or less than $l$, so that the value of j can be determined. As can be seen that when meeting alignment patterns, the arrangement of codewords need to leave space for them. In other words, the same number of codewords will need bigger regions if containing alignment patterns with size of $5 \times 5$. So, when containing alignment patterns, the number of codewords of the region altered with size of $n$ is less than $l$. Considering the relationship between the total number of alignment patterns contained in the region altered and the value of $(p-7)$, the arrangement of the data codewords, other possible errors that affect the QR code with high version scanned correctly, the range of j will be as follow:

$$\left\lfloor \frac{n}{p-7} \right\rfloor - 1 \leq j \leq \left\lfloor \frac{n}{p-7} \right\rfloor + 1 \tag{2}$$

Here, the coordinate of the lower right corner is $(p, p)$, $(p - 7)$ represents the number of lines in the blue region. In this way, the region altered of QR code with version from two up to forty would reach the maximum that match the capacity of QR code with error correction H.

As alignment Patterns only occur from version two up to forty, if QR code version 1 with error correction H using the method above, the region can be altered wouldn't reach maximum. After analysis, we find the region altered that

from the coordinate of $(7, 13)$ to $(17, 21)$ is maximum and the QR code can be decoded correctly.

The QR code error correction level of H $\sim 30\%$, is merely approximate value. The total number of codewords in each QR code version can be referred to as $N$, where $N = m + t$, $t$ is the total number of data codewords. To analyze the error correction blocks of 40 versions, we can find that only version 1 of QR code need one error correction codeword for error detection and other versions do not. In QR code version 1 with error correction level H, there are 17 error correction codewords which can correct 8 data codewords. AS the total codewords are 26, the error correction rate is 30.7%. From version 2 to 40 of QR code, two error correction codewords can correct one data codeword, so the error correction rate of QR code H, will be referred to as

$$H = \frac{m}{2N} \tag{3}$$

Hence, the relationship between the total number of error correction codewords and data codewords can be defined as

$$\frac{m}{t} = \frac{2H}{1 - 2H} \tag{4}$$

The value of $m/t$ range from 1.7 to 1.96 with the research of data codewords and error correction codewords from version 2 to 40 of QR code with error correction level H. Based on the value of $m/t$, the error correction rate of QR code with error correction level H is range from 31.5% to 33.2%. Theoretically, the error correction rate will range from 30.7% to 33.2%. As some alignment patterns in the region altered and the arrangement of the data codewords, sometimes the error correction rate may be larger than 33.2% or smaller than the rate of 30.7% as the method of the region altered and other possible errors. Although the rate is change, it is very small. The first embedding way would be applied in all versions of QR code and it can reach the maximum capacity.

The second embedding way is to separate columns in blue region which is easy to alter and wouldn't affect the appearance of QR codes, as shown in Fig. 1. In this case, we can control the total codewords altered in QR code less than $l$ and guarantee the number of codewords altered per block wouldn't more than r. Although this embedding way couldn't reach high capacity, it can be applied in many occasions while the first embedding way couldn't.

## 4 Experimental Results and Analyses

In this section, the effectiveness of methods proposed are evaluated by our experiments. A large number of QR code versions with error correction level H are used to test the efficiency of the proposed methods.

### 4.1 Image Illustration

In our experiments, the simulation environment of the proposed process is python language. In the first embedding way, Fig. 2 shows the simulation results for the QR code version 6 with $41 \times 41$ modules and error correction H. Figure 2(a) is the cover QR code with the content "the important things", $S$. The region altered of QR code, $SC_1$, from the coordinate of $(7, 29)$ to $(41, 41)$ is shown in Fig. 2(b) while the region altered from the coordinate of $(7, 28)$ to $(41, 41)$ is shown in Fig. 2(c), $SC_2$. Figure 2(d)–(f) show the decoding information for $S$, $SC_1$, $SC_2$. It can be seen that the altered QR code shown in Fig. 2(c) can't be decoded correctly while the altered QR code shown in Fig. 2(b) can be scanned. So, the altered QR code shown in Fig. 2(b) reaches the maximum error correction capability.

Figure 3 demonstrates the results of the QR code version 40 with 177×177 modules and error correction level H. Figure 3(a) is the cover QR code, $S$, and the region altered of QR code, $SC_1$, from the coordinate of $(7, 121)$ to $(177, 177)$ is shown in Fig. 3(b). Figure 3(c) shows the region altered of QR code, $SC_2$, from the coordinate of $(7, 58)$ to $(85, 85)$. Figure 3(d)–(f) show the decoding information for $SC_1$, $SC_2$. The altered QR code shown in Fig. 3(c) can't be decoded correctly while the altered QR code shown in Fig. 3(b) can be scanned. So, the altered QR code shown in Fig. 3(b) reaches the maximum error correction capability.

(a) Original QR S

(b) SC1

(c) SC2

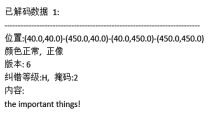


(d) the decoding information for S

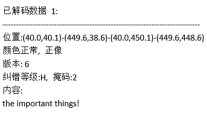


(e) the decoding information for SC1

(f) the decoding information for SC2

**Fig. 2.** The results of QR code version 6 with error correction level H by the first embedding way proposed.

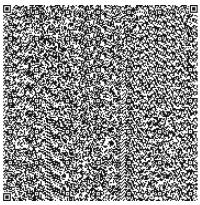

(a) Original QR S

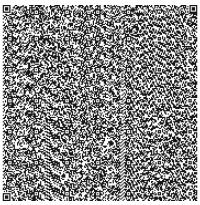

(b) SC1

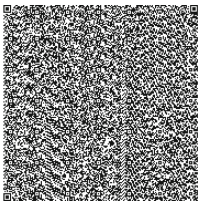

(c) SC2

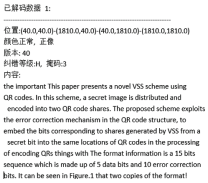


(d) the decoding information for S

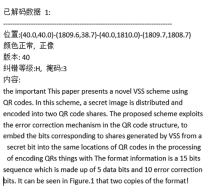


(e) the decoding information for SC1

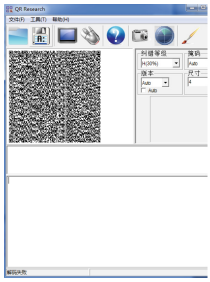

(f) the decoding information for SC2

**Fig. 3.** The results of QR code version 40 with error correction level H by the first embedding way proposed.

**Table 1.** The payload and rate of region altered of the proposed first embedding way

| Version | Size | N | m | l | j | payload | rate |
|---|---|---|---|---|---|---|---|
| 1-H | 441 | 26 | 17 | 8 | | 80 | 38.46% |
| 2-H | 625 | 44 | 28 | 14 | 7 | 126 | 35.79% |
| 3-H | 841 | 70 | 44 | 22 | 8 | 176 | 31.42% |
| 4-H | 1089 | 100 | 64 | 32 | 10 | 260 | 32.5% |
| 5-H | 1369 | 134 | 88 | 44 | 12 | 360 | 33.58% |
| 6-H | 1681 | 172 | 112 | 56 | 12 | 408 | 29.65% |
| 7-H | 2025 | 196 | 130 | 65 | 14 | 532 | 33.92% |
| 10-H | 3249 | 346 | 224 | 112 | 18 | 900 | 32.5% |
| 17-H | 7225 | 815 | 532 | 266 | 26 | 2028 | 31.1% |
| 20-H | 9409 | 1085 | 700 | 350 | 30 | 2700 | 31.1% |
| 27-H | 15625 | 1828 | 1200 | 600 | 40 | 4720 | 32.27% |
| 30-H | 18769 | 2185 | 1440 | 720 | 44 | 5720 | 32.72% |
| 35-H | 24649 | 2876 | 1890 | 945 | 50 | 7500 | 32.59% |
| 40-H | 31329 | 3706 | 2430 | 1215 | 56 | 9520 | 32.11% |

**Table 2.** The results of the second embedding way

| The number of columns separated version-error correction level | 4 | 5 | 6 | 7 | 8 | 9 |
|---|---|---|---|---|---|---|
| 1-H | No | Yes | | | | |
| 2-H,3-H,4-H,5-H,6-H,7-H,8-H,12-H,18-H | No | No | Yes | | | |
| 9-H,10-H,11-H,13-H,15-H,17-H,19-H,20-H,21-H,23-H,24-H,25-H,26-H,27-H | No | No | No | Yes | | |
| 14-H,16-H,22-H,28-H,29-H,30-H,32-H,33-H,35-H,36-H,37-H,38-H,39-H | No | No | No | No | Yes | |
| 31-H,34-H,40-H | No | No | No | No | No | Yes |

Table 1 lists the payload of region altered of the proposed first embedding way under different QR versions with error correction H. As the QR code version 1 contains no alignment pattern is analyzed before, for the sake of brevity, we list several versions with different alignment patterns between the Version 2 ($25 \times 25$ modules = 625 modules) and the largest Version 40 ($177 \times 177$ modules = 31,329 modules). The designed mechanism exploits the characteristics of the error correction capability and the arrangement of codewords of the QR code to achieve the purpose.

Table 2 lists the results of the second embedding way under different QR code versions with error correction H. The operation of separating columns is in the blue region of all QR code versions as shown in Fig. 1. The value of columns separated in blue region is listed in table. 'Yes' represents the QR code altered can be decoded correctly while 'No' represent the QR code altered couldn't.

### 4.2 Analysis

From the statistical data, we can conclude that the region altered of the proposed first embedding way can reach the error correction capability. In this way, the number of modules that can be modified would reach almost the maximum with the error correction level H. From the second embedding way, it can be seen that the value of the columns separated is between five and night. In general, the value of the columns separated in the blue region of most QR code versions is range from six to eight and with the QR code version higher, the value of the columns separated would be bigger. Although the second embedding way couldn't reach high capacity, it can be applied in many occasions which may contain image information hiding and so on, when the first embedding way couldn't.

## 5 Conclusion and Future Work

This paper presents two methods about how to embed message into QR code. Due to different application scenarios, two different embedding ways are given. The first embedding way can reach the maximum error correction capability

within the error correction level H for all QR code versions. In addition, the output QR code can be so as to scanned correctly. The second embedding way is to modify each column separately in coding regions that the QR code altered can still be decoded and would be applied in all QR code versions. In general, the value of the columns separated in the blue region of most QR code versions is range from six to eight. Although the second embedding way couldn't reach high capacity, it can be applied in many occasions while the first embedding way couldn't. The future work will be implemented some applications which exploiting the high capacity embedding methods of QR code error correction.

**Acknowledgement.** The authors would like to thank the anonymous reviewers for their valuable comments. This work is supported by the National Natural Science Foundation of China (Grant Number 61602491) and Hefei Electronic Engineering Institute Foundation (KY16A654).

## References

1. Jtc1/Sc, I.: Information technology - automatic identification and data capture techniques - qr code 2005 bar code symbology specification (2006)
2. Várallyai, L.: From barcode to QR code applications. Agrárinformatika Folyóirat **3**(2) (2013)
3. Wang, G., Liu, F., Yan, W.Q.: 2D barcodes for visual cryptography. Multimedia Tools Appl. **75**(2), 1223–1241 (2016)
4. Kan, T.W., Teng, C.H., Chen, M.Y.: QR code based augmented reality applications. In: Furht, B. (ed.) Handbook of Augmented Reality. Springer, New York (2011). https://doi.org/10.1007/978-1-4614-0064-6_16
5. Wan, S., Lu, Y., Yan, X., Liu, L.: Visual secret sharing scheme with (k, n) threshold based on QR codes. In: 12th International Conference on Mobile Ad-hoc and Sensor Networks (2016)
6. Denso Wave Inc. (2002). http://www.qrcode.com
7. Yan, X., Guan, S., Niu, X.: Research on the capacity of error-correcting codes-based information hiding, pp. 1158–1161. IEEE Computer Society (2008)
8. Saito, K., Morii, M.: Efficient decoding of QR code using error correcting capability: Decoding method using erasure error correction and the ability. Technical Report of IEICE ISEC, vol. 111, pp. 79–84 (2011)
9. Chow, Y.-W., Susilo, W., Yang, G., Phillips, J.G., Pranata, I., Barmawi, A.M.: Exploiting the error correction mechanism in QR codes for secret sharing. In: Liu, J.K.K., Steinfeld, R. (eds.) ACISP 2016. LNCS, vol. 9722, pp. 409–425. Springer, Cham (2016). https://doi.org/10.1007/978-3-319-40253-6_25

# Perceptual Secret Sharing Scheme Based on Boolean Operations and Random Grids

Xuehu Yan(✉), Yuliang Lu, Lintao Liu, Song Wan, Wanmeng Ding, and Hanlin Liu

Hefei Electronic Engineering Institute, Hefei 230037, China
publictiger@126.com

**Abstract.** In this paper, a new perceptual secret sharing (PSS) scheme is developed based on Boolean operations and random grids. In the developed scheme, the secret image is shared among $n$ shadows using $(l, n, n)$ threshold scheme, while the restored secret image is restored from l out of $n$ shadows. $P(l, n, n)$ threshold is satisfied in this developed scheme, by acquiring this property no information recovery occurs when less than $l$ shares are stacked, imperfect recovery occurs when more than $l$ but less than $n$ shares are presented and perfect recovery occurs when $n$ shares are collected.

**Keywords:** Visual secret sharing · Perceptual secret sharing
Threshold · Boolean operations · Random grids

## 1 Introduction

In many applications like Pay- TV/Music and art-work image vending, pay-per-view video on demand (VOD), a feature of "perceptual secret sharing (*PSS*)" is very useful [1]. The *PSS* model is defined as the secret sharing scheme that degrades the quality of media data according to quality or security requirements [1–4] and recovers the secret lossless when sufficient shares are collected.

Secret image sharing technique is one alternative method to protect the secret images. It assigns a secret image among some owners by encrypting the secret image into noise-like shadows (also called shares or shadow images) and restoring the secret image by obtaining sufficient authorized owners (shadows). It attracted more attention of engineers and scientists. Visual secret sharing (VSS) [5,6] (also called visual cryptographic scheme (VCS)) is one primary branch in this domain.

The main properties of traditional VCSs [3,5–7] are free order of the shadows and simple recovery, i.e., the restoration of secret image is only based on human vision system (HVS) with no any cryptographic computation. Unfortunately, these schemes suffer from lossy recovery, pixel expansion or codebook design. Although VCSs by random grids (RG) [8–12] have no pixel expansion or complex codebook, they are lossy recovery. Progressive secret sharing methods, based on the ideas of VCS [13–16], RG [17], and Shamir's polynomial [18] or in transform domain [19], have perceptual quality for the restored secret image when more


M. Huang et al. (Eds.): WICON 2016, LNICST 214, pp. 80–90, 2018.
https://doi.org/10.1007/978-3-319-72998-5_9

shadows are obtained. Unfortunately, they overall suffer from limitations such as the pixel expansion, poor visual quality of the restored secret image or lossy recovery.

It is noted that the aforementioned schemes could not satisfy the properties of *PSS* that is mentioned previously. Recently, in [1], a $(l, k, n)$ threshold *PSS* model is defined, and a $(1, k, n)$ threshold *PSS* by maximum likelihood estimation (MLE) was developed, which could satisfy $P(1, k, n)$ threshold. Unfortunately, the scheme has complex computation in the recovery phase, and shadows have a little cross interference of the secret which may be not secure in some applications.

In this paper, a new perceptual secret sharing (*PSS*) scheme is developed to improve the security with low computational complexity of traditional PSS [1]. In the new scheme, a $(l, n, n)$ threshold *PSS* scheme is developed based on Boolean operations (Boolean XOR and stacking operations) and RGs through utilizing the random bits to obtain better features, such as threshold and lossless recovery. The secret image is generated into $n$ RGs, then the restored secret image is restored from $l$ *out of* $n$ shadows. The developed scheme has lower computational complexity with no cross interference of secret image. It satisfies $P(l, n, n)$ threshold and by acquiring this property no information recovery occurs when less than $l$ shares are stacked, imperfect recovery occurs when more than $l$ but less than $n$ shares are present and perfect recovery occurs when $n$ shares are collected. In addition, the developed scheme can realize other features such as lower computational complexity, free order of shadows in recovery, no pixel expansion and no codebook design. Experimental results and analyses indicate the feasibility and effectiveness of the developed scheme.

The rest of this article is stated as follows. The basic definitions and preliminaries are illustrated in Sect. 2. The developed $(l, n, n)$ threshold *PSS* scheme is given in Sect. 3. Section 4 focuses on the experimental results and analyses. Finally, Sect. 5 concludes this article.

## 2 Definitions and Preliminaries

In this section, we illustrate some fundamental definitions and preliminaries for the developed scheme. Symbols $\oplus$, & and $\otimes$ denote the Boolean XOR, AND and OR operations, respectively. $\overline{x}$ indicates a bit-wise complementary operation of any bit $x$. A binary secret image $S$ is generated among $n$ (generally $2 \leq \text{n} \leq 5, n \in \text{Z}^+$) shadows, and the restored secret image $S'$ is restored from any $t (2 \leq t \leq n, t \in \text{Z}^+)$ shadows based on stacking or Boolean XOR operations.

### 2.1 Fundamental Definitions [1]

**Definition 1** ***(PSS)*:** The original binary secret image is represented by $S$ whose pixel value denoted as $S(i,\ j)\quad (1 \leq i \leq M, 1 \leq j \leq N),\ size\,(S) = (M, N)$, where function *size* tells size of $S$. For a *P(l, k, n) PSS*, the binary secret

image $S$ is generated into $n$ $(2 \leq n, n \in \mathrm{Z}^+)$ shadows $SC_1, SC_2, \cdots SC_n$ according to generation function $(Gf)$, $(SC_1, SC_2, \cdots SC_n) = Gf(S, l, k, n) 1 \leq l \leq k \leq n$; Then the restored secret image $S'$ is restored from any $t$ $(1 \leq t \leq n, t \in \mathrm{Z}^+)$ shadows by recovery function $(Rf)$, i.e., $S'_t = Rf(SC_{i_1}, SC_{i_2}, \cdots SC_{i_t})$, where $(i_1, i_2, \cdots, i_t)$ demonstrates a subsequence of $(1, 2, \cdots, n)$. $VQ(S'_t)$ means the perceptual visual quality of the restored secret image $S'_t$. A *P(l, k, n) PSS* satisfies:

$$VQ(S'_t = Rf(SC_{i_1}, SC_{i_2}, \cdots SC_{i_t})) = 0 t < l;$$

$$VQ(S'_{t_2}) \geq VQ(S'_{t_1}) > 0 k \geq t_2 \geq t_1 \geq l; S'_t = Rf(SC_{i_1}, SC_{i_2}, \cdots SC_{i_t}) = S t \geq k.$$

Restoring function $Rf$ is simple.

$S'_{t_m} = Rf(SC_{i_{m_1}}, SC_{i_{m_2}}, \cdots SC_{i_{m_t}}) = S'_t = Rf(SC_{i_1}, SC_{i_2}, \cdots SC_{i_t})$, where $(m_1, m_2, \cdots, m_t)$ denotes a permutation of $(1, 2, \cdots, t)$.

$$size(S') = size(SC_i) = size(S), i = 1, 2, \cdots, n$$

$Gf$ and $Rf$ don't have extra codebook besides the parameters and input images.

Here "1" means white pixel and "0" is black pixel, which is the same as digital multimedia.

**Definition 2 (Contrast, denoted as $\alpha$) [9]:** In *PSS*, the visual quality of the restored secret image $S'_t$, which can decide how well human eyes will recognize the restored image, for the secret image $S$ is evaluated by contrast given as follows:

$$\frac{P_1 - P_0}{1 + P_0} = \frac{P(S'[AS1] = 1) - P(S'[AS0] = 1)}{1 + P(S'[AS0] = 1)} \tag{1}$$

where $P_0$(resp., $P_1$) illustrates appearance probability of white pixels in the restored image $S'$ in the corresponding black (resp., white) area of the secret image. $SAS0$ (resp., $AS1$) tells the black (resp., white) area of the secret image $S$ as $S0 = \{(i, j) | S(i, j) = 0, 1 \leq i \leq M, 1 \leq j \leq N\}$(resp., $S1 = \{(i, j) | S(i, j) = 1, 1 \leq i \leq M, 1 \leq j \leq N\}$).

**Definition 3 (Visually recognizable and security) [5]:** The restored secret image $S'$ will be recognized as the content of the secret image $S$ if $\alpha > 0$. The scheme is secure if $\alpha < 1$ when $l \leq t < k$ which tells part of secret (including content and details) of $S$ can be recognized from $S'$; $\alpha = 0$ when $t < l$ indicating no any secret (including content and details) of $S$ will be recognized from $S'$. The restored secret image $S'$ is lossless when $\alpha = 1$ under $t \geq k$, which tells all secret information (including content and details) of $S$ is recognized from $S'$.

### 2.2 RG-Based VSS

In RG-based VSS [10], "0" means white pixel, "1" is black pixel. The generation and restoration phases of an original (2, 2) RG-based [10] VSS will be given below.

Step 1: Generate 1 RG$SC_1$ randomly.

Step 2: Compute $SC_2$ according to Eq. (2).

Restoration: $S' = SC_1 \otimes SC_2$ as Eq. (3). If a certain pixel $s = S(i,j)$ of $S$ is 1, the restoration result $SC_1 \otimes SC_2 = 1$ will be always black. If a certain pixel is 0, the restoration result $SC_1 \otimes SC_2 = SC_1(i,j) \otimes SC_1(i,j)$ will have half chance to be black or white since $SC_1$ is random.

$$SC_2(i,j) = \begin{cases} SC_1(i,j) & if\ S(i,j) = 0 \\ \overline{SC_1}(i,j) & if\ S(i,j) = 1 \end{cases} \tag{2}$$

$$S'(i,j) = SC_1(i,j) \otimes SC_2(i,j) = \begin{cases} SC_1(i,j) \otimes SC_1(i,j) & if\ S(i,j) = 0 \\ SC_1(i,j) \otimes \overline{SC_1}(i,j) & = 1\ if\ S(i,j) = 1 \end{cases} \tag{3}$$

The same approach will be extended to $(l,n)$ threshold through applying the above process repeatedly on the first $l$ bits and setting the last $n-l$ bits randomly.

In addition, [12] improves the contrast of [10] through changing the last $n-l$ bits to be equal to the $l$th bit. However, the schemes in [10,12] are lossy. Besides, the color representation is different from that of digital images, which will not be convenient in digital images applications. Hence, a (2, 2) threshold scheme is used first as an example to show the main idea of the same color representation. The generation and restoration phases are given below, where "1" means white pixel and "0" is black pixel, which are the same as that of digital images.

Step 1: Generate 1 RG$SC_1$ randomly.

Step 2: Compute $SC_2$ as Eq. (4).

Restoration: $S' = SC_1 \& SC_2$ as in Eq. (5). If a certain pixel of $S(i,j)$ is 0, the restoration result $SC_1 \& SC_2 = 0$ will be always black. If a certain pixel of $S(i,j)$ is 1, the restoration result $SC_1 \& SC_2 = SC_1(i,j) \& SC_1(i,j)$ will have half chance to be black or white due to $SC_1$ are random.

$$SC_2(i,j) = \begin{cases} SC_1(i,j) & if\ S(i,j) = 0 \\ \overline{SC_1}(i,j) & if\ S(i,j) = 1 \end{cases} \tag{4}$$

$$S'(i,j) = SC_1(i,j) \& SC_2(i,j) = \begin{cases} SC_1(i,j) \& SC_1(i,j) & if\ S(i,j) = 1 \\ SC_1(i,j) \& \overline{SC_1}(i,j) & = 0\ if\ S(i,j) = 0 \end{cases} \tag{5}$$

Equations (2) and (4) focus on the generation phase of one secret bit $S(i,j)$, and Eqs. (3) and (5) the restoration phase. The difference of Eqs. (2) and (4) lies in the color representation method. Equations (3) and (5) utilize different restored operations.

## 3 The Developed PSS Scheme

In this section, we introduce a novel *PSS* scheme based on Boolean operations and RG to realize the *PSS* model defined in Sect. 2. Performance analyses are performed to show security of the developed scheme. Here "1" denotes white

pixel, "0" denotes black pixel, which are the same as the color representation method of digital images.

Before giving the details of the developed scheme, the principal of the developed scheme is stated as follows: $(l, n)$ threshold RG-based VSS is applied to obtain $(l, n)$ threshold first. Then the random bits in the $n$ bits are utilized to gain lossless restoration.

### 3.1 Shadows Generation and Restoration Phases

The shadows generation designed concept is in Fig. 1, whose algorithmic steps are given in Algorithm 1.

The secret restoration algorithmic steps are in Algorithm 2.

The ideas of Algorithms 1 and 2 are discussed precisely as follows:

Some random bits in the $n$ bits corresponding to the $n$ shadows. The random bits will be utilized to obtain better properties, e.g., threshold mechanism, improved visual quality and lossless restoration. In Step 2 of Algorithm 1, the $l$ bits are utilized to achieve threshold mechanism [10], i.e., when less than $l$ shadows are obtained, the secret cannot be restored. Step 2 in Algorithm 1 aims at improving the visual quality of restored secret image [12]. Flipping one of the last $n - l$ bits in step 5 of Algorithm 1 aims at satisfying $S(i, j) = b_1 \oplus b_2 \oplus \cdots \oplus b_n$, i.e., to be lossless restoration in Step 2 of Algorithm 2. Hence, the developed scheme is PSS (*l,n,n*). In step 6 of Algorithm 1, in order to make all the shadows be equal to each other, i.e., owning the same importance, the outputted $n$ bits are randomly rearranged to $n$ shadows bits.

**Algorithm 1.** The developed *PSS (l, n, n)* scheme.

**Input**: A binary secret image $S$ with size of $M \times N$, threshold parameters *PSS (l, n, n)*

**Output**: $n$ generated shadows $SC_1, SC_2, \cdots SC_n$

**Step 1:** For each position$(i, j) \in \{(i, j)|1 \le i \le M, 1 \le j \le N\}$, i.e., $S(i, j)$ , repeat Steps 2–6.

**Step 2:** Compute $b_1, b_2, \cdots b_l$ one by one repeatedly using Eq.(4), i.e., set $\tilde{b}_1 = S\,(i, j)$ for $p = 1, 2, \ldots, l - 1$ , generate $b_p$ randomly by flip-coin function. If $\tilde{b}_p = 0\tilde{b}_{p+1} = b_p$; otherwise, $\tilde{b}_{p+1} = \bar{b}_p$ Set $b_l = \tilde{b}_l$

Where $b_x$ and $\tilde{b}_x$denote the temporary pixels, $x = 1, 2, \ldots, n - 1, n$

**Step 3:** Set $b_{l+1} = b_l, b_{l+2} = b_l, \cdots b_n = b_l$

**Step 4:** If $n > l$, go to Step 5; else go to Step 6

**Step 5:** If $S(i, j) = b_1 \oplus b_2 \oplus \cdots \oplus b_n$ go to Step 6; else randomly select $q \in \{l+1, \cdots, n\}$, flip $b_q = \overline{b_q}$(that is 0→1 or 1→0).

**Step 6:** The order of the $n$ pixels $b_1, b_2, \cdots b_{n-1}, b_n$ are rearranged and the rearranged $n$ pixels are assigned to $SC_1(i, j), SC_2(i, j), \cdots SC_n(i, j)$

**Step 7:** Output the $n$ shadows $SC_1, SC_2, \cdots SC_n$

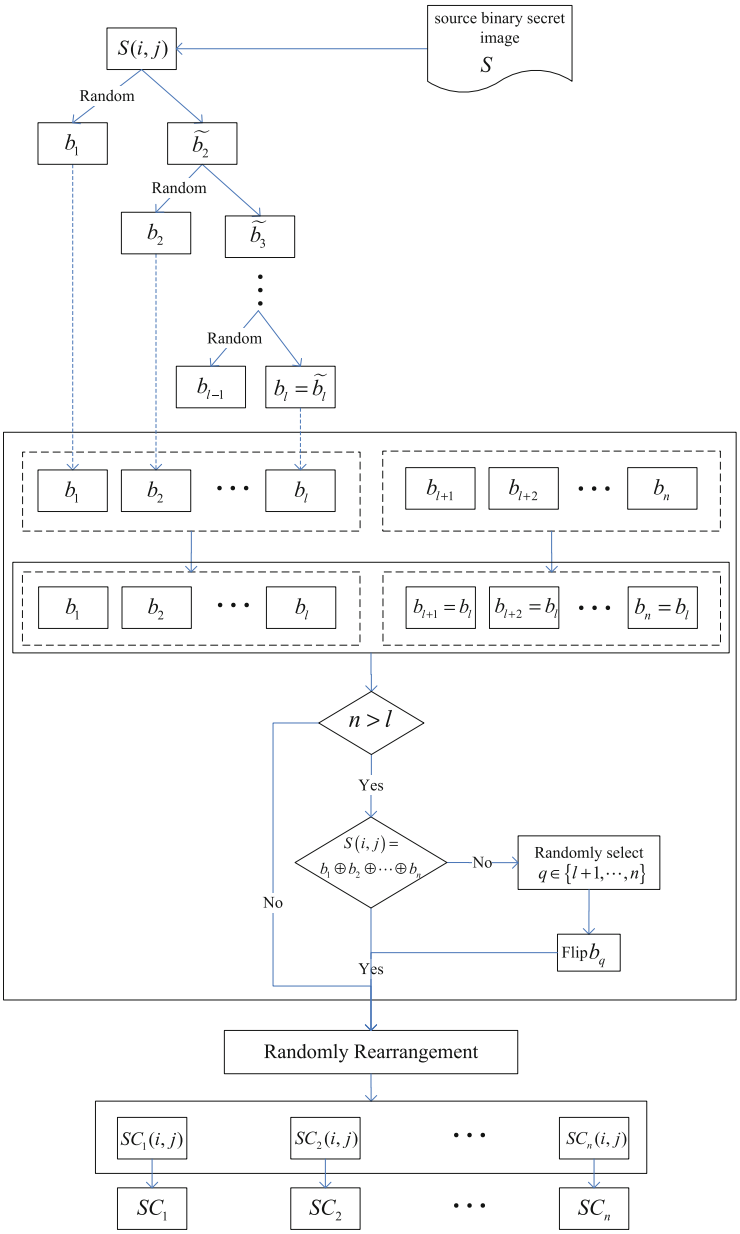


**Fig. 1.** Shadows generation design concept of our developed scheme

| **Algorithm 2.** Secret image restoration of the developed scheme. |
|---|
| **Input**: any $t$ shadows $SC_{j_1}, SC_{j_2}, \cdots SC_{j_t}$.<br>**Output**: A $M \times N$ binary restored secret image $S'$ |
| **Step 1:** If $t < n$, $S' = SC_{j_1} \& SC_{j_2} \& \cdots SC_{j_t}$ go to Step 3; else go to Step 2.<br>**Step 2:** $S' = SC_{j_1} \oplus SC_{j_2} \oplus \cdots \oplus SC_{j_t}$ If $n = l, l \in 2Z^+$, $S' = \overline{S}'$; else go to Step 3.<br>**Step 3:** Output the restored binary secret image $S'$. |

## 4 Experimental Results and Analyses

Herein, we will perform experiments and analyses to demonstrate the effectiveness of our developed scheme. In the experiments, binary secret images with size of $512 \times 512$, are employed to do the test.

In our experiments, $PSS\ (3, 4, 4)$ (i.e. $l = 3, k = \ n\ = 4$) threshold with secret image1, $PSS\ (2, 5, 5)$ (i.e. $l = 2, k = \ n\ = 5$) threshold with secret image2, and $PSS\ (2, 3, 3)$ with secret image3 are employed.

Figure 2(b–e) show the obtained 4 shadows $SC_1$, $SC_2$, $SC_3$ and $SC_4$ from binary secret image 1, which are noise-like. Figure 2(f–j) show the restored binary secret image with any 3 or 4 shadows, from which the secret image1 restored by $t = l = 3$ shadows can be recognized, and the secret image1 restored by $t = k = n = 4$ shadows is lossless. Figure 2(k–p) demonstrate the restored secret image with any less than $l$ shadows, from which no information can be recognized.

In addition, we analysis the security of the developed $PSS\ (3, 4, 4)$ shown in Fig. 2 in terms of contrast, histogram and information entropy.

Contrast $\alpha$ is defined in Definition 2. Based on Definition 3, when $t < l\alpha = 0$ which means no information of $S$ could be recognized through $S'$. Entropy is a statistical measure of randomness in information theory. The entropy $H(m)$ is computed as in Eq. (6) where $P(m_i)$ represents the probability of symbol $m_i$ and the entropy is expressed in bits. An image histogram illustrates how pixels in an image are distributed by graphing the number of pixels at each level. A good image encryption scheme should always generate a cipher image having uniform histogram for any plain image.

$$H(m) = -\sum_{i=0}^{2^N-1} p(m_i) * \log_2 p(m_i) \quad bits \tag{6}$$

The corresponding results for the shares and restored secret by 2 shadow images of Fig. 2 are shown in Fig. 3. Contrast is close to 0 which shows the satisfaction of Definition 3. Entropy of the shares agrees with the theory, while the histogram of shares doesn't which could be explained by Lemma 3. From Lemma 3, the black proportion will be greater than white one, which will not affect the security since the fixed pixel value has no relation with the secret bit. Neither entropy nor histogram of inadequate shadow images satisfies the theory, which are caused by Lemma 3 and the stacking restoration since stacking operation leads to more black ones. From the above results, we know that.

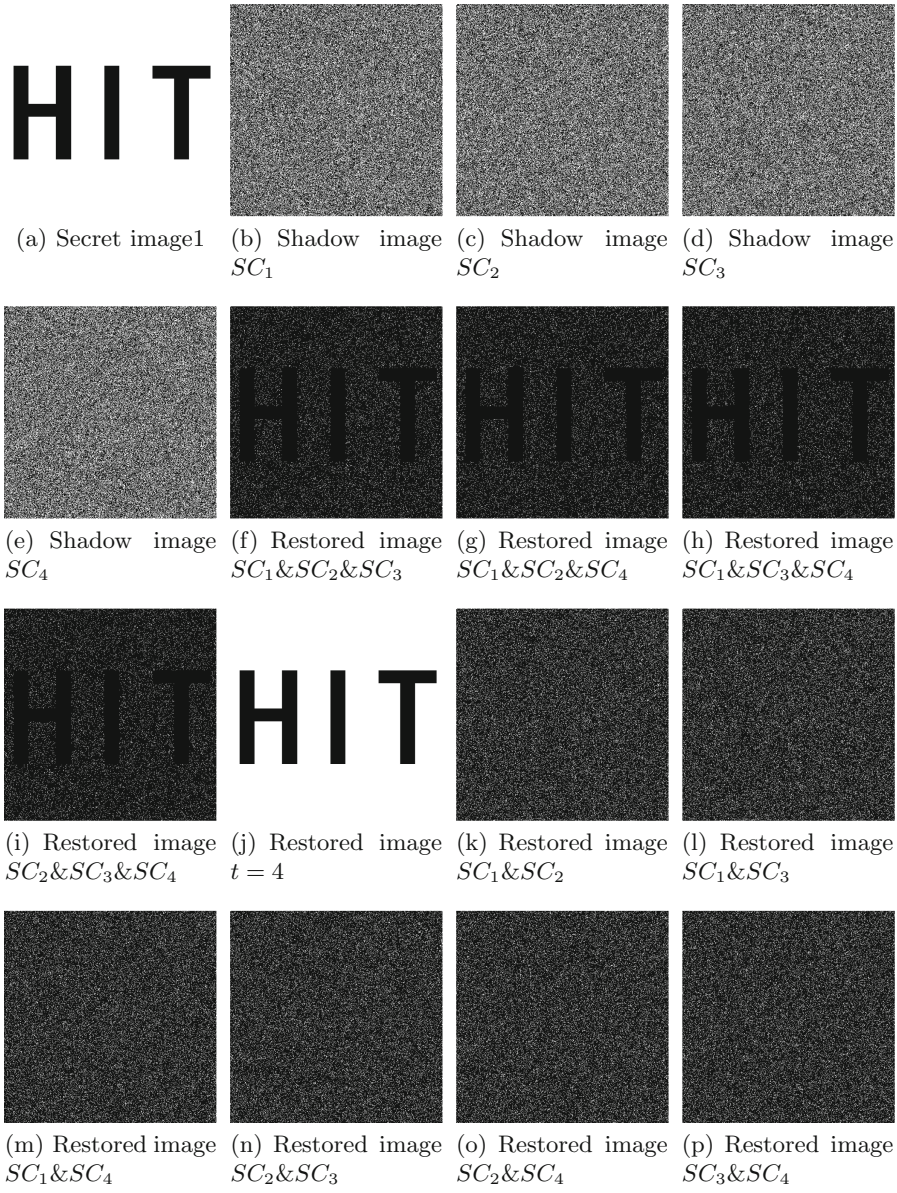

(a) Secret image1 (b) Shadow image $SC_1$ (c) Shadow image $SC_2$ (d) Shadow image $SC_3$

(e) Shadow image $SC_4$ (f) Restored image $SC_1\&SC_2\&SC_3$ (g) Restored image $SC_1\&SC_2\&SC_4$ (h) Restored image $SC_1\&SC_3\&SC_4$

(i) Restored image $SC_2\&SC_3\&SC_4$ (j) Restored image $t = 4$ (k) Restored image $SC_1\&SC_2$ (l) Restored image $SC_1\&SC_3$

(m) Restored image $SC_1\&SC_4$ (n) Restored image $SC_2\&SC_3$ (o) Restored image $SC_2\&SC_4$ (p) Restored image $SC_3\&SC_4$

**Fig. 2.** Experiments of our developed PSS(3, 4, 4) scheme for binary secret image1

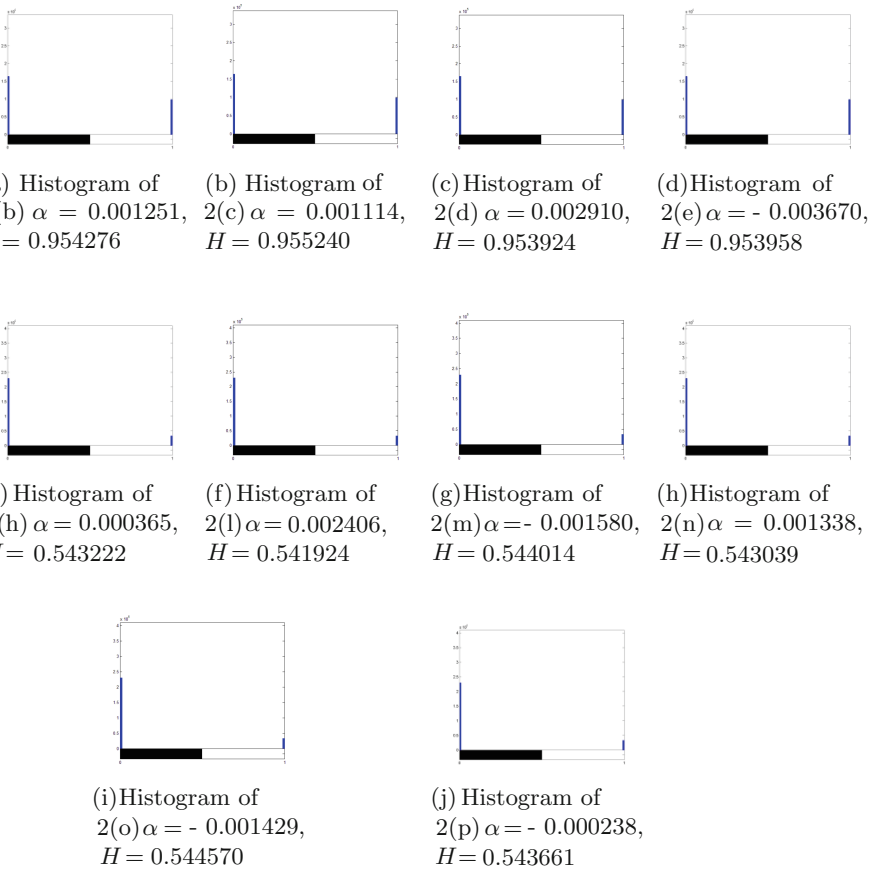

(a) Histogram of 2(b) $\alpha = 0.001251$, $H = 0.954276$

(b) Histogram of 2(c) $\alpha = 0.001114$, $H = 0.955240$

(c) Histogram of 2(d) $\alpha = 0.002910$, $H = 0.953924$

(d) Histogram of 2(e) $\alpha = -0.003670$, $H = 0.953958$

(e) Histogram of 2(h) $\alpha = 0.000365$, $H = 0.543222$

(f) Histogram of 2(l) $\alpha = 0.002406$, $H = 0.541924$

(g) Histogram of 2(m) $\alpha = -0.001580$, $H = 0.544014$

(h) Histogram of 2(n) $\alpha = 0.001338$, $H = 0.543039$

(i) Histogram of 2(o) $\alpha = -0.001429$, $H = 0.544570$

(j) Histogram of 2(p) $\alpha = -0.000238$, $H = 0.543661$

**Fig. 3.** Histogram analysis of developed *PSS* (3, 4, 4) scheme example shown in Fig. 2

- The shadows are noisy so that our developed scheme has no cross interference of the secret on shadows.
- When $t(l \leq t \leq k = n)$ shadows are obtained, the secret image will be recognized, and the image quality of restored secret image increases as $t$ increases.
- When $t < l$ shadows are inspected, no information of the secret can be recognized, which demonstrates the security of our developed scheme.

## 5 Concluding Remarks

A simple and efficient perceptual secret sharing (PSS) scheme based on Boolean operations and RG is developed in this article. The developed scheme can satisfy valuable features in secret sharing. It satisfies $P(l, n, n)$ threshold sharing, which can achieve different perceptual quality as well as preserves the same color representation method as digital images. It also inherits conventional VSS

benefits, such as no pixel expansion or codebook. Furthermore, it has lower computational complexity as well as avoids the cross interference of secret on the shadows. Simulations results and analyses demonstrate the effectiveness of our developed scheme.

**Acknowledgement.** The authors would like to thank the anonymous reviewers for their valuable discussions and comments. This work is supported by the National Natural Science Foundation of China (Grant Number: 61602491).

## References

1. Yan, X., Wang, S., El-Latif, A.A.A., Sang, J., Niu, X.: A novel perceptual secret sharing scheme. In: Shi, Y.Q., Liu, F., Yan, W. (eds.) Transactions on Data Hiding and Multimedia Security IX. LNCS, vol. 8363, pp. 68–90. Springer, Heidelberg (2014). https://doi.org/10.1007/978-3-642-55046-1_5
2. Liu, F., Chuankun, W.: Embedded extended visual cryptography schemes. IEEE Trans. Inf. Foren. Secur. **6**(2), 307–322 (2011)
3. Wang, D.-S., Zhang, L., Ma, N., et al.: Two secret sharing schemes based on boolean operations. Pattern Recogn. **40**(10), 2776–2785 (2007)
4. Wang, Z., Arce, G.R.: Halftone visual cryptography through error diffusion. In: ICIP, pp. 109–112 (2006)
5. Naor, M., Shamir, A.: Visual cryptography. In: De Santis, A. (ed.) EUROCRYPT 1994. LNCS, vol. 950, pp. 1–12. Springer, Heidelberg (1995). https://doi.org/10.1007/BFb0053419
6. Weir, J., Yan, W.Q.: A comprehensive study of visual cryptography. In: Shi, Y.Q. (ed.) Transactions on Data Hiding and Multimedia Security V. LNCS, vol. 6010, pp. 70–105. Springer, Heidelberg (2010). https://doi.org/10.1007/978-3-642-14298-7_5
7. Ateniese, G., Blundo, C., De Santis, A., Stinson, D.R.: Extended capabilities for visual cryptography. Theoret. Comput. Sci. **250**(1/2), 143–161 (2001)
8. Kafri, O., Keren, E.: Encryption of pictures and shapes by random grids. Optics Lett. **12**(6), 377–379 (1987)
9. Shyu, S.J.: Image encryption by random grids. Pattern Recogn. **40**(3), 1014–1031 (2007)
10. Chen, T., Tsao, K.: Threshold visual secret sharing by random grids. J. Syst. Softw. **84**, 1197–1208 (2011)
11. Shyu, S.J.: Image encryption by multiple random grids. Pattern Recogn. **42**, 1582–1596 (2009)
12. Wu, X., Sun, W.: Improving the visual quality of random grid-based visual secret sharing. Signal Process. **93**(5), 977–995 (2013)
13. Jin, D., Yan, W.-Q., Kankanhalli, M.S.: Progressive color visual cryptography. J. Electron. Imaging **14**(3) (2005)
14. Hou, Y.-C., Quan, Z.-Y., Tsai, C.-F.: Block-based progressive visual secret sharing. Inf. Sci. **233**, 290–304 (2013)
15. Fang, W.-P., Lin, J.-C.: Progressive viewing and sharing of sensitive images. Pattern Recogn. Image Anal. **16**(4), 632–636 (2006)
16. Hou, Y.-C., Quan, Z.-Y.: Progressive visual cryptography with unexpanded shares. IEEE Trans. Circ. Syst. Video Technol. **21**(11), 1760–1764 (2011)

17. Chen, S.-K.: Friendly progressive visual secret sharing using generalized random grids. Optical Eng. **48**(11), 117001-1–117001-7 (2009)
18. Chen, S.-K., Lin, J.-C.: Fault-tolerant and progressive transmission of images. Pattern Recogn. **38**(12), 2466–2471 (2005)
19. Huang, C.-P., Hsieh, C.-H., Huang, P.S.: Progressive sharing for a secret image. J. Syst. Softw. **83**, 517–527 (2010)

# Security-Aware Distributed Service Composition for Wireless Sensor Networks Based Smart Metering in Smart Grid Using Software Defined Networks

Gaolei Li[1], Yang Wu[2], Jun Wu[1(✉)], Jianhua Li[1], and Chengcheng Zhao[1]

[1] School of Electronic Information and Electrical Engineering, Shanghai Jiao Tong University, Shanghai 200240, China
{gaolei_li, junwuhn, lijh888, zcc_2633}@sjtu.edu.cn
[2] Electronic Technology Information Research Institute (ETIRI), Ministry of Industry and Information Technology (MIIT), Beijing 100040, China
wuyang02@163.com

**Abstract.** To monitor and control the states of surrounding infrastructures in smart grid, wireless sensor networks (WSNs) have been perceived to play an important role in connecting diverse smart meters. However, it also incurs many challenges on network security. Firstly, for WSNs, as data are stored and maintained by a large number of sensors deployed in a distributed way, it is significantly hard to ensure distributed data security by using traditional security protection technologies that only can provides guarantees for small scale centralized local networks. Secondly, more fine-grained access control should be provided for smart meters to adapt to the requirements of the multiparty communications between smart grid stakeholders. In this paper, we propose a security-aware distributed service composition scheme for WSNs based smart metering in smart grid based on software defined networks (SDN). Case studies demonstrate the feasibility of proposed scheme. To our best knowledge, this paper is the first to realize software defined security architecture for WSNs based smart metering in smart grid.

**Keywords:** Smart grid · Wireless sensor networks (WSNs) · Security-aware Service composition · Software defined networks (SDN)

## 1 Introduction

Nowadays, since smart grid is evolving towards a user-centered and time-critical application, both data security and networking security have gained increasing popularity to support for various smart grid applications. Security protection usually requires to monitor and control the states of underlying infrastructures. As a critical tool to monitor and control the underlying infrastructures, wireless sensor networks (WSNs) is supposed to have tremendous potentials for smart metering in smart grid [1].


M. Huang et al. (Eds.): WICON 2016, LNICST 214, pp. 91–97, 2018.
https://doi.org/10.1007/978-3-319-72998-5_10

The existing security issues in smart grid can be divided into two main branches roughly including cyberspace security and physical infrastructure safety [2]. In cyberspace security aspect, as a large number of smart devices are deployed in smart grid, more and more data are stored and maintained in a distributed way that enables it significantly harder to ensure distributed data security. In physical infrastructure safety aspect, security threats incurred by hardware aging and misoperations have been minimized significantly with advancement of various novel technologies [3]. Unfortunately, communication latency and network congestion limit the direct usage of existing security policies with high complexity and high time consuming [4], and high packet loss rate may lead to service interruption, even cause a chain of accidents in field-level networks of smart metering in smart grid [5].

Recently, researchers presented WSNs to monitor and control smart grid infrastructures. However, different from traditional centralized security architecture, in which firewall, traffic control software and other complex products are usually deployed at the export of an internal network. WSNs based smart metering achieves security threats by deploying distributed sensors and aggregates data from the surrounding sensors. In this paper, we propose a security-aware distributed service composition (SDSC) scheme. It exploits software defined networks (SDN) to improve WSNs based smart metering in smart grid.

## 2 Related Work

The existing security prevention approaches can be divided into two branches roughly: (1) centralized model, and (2) distributed model. While cloud based smart grid have better resilience, cloud itself faces many challenges on remote communication efficiency. Distributed model consumes less bandwidth and energy. Therefore, distributed model has gained increasing attention in recent years. For example, literature [6] proposed a fine-grained distributed data access control to ensure sensed data security in WSNs. However, different from traditional WSNs, it is infeasible for smart grid monitoring to deploy diverse complex security applications due to high time-consuming. Therefore, there are many challenges on WSNs based smart grid monitoring [7].

SDN is a novel paradigm that decouples logic functions from data plane, and implements them in a centralized controller. It has been perceived to have specific capability for utilization by various wireless scenes. In [8], a stateful SDN solution proposed for WSNs can reduce the amount of information exchanged between sensor nodes and make sensor nodes programmable.

The Service Composition (SC) is a popular approach to implement value-added services by combining other basic services in many application scenes (such as smart building, QoS provisioning and next-generation service overlay network [9]). And also, the prospects of SC for intelligent transportation and smart grid have traditionally been addressed separately in literature [10]. With the SC, interoperability, flexibility and reusability of a system can be improved significantly. However, due to the dynamicity and heterogeneity of the target smart meters, the security services offered by advanced metering infrastructure (AMI) cannot be composed by extending existing Service

Oriented Architecture (SOA) approaches simply. For SC in AMI, it may need the integration of a number of real-world services, which must be an security-aware process.

## 3 Modeling of SDSC Scheme

In this section, we describe the proposed SDSC scheme that allows networking security functions to be deployed at sides of infrastructures in a distributed way adaptively and dynamically.

### 3.1 Networking Model

The basic architecture is shown as illustrated in Fig. 1. With this architecture, the visibility, flexibility and scalability of the whole network for WSNs based smart grid metering can be improved significantly.

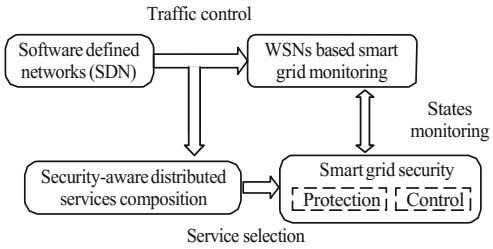


**Fig. 1.** Basic logic architecture of the proposed SDSC scheme.

In smart grid, there are three constraints limiting the application of security policy for dispersive infrastructures: (1) energy; (2) and network capability. In the following, we set up a fined-grained optimization model to present proposed SDSC scheme. The basic network model $L$ is modeled as a non-reflexive logic graph $H^L = (V^L, E^L)$, where $V^L = \{n_1, n_2, \ldots, n_N\}$ is a set $N$ logic nodes and $E^L = \{e_{ij}\}$, with $i$ and $j = 1, 2, \ldots, N$, is a set of logic nodes, with $\{e_{ij}\}$ connecting $n_i$ to $n_j$. The security optimization model is described by a *Security Configuration Matrix*. The *Security Configuration Matrix* is defined by $AB = [AB_{ij}]$, where $AB_{ij}$ defines the security states after security policy configured. For logic nodes $V^L$, it is noted as $AB_{ij}^V$; for links $\{e_{ij}\}$, it is noted as $AB_{ij}^E$. The *Used Logic Nodes Security Configuration Matrix* is defined by $ABu^V = \left[ABu_{ij}^V\right]$, where $ABu_{ij}^V$ defines the security states of $V^L$ already configured to logic nodes. $ABu_{ij}^V = \infty$, when $j \geq 2$. The *Used Link Security Configuration Matrix* is defined by $ABu^E = \left[ABu_{ij}^E\right]$, where $ABu_{ij}^E$ defines the security states of $\{e_{ij}\}$ already configured to links.

### 3.2 The Resource-Constrained Model

The resource-constrained model is formulated by a *Energy Matrix*, a *Network Capability Matrix*. The *Energy Matrix* for logic nodes is defined by $E^V = \left[E_{ij}^V\right]$. The *Used Logic Nodes Energy Matrix* is defined by $Eu^V = \left[Eu_{ij}^V\right]$, where $Eu_{ij}^V$ defines the energy of $V^L$ has been occupied. $Eu_{ij}^V = 0$. The *Network Capability Matrix* is defined by $AD^E = \left[AD_{ij}^E\right]$. The *Used Network Capability Matrix* is defined by $ADu^E = \left[ADu_{ij}^E\right]$, where $ADu_{ij}^E$ defines the total network capability of $\left\{e_{ij}\right\}$ already allocated to links.

### 3.3 Security Optimization

Both link security and node security are supported in our proposed scheme. The Security Request Model are shown by divisions into the link security request model and the node security request model as follows.

**The Link Security Model**

Let $G$ be the number of requests that are processed simultaneously. The *g-th* request, with $g = 1, 2, \ldots, G$, is defined by a set of $K_g$ 2-node directed virtual graph $H^{V_{kg}} = (V^{V_{kg}}, E^{V_{kg}})$, with $k = 1, 2, \ldots, K_g \cdot K_g > 1$ represents for a complex data delivery process, in which multiple source nodes and multiple destination nodes should be connected. For each $k$, $V^{V_{kg}} = \left\{n_s^{kg}, n_d^{kg}\right\}$ is a set of 2-nodes that consist of the source node $n_s^{kg}$ and the destination node $n_d^{kg} \cdot E^{V_{kg}} = \left\{e_{sd}^{kg}\right\}$ denotes the virtual link connecting $n_s^{kg}$ and $n_d^{kg}$ with bandwidth which is equal to $ad_{kg}$. We define boolean $X^{kg} = \left[x_{ij}^{kg}\right]$, where:

$$x_{ij}^{kg} = \begin{cases} 1 & \text{if } \left\{e_{ij}^{kg}\right\} \text{uses} \left\{e_{ij}\right\} \\ 0 & \text{otherwise} \end{cases} \tag{1}$$

and by definition $x_{ii}^{kg} = 0, \forall i$.

The virtual-to-logic link mapping is formulated as $x_{ij}^{kg} \leq A_{ij}, \forall (i,j)$, which guarantees only existing links are assigned for link requests. The network capability of each link is usually limited, bandwidth allocated for each link should satisfy this constraint:

$$\sum_{g=1}^{G} \sum_{k=1}^{K_g} x_{ij}^{kg} \cdot \mathrm{ad}_{kg}^E \leq AD_{ij}^E - ADu_{ij}^E, \forall (i,j) \tag{2}$$

This constraint guarantees that link bandwidth will not exceed the total network capability. The link security request mapping is formulated as the following equation:

$$\sum_{g=1}^{G}\sum_{k=1}^{K_g} x_{ij}^{kg} \cdot Z_{ij}^{kg} \leq AB_{ij}^{E} - ABu_{ij}^{E}, \forall(i,j) \tag{3}$$

**The Node Security Model**

In this paper, the energy consumption of security service on a logic node is defined by $E = [E_x]$, with $x = \{c, e, r, a\}$. For logic nodes $V^L$, it is noted as $E_x^V$. Considering the *Energy Matrix* $E^V = \left[E_{ij}^V\right]$ defined in advance, the g-th request of logic node require $E_x^g$ energy. They should satisfy the following constraints:

$$\sum_{g=1}^{G} sum\left\{E_x^g\right\} \leq E_{ij}^V \tag{4}$$

Where $sum\{\cdot\}$ is an addition operator. For example, $sum\left\{E_x^g\right\} = E_c^g + E_e^g + E_r^g + E_a^g$.

The design of the *Objective Function* is affected by multidimensional considerations. Firstly, data are usually delivered by using publisher/subscriber mode or broadcast/multicast mode. Therefore, data flows in the network often suffer from traffic fluctuation. To reduce packet loss and latency time, and guarantee the end-to-end communication efficiency, traffic control involved network applications such as multi-path transmission, rate control and congestion must try to gain the highest revenues.

## 4 Analysis

In this section, we will discuss how our proposed scheme applies to the WSNs based smart grid metering. We use $T_x$, $U_x, A_x$, $E_x$ to represent traffic control, user authentication, access control and exception auditing separately. The value of each element may not be quantified. For non-quantified attributes in Table 1, classical binary-classifier can be used to build a machine learning system. Each node has to compute a a series of energy consumption $E_c$ and computation complexity $C_c$. The computation equation is listed as deduced in Sect. 3.

**Table 1.** Security services and protection level.

| Protection level | QoS services | Traffic control | User authentication | Access control | Exception auditing |
|---|---|---|---|---|---|
| 1 | $\leq Q_1$ | $\leq T_1$ | $\leq U_1$ | $\leq A_1$ | $\leq E_1$ |
| 2 | $\leq Q_2$ | $\leq T_2$ | $\leq U_2$ | $\leq A_2$ | $\leq E_2$ |
| 3 | $\leq Q_3$ | $\leq T_3$ | $\leq U_3$ | $\leq A_3$ | $\leq E_3$ |
| … | … | … | … | … | … |
| $W$ | $\leq Q_w$ | $\leq T_w$ | $\leq U_w$ | $\leq A_w$ | $\leq E_w$ |

Compared with other works, our work provides a multidimensional security-aware functions including priority, configuration, access control and authentication, while others work usually focusing on data aggregation. The security of WSNs based smart grid metering is enhanced at the cost of additional overhead. The SDSC scheme designed for WSNs based smart grid using SDN simplifies the logic management complexity at a price of extra implementation computation. The more sensors deployed in the network, the less average extra overhead the scheme will cost (Table 2).

**Table 2.** Objective value.

| | Confidentiality | Encryption | Redundancy | Authorization |
|---|---|---|---|---|
| Energy consumption | $\leq E_c$ | $\leq E_e$ | $\leq E_r$ | $\leq E_a$ |
| Computation complexity | $\leq C_c$ | $\leq C_e$ | $\leq C_r$ | $\leq C_a$ |

## 5 Conclusion

In this paper, we propose a security-aware distributed service composition (SDSC) scheme for WSNs based smart grid metering based on software defined networks (SDN). The feasibility of the proposed scheme is demonstrated by analysis. For distributed data security, SDSC scheme supports LN-aware fine-grained protection by using dynamic security policy configuration. For time-critical applications, communication latency and network congestion can be reduced significantly.

**Acknowledgement.** This work is supported by National Natural Science Foundation of China (Grant No. 61431008, 61571300, 61401273).

## References

1. Al-Anbagi, I., Erol-Kantarci, M., Mouftah, H.T.: An adaptive QoS scheme for WSN-based smart grid monitoring. In: IEEE International Conference on Communications Workshops (ICC), pp. 1046–1051 (2013)
2. Yan, Y., Qian, Y., Shariff, H., Tipper, D.: A survey on cyber security for smart grid communications. IEEE Commun. Surv. Tutorials **14**(4), 998–1010 (2012)
3. Rashid, M.T.A., Yussof, S., Yusoff, Y., Ismail, R.: A review of security attacks on IEC61850 substation automation system network. In: Information Technology and Multimedia (ICIMU), pp. 5–10 (2014)
4. Premaratne, U., Samarabandu, J., Sidhu, T., Beresh, R., Tan, J.-C.: Security analysis and auditing of IEC61850 based automated substations. IEEE Trans. Power Deliv. **25**(4), 2346–2355 (2010)
5. Kong, P.Y.: Wireless neighborhood area networks with QoS support for demand response in smart grid. IEEE Trans. Smart Grid **7**(4), 1913–1923 (2016)
6. Yu, S., Ren, K., Lou, W.: FDAC: Toward fine-grained distributed data access control in wireless sensor networks. IEEE Trans. Parallel Distrib. Syst. **22**(4), 673–686 (2011)
7. Yassine, A., Rahimi, H., Shirmohammadi, S.: Software defined network traffic measurement: current trends and challenges. IEEE Instrum. Meas. Mag. **18**(2), 42–50 (2015)

8. Galluccioa, L., et al.: SDN-WISE: design, prototyping and experimentation of a stateful SDN solution for WIreless SEnsor networks. In: IEEE Conference on Computer Communications (INFOCOM), pp. 513–521 (2015)
9. Paganelli, F., Ulema, M., Martini, B.: Context-aware service composition and delivery in NGSONs over SDN. IEEE Commun. Mag. **52**(8), 97–105 (2014)
10. Dán, G., Bobba, R.B., Gross, G., Campbell, R.H.: Cloud computing for the power grid: from service composition to assured clouds. In: 5th USENIX Workshop on HotCloud (2013)

# Wireless Networks

# A Simplified Interference Model for Outdoor Millimeter Wave Networks

Xiaolin Jiang[1(✉)], Hossein Shokri-Ghadikolaei[1], Carlo Fischione[1], and Zhibo Pang[2]

[1] KTH Royal Institute of Technology, Stockholm, Sweden
{xiaolinj,hshokri,carlofi}@kth.se
[2] ABB Corporate Research, Västerås, Sweden
pang.zhibo@se.abb.com

**Abstract.** Industry 4.0 is the emerging trend of the industrial automation. Millimeter-wave (mmWave) communication is a prominent technology for wireless networks to support the Industry 4.0 implementation. The availability of tractable accurate interference models would greatly facilitate the design of these networks. In this paper, we investigate the accuracy of an interference model that assumes impenetrable obstacles and neglects the sidelobes. We quantify the error of such a model in terms of statistical distribution of the signal to noise plus interference ratio for outdoor mmWave networks under different antenna array settings. The results show that assuming impenetrable obstacle comes at almost no accuracy penalty, and the accuracy of neglecting antenna sidelobes can be guaranteed with sufficiently large number of antenna elements.

**Keywords:** Millimeter-wave network · Interference model
Simplicity-accuracy tradeoff · Interference model accuracy index

## 1 Introduction

Industry 4.0, or the fourth industrial revolution is the current trend of the industrial automation [1]. It is based on the base of Internet of Things, which enables the industrial modules to communicate and cooperate with each other in real time. The industrial manufacturing requires high reliability and stringent delay guarantee, and is usually realized by the wired communication. However, to support mobility, flexibility, and to get rid of the heavy and expensive cables, wireless communication is the promising solution for the future deployment [2].

Millimeter wave (mmWave) is a potential technology for wireless communication network of Industry 4.0, as it has abundant bandwidth to support high data rate, which is essential for the applications to transmit the real-time video [3]. Moreover, as the delay spread of mmWave is lower than the microwave band, which is helpful to reduce the guard interval for the inter symbol interference mitigation. This can efficiently improve the transmission efficiency, especially for the machine to machine type communication transmitting short packets [4].


M. Huang et al. (Eds.): WICON 2016, LNICST 214, pp. 101–108, 2018.
https://doi.org/10.1007/978-3-319-72998-5_11

The availability of accurate interference models is essential to evaluate the performance of mmWave networks. However, exact or very accurate interference models are generally quite complex and sometimes mathematically intractable. Interference models with different accuracy and complexity have been used in the literature. A simple interference model considering infinite penetration loss and no sidelobe transmission/reception is used to develop multihop medium access control layer in mmWave wireless networks [5]. This simple interference model enables deriving tractable closed-form expressions for the main performance metrics and delivering useful design insights. However, the accuracy of the underlying interference model is not therein quantified. In [6], the blockage is modeled by a line-of-sight (LOS) ball, i.e., all the transmitters within a certain distance of the receiver are always in the LOS condition, and all the other transmitters have a non-LOS condition. This approximation greatly simplifies mathematical analysis. This blockage model is extended to a more complex two-ball model with better accuracy in [7]. The accuracy of such interference model comes at the price of complexity and less tractability. In [8], an index is proposed that allows quantifying the accuracy of any interference model.

In this paper, we assess the accuracy of the simple interference model of [5], namely assuming impenetrable obstacles and no antenna sidelobes. We investigate the accuracy index defined in [8] and the relative difference in 50th percentile rate under a uniform planar array (UPA) of antennas at 28 GHz. The results show that the assumption of impenetrable obstacles introduces negligible loss in the accuracy of the interference model, thanks to the special characteristics of the mmWave communications. Moreover, considering no sidelobes may cause non-negligible accuracy loss with small antenna size, which can be compensated by increasing the number of antenna elements.

## 2 System Model

We consider a downlink scenario for an outdoor network operating at the mmWave frequencies. The number of BSs and obstacles are random variables with densities $\lambda_b$ and $\lambda_o$ per square kilometer respectively, and they are randomly uniformly distributed in the plane, as shown in Fig. 1. We assume that

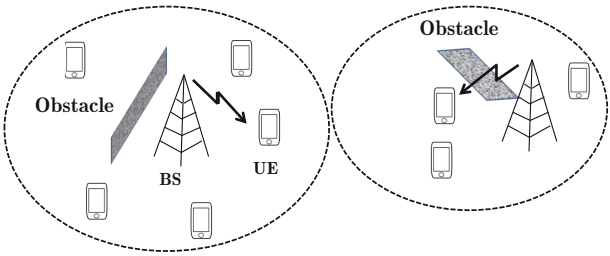


**Fig. 1.** Outdoor mmWave network. The dashed lines show the base station coverage boundaries, and may not be that regular in practice.

each obstacle has a rectangular shape with a random width that is independently uniformly taken from [0,5] m, a random length uniformly taken from [0,10] m, and a random orientation that is independently uniformly taken from $[0, 2\pi]$. We study the performance of a reference user UE 0 located at the origin of the Cartesian coordinate, which will be associated to the BS with the smallest pathloss. We consider a single path narrowband geometrical channel model between every BS to its serving UE [4]. Then, the downlink channel response between BS $i$ and UE $j$ is given by

$$\mathbf{H}_{ij} = \sqrt{N_t N_r} g_{ij} \mathbf{a}_{\mathrm{UE}} \left(\phi_{ij}^{\mathrm{UE}}, \theta_{ij}^{\mathrm{UE}}\right) \left(\mathbf{a}_{\mathrm{BS}} \left(\phi_{ij}^{\mathrm{BS}}, \theta_{ij}^{\mathrm{BS}}\right)\right)^{*}, \tag{1}$$

where $N_t$ and $N_r$ are the number of antenna elements at the transmitter side and at the receiver side, $\phi_{ij}^{\mathrm{UE}}$ and $\theta_{ij}^{\mathrm{UE}}$ are the horizontal and vertical angles of arrival (AoA) at the UE $j$ from BS $i$, $\phi_{ij}^{\mathrm{BS}}$ and $\theta_{ij}^{\mathrm{BS}}$ are the horizontal and vertical angles of departure (AoD) from the BS $i$ to UE $j$, $\mathbf{a}_{\mathrm{BS}} \left(\phi_{ij}^{\mathrm{BS}}, \theta_{ij}^{\mathrm{BS}}\right)$ and $\mathbf{a}_{\mathrm{UE}} \left(\phi_{ij}^{\mathrm{UE}}, \theta_{ij}^{\mathrm{UE}}\right)$ are normalized array responses to the AoD and AoA along this link, and $(\cdot)^*$ is the Hermitian operator. Without loss of generality, we consider half-wavelength UPAs of size $N_b \times N_b$ at the BSs and of size $N_u \times N_u$ at the UEs. For half wavelength UPA of $N \times N$ antennas, we have [9]

$$\mathbf{a}\left(\phi, \theta\right) = \frac{1}{N}[1, \ldots, e^{j\pi(m \sin\phi \, \sin\theta + n \cos\theta)}, \ldots, e^{j\pi((N-1)\sin\phi \, \sin\theta + (N-1)\cos\theta)}]^{*}, \tag{2}$$

where $0 \leq m < N$, and $0 \leq n < N$ are the indices of an antenna element along the two dimensions in the UPA array. The term $g_{ij}$ in (1) is a zero-mean complex Gaussian random variable with variance $10^{-0.1 L_{ij}}$, where $L_{ij}$ is the path loss in dB [4]. Let $d_{ij}$ be the distance between BS $i$ and UE $j$ (path length) in meters, $n_{ij}$ be the number of obstacles in this path, $l_o$ be the penetration loss of each obstacle in dB, $\alpha$ be the attenuation factor due to atmospheric absorption, and $l_\alpha = 10 \log(e^{\alpha d_{ij}})$ be the absorption loss in dB, which is $1.15 \times 10^{-5}$ at 28 GHz. Then, the path loss is

$$L_{ij}\,[\mathrm{dB}] = c + 20 \log(d_{ij}) + l_\alpha + n_{ij} l_o + X\,, \tag{3}$$

where $c$ is a constant attenuation, and equals 61.4 dB at 28 GHz, $X$ is a zero-mean i.i.d. Gaussian random variable with standard deviation $n = 5.8$ dB.

We assume a universal frequency reuse, so all non-serving BSs can cause interference to UE 0. The associated BS is indexed by 0, and the set of all interfering BSs is denoted by $\mathcal{I}$. Then, the SINR at UE 0 is

$$\gamma = \frac{p_0 \left| \left(\mathbf{w}_0^{\mathrm{UE}}\right)^{\mathrm{H}} \mathbf{H}_{00} \, \mathbf{w}_0^{\mathrm{BS}} \right|^2}{\sum\limits_{i \in \mathcal{I}} p_i \left| \left(\mathbf{w}_0^{\mathrm{UE}}\right)^{\mathrm{H}} \mathbf{H}_{i0} \, \mathbf{w}_i^{\mathrm{BS}} \right|^2 + \sigma}\,, \tag{4}$$

where $p_i$ is the transmission power of BS $i$, $\sigma$ is the noise power, $\mathbf{w}_0^{\mathrm{UE}}$ is the combining vector at UE 0, and $\mathbf{w}_i^{\mathrm{BS}}$ denotes the precoding vector at BS $i$.

To reduce the complexity and cost of beamforming, we assume an analog precoder both at the BSs and at the UEs; however, the framework of this paper can be easily extended to other beamforming strategies. At each BS, the transmitting beam is matched to the AoD direction to its associated UE. Similarly, the combining vector at each UE $i$ is matched to the AOA from its serving BS. That is given BS $i$ will serve UE $j$, $\mathbf{w}_i^{\mathrm{BS}} = \mathbf{a}_{\mathrm{BS}}\left(\phi_{ij}^{\mathrm{BS}}, \theta_{ij}^{\mathrm{BS}}\right)$ and $\mathbf{w}_j^{\mathrm{UE}} = \mathbf{a}_{\mathrm{UE}}\left(\phi_{ij}^{\mathrm{UE}}, \theta_{ij}^{\mathrm{UE}}\right)$. This precoding and combining vectors can maximize the link SNR, namely $|(\mathbf{w}_j^{\mathrm{UE}})^* \mathbf{H}_{ij} \mathbf{w}_i^{\mathrm{BS}}|^2$, see [10].

An interference model attempts at modeling different components of (3). For mathematical tractability, usually, antenna pattern or channel models are simplified. These approximations make it possible to evaluate the SINR distribution and thereby performance metrics such as the data rate. However, the derived SINR distribution may not necessarily be close to the actual SINR distribution before all those approximations. In the next section, we introduce two metrics that allow quantifying the closeness of two statistical distributions.

## 3 Measuring Accuracy of SINR and Rate Analysis

Consider a reference interference model y, which results in SINR $\gamma^{\mathrm{y}}$ with distribution $f_{\gamma^{\mathrm{y}}}(t)$, and any test interference model x, which results in SINR $\gamma^{\mathrm{x}}$ with distribution $f_{\gamma^{\mathrm{x}}}(t)$. In the following, we consider the interference model accuracy index [8] and the relative difference in the 50th percentile rate.

### 3.1 Interference Model Accuracy Index

The interference model accuracy (IMA) index describes how close the PDF of $\gamma^{\mathrm{x}}$ is compared to PDF of $\gamma^{\mathrm{y}}$. To formally define IMA index, let $\beta > 0$ denote the SINR threshold corresponding to a certain target bit error rate, then an outage on the receiver occurs when $\gamma < \beta$. Suppose that the interference model y can perfectly capture outage events. Let hypotheses $H_0$ and $H_1$ denote the absence (i.e., $\gamma^{\mathrm{y}} \geq \beta$) and the presence (i.e., $\gamma^{\mathrm{y}} < \beta$) of outage under reference model y. For any constant $0 \leq \xi \leq 1$, the interference model accuracy index is defined as

$$\mathrm{IMA}\left(\mathrm{x}, \mathrm{y}, \xi, \beta\right) = \xi\left(1 - p_{\mathrm{fa}}^{\mathrm{x|y}}(\beta)\right) + (1-\xi)\left(1 - p_{\mathrm{md}}^{\mathrm{x|y}}(\beta)\right), \tag{5}$$

where $p_{\mathrm{fa}}^{\mathrm{x|y}}(\beta) = \Pr\left[\gamma^{\mathrm{x}} < \beta \mid \gamma^{\mathrm{y}} \geq \beta\right]$ is the false alarm probability, and $p_{\mathrm{md}}^{\mathrm{x|y}}(\beta) = \Pr\left[\gamma^{\mathrm{x}} \geq \beta \mid \gamma^{\mathrm{y}} < \beta\right]$ is the miss-detection probability. $\mathrm{IMA}\left(\mathrm{x}, \mathrm{y}, \xi, \beta\right)$ is a unitless real-valued quantity ranging within $[0, 1]$, where higher values represent higher similarity between x and y. By setting $\xi = \Pr\left[\gamma^{\mathrm{y}} \geq \beta\right]$, parameter $\mathrm{IMA}\left(\mathrm{x}, \mathrm{y}, \Pr\left[\gamma^{\mathrm{y}} \geq \beta\right], \beta\right)$ is equal to the average probability that interference model x gives the same decision as the reference model y.

We define the minimum IMA index as,

$$\min \mathrm{IMA}\left(\mathrm{x}, \mathrm{y}\right) = \min_{\beta}\ \mathrm{IMA}\left(\mathrm{x}, \mathrm{y}, \Pr\left[\gamma^{\mathrm{y}} \geq \beta\right], \beta\right)\ . \tag{6}$$

The term $\min \mathrm{IMA}\left(\mathrm{x}, \mathrm{y}\right)$ shows the minimum value (worst case) of the accuracy of interference model x compared to the reference model y.

### 3.2 The Relative Difference in the 50th Percentile Rate

The transmit data rate is an important index to assess the network performance. We consider maximum achievable rate as

$$\text{Rate} = \text{B}\log_2(1+\gamma), \tag{7}$$

where B is the bandwidth and $\gamma$ is the SINR. The rate coverage as the complementary cumulative distribution function of rate is

$$P(\rho) = \Pr(\text{Rate} > \rho), \tag{8}$$

where $\rho$ is the rate threshold that determines different rate coverage values. Denote the 50th percentile rate calculated by interference model x and y by $\rho^{\text{x}}_{50\text{th}}$ and $\rho^{\text{y}}_{50\text{th}}$, respectively. Besides rate coverage, we calculate the relative difference in the 50th percentile rates calculated by two interference models x and y as a metric of accuracy of rate analysis:

$$\text{Rate}_{\text{diff}-50\%} = \frac{|\rho^{\text{x}}_{50\text{th}} - \rho^{\text{y}}_{50\text{th}}|}{\rho^{\text{y}}_{50\text{th}}}. \tag{9}$$

The parameter min IMA ranges within $[0, 1]$ with higher value representing better similarity, while $\text{Rate}_{\text{diff}-50\%}$ ranges within $[0, \infty]$ with smaller value representing better similarity.

## 4 Simplified Interference Model for Outdoor MmWave Networks

Interference models in mmWave networks are generally very complicated due to both blockage and directionality. Simplifying the blockage model and antenna patterns, as done in [5], will significantly increase tractability of mathematical performance evaluation and optimization of mmWave networks, and can lead to better design insights. These insights are valid as long as the underlying simple interference model is of sufficient accuracy. In the following, we investigate the accuracy of such interference model.

We consider a "realistic" reference physical model y with a finite penetration loss and actual antenna pattern, created by the analog precoding and combining vectors. We then approximate such simplified interference model by x wherein we consider infinite penetration loss and no antenna sidelobes.

To evaluate the effect of infinite penetration loss assumption, we consider a test model $\text{x}_a$ with $l_o = \infty$ in (3). Other parameters of $\text{x}_a$ are similar to those of y. To evaluate the effect of the no-sidelobe approximation, we take a test model $\text{x}_b$ similar to y except that the sidelobe gain is ignored in $\text{x}_b$. The 28 GHz band is 27.5–29.5 GHz, and in the following and without loss of generality, we consider 30 dBm transmission power, 500 MHz bandwidth (so −87 dBm noise power).

### 4.1 Impact of Assuming Infinite Penetration Loss

In this subsection, we evaluate the impact of assuming impenetrable obstacles on the SINR distribution. Figure 2 shows min IMA against the penetration loss in y (it is always $\infty$ in $x_a$). To calculate min IMA, we sweep $\beta$ from 0 to 30 dB to capture the smallest accuracy value in this SINR threshold region. From this figure, assuming impenetrable obstacles is more accurate for higher penetration loss values. Moreover, the accuracy index increases with the density of BSs, as more BSs is equivalent to shorter distances between the interfering BSs and UE 0, and higher likelihood of having interferes with LOS condition to the UE 0. For penetration loss less than 15 dB, the assumption of impenetrable obstacle reduces min IMA by less than 1% when the obstacle density is $20/\text{km}^2$. On the other hand, the accuracy index expectedly decreases with the density of obstacles. The accuracy loss, however, is very limited, e.g., only 1% additional loss when increasing the obstacle density from $20/\text{km}^2$ to $50/\text{km}^2$ for the penetration loss of 5 dB. Even this such small loss vanishes when the penetration loss is larger than 35 dB.

Figure 3 shows $\text{Rate}_{\text{diff}-50\%}$ between y and $x_a$. Similarly as Fig. 2, $\text{Rate}_{\text{diff}-50\%}$ decreases with the density of BSs, and minimal difference exists when $\lambda_b = 50/\text{km}^2$ and penetration loss larger than 15 dB. Overall, the assumption of impenetrable obstacles introduces negligible loss in calculating SINR and

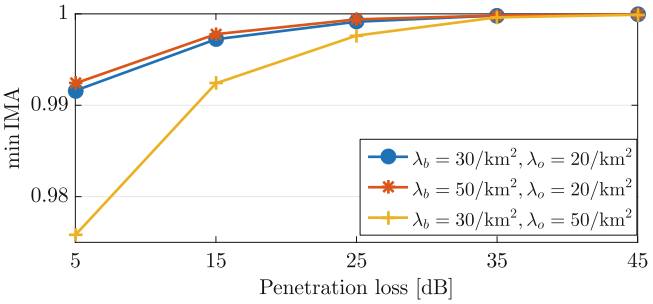


**Fig. 2.** Impact of infinite penetration loss on min IMA.

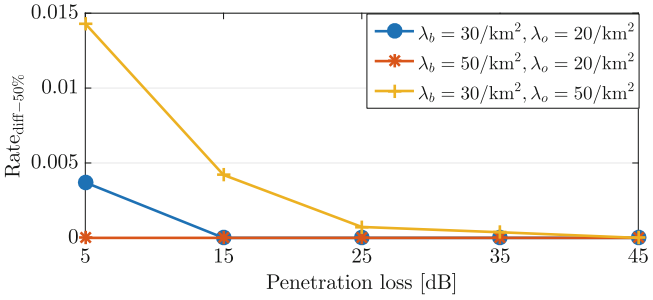


**Fig. 3.** Impact of infinite penetration loss on $\text{Rate}_{\text{diff}-50\%}$.

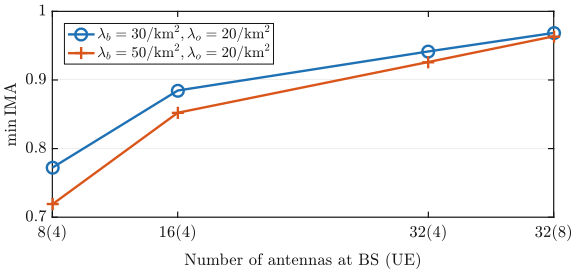


**Fig. 4.** Impact of ignoring antenna sidelobes on min IMA. Antenna elements are in the form of UPA of N×N antennas.

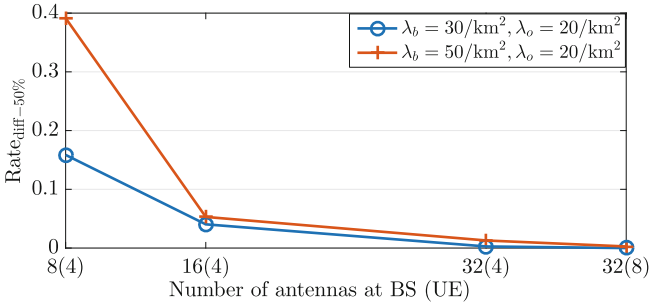


**Fig. 5.** Impact of ignoring antenna sidelobes on $\text{Rate}_{\text{diff}-50\%}$. Antenna elements are in the form of UPA of N×N antennas.

rate distributions, but improves the mathematical tractability. This assumption works very well in mmWave networks with denser BS deployments.

### 4.2 Impact of Neglecting Antenna Sidelobes

Figure 4 presents the effect of neglecting the sidelobes. The antenna patterns at BSs and UEs are set as the parameters at the x label. Neglecting the sidelobes can lead to clear difference between $x_b$ and y. The accuracy index increases with the number of antennas at each side, as more antennas enable narrower beamwidth and less sidelobe gain, e.g., the min IMA indexes increase from 0.73 to 0.96, and from 0.86 to 0.97 respectively with the antenna number increase from $8 \times 8$ UPA to $32 \times 32$ UPA at BSs, and $4 \times 4$ UPA to $8 \times 8$ UPA at UEs in the two scenarios. It is also observed that the min IMA index decreases with more interfering BSs, as the increased aggregated interferes lead to less similarity between the two models.

Ignoring antenna sidelobes can also introduce a noticeable difference to the rate distribution, as shown in Fig. 5. With dense BS deployment and moderate number of antennas at both BS and UE, $\text{Rate}_{\text{diff}-50\%}$ is as large as 39%. With the increase of the number of the antenna elements, $\text{Rate}_{\text{diff}-50\%}$ of the two scenarios decrease to around 5% when using $16 \times 16$ UPA at the BS side.

## 5 Conclusions

We proposed a simplified interference model in outdoor mmWave networks that considers infinite penetration loss and no sidelobe. Then we investigated the similarity of SINR and rate distributions between this simplified model with realistic model using an interference model accuracy index and the relative difference in the 50th percentile rate. The impact of the first assumption on the accuracy of the simplified interference model can be neglected, while the impact of considering no sidelobe can not be neglected in denser BS settings. However, by increasing the number of antennas can increase the accuracy. The accuracy index can be further improved by effective frequency reuse and proper scheduling to limit the number of interfering BSs transmitting simultaneously. The simplified interference model can be a good base for the research of other techniques in mmWave networks such as beamforming and association between BSs and UEs.

## References

1. Schwab, K.: The fourth industrial revolution. World Economic Forum, Geneva (2016)
2. Willig, A., Matheus, K., Wolisz, A.: Wireless technology in industrial networks. Proc. IEEE **93**(6), 1130–1151 (2005)
3. Rangan, S., Rappaport, T.S., Erkip, E.: Millimeter-wave cellular wireless networks: potentials and challenges. J. Proc. IEEE **102**(3), 366–385 (2014)
4. Akdeniz, M.R., Liu, Y., Samimi, M.K., Sun, S., Rangan, S., Rappaport, T.S., Erkip, E.: Millimeter wave channel modeling and cellular capacity evaluation. J. IEEE J. Sel. Areas Commun. **32**(6), 1164–1179 (2014)
5. Singh, S., Ziliotto, F., Madhow, U., Belding, E., Rodwell, M.: Blockage and directivity in 60 GHz wireless personal area networks: from cross-layer model to multihop MAC design. J. IEEE J. Sel. Areas Commun. **27**(8), 1400–1413 (2009)
6. Singh, S., Kulkarni, M.N., Ghosh, A., Andrews, J.G.: Tractable model for rate in self-backhauled millimeter wave cellular networks. J. IEEE J. Sel. Areas Commun. **33**(10), 2196–2211 (2015)
7. Di Renzo, M.: Stochastic geometry modeling and analysis of multi-tier millimeter wave cellular networks. J. IEEE Trans. Wireless Commun. **14**(9), 5038–5057 (2015)
8. Shokri-Ghadikolaei, H., Fischione, C., Modiano, E.: On the accuracy of interference models in wireless communications. In: IEEE International Conference on Communications, Kuala Lumpur, pp. 1–6 (2016)
9. El Ayach, O., Rajagopal, S., Abu-Surra, S., Pi, Z., Heath, R.W.: Spatially sparse precoding in millimeter wave MIMO systems. J. IEEE Trans. Wireless Commun. **13**(3), 1499–1513 (2014)
10. El Ayach, O., Heath, R.W., Abu-Surra, S., Rajagopal, S., Pi, Z.: The capacity optimality of beam steering in large millimeter wave MIMO systems. In: 13th IEEE International Workshop on Signal Processing Advances in Wireless Communications, Cesme, pp. 100–104 (2012)

# A CWMN Spectrum Allocation Based on Multi-strategy Fusion Glowworm Swarm Optimization Algorithm

Zhuhua Hu[1,2], Yugui Han[2], Lu Cao[2], Yong Bai[1,2(✉)], and Yaochi Zhao[2]

[1] State Key Laboratory of Marine Resource Utilization in the South China Sea, Hainan University, No. 58, Renmin Avenue, Haikou 570228, Hainan, People's Republic of China
{eagler_hu,bai}@hainu.edu.cn
[2] College of Information Science and Technology, Hainan University, No. 58, Renmin Avenue, Haikou 570228, Hainan, People's Republic of China

**Abstract.** In cognitive wireless mesh networks, genetic algorithm based spectrum allocation has the problems of easily falling into local optimum, low accuracy and slow convergence. Aiming at the problems, glowworm swarm optimization is applied into spectrum allocation, and a multi-strategy fusion glowworm swarm optimization algorithm is proposed in this paper, in which step size and fluorescein volatilization factor are dynamically optimized and positions of the glowworms that has fallen into local optimum can be disturbed by Gauss mutation operator. Compared with genetic algorithm and basic glowworm swarm algorithm, the theoretical analysis and simulation results show that the proposed algorithm can avoid falling into local optimum, converge more quickly to the global optimal solution, and obtain higher system bandwidth reward.

**Keywords:** Cognitive wireless mesh network (CWMN) · Spectrum allocation Glowworm swarm optimization (GSO) · Multi-strategy fusion

## 1 Introduction

Cognitive radio (CR) [1] is a new technology implementing dynamic spectrum access of wireless network, while cognitive wireless mesh network (CWMN) [2, 3] is a wireless mesh network integrating the technology of cognitive radio. The significant feature of CWMN is the absence of infrastructure, where each mesh node is the cognitive node. Based on the mechanism of spectrum allocation and sharing, mesh node has the ability of perceiving the surrounding wireless environment and intelligently get access to the bands that not used by the primary user (PU), for the purpose of solving the increasingly serious problem of lacking of spectrum resource.

In CWMN, when cognitive nodes dynamically using licensed bands must guarantee that it has no effect on the communication quality of the primary user. So the current main research problem is how to properly allocate unused authorized spectrum holes to cognitive mesh nodes. In recent years, the commonly used wireless spectrum


M. Huang et al. (Eds.): WICON 2016, LNICST 214, pp. 109–120, 2018.
https://doi.org/10.1007/978-3-319-72998-5_12

dynamic allocation methods mainly include game theory [4], auction theory [5], evolutionary theory [6–9] and the graph coloring [10], where graph theory method has become the key point method of spectrum allocation for its flexibility and efficiency. But there unavoidably exists unfair allocation and high time cost in graph theory method. Later, some classical evolutionary algorithms combined with graph theory coloring method are proposed applying to the research of spectrum allocation.

In evolutionary theory, glowworm swarm optimization algorithm (GSO) is a new kind of bionic swarm intelligent stochastic optimization algorithm proposed in recent years, which has been successfully applied to different fields with strong ability of problem solving [11–14]. Literature [15] aims at the problem of precocity and stagnation of multi peak function when using basic GSO, an adaptive step size algorithm was put forward that enable avoiding glowworms falling into the local optima to a certain extent. But there were no in-depth studies on the parameter optimization and other applications of algorithm. To overcome the shortcoming, this paper proposed a CWMN network spectrum allocation algorithm based on multi-strategy fusion glowworm swarm optimization combined with the graph coloring model of spectrum allocation. The step size and volatile factor are optimized for adaptive adjustment in the algorithm. Besides, the updating formula of glowworm dynamic decision domain radius is adjusted for avoiding the existence of isolated glowworms, and Gauss mutation is applied to glowworms falling into the local optimum in the process of evolutionary. What's more, when necessary, the algorithm would retrospect after the disturbance. Through the improvement of the above aspects, the simulation results show that the multi-strategy fusion glowworm swarm optimization algorithm improves the optimization ability and convergence rate in spectrum allocation.

## 2 Network Model and Problem Description

Similar to the traditional wireless mesh network, cognitive wireless mesh network has the ability of cognition, reconfiguration and self-organizing, and could automatically establish nodes and maintain network connectivity. Cognitive Mesh nodes (Mesh router, client nodes and other network devices) in CWMN improve network performance through the search and sharing of the available authorized spectrum. Target for channel allocation in cognitive wireless mesh networks is assigning the available channels to SU (secondary user) in order to improve the spectrum utilization rate and maximizing reduces the interference to the PU (primary user) user. Figure 1 illustrates the structure of cognitive wireless mesh networks.

Correspondingly, CWMN network spectrum allocation model based on graph theory shown in Fig. 2 can be described as channel availability matrix, channel reward matrix, interference constraint matrix and valid channel allocation matrix. Supposing that there are $N$ cognitive users waiting to communicate at a certain time, while there are $M$ idle frequency bands can be used at the same time. The definition of the matrix is as follows:

(1) Channel availability matrix $L_0L = \left\{l_{n,m} \middle| l_{n,m} \in \{0,1\}\right\}_{N\times M}$ represents the channel availability. If $l_{n,m} = 1$, then channel $m$ is available for cognitive user $n$.

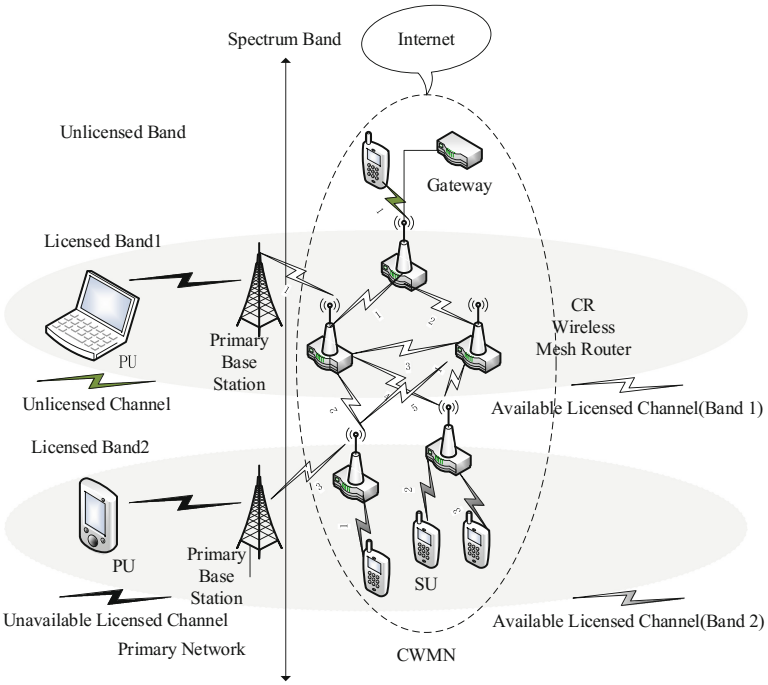


**Fig. 1.** Structure of cognitive wireless mesh network

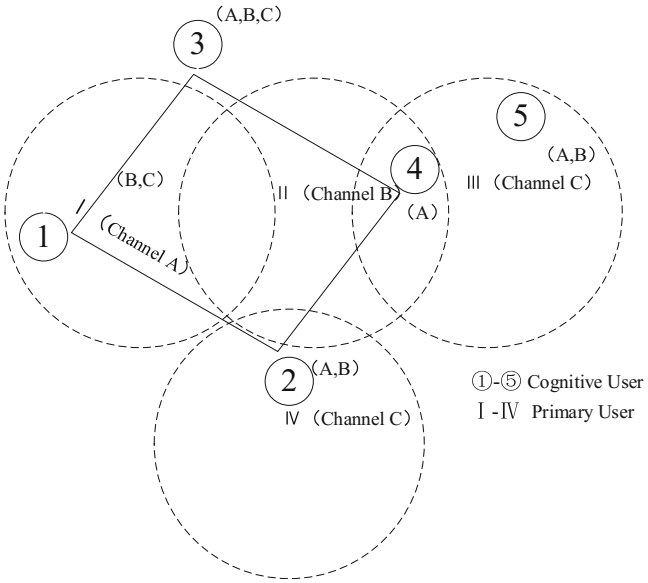


**Fig. 2.** Graph theoretic model for cognitive radio systems

(2) Channel reward matrix $B_0B = \{b_{n,m}\}_{N\times M}$, $b_{n,m}$ represents the channel reward of cognitive user $n$ using channel $m$.
(3) Interference constraint matrix $C_0C = \{c_{n,k,m} | c_{n,k,m} \in \{0,1\}\}_{N\times N\times M}$, if $c_{n,k,m} = 1$, then it means that cognitive user $n$ and $k$ using the frequency band $m$ simultaneously will cause conflict.
(4) Valid channel allocation matrix $A_0A = \{a_{n,m} | a_{n,m} \in \{0,1\}\}_{N\times M}$, if $a_{n,m}$=1, then it means that channel $m$ is assigned to cognitive user $n$.

$$\begin{cases} a_{n,m} \cdot a_{k,m} = 0 \\ c_{n,k,m} = 1 \end{cases}; 0 \le n,k < N, 0 \le m < M \tag{1}$$

(5) Under the premise of valid channel allocation matrix, the total system bandwidth reward can be described as follows:

$$U = \sum_{n=1}^{N} \sum_{m=1}^{M} a_{n,m} \cdot b_{n,m} \tag{2}$$

## 3 Multi-strategy Fusion Glowworm Swarm Optimization Algorithm

Aiming at the shortness of the basic glowworm swarm optimization algorithm, a multi-strategy fusion glowworm swarm optimization algorithm (MSF-GSO) was proposed in this paper, which mainly realizes the following improvements:

(1) To avoid glowworms falling into the local optimum, the Gauss mutation is used to help glowworms jump out of the local optimum, and to search for the global optimum.
(2) Step size $s$ was adjusted to make adaptive adjustment to coordinate the relationship between global search and local search.
(3) Volatile factor $\rho$ was adjusted to make adaptive adjustment to improve the convergence speed and accuracy of the algorithm.
(4) In formula of updating neighborhood radius, the first parameter in adjusted to a parameter changing max from 0 to 0.1 to avoid the presence of isolated glowworms.

### 3.1 Gauss Mutation Operator

Aiming at the problems that glowworm swarm optimization algorithm easily falls into the local optima and has rather slow convergence speed. Gauss mutation was introduced, which adds random vectors obeying the Gauss distribution to the state of the original individual. The definition of Gauss mutation is as follows:

$$X_i = X_i \times [1 + k \times N(0,1)] \tag{3}$$

Where $X_i$ represents the state of the first $i$ glowworm individual, $k$ is the decreasing variable varying from 1 to 0, $N(0,1)$ is the random vector of the Gauss distribution with the mean of 0 and the variance of 1. Formula (3) adds decreasing stochastic disturbance term of Gauss distribution $X_i \times k \times N(0,1)$ to original $X_i$, which makes full use of the interference of the current population information, increases the diversity of the population, and helps glowworm jump out of the local optima to search the global optima, improves the search speed, also. In the iterative process of algorithm, once glowworms fall into local optima, the convergence rate of the algorithm would be affected greatly. So, it's urgent that the worst states of glowworm need to be eliminated, which are replaced by historical best glowworm. Then the intermediate populations of glowworm are obtained, which would need to carry out Gauss mutation. To check whether the results are improved with the increase of the number of iterations, the algorithm sets up a bulletin board to record the state of the best glowworm in history and the value of the objective function. When the bulletin board has not be changed or changed a little (e.g. the amplitude of change is less than $\mu$) in the three successive iterations. At the time, we can see the glowworm as fallen into local optima, then the mutation operation need to be carried out, where $\mu$ is the parameter to control Gauss mutation, the greater the parameter $\mu$, the greater the probability of Gauss mutation, the faster the convergence speed will be, but it will increase the amount of computation. Therefore, the value of $\mu$ should not be too large, generally take the number between $10^{-4} - 10^{-5}$.

In addition, the process of retrospect is increased in the iterative process. If the value of the step size is still larger, the algorithm then shifts to the location updating after the disturbance and start a new round of optimization.

### 3.2 Variable Step Size Strategy

In the glowworm swarm optimization algorithm, the experimental results can be limited by two aspects for step size is constant. If step size is smaller, the convergence of the algorithm would be affected; if step size is larger, it's very easy to skip the global optimum in the search process. In the later period of algorithm, the glowworm individuals would face oscillation phenomenon in the vicinity of the peak, which would lead to the decrease in the accuracy of search. Therefore, the constant step size can't be well used to solve the problem of different need of step size in the period of early stage and later stage. To solve the problem, an improved variable step size optimization algorithm was proposed, formula (4) and (5) are used to adjust the step size. It can be seen that $c$ is negative value, $s(t)$ is in the slow decline with the number of iterations increasing. It means that allocating larger step values for the glowworm individuals in early iterations to improve the search speed, and allocating smaller step values for the glowworm individuals in later iterations to avoid skipping optimal to achieve the purpose of optimization.

$$c = \frac{1}{t_{\max}} \ln\left(\frac{S_{\min}}{S_{\max}}\right) \tag{4}$$

$$s(t) = S_{\max} e^{c \cdot g_t} \tag{5}$$

In the formula (4) and (5), current iteration number and the maximum number of iterations are respectively expressed as $g_t$ and $t_{\max}$, the minimum value and maximum value of $s$ are respectively expressed as $S_{min}$, $S_{\max}$. All those are given values in the simulation.

### 3.3 Parameter Adaptive Strategy

In addition, there are also some important factors affecting the convergence speed and the accuracy of algorithm, such as volatile factor. In the glowworm swarm optimization algorithm, the value of volatile factor is a constant value. The limitation of constant $\rho$ is very obvious. If $\rho$ is relatively small, the updating of fluorescein would be greatly affected by previous accumulated fluorescein, which seriously weakens the search randomness and easily falling into local optimum, therefore it is not conducive to the expansion of space of algorithm. If $\rho$ is relatively larger, the updating of fluorescein would reduce effects from previous accumulated fluorescein, which then strength $\rho$ hens the search randomness, but it results in lower convergence speed. Therefore, this paper improves the performance of the algorithm by means of adaptive variation of the fluorescein volatile factor $\rho$, and the adaptive adjustment is based on the formula (6). Besides, with the increase of the number of iterations, it becomes a trend that glowworm individuals would gather together gradually. Then there would be a large number of glowworms in a small neighborhood. Therefore, the dynamic decision domain radius of glowworm easily reduces to 0, which leads to the formation of isolated glowworms and is not conducive to share group information and conduct cooperative search. Therefore, to avoid the existence of isolated glowworm, the dynamic decision domain radius needs to be adjusted as shown in the formula (7).

$$\rho = \begin{cases} 1 - \rho_{\max} \exp\left(-ct^{\frac{1}{N}}\right) & \rho < \rho_{\max} \\ \rho_{\max} & \rho \geq \rho_{\max} \end{cases} \tag{6}$$

In the formula (6), $t$ means the number of iterations, $c$ means regulator, $N$ means the number of cognitive radio users, $\rho_{\max}$ means the maximum value of $\rho$, which is set to the prevent convergence speed reducing for $\rho$ is too larger.

$$r_d^i(t+1) = \min\left\{ r_s, \max\left\{ 0.1 \times \frac{i}{T-1}, r_d^i(t) + \beta(n_l - |N_i(t)|) \right\} \right\} \tag{7}$$

In the formula (7), the value of $i$ is $0, 1, 2, 3, \ldots, T-1$, which is to make the first parameter value between $0 - 0.1$.

### 3.4 Multi-strategy Fusion Glowworm Swarm Optimization Algorithm

The glowworm swarm optimization algorithm is as follows:

**Algorithm 1.** Glowworm swarmoptimization algorithm

Set number of dimensions and glowworms
Let $s$ be the step size
Initialize all other parameters
For $i=1$ to $n$ do $l_i(0)=l_0$
Set maximum iteration number $=T_{max}$
Set $t=1$;
**while** $t \le T_{max}$ **do**
  **for** each glowworm $i$ **do**
    **for** each glowworm $i$ $j \in N_i(\mathrm{t})$ **do**

$$l_i(t)=(1-\rho)l_i(t-1)+\gamma J\left(\chi_i(t)\right) \tag{8}$$

$$p_{ij}(\mathrm{t})=(l_j(\mathrm{t})-l_i(\mathrm{t}))/\sum_{k\in N_i(\mathrm{t})}(l_k(\mathrm{t})-l_i(\mathrm{t})) \tag{9}$$

$$j=select\_glowworm(\vec{\mathrm{p}})$$

$$x_i(\mathrm{t}+1)=x_i(\mathrm{t})+\mathrm{s}((x_j(\mathrm{t})-x_i(\mathrm{t}))/(\|(x_i(\mathrm{t})-x_i(\mathrm{t})\|)) \tag{10}$$

$$r_d^{\,i}(\mathrm{t}+1)=\min\{r_s,\max\{0,r_d^{\,i}(\mathrm{t})+\beta(\mathrm{n_t}-|N_i(\mathrm{t})|)\}\} \tag{11}$$

    **end for**
    $index=\max(l)$
    $x_{index}=brighest$
    $t=t+1$;
  **end for**
**end while**

Where $t$ means the number of iteration, $\rho$ means the fluorescein volatile factor, $\gamma$ means the fluorescein update rate, $l_i(0)$ means the fluorescein initial value, $n$ means the total number of glowworms, $T_{max}$ means maximum number of iterations, $r_s$ means the sensing radius of glowworm individual, $\beta$ means the renewal rate of dynamic decision domain, $n_t$ means the threshold of the number of glowworm within neighborhood.

The multi-strategy fusion glowworm swarm optimization algorithm is as follows:

**Algorithm 2.** Multi-strategy fusion glowworm swarm optimization algorithm

1: *Step 1:* Initialize population
Generate glowworms in the solution space randomly and initialize a series of parameters.
2: *Step 2:* Initialize the bulletin board
Make the location of the glowworm to meet the constraints and calculate the initial value of the target function of the glowworm and initialize the bulletin board.
3: *Step 3:* Bulletin board update
Calculate the current target function value of the glowworm, if it's better than the bulletin board information, then update the bulletin board.
4: *Step 4:* Gauss mutation
Current worst glowworm population is replaced by the best glowworm in history to obtain the intermediate glowworm population.
5: *Step 5:* Fluorescein value update
All glowworms update the fluorescein value according to formula (8).
6: *Step 6:* Glowworm motion stage
Calculate neighborhood set of each glowworm. Select the moving direction according to the roulette method. Then the position would be updated according to the formula (10) and the radius of the decision domain would be updated according to formula (11).
7: *Step 7:* Retrospect determine
Carry out the glowworm swarm disturbance once again, then check the value of step size. If the step size is still larger, then retrospect again, that's turning to step 2. Otherwise, turning to step 8.
8: *Step 8:* Termination determine
Complete one iteration and check whether reaching the maximum number of iterations $T$, if not satisfied, then turn to Step 2 to start the optimization process of next generation of glowworm, otherwise end the iteration.

The flow chart of the MSF-GSO algorithm is as follows (Fig. 3):

## 4 Experimental Result and Analysis

To verify the performance of the multi-strategy fusion glowworm swarm optimization algorithm, the original glowworm swarm optimization algorithm and genetic algorithm in spectrum allocation, system reward obtained by different algorithms are compared. In the simulation, the number of cognitive users is 20; the number of available channel is 12. We use MATLAB to simulate. In order to simplify the problem, we assume that available channel and interference relations of each cognitive user remain the same, and all cognitive users have the same interference radius in the complete process of spectrum allocation.

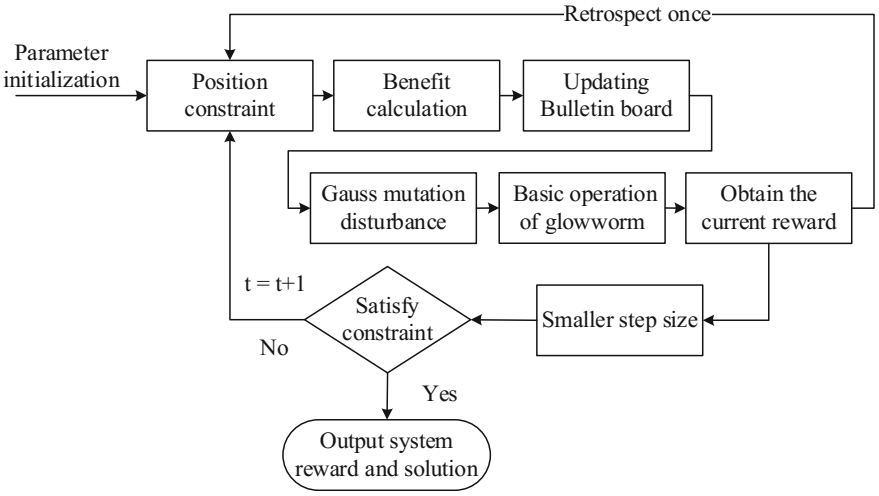


**Fig. 3.** Flow chart of MSF-GSO

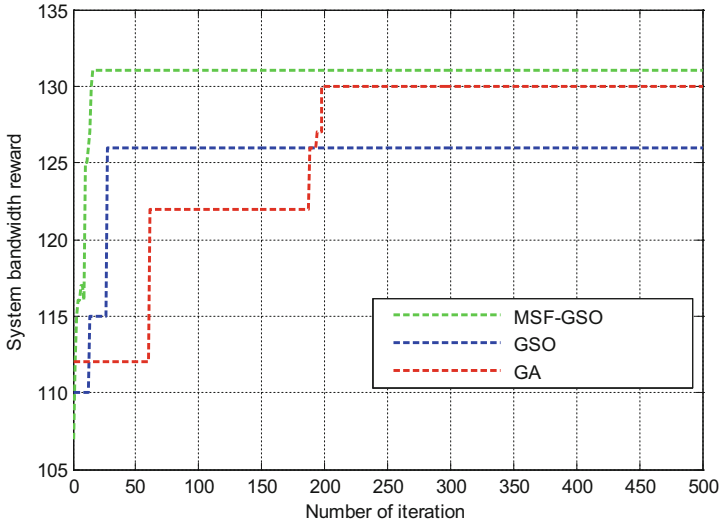


**Fig. 4.** The changes of system bandwidth reward with the number of iterations

Figure 4 shows the curve of system bandwidth reward changing with the number of iterations by using genetic algorithm, glowworm swarm optimization algorithm and multi-strategy fusion glowworm swarm optimization algorithm respectively. As can be seen from the above figure, the convergence speed of glowworm swarm optimization algorithm is faster than the genetic algorithm, but the system reward is a bit worse. The convergence speed of multi-strategy fusion glowworm swarm optimization algorithm is

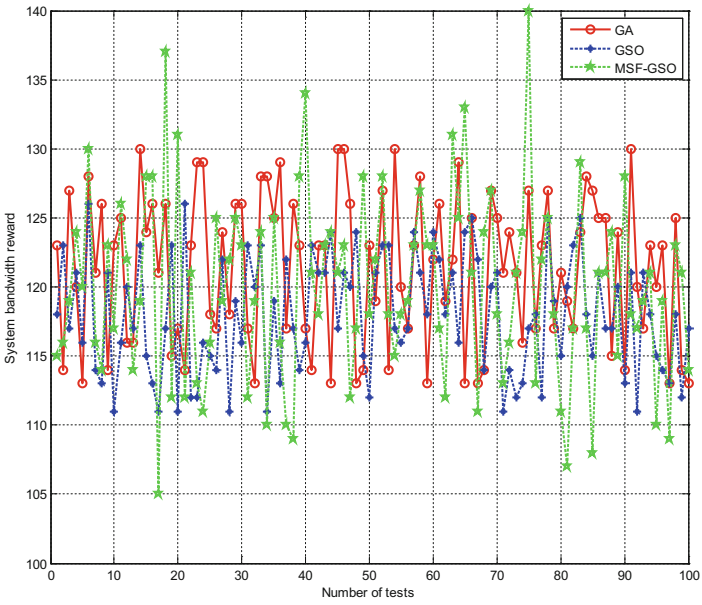


**Fig. 5.** The changes of system bandwidth reward with the number of tests

faster, and the maximum system reward reaches to 132, which are obtained at the 15 times of the iteration, and the system reward is better than that of the genetic algorithm.

Figure 5 shows the system bandwidth reward changes with the number of tests. It can be seen from the figure that the system reward obtained by multi-strategy fusion glowworm swarm optimization algorithm is obviously superior to the other two algorithms. Although every result is not the optimal result, but the average value is optimal. This is due to the MSF-GSO algorithm is a randomized algorithm. The performance of algorithm is easily affected by population size, maximum number of iterations and the threshold of neighborhood glowworm. So in practical application, the parameter should be adjusted properly based on the different conditions to obtain optimal results.

## 5 Conclusion

The key-point of spectrum allocation in cognitive wireless mesh network is to search the optimal solution to system maximum reward. A multi-strategy fusion glowworm swarm optimization algorithm is proposed based on the original glowworm swarm optimization algorithm in this paper. Firstly, the algorithm optimize the step size and volatile factor setting, which make both adaptive change with the number of iterations.

And adjust the updating formula of glowworm decision domain radius, which could effectively avoid the presence of isolated glowworm. Secondly, the process of Gauss mutation is added to the process of algorithm to disturb the local optima of the glowworm. After the disturbance, the step size needs to be checked. When necessary,

the algorithm needs to retrospect. The simulation results show that compared with the glowworm swarm optimization algorithm and genetic algorithm, the multi-strategy fusion glowworm swarm optimization algorithm not only converges faster, but also has better system reward.

In future, we are planning to show the comparison with the genetic algorithm and glowworm swarm optimization and the changes of system bandwidth reward with the number of cognitive users. Moreover, we are also developing a model to analyze the transmission power consumption of the system by using different spectrum allocation algorithm.

**Acknowledgments.** This paper was supported by the National Natural Science Foundation of China (Grant No. 61561017, Grant No. 61261024, and Grant No. 61363071), Doctoral Candidate Excellent Dissertation Cultivating Project of Hainan University, Postgraduate Practice and Innovation Project of Hainan University, and Major Science and Technology Project of Hainan Province under Grant No. ZDKJ2016015.

## References

1. Mitola, J., Maguire, G.Q.: Cognitive radio: making software radios more personal. J. IEEE Pers. Commun. **6**(4), 13–18 (1999)
2. Chen, T., Zhang, H., Matinmikko, M., et al: Cogmesh: cognitive wireless mesh networks. In: 2008 IEEE Globecom Workshops, New Orleans, pp. 1–6. IEEE Press (2008)
3. Ahmed, E., Gani, A., Abolfazli, S., et al.: Channel assignment algorithms in cognitive radio networks: taxonomy, open issues, and challenges. IEEE Commun. Surv. Tutor. **18**(1), 795–823 (2014)
4. Yang, T., Yang, C., Sun, Z., Feng, H., Yang, J., Sun, F., Deng, R.: Resource allocation in cooperative cognitive maritime wireless mesh/ad hoc networks: an game theory view. In: Xu, K., Zhu, H. (eds.) WASA 2015. LNCS, vol. 9204, pp. 674–684. Springer, Cham (2015). https://doi.org/10.1007/978-3-319-21837-3_66
5. Huang, J., Berry, R.A., Honig, M.L.: Auction-based spectrum sharing. J. Mob. Netw. Appl. **11**(3), 405–418 (2006)
6. Ahmad, A., Ahmad, S., Rehmani, M.H., et al.: A survey on radio resource allocation in cognitive radio sensor networks. J. IEEE Commun. Surv. Tutor. **17**(2), 888–917 (2015)
7. Zhao, Z., Peng, Z., Zheng, S., et al.: Cognitive radio spectrum allocation using evolutionary algorithms. J. IEEE Trans. Wirel. Commun. **8**(9), 4421–4425 (2009)
8. Zhi, J.Z., Zhen, P., Shi, L.Z., et al.: Cognitive radio spectrum assignment based on quantum genetic algorithm. J. Acta Physica Sin. **58**(2), 1358–1363 (2009). (in Chinese)
9. El, M.Y., Mrabti, F., Abarkan, E.H.: Spectrum allocation using genetic algorithm in cognitive radio networks. In: 3th International Workshop on RFID and Adaptive Wireless Sensor Networks (RAWSN), Agadir, pp. 90–93, IEEE Press (2015)
10. Peng, C., Zheng, H., Zhao, B.Y.: Utilization and fairness in spectrum assignment for opportunistic spectrum access. J. Mob. Netw. Appl. **11**(4), 555–576 (2006)
11. Krishnanand, K.N., Ghose, D.: Detection of multiple source locations using a glowworm metaphor with applications to collective robotics. In: 2005 IEEE Swarm Intelligence Symposium, Pasadena, pp. 84–91. IEEE Press (2005)
12. Krishnanand, K.N.: Glowworm swarm optimization: a new method for optimizing multi-modal functions. J. Comput. Intell. Stud. **1**(1), 93–119 (2009)

13. Senthilnath, J., Omkar, S.N., Mani, V., et al: Multi-spectral satellite image classification using glowworm swarm optimization. In: IEEE International Geoscience and Remote Sensing Symposium (IGARSS), Vancouver, pp. 47–50, IEEE Press (2011)
14. Zeng, Y., Zhang, J.: Glowworm swarm optimization and heuristic algorithm for rectangle packing problem. In: IEEE International Conference on Information Science and Technology, Wuhan, pp. 136–140, IEEE Press (2012)
15. Ouyang, Z., Zhou, Y.Q.: Self-adaptive step glowworm swarm optimization algorithm. J. Comput. Appl. **7**, 021 (2011). (in Chinese)

# Decode-and-Forward Full-Duplex Relay Selection Under Rayleigh Fading Environment

Qinghai Ou[1], Qingsu He[2], Lingkang Zeng[1], Wenjing Li[1], Xiao Liao[1], Shaofeng Fang[3(✉)], Fang Liu[3], Yuanan Liu[3], and Xinjing Hou[3]

[1] State Grid Information & Telecommunication Group Co. Ltd., Beijing 102211, China
{ouqinghai,zenglingkang,liwenjing,liaoxiao}@sgitg.cgss.com.cn
[2] Beijing Huitong Financial Information Technology Co. Ltd., Beijing 100053, China
heqingsu@sgitg.sgcc.com.cn
[3] Beijing University of Posts and Telecommunications, Beijing 100876, China
{fsf,lf,yuliu,hxj_y}@bupt.edu.cn

**Abstract.** In this paper, under Rayleigh fading environment, we focus on the relay selection problem in the multiple full-duplex (FD) relay networks consisting of one source, one destination, and N FD decode-and-forward (DF) relays. The optimal relay selection that requires global channel state information (CSI) and three suboptimal relay selection schemes that utilize partial CSI are discussed over independent- and identically- distributed (I.I.D.) Rayleigh fading channels. Moreover, to facilitate analysis, outage probability expressions of these schemes are derived. Then, Comparing DF protocol with amplify-to-forward protocol (AF), numerical results show that DF-relay can achieve a better performance. Besides, the effects of self-interference-to-noise ratio (INR) and the number of relay on outage probability for different selection schemes are investigated. Correspondingly, the best suboptimal scheme and relay arrangement policy have been obtained. Finally, Monte-Carlo simulations are performed to demonstrate the validity of the analytical results.

**Keywords:** Full-duplex relay selection · Decode-and-forward
Outage probability · Fading channels

## 1 Introduction

In recent years, cooperative communication technology has attracted massive attention of researchers throughout the world. It can expand coverage area, reach larger system capacity and obtain higher spectrum efficiency [1–3]. For traditional half-duplex (HD) mode, relays retransmit the source data in orthogonal and dedicated channels. Hence, the system spectrum efficiency would be reduced by 50% [4,5]. In order to conquer spectrum loss, FD relay is preferred in recent researches. However, FD mode has been considered impractical in the


M. Huang et al. (Eds.): WICON 2016, LNICST 214, pp. 121–130, 2018.
https://doi.org/10.1007/978-3-319-72998-5_13

past due to the self-interference caused by signal leakage between the relay output and input. But recent advanced self-interference elimination techniques make it feasible [6–8].

On account of the unstable channel environment for a single relay system, multiple relay system has been adopted to further improve performance [9]. Thus, how to select an optimal relay from many candidates has become an advanced research hotspot [10]. Accordingly, a research proves that selects an optimal relay for transmission is the ideal solution to balance diversity gain and spectrum efficiency [11].

Nowadays, most of the relay receives and retransmits the signal by two kinds of relaying protocol, namely, amplify-to-forward protocol (AF) and decode-to-forward protocol (DF). The principle of AF relay is that amplifying the received signal in accordance with a specific coefficient, and forwards it to destination node without other processing. Therefore, using AF-relay for communication has the advantage that system design is relatively simple, easy to implement, and the deployment cost is low. Therefore, most of the researcher studies on it. In [12], different relay selection policies are proposed in FD AF relay networks. In addition, exact outage probability expressions and asymptotic approximations of these policies that show a zero diversity order are derived. Moreover, the authors of [13] proposes a joint relay and antenna selection scheme in general full-duplex (FD) relay networks with one source, one destination and N FD AF relays. In addition, relay selection technique in the two-way FD relay system using AF protocol is analyzed, and the exact expressions of bit error rate (BER), ergodic capacity and outage probability are derived [14].

However, the amplified signal at AF relay node contains not only the signal effectively, also contains a certain amount of noise, which will make performance degradation. In order to overcome the aforementioned problem, some researchers try to study the optimal and partial relay selection schemes in FD DF relay networks, which assume the self-interference channel is non-fading for simplified analysis [15,16]. However, there is no previous work on FD relay selection scheme over I.I.D. Rayleigh fading channels. And the comparison between AF protocol and DF protocol is missing. In this paper, an optimal and three suboptimal relay selection schemes are discussed in a multiple FD DF relay networks over I.I.D. Rayleigh fading channels firstly. Then, outage probability of these schemes is derived. Finally, compared to AF protocol, numerical results are presented to show a better performance of DF protocol. Furthermore, effects of INR and the number of relay on outage probability are analyzed. Then, the best suboptimal scheme and relay arrangement policy are given.

This paper is organized as follows: Sect. 2 sets up the system model. Section 3 deals with different relay selection schemes and the outage probability is derived. Simulation and analytical results are presented in Sect. 4, and are followed by conclusions in Sect. 5.

## 2 System Model

### 2.1 System Model

We consider a system with one source (S), one destination (D) and N relay nodes between the source and destination. The direct link between the source and destination is assumed to be unreliable due to a large distance between them. The S and D nodes operate on HD mode and are equipped with a single antenna. However, each relay node is equipped with two antennas, one receiving antenna and one transmitting antenna, enabling an FD operation at the price of self-interference.

The channel coefficients are assumed to be independent and identically distributed (i.i.d) complex Gaussian random variables. Let $h_{AB_k}$, $\{A, B\} \in \{S, R, D\}$, denotes the channel gain from S node to relay k, $S \rightarrow R_k$, and from relay k to D, node, $R_k \rightarrow D$, as well as from relay k output to relay k input, $R_k \rightarrow R_k$, with zero mean and variance $\delta_{AB_k}$. Therefore, the magnitude of channels $h_{AB_k}$ is Rayleigh distributions which follows the probability density function (PDF) of power channel gains, $|h_{AB_k}|^2$, to be an exponential distribution with parameters $\lambda_{AB_k}$. Additionally, we assume all noise terms have additive Gaussian noise (AWGN) with zero mean and equal variance, where power noise is denoted by $N_0$ (Fig. 1).

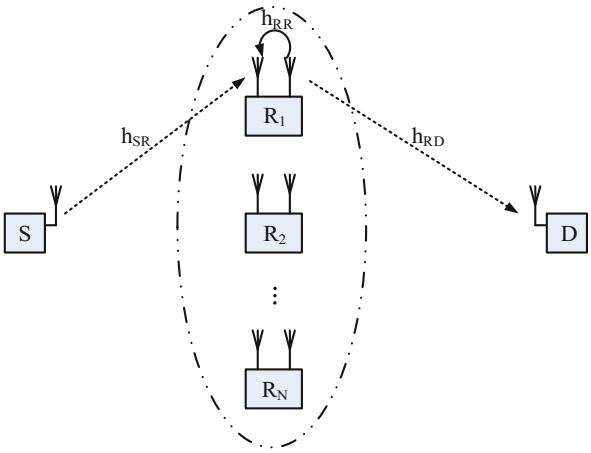


**Fig. 1.** System model of full-duplex DF-relay system

The proposed system model can be regarded as two phases. In phase-1, $S \rightarrow \overleftarrow{R}_k \cdots D$, S continuously transmits its information symbol $x_S$ to N relay nodes. Simultaneously, a relay node forwards the decoded-signal $x_R$ from the previous time slot, which imposes self-interference denoted as $\overleftarrow{R}_k$. Thus, the received signal at relay k can be written as

$$y_{R_k} = \sqrt{P_S} h_{SR_k} x_S + \sqrt{P_R} h_{RR_k} x_R + n_{R_k} \tag{1}$$

where $P_S$ and $P_R$ represent the transmit power at the source and relay respectively. $n_{R_k}$ represents additive Gaussian noise at relay. So, SNR $\gamma_{SR_k} = P_S|h_{SR_k}|^2/N_0$, INR $\gamma_{RR_k} = P_R|h_{RR_k}|^2/N_0$. Accordingly, the instantaneous signal-to-interference plus noise ratio (SINR) for the $S - R_k$ link is given as $\gamma_{R_k} = \gamma_{SR_k}/(\gamma_{RR_k} + 1)$.

In phase-2, $S \cdots \overleftarrow{R_k} \rightarrow D$, a single relay (the best relay) among N relay nodes providing the best end-to-end transmission path is selected to transmit the source signal to the destination. Meanwhile, N relay nodes receive a signal from the next time slot. Thus, the received signal at the destination is expressed as

$$y_D = \sqrt{P_R} h_{R_k D} x_R + n_D \tag{2}$$

$n_D$ represents additive Gaussian noise at destination. And, the SNR $\gamma_{R_k D} = P_R|h_{R_k D}|^2/N_0$.

Correspondingly, the capacity of the system can be written as

$$C = \log_2(1 + \min\{\gamma_{R_k}, \gamma_{R_k D}\}) \tag{3}$$

## 3 FD DF-Relay Selection Scheme over I.I.D. Rayleigh Fading Channels

In this section, the optimal relay selection that requires global CSI and three suboptimal relay selection schemes that utilize partial CSI are discussed in FD DF relay networks over I.I.D. Rayleigh fading channels. Then, exact expressions of outage probability for these schemes are derived. By considering the definition of outage probability, the undefined expressions can be written as:

$$\begin{aligned} P_* &= \Pr\{\log_2(1 + \min\{\gamma_{R_k}, \gamma_{R_k D}\}) < R_0\} \\ &= \Pr\{\min\{\gamma_{R_k}, \gamma_{R_k D}\} < 2^{R_0} - 1 = u\} \\ &= F_{\gamma_{eq}}(u) \end{aligned} \tag{4}$$

The * refers to different relay selection schemes, and Pr denotes the probability. In order to simplify notation, we define $\gamma_{eq} = \min\{\gamma_{R_k}, \gamma_{R_k D}\}$. $F_{\gamma_{eq}}(\cdot)$ is the CDF (Cumulative Distribution Function) of the random variables.

### 3.1 Optimal Relay Selection (OS)

Based on a full duplex channel capacity expression, the optimal relay selection scheme is easily obtained. According to the formula Eq. (3), the best relay $k$ is selected, and it is performed as follow:

$$k_{OS} = \arg\max_k \{\min\{\gamma_{R_k}, \gamma_{R_k D}\}\} \tag{5}$$

For a Rayleigh fading channel, the PDF of $\gamma_{AB}$ is given by

$$f_{\gamma_{AB}}(x) = \lambda_{AB} e^{-\lambda_{AB} x}, x \geq 0 \tag{6}$$

Then, the CDF of $\gamma_R$ can be derived as

$$F_{\gamma_R}(x) = \Pr\{\gamma_R < x\} = \Pr\{\frac{\gamma_{SR}}{\gamma_{RR}+1} < x\} \tag{7}$$

Since $\gamma_{SR}$ and $\gamma_{RR}$ are independent of each other, the joint PDF $\gamma_{SR}$ and $\gamma_{RR}$ can be expressed as:

$$f_{\gamma_{SR},\gamma_{RR}}(x,y) = \lambda_{SR}\lambda_{RR}e^{-\lambda_{SR}x-\lambda_{RR}y}, x \geq \&y \geq 0 \tag{8}$$

According to probability theory, $F_{\gamma_R}(x)$ can be shown as

$$\begin{aligned} F_{\gamma_R}(x) &= \int_0^{+\infty}\int_0^{(1+\gamma_{RR})x} f(\gamma_{SR},\gamma_{RR})d\gamma_{SR}d\gamma_{RR} \\ &= 1 - \frac{1}{1+\frac{\lambda_{SR}}{\lambda_{RR}}x}e^{-\lambda_{SR}x}, x \geq 0 \end{aligned} \tag{9}$$

Furthermore, by denoting $Z = \min\{\gamma_R, \gamma_{RD}\}$, the CDF of Z can be derived as

$$F_Z(x) = 1 - (1 - F_{\gamma_R}(x))(1 - F_{\gamma_{RD}}(x)), x \geq 0 \tag{10}$$

From Eq. (6), $F_{\gamma_{RD}}(x) = 1 - e^{-\lambda_{RD}x}$ can be obtained, and contact with Eq. (9), the CDF of Z can be expressed as

$$F_Z(x) = 1 - \frac{1}{1+\frac{\lambda_{SR}}{\lambda_{RR}}x}e^{-(\lambda_{SR}+\lambda_{RR})x}, x \geq 0 \tag{11}$$

Leading to

$$F_{\gamma_{eq}}(x) = [F_Z(x)]^N, x \geq 0 \tag{12}$$

### 3.2 Partial Relay Selection (PS)

Supposing only can CSI of first jump and relay output to input be got, then the optimal DF-relay is chosen. That is partial relay selection scheme with largest SINR. Hence, the best relay $k$ is performed as follow:

$$k_{PS} = \arg\max_k\{\gamma_{R_k}\} \tag{13}$$

For PS scheme, through Eq. (9) and order statistics theory, the CDF of SINR for the $S - R_k$ link can be given by

$$\begin{aligned} F_{\gamma_R}(x) &= [1 - \frac{1}{1+\frac{\lambda_{SR}}{\lambda_{RR}}x}e^{-\lambda_{SR}x}]^N, x \geq 0 \\ &= \sum_{n=0}^{N}(-1)^n\frac{1}{(1+\frac{\lambda_{SR}}{\lambda_{RR}}x)^n}e^{-\lambda_{SR}nx}, x \geq 0 \end{aligned} \tag{14}$$

The above deducing process applies the fact that $(1-x)^n = \sum_{n=0}^{N} \binom{N}{n} (-1)^n x^n$. Then, the CDF of SNR for the $S - R_k - D$ link can be given by

$$\begin{aligned} F_{\gamma_{eq}}(x) &= 1 - (1 - F_{\gamma_R}(x))(1 - F_{\gamma_{RD}}(x)), x \geq 0 \\ &= \sum_{n=1}^{N} (-1)^{n-1} \frac{1}{(1 + \frac{\lambda_{SR}}{\lambda_{RR}} x)^n} e^{-(\lambda_{SR} n + \lambda_{RD})x}, x \geq 0 \end{aligned} \tag{15}$$

### 3.3 Max-Min Relay Selection (MM)

In a conventional half-duplex relay system, the influence of self-interference is not taken into consideration in the optimal relay selection scheme. Applying to full duplex relay system, the best relay $k$ is performed as follow:

$$k_{MM} = \arg\max_{k} \{\min\{\gamma_{SR_k}, \gamma_{R_k D}\}\} \tag{16}$$

Ignoring the interference, the MM scheme is based on the link of $S - R$ and $R - D$. Then, using basic probability theory and symmetry, $F_{\gamma_{SR_k}}(x)$ can be written as

$$\begin{aligned} F_{\gamma_{SR_k}}(x) &= N \times \Pr\{\gamma_{SR_i} < x \cap k = i\} \\ &= N \int_0^x \Pr\{k = i | \gamma_{SR_i} = y\} f_{\gamma_{SR}}(y) dy \end{aligned} \tag{17}$$

There are two cases should be taken into account, $\gamma_{SR} > \gamma_{RD}$ and $\gamma_{SR} < \gamma_{RD}$. According to [17], $F_{\gamma_{SR_k}}(x)$ can be expressed as

$$\begin{aligned} F_{\gamma_{SR_k}}(x) = N( & \frac{1 - e^{-\lambda_{SR} x}}{\lambda_{SR} + \lambda_{RD}} \sum_{n=0}^{N-1} \frac{(-1)^n \binom{N-1}{n}}{\frac{n}{\lambda_{RD}} + \frac{1}{\lambda_{SR} + \lambda_{RD}}} \\ & - \frac{\lambda_{SR}}{\lambda_{SR} + \lambda_{RD}} \sum_{n=0}^{N-1} (-1)^n \binom{N-1}{n} \\ & \times \frac{(1 - e^{-(n+1)(\lambda_{SR} + \lambda_{RD})x})}{(\frac{n}{\lambda_{RD}} + \frac{1}{\lambda_{SR} + \lambda_{RD}})(n+1)(\lambda_{SR} + \lambda_{RD})} \\ & + \lambda_{SR} \sum_{n=0}^{N-1} \frac{(-1)^n \binom{N-1}{n} (1 - e^{-(n+1)(\lambda_{SR} + \lambda_{RD})x})}{(n+1)(\lambda_{SR} + \lambda_{RD})} ) \end{aligned} \tag{18}$$

Using Eq. (18), the required CDF of $F_{\gamma_R}(x) = \lambda_{RR}\int_0^\infty F_{\gamma_{SR_k}}((y+1)x)e^{-\lambda_{RR}y}dy$ can be calculated as

$$\begin{aligned} F_{\gamma_R}(x) = \frac{N}{\lambda_{SR}+\lambda_{RD}}[&\sum_{n=0}^{N-1}\frac{(-1)^n\binom{N-1}{n}}{\frac{n}{\lambda_{RD}}+\frac{1}{\lambda_{SR}+\lambda_{RD}}} \\ &\times(1-\frac{1}{1+\frac{\lambda_{SR}}{\lambda_{LI}}x}e^{-\lambda_{SR}x}) - \frac{\lambda_{SR}}{\lambda_{SR}+\lambda_{RD}}\sum_{n=0}^{N-1}(-1)^n \\ &\times\binom{N-1}{n}\frac{(1-\frac{e^{-(n+1)(\lambda_{SR}+\lambda_{RD})x}}{1+\frac{(n+1)(\lambda_{SR}+\lambda_{RD})x}{\lambda_{LI}}})}{(\frac{n}{\lambda_{RD}}+\frac{1}{\lambda_{SR}+\lambda_{RD}})(n+1)} \\ &+\lambda_{SR}\sum_{n=0}^{N-1}\frac{(-1)^n\binom{N-1}{n}(1-\frac{e^{-(n+1)(\lambda_{SR}+\lambda_{RD})x}}{1+\frac{(n+1)(\lambda_{SR}+\lambda_{RD})x}{\lambda_{LI}}})}{(n+1)}] \end{aligned} \tag{19}$$

Then, the CDF of $F_{\gamma_{R_kD}}(x)$ can be obtained from Eq. (18) by mutually exchanging $\lambda_{SR}$ and $\lambda_{RD}$ to yield

$$\begin{aligned} F_{\gamma_{RD}}(x) = N(&\frac{1-e^{-\lambda_{RD}x}}{\lambda_{SR}+\lambda_{RD}}\sum_{n=0}^{N-1}\frac{(-1)^n\binom{N-1}{n}}{\frac{n}{\lambda_{SR}}+\frac{1}{\lambda_{RD}+\lambda_{SR}}} \\ &-\frac{\lambda_{RD}}{\lambda_{RD}+\lambda_{SR}}\sum_{n=0}^{N-1}(-1)^n\binom{N-1}{n} \\ &\times\frac{(1-e^{-(n+1)(\lambda_{SR}+\lambda_{RD})x})}{(\frac{n}{\lambda_{SR}}+\frac{1}{\lambda_{SR}+\lambda_{RD}})(n+1)(\lambda_{SR}+\lambda_{RD})} \\ &+\lambda_{RD}\sum_{n=0}^{N-1}\frac{(-1)^n\binom{N-1}{n}(1-e^{-(n+1)(\lambda_{SR}+\lambda_{RD})x})}{(n+1)(\lambda_{SR}+\lambda_{RD})}) \end{aligned} \tag{20}$$

Finally, substituting Eqs. (19) and (20) into Eq. (10) to calculates exact outage probability.

### 3.4 Self-interference Relay Selection (SI)

Since the self-interference relay selection scheme only considers the interference, it's easy to get the best relay $k$:

$$k_{SI} = \arg\min_k\{\gamma_{RR_k}\} \tag{21}$$

For SI scheme, Relay selection is only related to the self-interference. According to the order statistics, the CDF of the self-interference can be given by

$$F_{\gamma_{RR_k}}(x) = (1-(1-F_{\gamma_{RR}}(x))^N), x \geq 0 \tag{22}$$

Taking a derivative of $F_{\gamma_{RR_k}}(x)$, $f_{\gamma_{RR_k}}(x) = N\lambda_{RR}e^{-N\lambda_{RR}x}$. Like Eq. (9), jointing $f_{\gamma_{RR_k}}(x)$ and $f_{\gamma_{SR}}(x)$, the CDF of $\gamma_R$ can be expressed as

$$F_{\gamma_{R_k}}(x) = 1 - \frac{1}{1 + \frac{\lambda_{SR}}{N\lambda_{RR}}x} e^{-\lambda_{SR}x}, x \geq 0 \tag{23}$$

Finally joining the SNR of $R_k - D$ link, through some reduction, the CDF of system's SNR can be given by

$$\begin{aligned} F_{\gamma_{eq}}(x) &= [1 - (1 - F_{\gamma_{R_k}}(x))(1 - F_{\gamma_{RD}}(x))] \\ &= \frac{1}{1 + \frac{\lambda_{SR}}{N\lambda_{RR}}x} e^{-(\lambda_{SR}+\lambda_{RD})x}, x \geq 0 \end{aligned} \tag{24}$$

## 4 Numerical and Simulation Results

In this Section, numerical examples for the outage probability are presented. The simulation system follows the system model of Sect. 2 with $R_0 = 2BPCU$, and the considered relay selection schemes are: OS, PS, MM and SI.

Figure 2 plots outage probability curves along with the change of $\gamma_{SR}$ with $N = 3$, $\lambda_{RR} = 1$ and $\lambda_{RD} = \lambda_{SR}$. It proves that the performance of DF-relay is always better than AF-relay. The reason is that DF-relay recodes and modulates the received signal to avoid the system noise and error accumulation spread. However, DF-relay system and AF-relay system come to the same level as $\gamma_{SR}$ growing, because the effect of the noise on the first link can be neglected when $\gamma_{SR}$ is lager enough.

Figure 3 shows outage probability as a function of INR for the different relay selection schemes with $N = 3$, $\lambda_{SR} = \lambda_{RD} = 0.01$. As you can see, OS scheme is

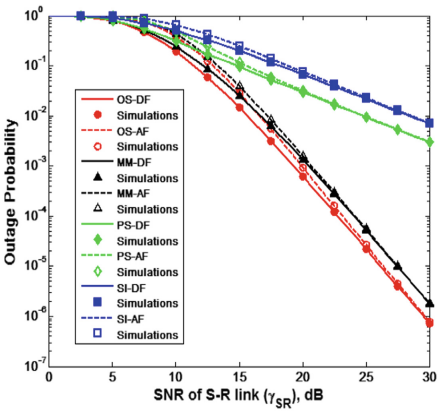


**Fig. 2.** Outage probability versus $\gamma_{SR}$, $N = 3$, $\gamma_{RD} = \gamma_{SR}$, $\lambda_{RR} = 1$.

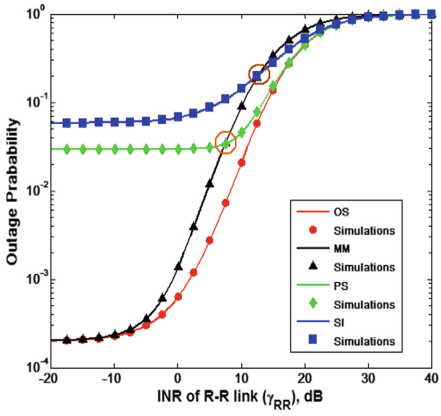


**Fig. 3.** Outage probability versus INR $\gamma_{RR}$, $N = 3$, $\lambda_{SR} = \lambda_{RD} = 0.01$.

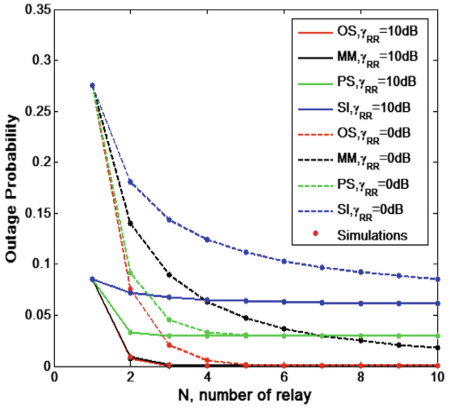


**Fig. 4.** Outage probability versus number of relay N, $\lambda_{SR} = \lambda_{RD} = 0.01$.

always the best one, but MM scheme close to it. PS scheme is always better than SI scheme, because PS scheme takes $\gamma_{RR}$ into account additionally. Moreover, there are two points of intersection as $\gamma_{RR}$ becomes more and more impactive. Therefore, when self-interference belongs to the lower levels, MM scheme can be used as an alternative to OS scheme. Accordingly, when self-interference at a higher level, OS scheme can be replaced by PS scheme.

Figure 4 presents the change of outage probability following the number of relay $N$ with $\lambda_{RR} = 1$ or $\lambda_{RR} = 0.1$, and $\lambda_{SR} = \lambda_{RD} = 0.01$. The outage probability will be lower when $N$ becomes lager. But it will reach to a saturation value. Therefore, we can obtain best performance by deploying limited relays.

In the three picture, it can be seen that the analytical results are in good agreement with results obtained from Monte-Carlo simulations.

## 5 Conclusion

This paper has dealt with the problem of relay selection for the multiple FD relay networks consisting of one source, one destination, and N FD DF relays over I.I.D. Rayleigh fading channels. Firstly, the optimal and three suboptimal relay selection schemes requiring global CSI or partial CSI have been investigated respectively. Then, the relay selection schemes have been analyzed in terms of outage probability. Compared to AF protocol, numerical results show the superiority of DF protocol. Besides, the best suboptimal relay selection scheme substituted for OS scheme and the relay arrangement policy have been presented.

**Acknowledgment.** The authors would like to thank National Natural Science Foundation of China (No. 6 1401042). And it is supported by science and technology project of SGCC: Study on Key Techniques of 4G Multi-Service Bearing for the Electric Power Mobile Internet Application (SGRIXTKJ[2015]349).

## References


1. Zhang, Z., Long, K., Wang, J.: Self-organization paradigms and optimization approaches for cognitive radio technologies: a survey. IEEE Wirel. Commun. **20**(2), 36–42 (2013)
2. Zhang, Z., Long, K., Wang, J., et al.: On swarm intelligence inspired self-organized networking: its bionic mechanisms, designing principles and optimization approaches. IEEE Commun. Surv. Tutor. **16**(1), 513–537 (2014)
3. Xing, C., Ma, S., Fei, Z., et al.: A general robust linear transceiver design for multi-hop amplify-and-forward MIMO relaying systems. IEEE Trans. Sig. Process. **61**(5), 1196–1209 (2013)
4. Jing, Y., Jafarkhani, H.: Single and multiple relay selection schemes and their achievable diversity orders. IEEE Trans. Wirel. Commun. **8**(3), 1414–1423 (2009)
5. Soliman, S.S., Beaulieu, N.C.: Exact analysis of dual-hop AF maximum end-to-end SNR relay selection. IEEE Trans. Commun. **60**(8), 2135–2145 (2012)
6. Thangaraj, A., Ganti, R.K., Bhashyam, S.: Self-interference cancellation models for full-duplex wireless communications. In: 2012 International Conference on Signal Processing and Communications (SPCOM), pp. 1–5. IEEE (2012)
7. Lpez-Valcarce, R., Antonio-Rodriguez, E., Mosquera, C., et al.: An adaptive feedback canceller for full-duplex relays based on spectrum shaping. IEEE J. Sel. Areas Commun. **30**(8), 1566–1577 (2012)
8. Hong, S., Brand, J., Choi, J.I., et al.: Applications of self-interference cancellation in 5G and beyond. IEEE Commun. Mag. **52**(2), 114–121 (2014)
9. Xing, C., Xia, M., Gao, F., et al.: Robust transceiver with Tomlinson-Harashima precoding for amplify-and-forward MIMO relaying systems. IEEE J. Sel. Areas Commun. **30**(8), 1370–1382 (2012)
10. Da Silva, M.M., Correia, A., Dinis, R., et al.: Transmission Techniques for 4G Systems. CRC Press, Boca Raton (2012)
11. Ikhlef, A., Kim, J., Schober, R.: Mimicking full-duplex relaying using half-duplex relays with buffers. IEEE Trans. Veh. Technol. **61**(7), 3025–3037 (2012)
12. Krikidis, I., Suraweera, H.A., Smith, P.J., et al.: Full-duplex relay selection for amplify-and-forward cooperative networks. IEEE Trans. Wirel. Commun. **11**(12), 4381–4393 (2012)
13. Yang, K., Cui, H., Song, L., et al.: Joint relay and antenna selection for full-duplex AF relay networks. In: 2014 IEEE International Conference on Communications (ICC), pp. 4454–4459. IEEE (2014)
14. Cui, H., Ma, M., Song, L., et al.: Relay selection for two-way full duplex relay networks with amplify-and-forward protocol. IEEE Trans. Wirel. Commun. **13**(7), 3768–3777 (2014)
15. Rui, X., Hou, J., Zhou, L.: On the performance of full-duplex relaying with relay selection. Electron. Lett. **46**(25), 1 (2010)
16. Rui, X., Hou, J., Zhou, L.: On the capacity of full-duplex relaying with partial relay selection. Wirel. Pers. Commun. **75**(1), 723–728 (2014)
17. Michalopoulos, D.S., Suraweera, H.A., Karagiannidis, G.K., et al.: Amplify-and-forward relay selection with outdated channel estimates. IEEE Trans. Commun. **60**(5), 1278–1290 (2012)

# Parameter Control Scheme Among Multi-cell for Mobility Load Balancing in Ultra-dense Network

Xin Su[2], Qi Zhang[1], Jie Zeng[2(✉)], and Liping Rong[2]

[1] Broadband Wireless Access Laboratory,
Chongqing University of Posts and Telecommunications, Chongqing, China
[2] Tsinghua National Laboratory for Information Science and Technology,
Research Institute of Information Technology, Tsinghua University, Beijing, China
zengjie@tsinghua.edu.cn

**Abstract.** Ultra-Dense Network (UDN) can improve the system capacity and satisfy the increasing data traffic demands, and is considered as a candidate technology in the fifth generation (5G) networks. UDN has a smaller cell radius and a new network structure, so it needs some more efficient resource management methods. The characteristic of the smaller cell radius makes the mobility management more difficult. This paper creatively proposes a novel scheme with concurrent Mobility Load Balancing (MLB) among multi-cell in UDN. Simulation results show that our proposed method is more balanced than the traditional method.

**Keywords:** Ultra-dense network · Mobility load balancing · Quality of service

## 1 Introduction

In order to meet the 1000x data traffic demands in 2020, some advanced technologies are needed [1]. There are three widely accepted candidate technologies, those are Ultra-Dense Network (UDN), massive multiple-in-multiple-out (MIMO), and new multiple access (NMA) [2]. In recent years, UDN attracts many researches in colleges and in industries. The common goal of the academia and the industry is to satisfy the great data traffic demand of the 5G systems [3, 4].

UDN has a smaller cell radius and a new network structure. It is different from the current LTE network. In urban area, there exist many potential hot spots, such as conference halls, hospitals, and schools. In these areas, users are more easily to aggregate in a small place. At the same time, many users require high data transmission rate to support kinds of multimedia business. So it becomes an overloaded cell easily, and it needs to

This work was supported by the China's 863 Project (No. 2015AA01A706), the National S&T Major Project (No. 2014ZX03004003), Science and Technology Program of Beijing (No. D161100001016002), State Key Laboratory of Wireless Mobile Communications, China Academy of Telecommunications Technology (CATT), and by Beijing Samsung Telecom R&D Center.


M. Huang et al. (Eds.): WICON 2016, LNICST 214, pp. 131–138, 2018.
https://doi.org/10.1007/978-3-319-72998-5_14

offload some users to the light cells. But the offloading procedure will cause a very high overhead at the processing procedure with an unsuitable scheme. Therefore, UDN needs an efficient resource management [5]. TOTal Expenditures (TOTEX) [5] will be a main problem due to the UDN. Next Generation Mobile Networks (NGMN) [6] and 3rd Generation Partnership Project (3GPP) [7] have proposed Self-Organizing Network (SON) to decrease TOTEX in UDN, and 3GPP has detailed some SON use cases in [6].

MLB can balance the loads among ultra-dense cells. In [8], MLB is automatically adjusting the Cell Individual Offset (CIO) value which could optimally take advantage of overall network resources. Also, MLB is implemented between an overloaded cell and an appropriate neighbor cell by altering CIO. HandOvers (HOs) can be triggered by several kinds of events [9]. We consider the A3 event [8] as the trigger of the HO event in the paper.

This paper describes an offloading mechanism from the overloaded cells to the light loaded neighbor cells, its main idea is to adjust CIO and the number of the target cells i more than one, i.e. one overloaded may offload to more than one target cells at the same time. The remainder of this paper is organized as follows: The system model is shown in Sect. 2. Then the proposed MLB method is illustrated in Sect. 3. Section 4 sets up the simulation and gives the corresponding analysis. Finally, Sect. 5 concludes the whole paper.

## 2 System Model

In this section, we present the radio environment, cell load computation and the detailed HO procedure.

### 2.1 Radio Environment and Cell Load

Assume that cell i is the serving cell of User Equipment (UE) u. Let $L_{u,i}$ denote the path loss from UE u to cell i. For cell i, the transmitted power is $P_i$. The power received by UE u from cell i is $R_{u,i}$, which is given by Eq. (1). We assume White Gaussian Noise (WGN) Power Spectral Density (PSD) is $n_o$, with $B_{cell}$ is the cell bandwidth. Here, we assume all the cells are allocated with the same bandwidth. UE u's Signal to Interference plus Noise Ratio (SINR) is given by Eq. (2).

$$R_{u,i} = P_i \cdot L_{u,i}. \tag{1}$$

$$S_{u,i} = \frac{P_i \cdot L_{u,i}}{n_0 \cdot B_{cell} + \sum_{j \neq i} R_{u,j}}. \tag{2}$$

Let the number of Physical Resource Block (PRB) as the load metric. We calculate the number of PRBs that UE u requires by Eq. (3).

$$N_u = \left\lceil \frac{D_u}{C(x_u) \cdot BW_{PRB}} \right\rceil. \tag{3}$$

where $D_u$ represents the desired data rate of UE u, $C(x_u)$ represents the spectral efficiency (SE), which is connected with u's SINR in the served cell, given by Eq. (4) and $BW_{PRB}$ denotes the bandwidth of each PRB in Hz.

$$C(x) = \begin{cases} 0, x < -7.04 \\ -0.0001x^3 + 0.0074x^2 \\ +0.1397x + 0.6218, -7.04 \leq x \leq 20.2 \\ C(20.2).x > 20.2 \end{cases} \tag{4}$$

Let $\sum N_{u,i}$ denote the number of occupied PRBs of cell i. The load of cell i can be denoted as follows:

$$\rho_i(t_k) = \frac{\sum N_{u,i}}{B_{cell}/BW_{PRB}}. \tag{5}$$

### 2.2 HO Procedure

Assume cell 1 and cell 2 are the source cell and the target cell, respectively. HO event can be succinctly denoted as follows [10]:

$$R_2 > R_1 + Hys + O_{1,2} - O_{2,1}. \tag{6}$$

where R1 and R2 denote the Reference Signal Received Power (RSRP) from the serving cell 1 and from the target cell 2, $O_{i,j}$ denotes the cell CIO of cell i towards cell j, and Hys is the HO Margin.

Set $CIO_{1,2} = O_{1,2} - O_{2,1}$ and $CIO_{2,1} = O_{2,1} - O_{1,2}$, Eq. (6) can be rewritten as follows:

$$R_2 > R_1 + Hys + CIO_{1,2} \tag{7}$$

Equation (7) indicates that UEs in cell 1 will be more easily to be offloaded to cell 2 with the decreasing of $CIO_{1,2}$. Thus we can adjust $CIO_{1,2}$ to offload from cell 1 to cell 2.

## 3 The Proposed MLB Method

We categorize the load into three categories: passive, neutral and active. Through X2 interface, the adjacent cells in the network could know the load information with each other. Based on the $\rho_i$ and the two load thresholds $Th_{Low}$ and $Th_{High}$, expressed in Eq. (8), we can judge a cell is seen as passive, neutral or active (Table 1). $\rho_{Target}$ and $\rho_{hyst}$ are fixed values. We can get them from Table 2.

$$Th_c = \begin{cases} \rho_{Target} + \rho_{hyst}, c = High \\ \rho_{Target} - \rho_{hyst}, c = Low \end{cases}. \tag{8}$$

**Table 1.** Cell categories in MLB.

| Cell status | Condition | Action |
|---|---|---|
| Passive | $\rho_i < Th_{Low}$ | Receive UEs from overloaded cell |
| Neutral | $Th_{Low} \leq \rho_i \leq Th_{High}$ | Do not participate in MLB |
| Active | $\rho_i > Th_{High}$ | Request removing UEs to light loaded cell |

**Table 2.** Basic Parameters of Simulation scenario.

| Parameter | Value |
|---|---|
| Carrier frequency | 2 GHz |
| Bandwidth | 5 MHz |
| Cell layout | 19 regular hexagonal cells (wrap-around) |
| ISD | 35 m |
| Initial cell individual offset | 0 dB |
| BS transmitting power | 33 dBm |
| $\rho_{Target}$ | 0.75 (normalization load) |
| $\rho_{hyst}$ | 0.15 (normalization load) |
| $Th_{High}$ | 0.9 (normalization load) |
| $Th_{Low}$ | 0.6 (normalization load) |
| Hys | 0 dB |
| Number of UEs | 95 (random distribution) |
| Density of noise | −174 dBm/Hz |

After classification work, only passive cells and active cells can take part in MLB parameter adjustment. By this way, the active cell, i.e. overloaded cell, will offload to the passive cell, i.e. lighted cell. The UEs in active cell will gain higher QoS. At the same time, neutral cells do not take part in MLB. The load of a neutral cell itself is high, if UEs are unloaded to a neutral cell, it will be easy to make the neutral cell overloaded. So this can avoid ping-pong effect [11].

Figure 1 presents the proposed MLB method. First, the active cells individually select the neighbor passive cells in ascending order of cell IDs, i.e. cell 1 will determine its MLB region at first, then cell 4 and finally cell 7; Next, there exits only one active cell in the specific area. As shown in Fig. 1, cell 1, cell 4 and cell 7 take part in different MLB procedures. Finally, one passive cell only takes part in only one MLB process.

As shown in Fig. 1, cell 1 is an active cell and is overloaded. It firstly chooses cell 2 to offload. This can be easily achieved by adjusting $CIO_{1,2}$. Equation (7) indicates that the smaller the value of $CIO_{1,2}$ is, the earlier UEs will hand over from cell 1 to cell 2. Thus, the minimum $CIO_{1,2}$ can be obtained as follows:

$$CIO_{1,2min} = M_{TH} - M_{1high} - Hys. \tag{9}$$

where $M_{TH}$ denotes the minimum RSRP, when the RSRP which the UE receives from cell 2 is $M_{TH}$, the RSRP it receives from cell 1 is denoted as $M_{1high}$. To avoid that cell 1

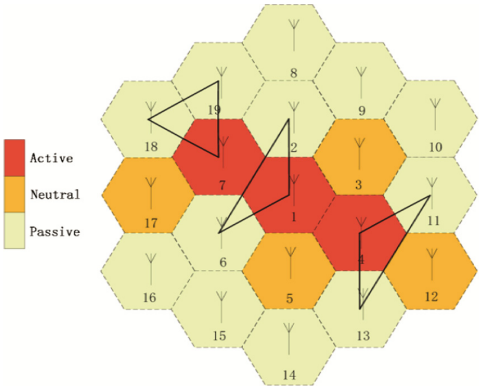


**Fig. 1.** Cell 1, cell 4 and cell 7 are active cells, so they need unload to other cells. Each cell chooses their own MLB region. Formation of MLB region is described in the figure.

handover to cell 2 too early, $CIO_{1,2}$ should be adjusted to be $CIO'_{1,2}$, which is between the value of the current $CIO_{1,2}$ and $CIO_{1,2\min}$. The following two equations express the adjusting rules:

$$\Delta_{1,2} = (CIO_{1,2} - CIO_{1,2\min}) \cdot (1 - \frac{\rho_2}{\rho_1}). \tag{10}$$

and

$$CIO'_{1,2} = CIO_{1,2} - \Delta_{1,2}. \tag{11}$$

where $\Delta_{1,2}$ is the step size, and is proportional to $\rho_1$ inversely proportional to $\rho_2$. By adjusting the value of $\Delta_{1,2}$, some UEs in cell 1 can be offloaded to cell 2 (Fig. 2).

MLB is triggered by active cells, and the MLB procedure is activated by the active cell and consist of the steps as follows:

(1) MLB functions in overloaded cells are triggered, and sort the load value of all cells;
(2) Sort the active cells ID list in ascending order;
(3) Every active cell decides its MLB region according the list order of active cells;
(4) Sort the passive cells ID list for each active cell in ascending order;
(5) The active cell adjusts the CIO parameter to a special passive cell according to the list order of its passive cells by Eq. (11). If the source cell is not an active cell, i.e. $\rho_i < Th_{High}$, the source cell does not change the CIO parameter to the latter passive cells in the list;
(6) The source cells transfer the parameters to its corresponding target cell, and these cells update the new parameters synchronically.

In the proposed MLB method, the target cells of the active cell is more than one. And several MLB procedures can be employed together. Also, Fig. 3 presents the flow chart of MLB procedure.

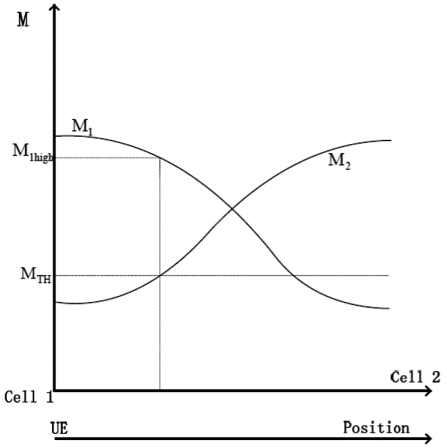


**Fig. 2.** UEs in the active cell (cell 1) need to be offload to the passive cell (cell 2).

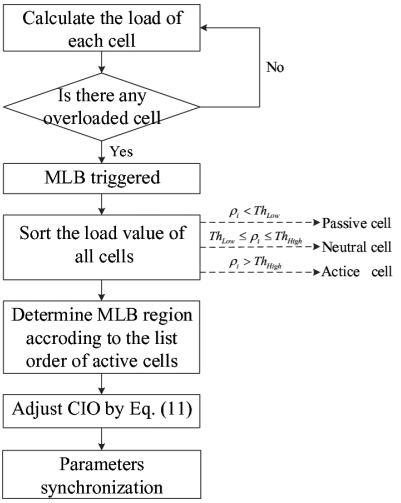


**Fig. 3.** The flow chart of MLB procedure.

## 4 Simulation Results and Analysis

This part evaluates our proposed method with simulations. In our simulation, 19 cells are mapped to be 61 cells with wrap-around, to accurately calculate the interference. In one simulation, 95 users are randomly dropped in the specific area [12]. More detailed parameters are listed in Table 2.

In traditional MLB, CIO values change in a pair of cells, that is, the overloaded cell always choose the lightest neighbor cell to offload by adjusting the parameter. Following simulation, we compared the proposed scheme with the traditional MLB.

Figure 4 displays the load histogram before doing MLB procedure, after implementing our proposed MLB procedure and after employing the traditional MLB procedure when the number of the cells is 19. The balanced load distribution among 19 cells is depicted by using MLB procedure. In specific, MLB decreases the load of active cells, and increases the load of passive cells. As shown in Fig. 4, cell 17 is overloaded before MLB, and it becomes light-loaded after employing our proposed MLB method, while with the traditional MLB method, cell 17 is still overloaded since its neighbor cell is not the most light-loaded. On the contrary, the cell 11 is light-loaded before MLB, and our proposed MLB method increases its load and makes full use of its resources. But with the traditional MLB method, the resources of cell 11 can't be fully utilized.

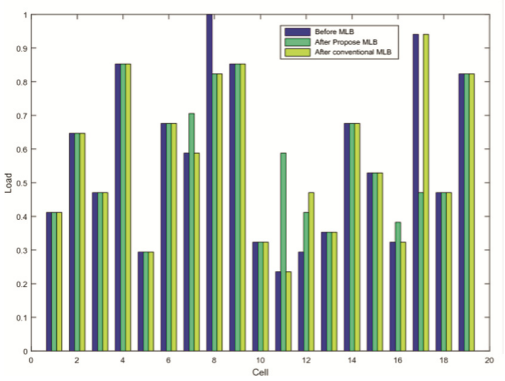


**Fig. 4.** The load of each cell in three conditions: before MLB, after our proposed MLB and after the traditional MLB when the number of cells is 19.

Figure 5 shows the variance of our proposed MLB method and the traditional MLB method, we can see that the red line is always under the blue one. It means our proposed MLB method can better balance the load of cells than the traditional MLB method

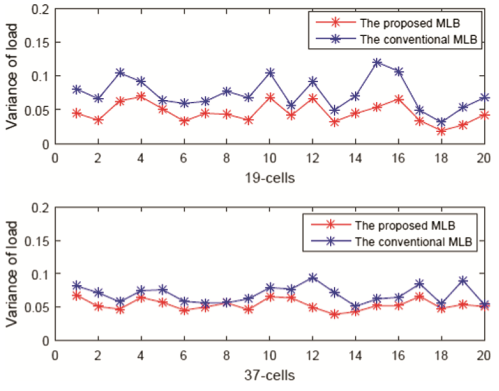


**Fig. 5.** The variance of load of the above two MLB methods with 19 cells and 37 cells. (Color figure online)

whatever in 19 cells or 37 cells. This is because the traditional MLB method chooses only one target cell to unload, but the proposed MLB scheme chooses more than one cell to unload. From Fig. 5, we can see that the proposed scheme has great malleability. And this scheme can be improved in subsequent research.

## 5 Conclusions

This paper has proposed a novel MLB method aiming to balance the loads among multi-cells in UDN. In addition, the multi-cell assistance is needed to acquire much more gains. The proposed method was based on multi-cell and decreasing too early HO times. Simulation results have shown that our proposed MLB method could better balance the load than the traditional MLB method, and could be better applied into UDN.

## References

1. Lopez-Perez, D., Ding, M., Claussen, H., Jafari, A.H.: Towards 1 Gbps/UE in cellular systems: understanding ultra-dense small cell deployments. IEEE Commun. Surv. Tutorials **17**(4), 2078–2101 (2015). 99
2. Boccardi, F., et al.: Five disruptive technology directions for 5G. IEEE Commun. Mag. **52**(2), 74–80 (2014)
3. Aspar, S., Wunder, G.: 5G cellular communications scenarios and system requirements. Technical report. https://www.5gnow.eu. Accessed 01 Oct 2014
4. Popovski, P., Braun, Y., Mayer, H.-P'., Fertl, P., et al.: ICT-3l7669-METIS/ D1.1 Scenarios, requirements and KPIs for 5G mobile and wireless system. Technical report. https://www.metis2020.com. Accessed 01 Oct 2014
5. Zia, N., Mwanje, S.S., Mitschele-Thiel, A.: A policy based conflict resolution mechanism for MLB and MRO in LTE self-optimizing networks. In: 2014 IEEE Symposium Computers and Communication (ISCC)
6. 3GPP.: Self-configuring and self-optimizing network (SON) use cases and solutions (Release 9). TR 36.902 v9.2.0, June 2010. www.3gpp.org
7. NGMN: Next Generation Mobile Networks Beyond HSPA ANG EVDO. White Paper v3.0, December 2006. www.ngmn.org
8. Nasri, R., Altman, Z.: Handover adaptation for dynamic load balancing in 3GPP long term evolution systems. In: Proceedings of International Conference on Advanced MoMM, pp. 1–9, December 2007
9. 3GPP: Radio Resource Control (RRC), Sophia-Antipolis, France, 3GPP TS36.331 V10.1.0, March 2011
10. 3GPP: E-UTRA Radio Resource Control (RRC) Protocol specification (Release 8). TS 36.331 V8.16.0, December 2011
11. Yang, C.: Concurrent mobility load balancing in LTE self-organized networks. In: IEEE ITC, pp. 288–292, May 2014. State Key Lab. of ISN, Xidian Univ., Xi'an, China
12. Zia, N., Mitschele-Thiel, A.: Self-organized neighborhood mobility load balancing for LTE networks. In: IEEE IFIP, pp. 2156–9711, November 2013

# Spectrum Sensing Based on Modulated Wideband Converter with CoSaMP Reconstruction Algorithm

Minglei Tong and Yong Bai(✉)

State Key Lab of Marine Resource Utilization in South China Sea,
College of Information Science and Technology, Hainan University,
58 Renmin Ave, Haikou 570228, Hainan, China
bai@hainu.edu.cn

**Abstract.** Modulated Wideband Converter (MWC) provides a sub-Nyquist sampling approach for wideband spectrum sensing. In previous studies, reconstruction algorithm, OMP (Orthogonal Matching Pursuit) is used in the CTF (continuous-to-finite) block of MWC for frequency support recovery. However, the percentage of correct support recovery is low at low SNR (Signal Noise Ratio) using OMP algorithm. In this paper, the reconstruction algorithm of CoSaMP (Compressive Sampling Matching Pursuit) is investigated to be used in the CTF block instead of OMP. Simulation results demonstrate that such a proposal can achieve higher percentage of correct support recovery than with OMP algorithm.

**Keywords:** Spectrum sensing · Modulated Wideband Converter (MWC)
Orthogonal Matching Pursuit (OMP)
Compressive Sampling Matching Pursuit (CoSaMP)

## 1 Introduction

In the field of wireless communications, spectrum resources become increasingly scarce with the emerged new services and growing number of users. Nevertheless, regulatory bodies found that allotted radio frequency spectrum can be inefficiently utilized. As a solution, cognitive radio (CR) technique can exploit the unused frequency regions on an opportunistic basis by using spectrum sensing to identify available spectrum holes [1, 2]. Hence, quick and efficient spectrum sensing is an essential component of CR functionality.

CR typically operates in a wideband environment, and the Nyquist sampling rate can be prohibitively large. When the band positions are unknown, it is a more challenging problem because standard demodulation cannot be used. The modulated wideband converter (MWC) provides a sub-Nyquist sampling approach for wideband spectrum sensing [3, 4]. It can blindly sample multiband analog signals at a low sub-Nyquist rate. The MWC first multiplies the analog signal by a bank of periodic waveforms. Then the product is lowpass filtered and sampled uniformly at a low rate, which is orders of magnitude smaller than the Nyquist rate. The spectral support can be


M. Huang et al. (Eds.): WICON 2016, LNICST 214, pp. 139–148, 2018.
https://doi.org/10.1007/978-3-319-72998-5_15

recovered by using sparse recovery algorithm of compressed sensing (CS) [5], which is performed in the CTF (continuous-to-finite) block in the MWC architecture [6]. The CTF constructs a frame from the input samples, then it solves a finite dimensional sparse representation problem, from which it identifies the indices of the active spectrum slices, namely those containing signal energy.

In the previous study of MWC, Orthogonal Matching Pursuit (OMP) algorithm is used in the CTF block [7–9]. However, the percentage of correct support recovery is low at low SNR (Signal Noise Ratio). In this paper, CoSaMP (Compressive Sampling Matching Pursuit) algorithm [10] is investigated to be used in the CTF block instead of OMP algorithm. Simulation results demonstrate that such a proposal can achieve higher percentage of correct support recovery than with OMP algorithm.

This paper is organized as follows. In Sect. 2, we describe the MWC architecture for wideband spectrum sensing. Section 3 describes sparse signal recovery algorithms, namely OMP algorithm and CoSaMP algorithm, which are used in the CTF block. Section 4 presents and discusses the simulation results of MWC with OMP algorithm and CoSaMP algorithm. Section 5 concludes this paper.

## 2 MWC Architecture for Wideband Spectrum Sensing

The MWC architecture for wideband spectrum sensing is shown in Fig. 1. The MWC performs sub-Nyquist sampling to obtain input samples, and the CTF block conducts frequency support recovery to identify spectrum holes.

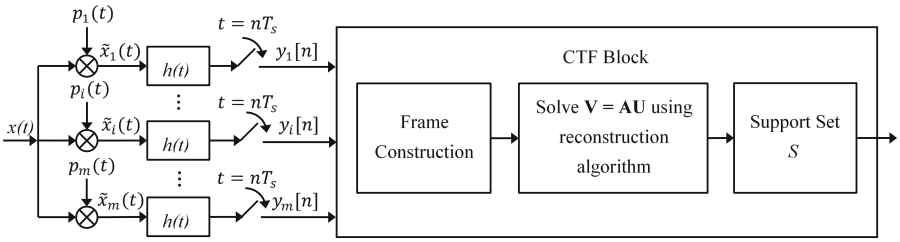


**Fig. 1.** MWC architecture for wideband spectrum sensing

### 2.1 MWC

The MWC can treat multiband signals when knowledge of the carrier frequencies is unknown. The only assumption is that the spectrum is concentrated on $N$ frequency intervals with individual widths not exceeding $B$. The sampling rate is proportional to the effective spectrum occupation $NB$ rather than $f_{NYQ}$ which represents Nyquist rate. Typically, the spectrum is underutilized so that $NB \ll f_{NYQ}$. For the purpose of spectrum sensing, the goal of MWC is to detect the inactive support. Other tasks such as reconstruction and processing of the primary transmissions are not required in the CR settings.

The MWC consists of a front end of $m$ channels. In the $i$th channel, the input signal $x(t)$ is multiplied by a periodic mixing waveform $p_i(t)$ with period $T_p$, low-pass filtered by $h(t)$, and then sampled at rate $1/T_s$. The basic MWC configuration has $f_p = 1/T_p \geq B$, $T_p = T_s$, $m \geq 4N$. Such a parameter choice results in a sampling rate, $mf_s \approx 4NB$, which, in general, is far below $f_{NYQ}$.

The mixing sequence $p_i(t)$ is periodic, and it has a Fourier expansion

$$p_i(t) = \sum_{l=-\infty}^{\infty} c_{il} e^{j2\pi f_p lt} \tag{1}$$

for some coefficients $c_{il}$.

Denoting by $z_l[n]$ the sequence that would have been obtained if the signal was mixed by a pure sinusoid $e^{j2\pi f_p lt}$ and low-pass filtered. This sequence corresponds to uniform samples at rate $f_p$ of a section of $x(t)$, conceptually obtained by bandpass filtering an $f_p$-width interval around $lf_p$ and demodulating to the origin. Since the system is linear, modulating by $p_i(t)$ and low-pass filtering is equivalent to summing the weighted combinations of all the sequences $z_l[n]$

$$y_i[n] = \sum_{l=-L}^{L} c_{il} z_l[n] \tag{2}$$

where the sum limits $-L \leq l \leq L$ represent the range of coefficients $c_{il}$, with nonnegligible amplitudes. It follows that the number of spectrum intervals that are aliased to the origin is $M = 2L + 1$.

Mixing by periodic waveforms aliases the spectrum to baseband, and each frequency interval of width $f_p = 1/T_p$ receives a different weight. The energy of the various spectral intervals is overlayed at baseband. Nonetheless, the fact that only a small portion of the wideband spectrum is occupied, together with the different weights in the different channels, permits the recovery of $x(t)$.

(2) can be rewritten as a linear system

$$\mathbf{y}[\mathrm{n}] = \mathbf{C}\mathbf{z}[\mathrm{n}] \tag{3}$$

where the vector $\mathbf{y}[\mathrm{n}]$ collects the measurements at $t = nTs$. The matrix $\mathbf{C}$ consists of the coefficients $c_{il}$, and $z_l[n]$ consists of the values of $z_l[n]$ arranged in vector form. From (3) and the definition of $z_l[n]$, it follows that at most $2N$ sequences, $z_l[n]$ are active, namely contain signal energy.

## 2.2 CTF Block

The CTF block constructs a finite-dimensional frame (or basis) from the samples, from which a small-size optimization problem is formulated. The solution of that problem indicates those spectrum slices that contain signal energy. The CTF outputs an index set $S$ of active slices.

The spectrum sensing functionality is to finding the index set

$$S = \{l | z_l[n] \neq 0\} \tag{4}$$

which reveals the spectrum support of $x(t)$ at a resolution of $f_p$ Hz.

Detecting $S$ by inverting $\mathbf{C}$ in (3) is not possible, since the $m \times M$ matrix $\mathbf{C}$ is underdetermined; the MWC uses $m \ll M$ to reduce the sampling rate below Nyquist rate. Underdetermined systems have in general infinitely many solutions. Nonetheless, under the parameter choice, and additional mild conditions on the waveforms $p_i(t)$, a sparse $\mathbf{z}[n]$ with at most $2N$ nonzero entries is unique and can be recovered in polynomial time by relying on results in the field of compressed sensing.

Solving for a sparse vector solution of an underdetermined system of equations has been widely studied in the literature of compressed sensing. Recovery of $\mathbf{z}[n]$ using any of the existing sparse recovery techniques is inefficient, since the sparsest solution $\mathbf{z}[n]$, even if obtained by a polynomial-time CS technique, is computed independently for every $n$. Instead, the CTF method exploits the fact that the bands occupy continuous spectral intervals. This analog continuity boils down to $\mathbf{z}[n]$ having a common nonzero location set $S$ over time. To take advantage of this joint sparsity, the CTF builds a frame from the measurements using

$$\mathbf{y}[n] \overset{\text{Frame construct}}{\rightarrow} \mathbf{Q} = \mathbf{y}[n]\mathbf{y}^H[n] \overset{\text{Decompose}}{\rightarrow} \mathbf{Q} = \mathbf{V}\mathbf{V}^H. \tag{5}$$

The active spectrum slices are detected from the sparse solution of the following finite dimensional system

$$\mathbf{V} = \mathbf{C}\mathbf{U}. \tag{6}$$

It is proven in [6] that (6) has a unique solution matrix $\mathbf{U}$ with minimal number of nonidentically zero rows, and that the locations of these rows coincide with the support set $S$ of $x(t)$. The CTF effectively locates the signal energy at a spectral resolution of $f_p$. From that support set, the CR device can decide the spectrum holes to be used as

$$\text{Spectrum holes} = \bigcup_{l \notin S} [lf_p - \frac{f_p}{2}, lf_p + \frac{f_p}{2}]. \tag{7}$$

In previous studies, OMP algorithm is used in the CTF block for frequency support recovery. However, the percentage of correct support recovery is low at low SNR using OMP algorithm. In this paper, CoSaMP algorithm is investigated to be used in the CTF block instead of OMP algorithm. In the sequel, we demonstrate by simulation that such a proposal can achieve higher percentage of correct support recovery than with OMP algorithm.

## 3 Sparse Signal Reconstruction Algorithm

The sparse signal reconstruction algorithms, OMP and CoSaMP, are presented as follows.

### 3.1 OMP Algorithm

MP (Matching Pursuit) is a greedy iterative algorithm for approximately solving the original $l_0$-norm problem for sparse signal recovery. MP works by finding a basis vector in the dictionary that maximizes the correlation with the residual, and then recomputing the residual and coefficients by projecting the residual on all atoms in the dictionary using existing coefficients. The main difference of OMP from MP is that after every step, all the coefficients extracted are updated by computing the orthogonal projection of the signal onto the set of atoms selected so far. The algorithm maintains an active set of atoms already picked, and adds a new atom at each iteration. The residual is projected on to a linear combination of all atoms in the active set, so that an orthogonal updated residual is obtained. The pseudo code of the OMP algorithm is given as follows.

Input:

(1) $M \times N$ dimensional sensing matrix $A = \Phi\Psi$
(2) $N \times 1$ dimensional measurement vector $y$
(3) Sparsity of signal $K$

Output:

(1) Estimation of signal sparse representation coefficient $\hat{\theta}$
(2) $N \times 1$ dimensional residual $r_K = y - A_K \hat{\theta}_K$

In the following processes, $r_t$ is the residual, $t$ is the number of iteration, $\varnothing$ is the empty set, $\Lambda_t$ is the column index set at $t$th iteration, $\lambda_t$ is the column index at the $t$th iteration, $a_j$ is the $j$th column of the matrix $A$, $A_t$ is the column set of $M \times t$ dimensional matrix of matrix $A$, which is chosen according to index $\Lambda_t$; $\theta_t$ is a $t \times 1$ dimensional column vector; the symbol $\cup$ refers to the union operation of sets; $\langle \cdot, \cdot \rangle$ refers to the inner product of vectors.

(1) Initializing $r_o = y$, $\Lambda_o = \varnothing$, $A_o = \varnothing$, $t = 1$;
(2) Finding the index $\lambda_t$, which satisfies $\lambda_t = \arg \max_{j=1,2,\cdots,N} \left| \langle r_{t-1}, a_j \rangle \right|$;
(3) Making $\Lambda_t = \Lambda_{t-1} \cup \{\lambda_t\}$, $A_t = A_{t-1} \cup a_\lambda$;
(4) Calculating the least square solution of $y = A_t \theta_t$ : $\hat{\theta}_t = \arg\min_{\theta_t} \|y - A_t \theta_t\| = \left(A_t^T A_t\right)^{-1} A_t^T y$;
(5) Updating the residual $r_t = y - A_t \hat{\theta}_t = y - A_t \left(A_t^T A_t\right)^{-1} A_t^T y$;
(6) $t = t + 1$, if $t \leq K$, the program will turn back to the second step to continue the iteration, otherwise the iteration will be stopped and the program will run the seventh step;

(7) The $\hat{\theta}$ from reconstruction has nonzero terms in $\Lambda_t$, and their values are $\hat{\theta}_t$ which are obtained from the last iteration respectively.

### 3.2 CoSaMP Algorithm

CoSaMP algorithm is another reconstruction algorithm which is proposed by Needell and Tropp [10]. CoSaMP algorithm chooses multiple atoms during each iteration rather than only one atom in OMP algorithm. In the selection criteria, the atoms in every iteration chosen by OMP algorithm are saved forever, whereas the atoms in every iteration chosen by CoSaMP algorithm may be discarded in next iteration. CoSaMP algorithm is better to approximate a compressible signal from noisy samples than OMP algorithm. The pseudo code of the CoSaMP algorithm is given as follows.

Input:

(1) $M \times N$ dimensional sensing matrix $A = \Phi\Psi$
(2) $N \times 1$ dimensional measurement vector $y$
(3) Sparsity of signal $K$

Output:

(1) Estimation of signal sparse representation coefficient $\hat{\theta}$
(2) $N \times 1$ dimensional residual $r_S = y - A_S \hat{\theta}_S$

In the following processes, $r_t$ is the residual, $t$ is the number of iteration, $\varnothing$ is the empty set, $J_0$ is the column index in each iteration, $\Lambda_t$ is the column index set at $t$th iteration, $a_j$ is the $j$th column of the matrix $A$, $A_t$ is the column set of matrix $A$ which is chosen according to index $\Lambda_t$, $\theta_t$ is a $L_t \times 1$ column vector; $abs[\cdot]$ is calculating the module value namely absolute value.

(1) Initializing $r_o = y$, $\Lambda_o = \varnothing$, $A_o = \varnothing$, $t = 1$;
(2) Calculating $u = abs[A^T r_{t-1}]$ (that is calculating $\langle r_{t-1}, a_j \rangle$, $1 \le j \le N$), choosing the $2K$ maximum in $u$, forming the set $J_0$ (column ordinal set) with the column ordinals $j$ of $A$ that correspond to these $2K$ maximum;
(3) Making $\Lambda_t = \Lambda_{t-1} \cup J_0$, $A_t = A_{t-1} \cup a_j$ (for all $j \in J_0$);
(4) Calculating the least square solution of $y = A_t \theta_t$ : $\hat{\theta}_t = \arg\min_{\theta_t} \|y - A_t \theta_t\| = \left(A_t^T A_t\right)^{-1} A_t^T y$;
(5) Choosing the $K$ largest absolute values of $\hat{\theta}_t$, and they are denoted as $\hat{\theta}_{tK}$. The $K$ columns corresponding to $A_t$ are denoted as $A_{tK}$ and the column ordinals corresponding to $A$ are denoted as $\Lambda_{tK}$, then updating the set $\Lambda_t = \Lambda_{tK}$;
(6) Updating the residual $r_t = y - A_{tK} \hat{\theta}_{tK} = y - A_{tK} \left(A_{tK}^T A_{tK}\right)^{-1} A_{tK}^T y$;
(7) $t = t + 1$, if $t \le S$, the program will turn back to the second step to continue the iteration, if $t > S$ or the residual $r_t = 0$, the iteration will be stopped and the program will run the eighth step;
(8) The $\hat{\theta}$ from reconstruction has nonzero terms in $\Lambda_{tK}$, and their values are $\hat{\theta}_{tK}$ which are obtained from the last iteration respectively.

## 4 Simulation and Discussion

In the simulation, the overall spectrum sensing range is 20 MHz. There are 2 active frequency bands ($2N = 4$). On each active frequency band, binary phase shift keying (BPSK) signal with Sinc waveforms is generated as the transmitted signal with bandwidth $B = 2$ MHz, and the signals on two frequency bands are modulated with frequency carriers 5 MHz and 15 MHz respectively. The signal energy is normalized to 1 at each band. The Nyquist rate is $f_{NYQ} = 40$ MHz. The sampling rate *fs* equals the aliasing rate *fp* whose value is 2.105264 MHz. The signals are sent over AWGN channel before reaching the MWC sensing device. The number of MWC channels is $m = 20$.

Figure 2 shows the time-domain signal waveform and PSD (Power Spectrum Density) of original signal, signal with noise and reconstructed signal when SNR is 30 dB.

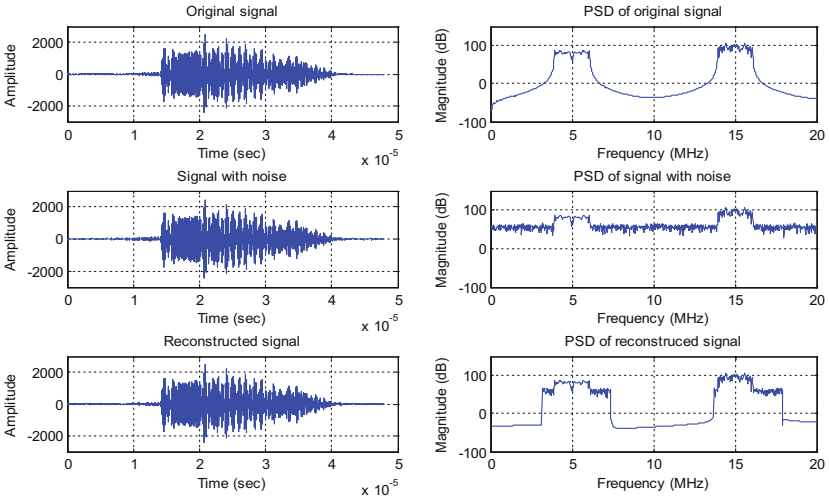


**Fig. 2.** Signal waveform and PSD of original signal, signal with noise, and reconstructed signal when SNR = 30 dB

Figure 3 shows the time-domain signal waveform and PSD (Power Spectrum Density) of original signal, signal with noise and reconstructed signal when SNR is 5 dB.

Figure 4 shows normalized residual of reconstructed signal versus SNR using OMP and CoSaMP algorithms. The normalized residual is defined as follows

$$residual = y - solution \tag{8}$$

$$normalized\,residual = resnorm/norm(solution) \tag{9}$$

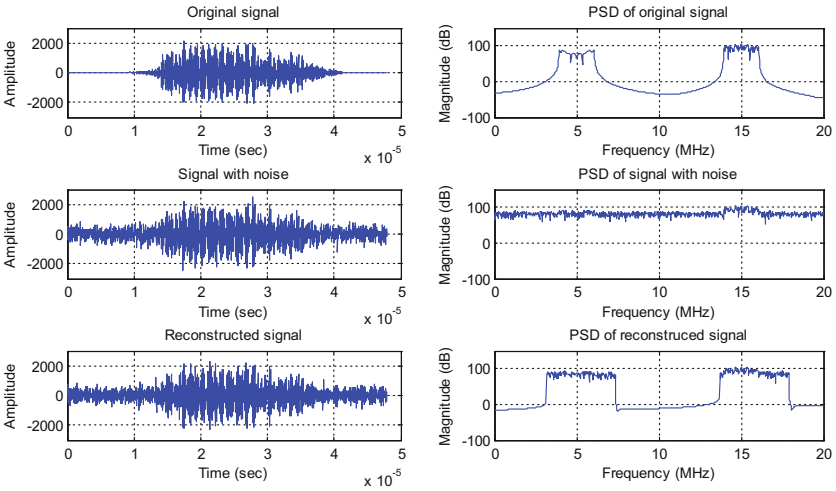


**Fig. 3.** Signal waveform and PSD of original signal, signal with noise, and reconstructed signal when SNR = 5 dB

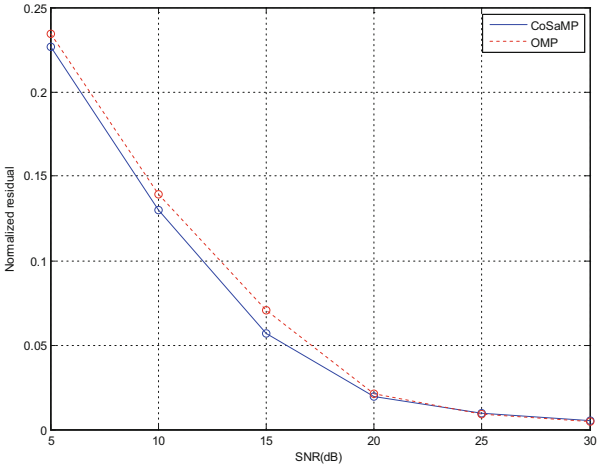


**Fig. 4.** Normalized residual of reconstructed signal at different SNRs

The *residual* can be calculated by (8), where $y$ is the observed signal; the *solution* is $A_t \hat{\theta}_t$ in the fifth step of OMP algorithm or $A_{tK} \hat{\theta}_{tK}$ in the sixth step of CoSaMP algorithm. The normalized residual is given in (9), where *resnorm* is the norm of residual.

It can be seen from Fig. 4 that the normalized residual of the reconstructed signal with CoSaMP algorithm is lower than that with OMP algorithm, though there is no significant difference.

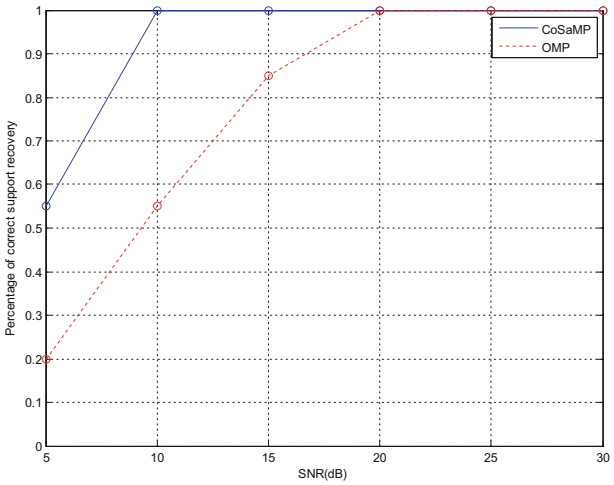


**Fig. 5.** Percentage of correct support recovery at different SNRs

Figure 5 shows that the percentage of correct support recovery at different SNRs using OMP and CoSaMP algorithms. It can be seen from Fig. 5 that the percentage of correct support recovery with CoSaMP algorithm is much higher than that with OMP algorithm at low SNR. Particularly, when SNR = 5 dB, the percentage of correct support recovery with CoSaMP algorithm is 55%. On the other hand, the percentage of correct support recovery with OMP algorithm is only 20% at the same SNR. Moreover, exact support recovery can be achieved when SNR is larger than 10 dB by using CoSaMP algorithm; OMP algorithm cannot reach such a performance until SNR is larger than 20 dB.

In addition, CoSaMP algorithm $(O(mn))$ has reduced complexity than OMP algorithm $(O(kmn))$ [10]. The notation $k$ refers to the sparsity level, the notation $m$ refers to the number of measurements and the notation $n$ refers to the signal length. Consequently, CoSaMP algorithm can be a better algorithm to be used in the CTF block of the system architecture for multiband spectrum sensing for support recovery than OMP algorithm.

## 5 Conclusion

In this paper, MWC with CoSaMP reconstruction algorithm for support recovery is proposed for multiband spectrum sensing. Our simulation results demonstrated that the method with CoSaMP algorithm can achieve higher percentage of correct support recovery than OMP algorithm, especially at low SNR regime. We also show that lower normalized residual can be achieved with CoSaMP algorithm than with OMP algorithm. In addition, CoSaMP algorithm has less complexity than OMP algorithm. These benefits make CoSaMP algorithm a better candidate to be used with MWC for wideband spectrum sensing.

**Acknowledgments.** This paper was supported by the National Natural Science Foundation of China (Grant No. 61561017 and Grant No. 61261024), National Science & Technology Pillar Program (Grant No. 2014BAD10B04), and Hainan Province Major Science & Technology Project (Grant No. ZDKJ2016015).

## References

1. Mitola III., J.: Cognitive radio for flexible mobile multimedia communications. J. Mob. Netw. Appl. **6**(5), 435–441 (2001)
2. Yücek, T., Arslan, H.: A survey of spectrum sensing algorithms for cognitive radio applications. J. IEEE Commun. Surv. Tutor. **11**(1), 116–130 (2009)
3. Mishali, M., Eldar, Y.C., Dounaevsky, O., et al.: Xampling: analog to digital at sub-nyquist rates. J. IET Circuits Dev. Syst. **5**(1), 8–20 (2011)
4. Mishali, M., Eldar, Y.C.: From theory to practice: sub-nyquist sampling of sparse wideband analog signals. IEEE J. Sel. Top. Signal Process. **4**(2), 375–391 (2015)
5. Donoho, D.L.: Compressed sensing. IEEE Trans. Inform. Theory. **52**(4), 1289–1306 (2006)
6. Mishali, M., Eldar, Y.C.: Blind multi-band signal reconstruction: compressed sensing for analog signals. IEEE Trans. Signal Process. **57**(3), 993–1009 (2009)
7. Pati, Y.C., Rezaiifar, R., Krishnaprasad, P.S.: Orthogonal matching pursuit: Recursive function approximation with applications to wavelet decomposition. In: Proceedings of Conference on Recommendation 27th Asilomar Conference on Signals, Systems and Computers, pp. 40–44 (1993)
8. Yang, Z.Z., Yang, Z., Sun, L.H.: A survey on orthogonal matching pursuit type algorithms for signal compression and reconstruction. J. Signal Process. **29**(4), 486–496 (2013)
9. Tropp, J.A., Gilbert, A.C.: Signal recovery from random measurements via orthogonal matching pursuit. IEEE Trans. Inform. Theory. **53**(12), 4655–4666 (2008)
10. Needell, D., Tropp, J.A.: CoSaMP: iterative signal recovery from incomplete and inaccurate samples. J. Appl. Comput. Harmon. Anal. **26**(3), 301–321 (2009)

# Joint Partial Relay and Antenna Selection for Full-Duplex Amplify-and-Forward Relay Networks

Qinghai Ou[1], Xinjing Hou[2(✉)], Fang Liu[2], Yuanan Liu[2], and Shaofeng Fang[2]

[1] State Grid Information and Telecommunication Group Co. Ltd., Beijing 102211, China
ouqinghai@sgitg.sgcc.com.cn
[2] Beijing University of Posts and Telecommunications, Beijing 100876, China
{hxj_y,lf,yuliu}@bupt.edu.cn, fsf77688@163.com

**Abstract.** In this paper, a joint partial relay and antenna selection (PRAS) scheme is proposed to further improve the capacity of full-duplex (FD) amplify-and-forward (AF) relay networks. The exact capacity expression for PRAS is derived. Furthermore, the simulation for the PRAS considering loop-interference and the relay numbers is analyzed by systems' capacity while making a comparison with primary relay selection schemes, e.g. optimal relay selection (ORS) and partial relay selection (PRS) scheme. The results show that the PRAS scheme can even get a capacity gain about 14% while it's 19% under the ORS comparing to the PRS scheme and presents the characteristic among the primary policies as well.

**Keywords:** Full-duplex · Amplify-and-forward · Capacity · Relay selection

## 1 Introduction

Full-duplex (FD) relay selection is seen as a promising technology to improve systems' capacity of wireless transmissions significantly, but the loop-interference (LI) caused by the signal leakage between the output and input antennas of the relay limits its development [1–3]. Fortunately, many LI cancellation projects including the antenna separation [4], directional antennas [5] and the time domain interference cancellation [6] etc. make that the residual loop-interference (RLI) on the FD relay can be nearly modeled as an additional noise, which means that FD relay networks can be possibly came true. As for existing relay selection policies, they mainly focus on an optimal relay selection (ORS) policy under a global CSI and three suboptimal relay selection policies such as Max-Min relay selection (MM); Partial relay selection (PRS), and Max-Min with Loop-Interference relay selection (MMLI) [2, 3, 7]. However, almost all the existing works for kinds of FD relay selection policies are analyzed by outage probability, the analysis on FD relay systems' capacity remains virtually unknown. For the antenna selection, a technology about antenna pair selection on the relay is analyzed in [8]. In [9, 10], they investigate an antenna selection at the relay based on the ORS scheme, which needs global CSI and leads to the increase of the system overhead.

In this paper, we proposed a joint relay and antenna partial selection (PRAS) scheme to improve the performance of PRS scheme from the aspect of saving resources


M. Huang et al. (Eds.): WICON 2016, LNICST 214, pp. 149–154, 2018.
https://doi.org/10.1007/978-3-319-72998-5_16

efficiently. Also the performance for the primary selection policies are investigated in terms of a new aspect about systems' capacity from the ability of loop-interference attenuation and the number of relays.

The remainder of this paper is organized as follows: Sect. 2 gives the system model and the capacity analysis; Sect. 3 shows the details of the proposed relay selection policies and primary policies. Simulation and analytical results are presented in Sect. 4. A brief conclusion is given in Sect. 5.

## 2 System Model

We assume a clustered network topology consisting of one half-duplex (HD) source (S), N FD relays ($R_i$ with $1 \leq i \leq N$) and one HD destination (D). The communication can be established only via the relays [2]. Each relay employ an AF protocol and is equipped with two antennas (one for receiving and one for transmitting) that enable a full-duplex operation. All wireless links are non-selective rayleigh block fading and an imperfect interference cancellation scheme is used at each relay. During one slot, we assume all fading channel coefficients $h_{A,B}$ (for the A → B link) remain constant and only one relay is selected, but change independently from one slot to another.

Assuming that the $i^{th}$ relay node $R_i$ is activated to forward the signal, the received signal at $R_i$ is given as

$$y_i[n] = h_{S,R_i} x[n] + h_{R_i} x_i[n] + n_i[n] \tag{1}$$

Where $h_{S,R_i}$ is the channel fading coefficient for the link S → $R_i$, and $h_{R_i}$ represents the channel coefficients of residual loop-interference (RLI) on the $i^{th}$ relay. $n_i$ is the additive white Gaussian noise (AWGN) with the power $\sigma^2$, $x[n]$ and $x_i[n]$ are the $n^{th}$ transmitting signal belongs to the S and the $i^{th}$ relay with a fixed transmit power $P_t$ in one transmission slot.

The retransmit signal at the AF FD relay node can be expressed as

$$x_i[n] = \beta y_i[n - \tau] \tag{2}$$

Where β is the power amplification factor and $\tau$ is the processing delay.

The amplification factor β ensures that the average power of signal $x_i[n]$ satisfies the power constraint. Therefore, the factor β can be obtained as

$$\beta = \sqrt{\frac{P_t}{\left|h_{S,R_i}\right|^2 P_t + \left|h_{R_i}\right|^2 P_t + \sigma^2}} \tag{3}$$

The received signal at the destination is given by

$$y_D[n] = h_{R_i,D} x_i[n] + n_D[n] \tag{4}$$

Where $h_{R_i,\mathrm{D}}$ is the channel fading coefficient from $R_i$ to D, and $n_D[n]$ is the AWGN with power $\sigma^2$. Then the end-to-end SINR considering the amplification factor β can be obtained.

Therefore, if an optimal amplification factor is employed for the AF process, the instantaneous end-to-end capacity of the i$^{th}$ FD relay is expressed as

$$C_{R_i}^{FD} = 2\log_2\left(1 + \frac{\dfrac{\gamma_{SR_i}}{\gamma_{R_i+1}}\gamma_{R_iD}}{\dfrac{\gamma_{SR_i}}{\gamma_{R_i+1}} + \gamma_{R_iD} + 1}\right) \tag{5}$$

Where $\gamma_{SR_i} = P_t\left|h_{S,R_i}\right|^2/\sigma^2$, $\gamma_{R_i} = \alpha P_t\left|h_{R_i}\right|^2/\sigma^2$, and $\gamma_{R_iD} = P_t\left|h_{R_i,\mathrm{D}}\right|^2/\sigma^2$.

## 3 Relay Selection Policies

In this section, we show the details of the proposed joint partial relay and antenna selection (PRAS) scheme, besides the primary relay selection policies. These schemes refer to a centralized architecture where a central unit decides the selected relay based on the available CSI.

### 3.1 Joint Partial Relay and Antenna Selection (PRAS)

In order to improve systems' capacity more effectively, we apply antenna selection technology to the existing PRS scheme and proposed a joint partial relay and antenna selection (PRAS) scheme. The policy consider a joint antenna and relay selection scheme, where the optimal relay and its transmit and receive antenna configuration are selected jointly based on the instantaneous channel conditions. The selection process is similar to the partial relay selection (PRS), which selects the relay that has the maximum SINR on the S → $R_i$ link considering LI, but each relay will adaptively select the optimal transmit antenna and receive antenna according to the condition on the link of S → $R_i$ in advance. The RLI remains unchanged despite of the configuration of the transmit/receive mode for the two antennas. Therefore, the policy activates the relay that satisfies the following condition

$$l_{i,AS} = \arg\max_i \left\{\gamma_{SR_i,T_1\to T_2}, \gamma_{SR_i,T_2\to T_1}\right\} \tag{6}$$

Where $T_1$ and $T_2$ denote the two antennas of the i$^{th}$ relay node, $\gamma_{SR_i,T_1\to T_2}$ denotes the SINR at the receiving terminal of relay when the i$^{th}$ relay node chooses the antenna $T_1$ as the receiving antenna and $T_2$ as the transmitting antenna in the next transmission and it's similar for $\gamma_{SR_i,T_2\to T_1}$ that the SINR at the receiving terminal of relay when the antenna $T_2$ is used to receive the signal from the source node, and $T_1$ is used to retransmit the signal to the destination.

Therefore, PARS scheme can be formulated as

$$K_{PRAS} = arg \max_i \left\{ \frac{\gamma_{SR_i}}{\gamma_{R_i} + 1} \right\} \tag{7}$$

Where $\gamma_{SR_i} = \max_i \left\{ \gamma_{SR_i, T_1 \to T_2}, \gamma_{SR_i, T_2 \to T_1} \right\}$.

### 3.2 The Primary Relay Selection Policies

**Optimal Relay Selection (ORS):** The ORS policy is based on the instantaneous capacity expression. Thus, it activates the relay with the optimal SINR

$$\mathrm{K} = \arg \max_i \left\{ \gamma_i \right\} \tag{8}$$

**Partial Relay Selection (PRS):** Activate the relay that has the maximum SNR on the $\mathrm{S} \to R_i$ link considering LI and is written as

$$\mathrm{K} = \arg \max_i \left\{ \frac{\gamma_{SR_i}}{\gamma_{R_i} + 1} \right\} \tag{9}$$

**Max−Min Relay Selection (MM):** Select the relay with the best end-to-end link without considering the LI and can be expressed as

$$\mathrm{K} = \arg \max_i \min \left\{ \gamma_{SR_i}, \gamma_{R_i D} \right\} \tag{10}$$

**Max-Min with Loop-Interference Relay Selection (MMLI):** This scheme is an improvement of the MM scheme and takes into account the LI. The selection metric is similar with the MM policy but updates the first branch with the SINR

$$\mathrm{K} = \arg \max_i \min \left\{ \frac{\gamma_{SR_i}}{\gamma_{R_i+1}}, \gamma_{R_i D} \right\}. \tag{11}$$

## 4 Simulation Results

In this section, we illustrate the performance of the above all relay selection policies with systems' capacity from the ability of loop-interference attenuation (α) and the number of relays (L) finding the differences between FD relay selection policies. The proposed PRAS scheme is compared with the PRS especially.

Figures 1 and 2 give numerical examples about capacity for primary FD relay selection schemes. Figure 1 plots system capacity versus L where α = 4 dB. The important observation is that the capacity of all policies increase with the growth of L and ORS is the best one while PRS outperforms MM with the growth of SNR. This is because that

the performance of PRS mainly focuses on the condition of R → D link. Figure 2 plots system capacity versus the α, where L = 4. It is worth noting that for this scenario, the intersection of MM > PRS move to a higher α while the signal noise to ratio (SNR) on the channel is fixed and α is growing, besides the main observations follow our previous remarks. For this result, we find the links that MM considered is more efficient than PRS.

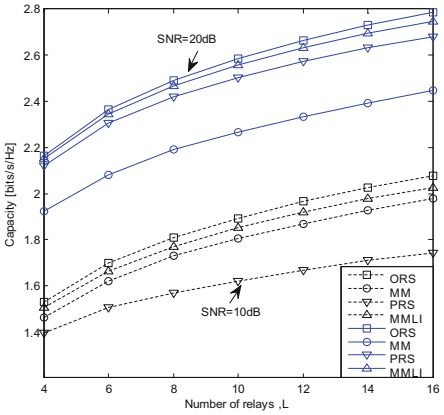


**Fig. 1.** System capacity versus the L

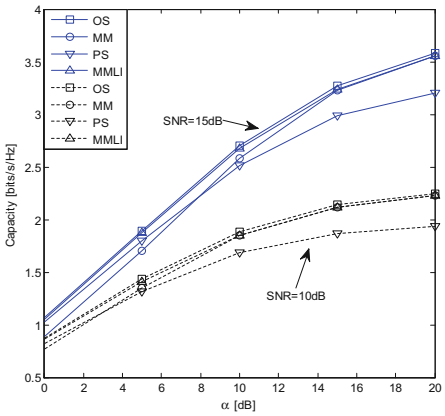


**Fig. 2.** System capacity versus the α

Therefore, we can conclude that ORS is the best one; the performance of the MMLI is almost same with the ORS; and the other two policies can nearly get the performance of ORS in some particular scenario, especially when unstable links conditions of the scenario can be considered by corresponding suboptimal policies efficiently.

Figures 3 and 4 show the simulation results among PRAS, PRS, and ORS from aspects about α and L. Figure 3 plots system capacity versus L, where SNR = 10 dB, α = 4 dB. Figure 4 plots system capacity versus the α, where L = 4.

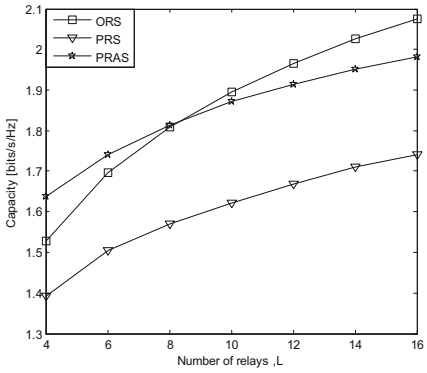


**Fig. 3.** System capacity versus the L

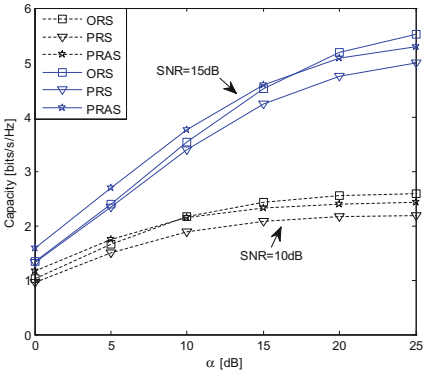


**Fig. 4.** System capacity versus the α

As can be seen, the performance of the proposed PRAS scheme is superior to PRS in all aspects and the PRAS is even better than the ORS in some specific scenarios, such as $L < 8$ in Fig. 3. From Fig. 3, we can also see that the PRAS can get a capacity gain about 14% while the gain of ORS is 19% ($L = 16$) comparing to the PRS scheme. And in Fig. 4 the capacity gain that the PRAS can get is about 15% while the ORS is similar to the PRS under a low loop-interference attenuation ($\alpha = 5$ dB, SNR = 15 dB).

## 5 Conclusion

In this paper, the proposed PRAS and the primary AF FD relay selection schemes have been analyzed in terms of systems' capacity. The numerical results reveal that the proposed PRAS scheme outperforms conventional PRS policy and it can even show better performance than the ORS in some particular scenarios. The ORS scheme is the best one among the primary policies and others will be similar to the ORS in some special scenarios.

**Acknowledgement.** The authors would like to thank National Natural Science Foundation of China (No. 61401042), and Science and Technology Project of State Grid Corporation (The research and application of the key technology of light and restructurable power wireless communication system based on spectrum sensing and flexibly carrier aggregation).

## References

1. Choi, J.I., Jain, M., Srinivasan, K., et al.: Achieving single channel, full duplex wireless communication. In: Proceedings of the Sixteenth Annual International Conference on Mobile Computing and Networking, pp. 1–12. ACM (2010)
2. Krikidis, I., Suraweera, H.A., Smith, P.J., et al.: Full-duplex relay selection for amplify-and-forward cooperative networks. IEEE Trans. Wirel. Commun. **11**(12), 4381–4393 (2012)
3. Cui, H., Ma, M., Song, L., et al.: Relay selection for two-way full duplex relay networks with amplify-and-forward protocol. IEEE Trans. Wirel. Commun. **13**(7), 3768–3777 (2014)
4. Riihonen, T., Werner, S., Wichman, R.: Mitigation of loopback self-interference in full-duplex MIMO relays. IEEE Trans. Signal Process. **59**(12), 5983–5993 (2011)
5. Everett, E., Duarte, M., Dick, C., et al.: Empowering full-duplex wireless communication by exploiting directional diversity. In: 2011 Conference Record of the Forty Fifth Asilomar Conference on Signals, Systems and Computers (ASILOMAR), pp. 2002–2006. IEEE (2011)
6. Jin, H., Leung, V.C.M.: Performance analysis of full-duplex relaying employing fiber-connected distributed antennas. IEEE Trans. Veh. Technol. **63**(1), 146–160 (2014)
7. Krikidis, I., Suraweera, H.A., Yuen, C.: Amplify-and-forward with full-duplex relay selection. In: 2012 IEEE International Conference on Communications (ICC), pp. 3532–3537. IEEE (2012)
8. Zhou, M., Cui, H., Song, L.: Transmit-receive antenna pair selection in full duplex systems. IEEE Wirel. Commun. Lett. **3**(1), 34–37 (2014)
9. Yang, K., Cui, H., Song, L., et al.: Joint relay and antenna selection for full-duplex AF relay networks. In: 2014 IEEE International Conference on Communications (ICC), pp. 4454–4459. IEEE (2014)
10. Yang, K., Cui, H., Song, L.: Efficient full-duplex relaying with joint antenna-relay selection and self-interference suppression. IEEE Trans. Wirel. Commun. **14**(7), 3991–4005 (2015)

# A Low-Complexity Power Allocation Method in Ultra-dense Network

Xin Su[1], Bei Liu[2], Jie Zeng[1(✉)], Jing Wang[1], and Xibin Xu[1]

[1] Tsinghua National Laboratory for Information Science and Technology, Research Institute of Information Technology, Tsinghua University, Beijing, China
zengjie@tsinghua.edu.cn
[2] Broadband Wireless Access Laboratory, Chongqing University of Posts and Telecommunications, Chongqing, China

**Abstract.** This paper considers the downlink power allocation in the ultra-dense network. To acquire the maximum sum rate of all the users, we first make the appropriate approximate hypothesis on the interference, and then adopt the Lagrangian Multiplier method and Karush-Kuhn-Tucker condition to obtain the expression of the optimum power allocation. Finally, the iteratively searching water filling algorithm is used to allocate power for each access node, when the total power is limited. Due to the consideration of the computation complexity of the iteratively searching algorithm, we applied the low-complexity water filling algorithm into the power allocation to reduce the iteration times. The simulation results have shown that the performance of the both two water filling algorithms are close, and can improve the sum rate of the users in the ultra-dense network, and the low-complexity water filling algorithm can converge to the optimum solution more quickly.

**Keywords:** Ultra-dense network · Water filling algorithm · Power allocation

## 1 Introduction

The fifth generation (5G) have been expected to provide the larger capacity to meet the rapidly increasing data traffic demands [1]. Ultra-dense network (UDN) shortens the distance of the user and the access node, and can substantially increase the area capacity, by densely deploying the access nodes [1]. However, because of the huge density of the access nodes, the interference in UDN is more complicated than traditional networks [2]. Thus, some better resource allocation methods and interference management algorithms should be studied.

This work was supported by the China's 863 Project (No. 2015AA01A709), the National S&T Major Project (2014ZX03004003), Science and Technology Program of Beijing (No. D161100001016002), S&T Cooperation Projects (No. 2015DFT10160B), State Key Laboratory of Wireless Mobile Communications, China Academy of Telecommunications Technology (CATT), and Beijing Samsung Telecom R&D Center.


M. Huang et al. (Eds.): WICON 2016, LNICST 214, pp. 155–163, 2018.
https://doi.org/10.1007/978-3-319-72998-5_17

Many academics have been committed to the studies of UDN. The authors of [3] analyses the relationship of the access node density and the network spectrum efficiency (SE), and concluded that SE can't always increase with the increase of the access node density. *Zhou et al.* [4] introduced the interference management methods from 1G to 5G, and proposed three potential technologies, which are the Coordinated Multi-Point transmission (CoMP) technique, the more advanced interface technique, and the interference alignment technique, to mitigate the more serious inter-cell interference in UDN. *Soret et al.* [5] considers the dominant interference and gives the time-domain and frequency-domain interference coordination to resist the interference in dense networks. *Wang et al.* [6] proposes a dynamical cell muting scheme considering the proportional fair (PF) scheduling of all the users. What's more, the resource allocation based on game theory is expected to obtain the performance improvement in UDN. [7] proposes a power allocation method based on non-cooperative game theory to suppress interference in the downlink dense network. [8] proposes a spectrum allocation combined with the CoMP to mitigate the interference in UDN. What's more, [9] proposes a multi-dimensional bisection search method which is based on the water filling algorithm to maximize the system capacity, but it is too high-complexity to be applied in UDN. In a word, some new interference management methods should be studied.

This paper considers the downlink transmission in UDN, and aims to get the optimal power allocation to maximize the sum rate of all the users in the area. Water filling is a classical algorithm which is always used in Orthogonal Frequency Division Multiplexing (OFDM) systems to allocate the power among the subcarriers [10]. However, the number of the access nodes and the number of the users are very large in UDN, and the inter-cell interference is more complicated. Luckily, we can make a hypothesis on the interference in UDN [9, 11]. Having this hypothesis in mind, we can transform the objective problem into the convex one. Then the water filling algorithm can be applied to search the optimal solution. In addition, considering the high computation complexity of the iteratively searching water filling (ISWF) algorithm, we further proposed the low-complexity water filling (LWF) algorithm, it can reach the nearly sum rate as ISWF with fewer iterations.

The remainder of the paper is organized as follows. Section 2 shows the system model and formulates the problem. Section 3 introduces two power allocation methods, which are the ISWF algorithm and the proposed LWF algorithm. Then the simulation is shown and the complexity is analyzed in Sect. 4. Finally, Sect. 5 concludes the paper.

## 2 System Model

This part shows the system model, as shown in Fig. 1. Assume the number of the users and the number of the access nodes are $K$ and $M$, $M \gg K$. And the access nodes and the users are equipped with the single antenna. Assume that each users choose the serving access nodes according to the reference signal receiving power (RSRP); and each access node serves only one user and each user is served by only one access node. Then in order to save energy, turn off the access nodes those serve no users, forming $K$ transmitter-receiver pairs. Simply, define $g_{kk}$ as the channel gain between the user $k$ and its serving

access node. $d_{mk}$ and $h_{mk}$ denote the distance and the channel coefficient between the access node $m$ and the user $k$, then the corresponding channel gain can be dented as $g_{mk} = \dfrac{h_{mk}}{d_{mk}^{\alpha}}$, where $\alpha$ denotes the pass loss exponent. The receiving signal of user $k$ can be denoted as

$$y_k = \sqrt{p_k g_{kk}} s_k + \sum_{i=1, i \neq k}^{K} \sqrt{p_i g_{ik}} s_i + n_k \tag{1}$$

where $s_i (i = 1, 2, \cdots, K)$ denotes the signal of the serving access node transmitting to user $i$. $p_i (i = 1, 2, \cdots K)$ denotes the allocated power of the serving access node, and $n_k \sim \mathcal{CN}\left(0, \sigma^2\right)$, which denotes the additional white Gaussian noise.

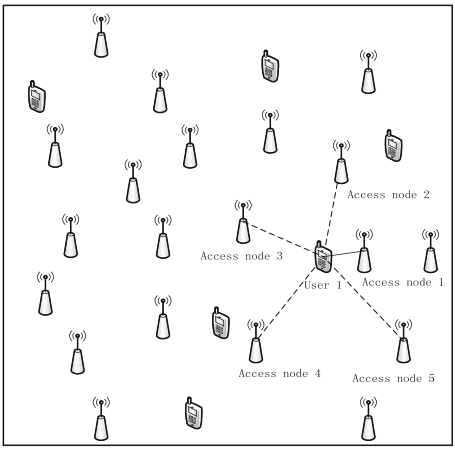


**Fig. 1.** UDN scenario: There are $M$ access nodes and $K$ users ($M \gg K$) randomly distributed in the specific area. The solid line in the figure represents the desired signal transmission, and the dotted lines represent the interference signal transmission.

We can easily find that the three parts on the right side of the Eq. (1) respectively denote the wanted signal, the interference and the noise. So the receiving signal to interference plus noise ratio (SINR) can be expressed as follows:

$$\text{SINR} = \frac{g_{kk} p_k}{\sum_{i \neq k}^{K} g_{ik} p_i + \sigma_k^2} \tag{2}$$

The rate of user $k$ could be written as follows [12]:

$$R_k = B_k \log_2\left(1 + \mathrm{SINR}_k\right) = B_k \log_2 \frac{\sum_{i=1}^{K} g_{ik} p_i + \sigma_k^2}{\sum_{i \neq k}^{K} g_{ik} p_i + \sigma_k^2} \tag{3}$$

where $B_k$ denotes the bandwidth allocated to the serving access node of user $k$. Assume $B_k = B\,(k = 1, 2, \cdots K)$. Thus we can denote the sum rate of all the users as follows:

$$R = B \sum_{k=1}^{K} \log_2 \frac{\sum_{i=1}^{K} g_{ik} p_i + \sigma_k^2}{\sum_{i \neq k}^{K} g_{ik} p_i + \sigma_k^2} \tag{4}$$

### 2.1 Problem Formulation

With the aim of the maximization of the sum rate of all the users with the restricted power, the following objective function is formed. Since the bandwidth of every access node is identical, we can express the optimization function for simplicity as:

$$\begin{aligned} &\max \sum_{k=1}^{K} \log_2 \frac{\sum_{i=1}^{K} g_{ik} p_i + \sigma_k^2}{\sum_{i \neq k}^{K} g_{ik} p_i + \sigma_k^2} \\ &st. \quad \sum_{k=1}^{K} p_k \leq P_{\max} \end{aligned} \tag{5}$$

Where the total power can be denoted as $P_{\max}$. Visibly, the interference make the optimization function non-convex. Fortunately, we can assume the interferences as constants to transform the function to a convex one [10, 11]. With this in mind, we adopt the Lagrangian Multiplier scheme to search the optimum solution [11]. First, the Lagrangian function is expressed as:

$$L(p_k, \lambda) = \sum_{k=1}^{K} \log_2 \frac{\sum_{i=1}^{K} g_{ik} p_i + \sigma_k^2}{\sum_{i \neq k}^{K} g_{ik} p_i + \sigma_k^2} + \lambda\left(P_{\max} - \sum_{k=1}^{K} p_k\right) \tag{6}$$

where $\lambda$ is the Lagrangian multiplier, which is for the power constraint. Then take the partial derivative with respect to $p_k$:

$$\frac{\partial L}{\partial p_k} = \frac{1}{\ln 2} \frac{g_{kk}}{g_{kk}p_k + \sum\limits_{i=1,i\neq k}^{K} g_{ik}p_i + \sigma_k^2} - \sum_{j=1,j\neq k}^{K} \frac{\gamma_j p_j g_{ik}}{\sum\limits_{i=1,i\neq j}^{K} g_{ij}p_i + \sigma_k^2} - \lambda \tag{7}$$

where $\gamma_k = \dfrac{g_{kk}}{\sum\limits_{i=1,i\neq k}^{K} g_{ik}p_i + \sigma_k^2}$.

Finally, we can easily acquire the illustration of $p_k$ with the Karush–Kuhn–Tucker (KKT) condition, as follows:

$$p_k = \left[ \frac{1}{\lambda \ln 2 + \sum\limits_{j=1,j\neq k}^{K} \dfrac{\gamma_j p_j g_{jk}}{\sum\limits_{j=1,j\neq k}^{K} g_{ij}p_i + \sigma_j^2}} - \frac{1}{\gamma_k} \right]^+ \tag{8}$$

## 3 Water Filling Based Power Allocation

### 3.1 ISWF Algorithm

Equation (8) indicates that $p_k$ is relative to $\gamma_k$. Having this in mind, the water filling algorithm can be applied. First, define the water-filling level as follows:

$$\beta = \frac{1}{\lambda \ln 2 + \sum\limits_{j=1,j\neq k}^{K} \dfrac{\gamma_j p_j g_{jk}}{\sum\limits_{i=1,i\neq j}^{K} g_{ij}p_i + \sigma_j^2}} \tag{9}$$

Then rewrite Eq. (8) as:

$$p_k = \left[ \beta - \frac{1}{\gamma_k} \right]^+ \tag{10}$$

First, we use the ISWF algorithm to solve the problem. Its main idea is to find the optimal water-filling level by updating the value of $\beta$ iteratively. In detail, the initial value of $\beta$ is denoted as follows:

$$\beta = \frac{1}{K}\left[P_{\max} + \sum_{k=1}^{K}\frac{1}{\gamma_k}\right] \tag{11}$$

Then, iteratively update the value of $\beta$ according to the expression below:

$$\beta \leftarrow \beta + \mu\frac{1}{N_{on}}\left(P_{\max} - \sum_{k=1}^{K} p_k\right) \tag{12}$$

where $0 < \mu < 1$ denotes the water-filling level modification step size. $N_{on}$ denotes the number of the access nodes whose allocated power is not zero. Update $\beta$ until its value converges to the optimum water filling level. Finally, we can get the optimal power allocation according to Eq. (10).

### 3.2 Proposed LWF Algorithm

Since the ISWF algorithm is very high-complexity, we propose the LWF algorithm and illustrate it in this part. In the first step, give the power of each access node as the following equation:

$$p_k = \frac{1}{K}\left(P_{\max} + \sum_{i=1}^{K}\frac{1}{\gamma_i}\right) - \frac{1}{\gamma_k} \tag{13}$$

Because different users have different channel gains, the access nodes whose have channel quality are bad may be allocated with negative powers. Then they are divided into the positive set and the negative set: $A = \{p_k | p_k > 0\}$ and $B = \{p_k | p_k < 0\}$. Then calculate the average value,

$$\Delta = \frac{\sum_{p_i \in B} p_i}{|A|} \tag{14}$$

Set the negative power in $B$ to zero, adjust the positive power in $A$ as follows

$$p_k' = p_k(p_k \in A) + \Delta \tag{15}$$

Repeat (14) and (15) until no negative powers exist and we can get the optimum power of each access node.

## 4 Simulation Results

### 4.1 Performance Comparison

This section compares the sum rates of above-mentioned methods by Monte Carlo simulations. In the simulation, the number of access nodes and the number of the users

are respectively set to 100 and 10. They are randomly positioned in the specific area. And the channels are the randomly generated unit variance Rayleigh fading channels in the simulations. In addition, the pass loss exponent is assumed as 3.75.

As we all know, the average power allocation is the fairest and the simplest method, and is presented as a contrast. Figure 2 shows the sum rate performance of the ISWF algorithm, the proposed LWF algorithm and the average power allocation. From the figure, both the ISWF based power allocation and the proposed LWF based power allocation can achieve the greatly improve the sum rate of the users. Furthermore, sum rates of the two water filling based power allocation methods are very close.

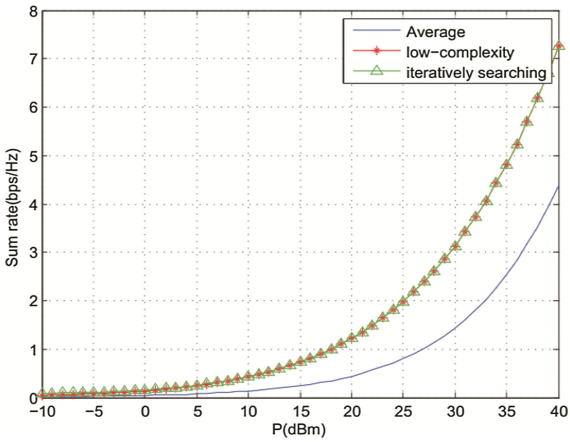


**Fig. 2.** The sum rate performance of the average power allocation algorithm, the ISWF algorithm, LWF algorithm.

### 4.2 Complexity Analysis

This part gives the complexity comparison of the above-mentioned algorithms. In one iteration, the ISWF algorithm needs $2K$ times of add operations and $K + 2$ times of multiply operations. While the proposed LWF algorithm only needs $2K$ times of add operations and one multiply operation. What's more, the proposed LWF algorithm needs much less iterations to converge than the ISWF algorithm.

Table 1 shows the average iteration times of the two algorithms when the Monte Carlo simulation time is 10000. From the table, the ISWF algorithm needs around 24 iterations to converge, but the LWF algorithm only needs around 4 iteration to converge to the optimal power allocation. In summary, the complexity of the LWF algorithm is much lower.

**Table 1.** The average iteration times of the two algorithms.

| Pmax (dBm) | −10 | 0 | 10 | 20 | 30 | 40 |
|---|---|---|---|---|---|---|
| ISWF | 24.5626 | 24.5587 | 24.5577 | 24.4310 | 23.9252 | 22.7437 |
| LWF | 4.2231 | 4.2110 | 4.1837 | 4.1347 | 3.8550 | 3.1835 |

In a summary, compared with the ISWF algorithm, the proposed LWF algorithm can reach nearly the same sum rate performance as the ISWF algorithms with much lower complexity.

## 5 Conclusions and Discussion

This paper creatively proposed an algorithm to obtain the optimal power allocation method, which aimed to maximize the sum rate in UDN. We first simply regarded the interference as content to make the objective problem convex. Then, the ISWF algorithm was applied, and it can significantly improve the sum rate. However, it needs many iterations, which makes it impractical to be applied in UDN. So we further proposed the LWF algorithm, which needs fewer iterations. It is proved that the proposed LWF algorithm reached nearly the same performance in terms of the sum rate to the ISWF algorithm. Both significantly improved the sum rate a lot, compared with the average power allocation. Furthermore, the proposed LWF algorithm needs less iterations to converge, which leads to a substantial complexity decrease. In a word, the proposed LWF based power allocation can be better applied to UDN.

## References

1. Bhushan, N., Li, J., Malladi, D., Gilmore, R., Brenner, D., Damnjanovic, A., Sukhavasi, R., Patel, C., Gerihofer, S.: Network densification: the dominant theme for wireless evolution into 5G. IEEE Commun. Mag. **52**, 82–89 (2014)
2. Lopez-Perez, D., Ding, M., Claussen, H., Jafari, A.H.: Towards 1 Gbps/UE in cellular systems: understanding ultra-dense small cell deployments. IEEE Commun. Surv. Tutor. **17**, 2078–2101 (2015)
3. Ren, Q., Fan, J., Luo, X., Xu, Z., Chen, Y.: Analysis of spectral and energy efficiency in ultra-dense network. In: Communication Workshop (ICCW), pp. 2812–2817, London (2015)
4. Yiqing, Z., Ling, L., Honhyan, D., et al.: An overview on inter-cell interference management in mobile cellular networks: from 2G to 5G. In: International Conference on Communication Systems (ICCS), pp. 217–221 (2015)
5. Soret, B., Pedersen, K.I., Jorgensen, N.T.K., et al.: Interference coordination for dense wireless networks. IEEE Commun. Mag. **53**(1), 102–109 (2015)
6. Xiaoyi, W., Visotsky, E., Ghosh, A.: Dynamic cell muting for ultra dense indoor small cell deployment scenario. In: IEEE International Conference on Communication Workshop (ICCW), pp. 148–153 (2015)
7. Yuehong, G., Lei, C., Xin, Z., et al.: Enhanced power allocation scheme in ultra-dense network. China Commun. **12**(2), 21–29 (2016)
8. Yang, S., Yongyu, C., Mengshi, H., et al.: A cluster-based hybrid access strategy using non-cooperative game theory for ultra-dense HetNet. In: IEEE International Conference on High Performance Computing and Communications (HPCC), pp. 14–19 (2015)
9. Gao, L., Cheng, X., Zhang, Y., Zhu, Y., Zhang, Y.: Enhanced power allocation scheme in ultra-dense small cell network. China Commun. **13**, 21–29 (2016)

10. Jang, J., Lee, K.B., Lee, Y.H.: Transmit power and bit allocations for OFDM systems in a fading channel. In: Global Communications Conference, San Francisco, pp. 283–288 (2003)
11. Kim, J., Lee, H.W., Chong, S.: Virtual cell beamforming in cooperative networks. IEEE J. Sel. Areas Commun. **32**, 1126–1138 (2014)
12. Shannon, C.E.: A mathematical theory of communication. Bell Syst. Tech. J. **27**, 379–423 (1948)

# QRD Architecture Using the Modified ILMGS Algorithm for MIMO Systems

Cang Liu[1(✉)], Chuan Tang[1], Zuocheng Xing[1], Luechao Yuan[1], Yu Wang[1], Lirui Chen[1], Yang Zhang[1], Suncheng Xiang[1], Wangfeng Zhao[1], Xing Hu[1], and Jinsong Xu[2]

[1] National Laboratory for Parallel and Distributed Processing, National University of Defense Technology, Changsha, China
{liucang,tc8831,zcxing,yuan.luechao,wangyu16,chenlirui14, zhangyang,xiangsuncheng14,zhaowangfeng}@nudt.edu.cn, 348883881@qq.com, 351749562@qq.com

[2] School of Cryptography Engineering, Information Engineering University, Zhengzhou, China
pine_xu@sohu.com

**Abstract.** QR decomposition (QRD) is one of the performance bottlenecks of transceiver processor in the multiuser multiple-input-multiple-output (MU-MIMO) systems. This paper proposes a QRD algorithm based on the existing modified Gram-Schmidt (MGS) algorithm and iteration look-ahead MGS (ILMGS) algorithm, which is named modified ILMGS (MILMGS) algorithm. A corresponding hardware architecture based on the proposed MILMGS algorithm is designed in 0.13 μm CMOS technique to decompose the 4×4 real matrix. The implementation results show that the gate count of the designed hardware architecture is 250.2 K, the throughput and the critical path are 95.2 M/s and 3.5 ns respectively.

**Keywords:** QRD · MU-MIMO · MGS · ILMGS · MILMGS

## 1 Introduction

The multiuser multiple-input-multiple-output (MU-MIMO) technique has attracted considerable interests, because of the continuously increasing demand for high data rates and high spectrum efficiency. And the MU-MIMO technique has been adopted in several wireless communication standards, such as IEEE 802.11n [1], IEEE 802.11ac [2] and IEEE 802.16e [3]. In order to simultaneously serve multiple users in the same frequency band, various precoding algorithms are proposed. Most of this algorithms are complicated and difficult to implement in MIMO systems [4,5]. Consequently, exploiting the hardware architecture for this algorithms has important significance.

For presubtraction of the multiuser interference (MUI), Costa [6] proposed the dirty paper coding (DPC) algorithm in his representative literature "writing


M. Huang et al. (Eds.): WICON 2016, LNICST 214, pp. 164–178, 2018.
https://doi.org/10.1007/978-3-319-72998-5_18

on dirty paper". The DPC algorithm is the optimal precoding algorithm, however, it is very difficult to implement in practical communication systems, due to its unreachable computational complexity [4,5]. Some practical DPC algorithms have been proposed to reduce the computational complexity. Tomlinson-Harashima precoding (THP) is one of the most popular practical algorithms, and has gained great attentions in some communication research communities [7–9]. And QR decomposition (QRD) is the primary part in most THP algorithms.

The existing QRD hardware architectures of MIMO systems mainly base on the Givens Rotation (GR) [10–12] algorithm and the modified Gram-Schmidt (MGS) [13–17] algorithm. Due to using the coordinate rotation digital computer (CORDIC) algorithm in the GR algorithm, it can significantly reduce the corresponding hardware overhead. However, because the GR algorithm annihilates the elements one by one, it leads to longer processing latency. Compared to the GR algorithm, the MGS algorithm annihilates the elements one column by one column. Therefore, it significantly reduces the processing latency. To further reduce the processing latency, the iteration look-ahead MGS (ILMGS) algorithm is propose in [18]. Due to involving several high computation complexity operations (square root and division) in ILMGS algorithm, the corresponding hardware architecture costs large hardware overhead.

In this paper, a modified ILMGS (MILMGS) algorithm is proposed for the QRD of MIMO systems, and a new triangular systolic array (TSA) architecture is designed based on the proposed MILMGS algorithm. The Newton-Raphson (NR) algorithm is used in the proposed MILMGS algorithm to reduce the hardware overhead. Moreover, the designed hardware architecture is implemented to decompose a $4 \times 4$ real matrix, the implementation results show that the throughput performance and the latency performance of the designed TSA hardware architecture are 95.2 MHz and 53 clock cycles respectively, the gate count and the critical path of the designed TSA architecture are 250.2 K and 3.5 ns respectively.

The rest of the paper is organised as the follows. In Sect. 2, we illustrate the traditional QRD algorithms and propose the MILMGS algorithm. In Sect. 3, the designed hardware architecture for QRD with MILMGS algorithm is presented. In Sect. 4, we provide the implementation results and some comparisons with the existing works. Finally, Sect. 5 draws the conclusions.

## 2 QR Decomposition Algorithm

The existing QRD hardware architectures for MIMO systems mainly base on the GR algorithm and the MGS algorithm respectively. The proposed QRD algorithm (MILMGS) is based on the modified MGS algorithm (ILMGS). Hence, we only focus on the MGS algorithm and the ILMGS algorithm in the following, the proposed MILMGS algorithm is also provided in this section.

A $n \times n$ real matrix $\mathbf{A}$ can be decomposed to an upper triangular matrix $\mathbf{R}$ and an unitary matrix $\mathbf{Q}$ by QRD algorithm. In order to simplify the description, the size of real matrix $\mathbf{A}$ is set to $4 \times 4$, $\mathbf{x_i}$ and $a_{i,j}$ represent the elements in $ith$ column and the $(i, j)$ element of matrix $\mathbf{X}$ respectively in this paper.

### 2.1 MGS Algorithm

The MGS algorithm performs QRD one column by one column. Firstly, The element $r_{1,1}$ of upper triangular matrix and the first column elements of unitary matrix $\mathbf{Q}$ can be computed as follows

$$r_{1,1} = \|\mathbf{a_1}\|_2 = \sqrt{(a_{1,1})^2 + (a_{2,1})^2 + (a_{3,1})^2 + (a_{4,1})^2} \tag{1}$$

$$\begin{aligned} &\mathbf{q_1} = \tfrac{\mathbf{a_1}}{r_{1,1}} \\ &q_{1,1} = \tfrac{a_{1,1}}{r_{1,1}}, q_{2,1} = \tfrac{a_{2,1}}{r_{1,1}}, q_{3,1} = \tfrac{a_{3,1}}{r_{1,1}}, q_{4,1} = \tfrac{a_{4,1}}{r_{1,1}} \end{aligned} \tag{2}$$

The elements $r_{1,j}, 1 < j \leq 4$ are obtained by elements $\mathbf{q_1}$ and the $jth$ column vector of matrix $\mathbf{A}$ as Eq. 3

$$\begin{aligned} r_{1,j} &= \mathbf{q_1^T} \cdot \mathbf{a_j} \\ &= q_{1,1}a_{1,j} + q_{2,1}a_{2,j} + q_{3,1}a_{3,j} + q_{4,1}a_{4,j}, \\ &\qquad 2 \leq j \leq 4; j \in N \end{aligned} \tag{3}$$

To obtain the other elements of upper triangular matrix $\mathbf{R}$ and unitary matrix $\mathbf{Q}$, the matrix $\mathbf{A}$ should be converted to the next iterative matrix $\mathbf{A^1}$ as Eq. 4

$$\begin{aligned} \mathbf{a_1^1} &= 0 \\ \mathbf{a_2^1} &= \mathbf{a_2} - r_{1,2}\mathbf{q_1} \\ \mathbf{a_3^1} &= \mathbf{a_3} - r_{1,3}\mathbf{q_1} \\ \mathbf{a_4^1} &= \mathbf{a_4} - r_{1,4}\mathbf{q_1} \end{aligned} \tag{4}$$

Secondly, the element $r_{2,2}$ of upper triangular matrix $\mathbf{R}$ and the second column vector of unitary matrix $\mathbf{Q}$ can be obtained as follows

$$r_{2,2} = \left\|\mathbf{a_2^1}\right\|_2 = \sqrt{\left(a_{1,2}^1\right)^2 + \left(a_{2,2}^1\right)^2 + \left(a_{3,2}^1\right)^2 + \left(a_{4,2}^1\right)^2} \tag{5}$$

$$\begin{aligned} &\mathbf{q_2} = \tfrac{\mathbf{a_2^1}}{r_{2,2}} \\ &q_{1,2} = \tfrac{a_{1,2}^1}{r_{2,2}}, q_{2,2} = \tfrac{a_{2,2}^1}{r_{2,2}}, q_{3,2} = \tfrac{a_{3,2}^1}{r_{2,2}}, q_{4,2} = \tfrac{a_{4,2}^1}{r_{2,2}} \end{aligned} \tag{6}$$

The second row vector $r_{2,j}, 2 < j \leq 4$ of upper triangular matrix $\mathbf{R}$ can be computed by Eq. 7

$$\begin{aligned} r_{2,j} &= \mathbf{q_2^T} \cdot \mathbf{a_j^1} \\ &= q_{1,2}a_{1,j}^1 + q_{2,2}a_{2,j}^1 + q_{3,2}a_{3,j}^1 + q_{4,2}a_{4,j}^1, \\ &\qquad 3 \leq j \leq 4; j \in N \end{aligned} \tag{7}$$

To further calculate the third row vector of upper triangular matrix $\mathbf{R}$ and the third column vector of unitary matrix $\mathbf{Q}$, the next iterative matrix $\mathbf{A^2}$ can be calculated as Eq. 8

$$\begin{aligned} \mathbf{a_1^2} &= 0 \\ \mathbf{a_2^2} &= 0 \\ \mathbf{a_3^2} &= \mathbf{a_3^1} - r_{2,3}\mathbf{q_2} \\ \mathbf{a_4^2} &= \mathbf{a_4^1} - r_{2,4}\mathbf{q_2} \end{aligned} \tag{8}$$

Thirdly, the elements $r_{3,3}$, $\mathbf{q_3}$ and $r_{3,4}$ can be computed as follows

$$r_{33} = \left\|\mathbf{a_3^2}\right\|_2 = \sqrt{\left(a_{1,3}^2\right)^2 + \left(a_{2,3}^2\right)^2 + \left(a_{3,3}^2\right)^2 + \left(a_{4,3}^2\right)^2} \tag{9}$$

$$\begin{aligned} &\mathbf{q_3} = \tfrac{\mathbf{a_3^2}}{r_{3,3}} \\ &q_{1,3} = \tfrac{a_{1,3}^2}{r_{3,3}}, q_{2,3} = \tfrac{a_{2,3}^2}{r_{3,3}}, q_{33} = \tfrac{a_{3,3}^2}{r_{3,3}}, q_{4,3} = \tfrac{a_{4,3}^2}{r_{3,3}} \end{aligned} \tag{10}$$

$$\begin{aligned} r_{3,4} &= \mathbf{q_3}^T \mathbf{a_4^2} \\ &= q_{1,3}a_{1,4}^2 + q_{2,3}a_{2,4}^2 + q_{3,3}a_{3,4}^2 + q_{4,3}a_{4,4}^2 \end{aligned} \tag{11}$$

Similarly, the next iterative matrix $\mathbf{A^3}$ can be obtained as Eq. 12 to calculate the elements $r_{4,4}$ and $\mathbf{q_4}$.

$$\begin{aligned} \mathbf{a_1^3} &= 0 \\ \mathbf{a_2^3} &= 0 \\ \mathbf{a_3^3} &= 0 \\ \mathbf{a_4^3} &= \mathbf{a_4^2} - r_{3,4}\mathbf{q_3} \end{aligned} \tag{12}$$

Finally, the fourth column vector of unitary matrix $\mathbf{Q}$ and the element $r_{4,4}$ of upper triangular matrix $\mathbf{R}$ can be obtained by Eqs. 13 and 14. The results (upper triangular matrix $\mathbf{R}$ and unitary matrix $\mathbf{Q}$) of MGS algorithm are obtained by the aforementioned steps.

$$r_{4,4} = \left\|\mathbf{a_4^3}\right\|_2 = \sqrt{\left(a_{1,4}^3\right)^2 + \left(a_{2,4}^3\right)^2 + \left(a_{3,4}^3\right)^2 + \left(a_{4,4}^3\right)^2} \tag{13}$$

$$\begin{aligned} &\mathbf{q_4} = \tfrac{\mathbf{a_4^3}}{r_{4,4}} \\ &q_{1,4} = \tfrac{a_{1,4}^3}{r_{4,4}}, q_{2,4} = \tfrac{a_{2,4}^3}{r_{4,4}}, q_{3,4} = \tfrac{a_{3,4}^3}{r_{4,4}}, q_{4,4} = \tfrac{a_{4,4}^3}{r_{4,4}} \end{aligned} \tag{14}$$

### 2.2 ILMGS Algorithm

To reduce the processing latency of QRD with MGS algorithm, the ILMGS algorithm is proposed in [18] for the MIMO systems. The QRD with ILMGS algorithm is presented in the following.

Firstly, the first column vector $\mathbf{q_1}$ of unitary matrix $\mathbf{Q}$ and the first row vector $r_{1,j}, 1 \le j \le 4$ of upper triangular matrix $\mathbf{R}$ can be obtained as the MGS algorithm.

$$r_{1,1} = \|\mathbf{a_1}\|_2 = \sqrt{\left(a_{1,1}\right)^2 + \left(a_{2,1}\right)^2 + \left(a_{3,1}\right)^2 + \left(a_{4,1}\right)^2} \tag{15}$$

$$\begin{aligned} &\mathbf{q_1} = \tfrac{\mathbf{a_1}}{r_{1,1}} \\ &q_{1,1} = \tfrac{a_{1,1}}{r_{1,1}}, q_{2,1} = \tfrac{a_{2,1}}{r_{1,1}}, q_{3,1} = \tfrac{a_{3,1}}{r_{1,1}}, q_{4,1} = \tfrac{a_{4,1}}{r_{1,1}} \end{aligned} \tag{16}$$

$$\begin{aligned} r_{1,j} &= \mathbf{q_1}^T \cdot \mathbf{a_j} \\ &= q_{1,1}a_{1,j} + q_{2,1}a_{2,j} + q_{3,1}a_{3,j} + q_{4,1}a_{4,j}, \\ &\qquad 2 \le j \le 4; j \in N \end{aligned} \tag{17}$$

Then, the matrix $\mathbf{A}$ need to be converted to the next iterative matrix $\mathbf{A^1}$ as Eq. 18. The converted method is the main difference between the ILMGS algorithm and the MGS algorithm.

$$\begin{aligned}
&\mathbf{a_1^1} = 0 \\
&\mathbf{a_2^1} = \mathbf{a_2} - r_{1,2}\mathbf{q_1} = \mathbf{a_2} - \mathbf{q_1}^T\mathbf{a_2}\mathbf{q_1} = \mathbf{a_2} - \frac{\mathbf{a_1}^T\mathbf{a_2}\mathbf{a_1}}{r_{1,1}^2} \\
&\mathbf{a_3^1} = \mathbf{a_3} - \frac{\mathbf{a_1}^T\mathbf{a_3}\mathbf{a_1}}{r_{1,1}^2} \\
&\mathbf{a_4^1} = \mathbf{a_3} - \frac{\mathbf{a_1}^T\mathbf{a_4}\mathbf{a_1}}{r_{1,1}^2}
\end{aligned} \tag{18}$$

Equation 18 shows that the next iterative matrix $\mathbf{A^1}$ can be computed after getting the value of $r_{1,1}^2$. Moreover, the value of $r_{1,1}^2$ is computed with $\mathbf{a_1}^T \cdot \mathbf{a_1}$, and the time overhead of $\mathbf{a_1}^T \cdot \mathbf{a_1}$ is equal to the time overhead of $\mathbf{a_1}^T \cdot \mathbf{a_2}$. Hence, the value of $\mathbf{A^1}$ can be calculated simultaneously with the calculation of $\mathbf{q_1}$ and $r_{1,j}, 1 \le j \le 4$, and not need to wait the results of $\mathbf{q_1}$ and $r_{1,j}, 1 \le j \le 4$.

Secondly, to compute the second column vector of $\mathbf{Q}$ and the second row vector of $\mathbf{R}$, we need to repeat the similar steps as shown in the following

$$r_{2,2} = \left\|\mathbf{a_2^1}\right\|_2 = \sqrt{\left(a_{1,2}^1\right)^2 + \left(a_{2,2}^1\right)^2 + \left(a_{3,2}^1\right)^2 + \left(a_{4,2}^1\right)^2} \tag{19}$$

$$\begin{aligned}
&\mathbf{q_2} = \frac{\mathbf{a_2^1}}{r_{2,2}} \\
&q_{1,2} = \frac{a_{1,2}^1}{r_{2,2}}, q_{2,2} = \frac{a_{2,2}^1}{r_{2,2}}, q_{3,2} = \frac{a_{3,2}^1}{r_{2,2}}, q_{4,2} = \frac{a_{4,2}^1}{r_{2,2}}
\end{aligned} \tag{20}$$

$$\begin{aligned}
r_{2,j} &= \mathbf{q_2}^T \cdot \mathbf{a_j^1} \\
&= q_{1,2}a_{1,j}^1 + q_{2,2}a_{2,j}^1 + q_{3,2}a_{3,j}^1 + q_{4,2}a_{4,j}^1, \\
&\qquad 3 \le j \le 4; j \in N
\end{aligned} \tag{21}$$

Then, the value of next iterative matrix $\mathbf{A^2}$ is similar to Eq. 18.

$$\begin{aligned}
&\mathbf{a_1^2} = 0 \\
&\mathbf{a_2^2} = 0 \\
&\mathbf{a_3^2} = \mathbf{a_3^1} - r_{2,3}\mathbf{q_2} = \mathbf{a_3^1} - \mathbf{q_2}^T\mathbf{a_3^1}\mathbf{q_2} = \mathbf{a_3^1} - \frac{\mathbf{a_2^1}^T\mathbf{a_3^1}\mathbf{a_2^1}}{r_{2,2}^2} \\
&\mathbf{a_4^2} = \mathbf{a_4^1} - \frac{\mathbf{a_2^1}^T\mathbf{a_4^1}\mathbf{a_2^1}}{r_{2,2}^2}
\end{aligned} \tag{22}$$

Thirdly, the elements $r_{3,j}, 3 \le j \le 4$ of upper triangular matrix $\mathbf{R}$ and the third column vector $\mathbf{q_3}$ of unitary matrix $\mathbf{Q}$ can be computed as follows

$$r_{33} = \left\|\mathbf{a_3^2}\right\|_2 = \sqrt{\left(a_{1,3}^2\right)^2 + \left(a_{2,3}^2\right)^2 + \left(a_{3,3}^2\right)^2 + \left(a_{4,3}^2\right)^2} \tag{23}$$

$$\begin{aligned}
&\mathbf{q_3} = \frac{\mathbf{a_3^2}}{r_{3,3}} \\
&q_{1,3} = \frac{a_{1,3}^2}{r_{3,3}}, q_{2,3} = \frac{a_{2,3}^2}{r_{3,3}}, q_{33} = \frac{a_{3,3}^2}{r_{3,3}}, q_{4,3} = \frac{a_{4,3}^2}{r_{3,3}}
\end{aligned} \tag{24}$$

$$\begin{aligned}
r_{3,4} &= \mathbf{q_3}^T\mathbf{a_4^2} \\
&= q_{1,3}a_{1,4}^2 + q_{2,3}a_{2,4}^2 + q_{3,3}a_{3,4}^2 + q_{4,3}a_{4,4}^2
\end{aligned} \tag{25}$$

The next iterative matrix $\mathbf{A^3}$ is calculated as Eq. 26

$$\begin{aligned}
&\mathbf{a_1^3} = 0 \\
&\mathbf{a_2^3} = 0 \\
&\mathbf{a_3^3} = 0 \\
&\mathbf{a_4^3} = \mathbf{a_4^2} - r_{3,4}\mathbf{q_3} = \mathbf{a_4^2} - \mathbf{q_3}^T\mathbf{a_4^2}\mathbf{q_3} = \mathbf{a_4^2} - \frac{\mathbf{a_3^{2T}}\mathbf{a_4^2}\mathbf{a_3^2}}{r_{3,3}^2}
\end{aligned} \tag{26}$$

Finally, repeating the similar operations in the matrix $\mathbf{A^3}$, the value of $r_{4,4}$ and column vector $\mathbf{q_4}$ can be obtained as follows

$$r_{4,4} = \left\|\mathbf{a_4^3}\right\|_2 = \sqrt{\left(a_{1,4}^3\right)^2 + \left(a_{2,4}^3\right)^2 + \left(a_{3,4}^3\right)^2 + \left(a_{4,4}^3\right)^2} \tag{27}$$

$$\begin{aligned}
&\mathbf{q_4} = \frac{\mathbf{a_4^3}}{r_{4,4}} \\
&q_{1,4} = \frac{a_{1,4}^3}{r_{4,4}}, q_{2,4} = \frac{a_{2,4}^3}{r_{4,4}}, q_{3,4} = \frac{a_{3,4}^3}{r_{4,4}}, q_{4,4} = \frac{a_{4,4}^3}{r_{4,4}}
\end{aligned} \tag{28}$$

### 2.3 MILMGS Algorithm

The ILMGS algorithm significantly reduces the processing latency. However, compared to the QRD hardware architecture based on the other algorithm, the main drawback of the MGS algorithm and the ILMGS algorithm is that they need more hardware overhead. To reduce the hardware overhead of QRD, this paper proposes the MILMGS algorithm based on the existing ILMGS algorithm. We will present the proposed MILMGS algorithm in the following.

The aforementioned description about the ILMGS algorithm shows than the value of $r_{i,i}, 1 \leq i \leq 4$ and each column vector of unitary matrix $\mathbf{Q}$ can be rewritten as $x \cdot \frac{1}{r_{i,i}}$. And the division in the calculation of the next iterative matrix $\mathbf{A^m}$ can also be rewritten as $x \cdot \frac{1}{r_{i,i}} \cdot \frac{1}{r_{i,i}}$. Due to the value of $\frac{1}{r_{i,i}}$ is equal to the value of $\frac{1}{\sqrt{{r_{i,i}}^2}}$, the value of $r_{i,i}^2$ is firstly calculated as Eq. 29

$${r_{1,1}}^2 = (a_{1,1})^2 + (a_{2,1})^2 + (a_{3,1})^2 + (a_{4,1})^2 \tag{29}$$

Then, the reciprocal square root (RSR) operation is used to obtain the value of $\frac{1}{\sqrt{{r_{i,i}}^2}}$ as follows

$$RSR\left({r_{1,1}}^2\right) = \frac{1}{\sqrt{{r_{1,1}}^2}} \tag{30}$$

Therefore, the value of $r_{1,1}$, the first column vector $\mathbf{q_1}$ of unitary matrix $\mathbf{Q}$ and the next iterative matrix $\mathbf{A^1}$ can be represented as follows

$$\begin{aligned}
q_{1,1} &= a_{1,1} \cdot RSR\left({r_{1,1}}^2\right), \\
q_{2,1} &= a_{2,1} \cdot RSR\left({r_{1,1}}^2\right), \\
q_{3,1} &= a_{3,1} \cdot RSR\left({r_{1,1}}^2\right), \\
q_{4,1} &= a_{4,1} \cdot RSR\left({r_{1,1}}^2\right), \\
r_{1,1} &= r_{1,1}^2 \cdot RSR\left({r_{1,1}}^2\right)
\end{aligned} \tag{31}$$

$$\begin{aligned}
\mathbf{a_1^1} &= 0 \\
\mathbf{a_2^1} &= \mathbf{a_2} - \mathbf{a_1^T a_2 a_1} \cdot RSR\left({r_{1,1}}^2\right) \cdot RSR\left({r_{1,1}}^2\right) \\
\mathbf{a_3^1} &= \mathbf{a}_3 - \mathbf{a_1^T a_3 a_1} \cdot RSR\left({r_{1,1}}^2\right) \cdot RSR\left({r_{1,1}}^2\right) \\
\mathbf{a_4^1} &= \mathbf{a_4} - \mathbf{a_1^T a_4 a_1} \cdot RSR\left({r_{1,1}}^2\right) \cdot RSR\left({r_{1,1}}^2\right)
\end{aligned} \tag{32}$$

The values of $r_{1,j}, 2 \leq j \leq 4$ can be obtained as the ILMGS method, and is presented in Eq. 17.

Similarly, to obtain the second row vector of upper triangular matrix $\mathbf{R}$ and the second column vector of unitary matrix $\mathbf{Q}$, the value of $r_{2,2}^2$ and $RSR(r_{2,2}^2)$ need to be obtained firstly as follows

$${r_{2,2}}^2 = \left(a_{1,2}^1\right)^2 + \left(a_{2,2}^1\right)^2 + \left(a_{3,2}^1\right)^2 + \left(a_{4,2}^1\right)^2 \tag{33}$$

$$RSR\left({r_{2,2}}^2\right) = \frac{1}{\sqrt{{r_{2,2}}^2}} \tag{34}$$

The second column vector $\mathbf{q_2}$ of unitary matrix $\mathbf{Q}$, the element $r_{2,2}$ and the next iterative matrix $\mathbf{A^2}$ can be calculated as follows

$$\begin{aligned}
q_{1,2} &= a_{1,2}^1 \cdot RSR\left({r_{2,2}}^2\right), \\
q_{2,2} &= a_{2,2}^1 \cdot RSR\left({r_{2,2}}^2\right), \\
q_{3,2} &= a_{3,2}^1 \cdot RSR\left({r_{2,2}}^2\right), \\
q_{4,2} &= a_{4,2}^1 \cdot RSR\left({r_{2,2}}^2\right), \\
r_{2,2} &= {r_{2,2}}^2 \cdot RSR\left({r_{2,2}}^2\right)
\end{aligned} \tag{35}$$

$$\begin{aligned}
\mathbf{a_1^2} &= 0 \\
\mathbf{a_2^2} &= 0 \\
\mathbf{a_3^2} &= \mathbf{a_3^1} - \mathbf{a_2^{1T} a_3^1 a_2^1} \cdot RSR\left({r_{2,2}}^2\right) \cdot RSR\left({r_{2,2}}^2\right) \\
\mathbf{a_4^2} &= \mathbf{a_4^1} - \mathbf{a_2^{1T} a_4^1 a_2^1} \cdot RSR\left({r_{2,2}}^2\right) \cdot RSR\left({r_{2,2}}^2\right)
\end{aligned} \tag{36}$$

The values of $r_{2,j}, 3 \leq j \leq 4$ can be obtained by Eq. 21.

Next, the values of $r_{3,3}^2$ and $RSR(r_{3,3}^2)$ are computed as Eqs. 37 and 38.

$${r_{3,3}}^2 = \left(a_{1,3}^2\right)^2 + \left(a_{2,3}^2\right)^2 + \left(a_{3,3}^2\right)^2 + \left(a_{4,3}^2\right)^2 \tag{37}$$

$$RSR\left({r_{3,3}}^2\right) = \frac{1}{\sqrt{{r_{3,3}}^2}} \tag{38}$$

The column vector $\mathbf{q_3}$, the elements $r_{3,3}$ and the next iterative matrix $\mathbf{A^3}$ can be computed as follows

$$\begin{aligned}
q_{1,3} &= a_{1,3}^2 \cdot RSR\left({r_{3,3}}^2\right), \\
q_{2,3} &= a_{2,3}^2 \cdot RSR\left({r_{3,3}}^2\right), \\
q_{3,3} &= a_{3,3}^2 \cdot RSR\left({r_{3,3}}^2\right), \\
q_{4,3} &= a_{4,3}^2 \cdot RSR\left({r_{3,3}}^2\right), \\
r_{3,3} &= {r_{3,3}}^2 \cdot RSR\left({r_{3,3}}^2\right)
\end{aligned} \tag{39}$$

$$\begin{aligned}
\mathbf{a_1^3} &= 0 \\
\mathbf{a_2^3} &= 0 \\
\mathbf{a_3^3} &= 0 \\
\mathbf{a_4^3} &= \mathbf{a_4^2} - \mathbf{a_3^{2T} a_4^2 a_3^2} \cdot RSR\left({r_{3,3}}^2\right) \cdot RSR\left({r_{3,3}}^2\right)
\end{aligned} \tag{40}$$

Finally, the values of ${r_{4,4}}^2$ and $RSR({r_{4,4}}^2)$ are shown as follows

$$ {r_{4,4}}^2 = \left(a_{1,4}^3\right)^2 + \left(a_{2,4}^3\right)^2 + \left(a_{3,4}^3\right)^2 + \left(a_{4,4}^3\right)^2 \tag{41} $$

$$ RSR\left({r_{4,4}}^2\right) = \frac{1}{\sqrt{{r_{4,4}}^2}} \tag{42} $$

Hence, the element $r_{4,4}$ and the fourth column vector $\mathbf{q_4}$ of $\mathbf{Q}$ can be get as Eq. 43

$$ \begin{aligned} q_{1,4} &= a_{1,4}^3 \cdot RSR\left({r_{4,4}}^2\right), \\ q_{2,4} &= a_{2,4}^3 \cdot RSR\left({r_{4,4}}^2\right), \\ q_{3,4} &= a_{3,4}^3 \cdot RSR\left({r_{4,4}}^2\right), \\ q_{4,4} &= a_{4,4}^3 \cdot RSR\left({r_{4,4}}^2\right), \\ r_{4,4} &= {r_{4,4}}^2 \cdot RSR\left({r_{4,4}}^2\right) \end{aligned} \tag{43} $$

To compute the value of $RSR(x)$, a NR based method is proposed in [19]. This method is made up of the following steps:

Firstly, $x$ should be scaled into the working range $wr = [0.5, 2]$ by Eq. 44. The value of $z$ is in the closed interval and $n$ represents the scaling factor. Therefore, the computation of $RSR(x)$ is converted to the computation of $RSR(z)$, and then de-scale the computation result by $\frac{1}{2^{\frac{n}{2}}}$.

$$ RSR(x) = \frac{1}{2^{\frac{n}{2}}\sqrt{\frac{x}{2^n}}} = \left(\frac{1}{2^{\frac{n}{2}}}\right)\left(\frac{1}{\sqrt{z}}\right) \tag{44} $$

Secondly, the piecewise polynomial approximation is used to compute the approximation result of $RSR(z)$ in the $wr$ range, that is shown as Eq. 45. Where $w_0$ is used to be the seed of the NR processing, and $a_i$ is the polynomial coefficients.

$$ w_0 = \sum_{i=0}^{2} a_i \cdot z_i \tag{45} $$

Thirdly, using the seed $(w_0)$ performs one iteration with the NR method as shown in Eq. 46.

$$ w_1 = \frac{w_0}{2}\left(3 - z{w_0}^2\right) \tag{46} $$

Finally, the value of $w_1$ should be de-scaled to the original data range by Eq. 47.

$$ RSR\left(x\right) = \left(\frac{1}{2^{\frac{n}{2}}}\right) w_1 \tag{47} $$

The aforementioned description is the proposed the MILMGS algorithm, which is completed by multiplier, adder and shifter. Compared to the existing MGS algorithm and the ILMGS algorithm, the proposed MILMGS algorithm eliminates the square-root and the division operations.

# 3 Hardware Architecture Design Based on the Proposed MILMGS Algorithm

The proposed MILMGS algorithm has been presented in Sect. 2.3. A new TSA architecture based on the proposed MILMGS for $4 \times 4$ real matrix will be presented in this section.

## 3.1 The TSA Architecture with MILMGS Algorithm

Figure 1 is the TSA hardware architecture based on the proposed MILMGS algorithm for the $4 \times 4$ real matrix. The designed architecture consists of four Block1, six Block2 and three Block3. Block1, Block2 and Block3 are the basic module to implement a basic operation. Block1 is used to calculate the value of $RSR({r_{i,i}}^2)$, $r_{i,i}$ and the column vector $\mathbf{q_i}$ of unitary matrix $\mathbf{Q}$. Block2 mainly computes the next iterative matrix by the current matrix and the value of $RSR({r_{i,i}}^2)$. Block3 is used to obtain the value of $r_{i,j}, i < j \leq 4$.

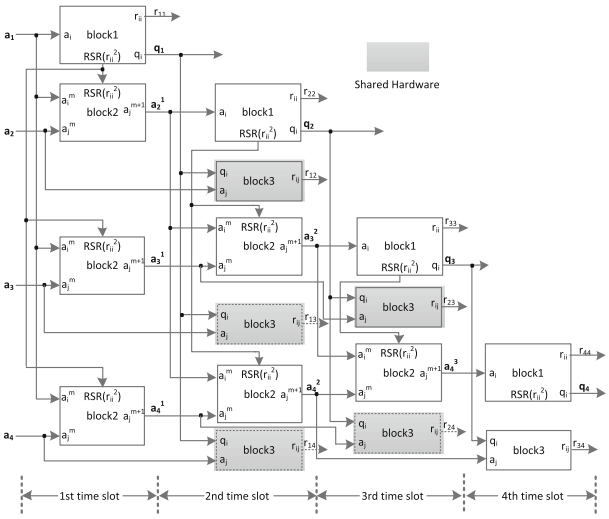


**Fig. 1.** The TSA architecture for $4 \times 4$ real matrix

The primary advantage of the TSA architecture is the simple and regular characteristic, and can easily implement high throughput. However, the TSA architecture needs more hardware overhead than the iterative architecture. As shown in Fig. 1, the hardware sharing technique is used to reduce the hardware overhead. In the second time slot, only one full pipelined Block3 is used to compute the value of $r_{1,j}, 2 \leq j \leq 4$. Similarly, in the third time slot, we use one full pipelined Block3 to compute $r_{2,3}$ and $r_{2,4}$.

### 3.2 The Basic Blocks

In this section, the detailed design of the basic blocks will be presented. Figure 2 is the hardware architecture of Block1, which is used to compute the value of $r_{i,i}$, $RSR({r_{i,i}}^2)$ and $\mathbf{q_i}$. Block1 contains the $RSR$ module, and the kernel of $RSR$ is shown in Fig. 3.

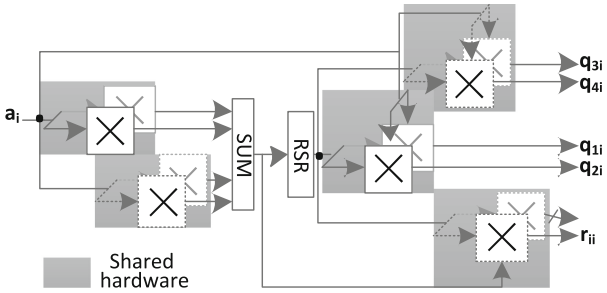


**Fig. 2.** The hardware architecture of Block1

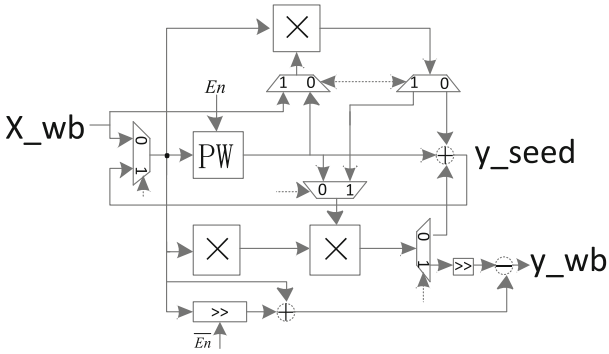


**Fig. 3.** The Kernel hardware architecture of RSR

The Fig. 3 shows that the designed $RSR$ hardware consists of three multipliers and five multiplexers. The processing latency and throughput are four clock cycles and three clock cycles respectively. Therefore, the hardware sharing technique is used to reduce the hardware overhead in the Block1, and the throughput of Block1 is also three clock cycles.

Figure 4 is the hardware architecture of Block2, which mainly consists five multipliers, three adders (module $SUM$ consists three adders), two subtractors. The aforementioned description shows that the throughput of $RSR$ is three clock cycles. Because we can obtain a new $RSR({r_{i,i}}^2)$ value every three clock cycles, the multipliers are shared in the designed Block2. The throughput of Block2 is also three clock cycles as the throughput of $RSR$ architecture.

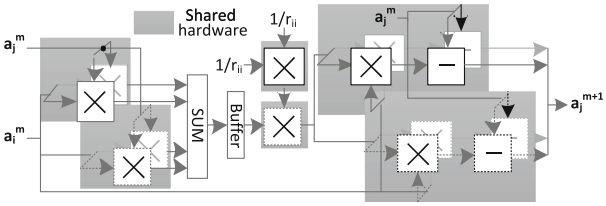


**Fig. 4.** The hardware architecture of Block2

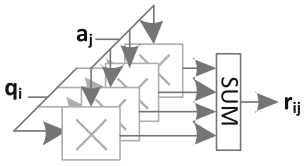


**Fig. 5.** The hardware architecture of Block3

Figure 5 shows the hardware architecture of Block3, which consists four multipliers and three adders (module $SUM$ consists three adders). The full pipelined architecture is used to design the Block3, hence, the Block3 can be shared in the TSA architecture, that is shown in Fig. 1.

## 4 Implementation Results and Comparisons

To verify the performance of the designed hardware architecture based on the MILMGS algorithm for $4 \times 4$ real matrix, the TSA hardware architecture shown in Fig. 1 is implemented in 0.13 µm CMOS technology. We will demonstrate the implementation results and some comparisons in the following.

The 16-bit word is used in our design. In order to choice the better fractional bits, we simulate the proposed MILMGS algorithm with various configurations in MATLAB. The mean error of upper triangular matrix $\mathbf{R}$ and the mean error of unitary matrix $\mathbf{Q}$ are presented in Figs. 6 and 7 respectively. The X-axle is the fractional bits of $RSR$ module, and curves represent the different fractional bits of data. According to the simulation results, the data format of $RSR$ module and the other modules are set to be one sign bit, two integer bits and thirteen fractional bits.

Table 1 shows the implementation results of the designed hardware architecture. To decompose a $4 \times 4$ real matrix, the designed hardware architecture needs 250.2 K gate count (GC). The critical path (CP) and throughput are 3.5 ns and 95.2 M/s respectively. The processing latency (PL) is defined as the number of clock cycles between the matrix feeding into the TSA architecture and the results outputting from the designed architecture. The PL of designed architecture is 53 clock cycles.

Compared to the existing hardware architectures based on the MGS algorithm [14] and the ILMGS algorithm [18], the designed hardware architecture based on the proposed MILMGS algorithm adopts the architecture of TSA,

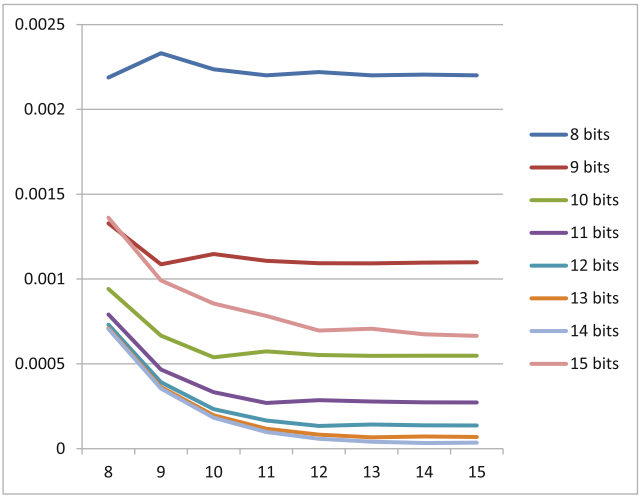


**Fig. 6.** The obtained **R** matrix performance by our designed hardware architecture versus word-length settings

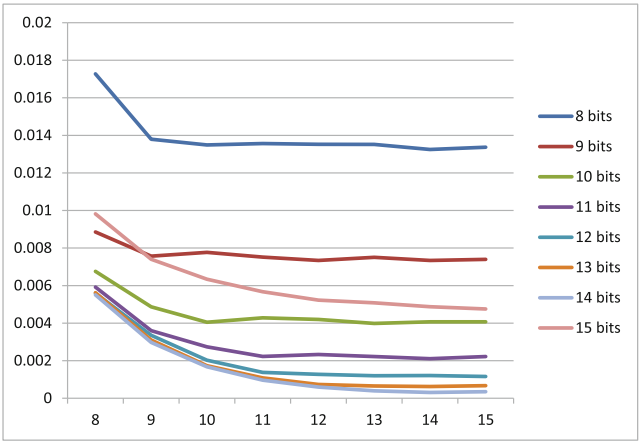


**Fig. 7.** The obtained **Q** matrix performance by our designed hardware architecture versus word-length settings

which is easy to implement higher throughput. Hence, the throughput of architecture designed in this paper is superior to the architecture designed in [14,18]. The drawback of TSA architecture is that it needs more area overhead than the iterative architecture, so our architecture needs more gate count than the architectures in [14,18]. Compared to the existing architectures proposed in [20,21], the throughput performance and the processing latency performance of our designed architecture are better. Moreover, the performance of gate count, throughput and processing latency are all better than the architectures designed in [22,23].

**Table 1.** Performance comparison of QRD.

| | Algorithm | Technology | Matrix size | WL | PL | GC | CP | Throughput |
|---|---|---|---|---|---|---|---|---|
| This work | MILMGS | 0.13 µm | Real 4 × 4 | 16 | 53 | 250.2 k | 3.5 ns | 95.2 M/s |
| Liu et al. [18] | ILMGS | 0.13 µm | Real 4 × 4 | 14 | 31 | 52.3 k | 1.5 ns | 21.5 M/s |
| Chang et al. [14] | MGS | 0.18 µm | Real 4 × 4 | 14 | 35 | 32.6 k | 2.5 ns | 11.4 M/s |
| Shabany et al. [20] | Hybrid | 0.13 µm | Complex 4 × 4 | 16 | 150 | 36 k | 3.6 ns | 6.95 M/s |
| Lin et al. [21] | GR | 0.18 µm | Complex 4 × 4 | 16 | 96 | 192.1 k | 5 ns | 25 M/s |
| Chen et al. [22] | GR | 90 nm | Complex 8 × 8 | 15 | – | 1098 k | 13.2 ns | 9.46 M/s |
| Zhang et al. [23] | CGRA | 65 nm | Complex 4 × 4 | 16 | – | 1055 k | 2 ns | 39.6 M/s |

## 5 Conclusion

QRD has been a vital component in the transceiver processor for the MU-MIMO wireless communication systems. This paper proposes a novel MILMGS algorithm based on the existing MGS algorithm and ILMGS algorithm for MIMO systems. To eliminate the square root and division operations, the NR algorithm is used in the proposed MILMGS algorithm. A TSA architecture based on the proposed MILMGS algorithm is also implemented in 0.13 µm CMOS technology. The results show that the designed architecture needs 250.2 gate count, the critical path and throughput are 3.5 ns and 95.2 M/s respectively. Compared to the architectures designed in [14,18,20–23], the throughput of our architecture is superior. Moreover, although only the hardware architecture for $4 \times 4$ real matrix is presented in this paper, the designed architecture is regular, and can be easily extended to the common size of MIMO wireless communication systems.

**Acknowledgments.** This work is supported by National Science Foundation of China (Grant No. 61170083) and Specialized Research Fund for the Doctoral Program of Higher Education (Grant No. 20114307110001).

## References

1. IEEE: IEEE standard for information technology– local and metropolitan area networks– specific requirements– part 11: Wireless LAN Medium Access Control (MAC) and physical layer (PHY) specifications amendment 6: Wireless access in vehicular environments. IEEE Std 802.11p-2010 (Amendment to IEEE Std 802.11-2007 as amended by IEEE Std 802.11k-2008, IEEE Std 802.11r-2008, IEEE Std 802.11y-2008, IEEE Std 802.11n-2009, and IEEE Std 802.11w-2009), pp. 1–51, July 2010
2. IEEE: IEEE standard for information technology - telecommunications and information exchange between systems - local and metropolitan area networks - specific requirements - part 11: Wireless LAN Medium Access Control (MAC) and physical layer (PHY) specifications amendment 5: Television white spaces (TVWS) operation. IEEE Std 802.11af-2013 (Amendment to IEEE Std 802.11-2012, as amended by IEEE Std 802.11ae-2012, IEEE Std 802.11aa-2012, IEEE Std 802.11ad-2012, and IEEE Std 802.11ac-2013), pp. 1–198, February 2014

3. IEEE: IEEE standard for local and metropolitan area networks part 16: air interface for broadband wireless access systems. IEEE Std 802.16-2009 (Revision of IEEE Std 802.16-2004), pp. 1–2080, May 2009
4. Acharya, J., Gao, L., Gaur, S.: Performance comparison of ZF-DPC to block diagonalization for quantized feedback. In: 2013 ASILOMAR Conference on Signals, Systems and Computers, pp. 1238–1242, November 2013
5. Li, H., Liu, S., Gudaitis, M.: Optimal interference pre-cancellation order in DPC-based broadcast and unicast hybrid network. In: 2013 47th Annual Conference on Information Sciences and Systems (CISS), pp. 1–6, March 2013
6. Costa, M.: Writing on dirty paper (corresp.). IEEE Trans. Inf. Theory **29**(3), 439–441 (1983)
7. Krikidis, I., Ottersten, B.: Diversity fairness in Tomlinson-Harashima Precoded multiuser MIMO through retransmission. IEEE Sig. Process. Lett. **20**(4), 375–378 (2013)
8. Tseng, F.-S., Wang, Y.-C., Hsu, C.-Y., Lin, S.-S.: Robust Tomlinson-Harashima Precoder design with random vector quantization in MIMO systems. IEEE Commun. Lett. **18**(2), 265–268 (2014)
9. Chen, C.-E., Cho, T.-W., Chung, W.-H.: Blockwise-lattice-reduction-aided Tomlinson-Harashima Precoder designs for MU-MIMO downlink communications with clusters of correlated users. IEEE Trans. Veh. Technol. **63**(3), 1146–1159 (2014)
10. Hwang, Y.-T., Chen, W.-D.: A low complexity complex QR factorization design for signal detection in MIMO OFDM systems. In: IEEE International Symposium on Circuits and Systems, ISCAS 2008, pp. 932–935, May 2008
11. Patel, D., Shabany, M., Gulak, P.: A low-complexity high-speed QR decomposition implementation for MIMO receivers. In: IEEE International Symposium on Circuits and Systems, ISCAS 2009, pp. 33–36, May 2009
12. Liu, T.H., Chiu, C.N., Liu, P.Y., Chu, Y.S.: Block-wise QR-decomposition for the layered and hybrid alamouti STBC MIMO systems: algorithms and hardware architectures. IEEE Trans. Sig. Process. **62**(18), 4737–4747 (2014)
13. Liu, C., Xing, Z., Yuan, L., Tang, C., Zhang, Y.: A novel architecture to eliminate bottlenecks in parallel tiled QRD algorithm for future MIMO systems. IEEE Trans. Circ. Syst. II Express Briefs **64**(1), 26–30 (2016)
14. Chang, R.-H., Lin, C.-H., Lin, K.-H., Huang, C.-L., Chen, F.-C.: Iterative QR decomposition architecture using the modified gram-schmidt algorithm for MIMO systems. IEEE Trans. Circuits Syst. I Regul. Pap. **57**(5), 1095–1102 (2010)
15. Singh, C., Prasad, S.H., Balsara, P.: VLSI architecture for matrix inversion using modified Gram-Schmidt based QR decomposition. In: 20th International Conference on VLSI Design, Held Jointly with 6th International Conference on Embedded Systems, pp. 836–841, January 2007
16. Lin, K.-H., Chang, R.-H., Lin, H.-L., Wu, C.-F.: Analysis and architecture design of a downlink M-Modification MC-CDMA system using the Tomlinson-Harashima precoding technique. IEEE Trans. Veh. Technol. **57**(3), 1387–1397 (2008)
17. Lin, K.-H., Lin, C.-H., Chang, R.-H., Huang, C.-L., Chen, F.-C.: Iterative QR decomposition architecture using the modified Gram-Schmidt algorithm. In: IEEE International Symposium on Circuits and Systems, ISCAS 2009, pp. 1409–1412, May 2009
18. Liu, C., Tang, C., Yuan, L., Xing, Z., Zhang, Y.: QR decomposition architecture using the iteration look-ahead modified Gram-Schmidt algorithm. IET Circuits Devices Syst. **10**(5), 402–409 (2016)

19. Pizano-Escalante, L., Parra-Michel, R., Castillo, J.V., Longoria-Gandara, O.: Fast bit-accurate reciprocal square root. Microprocess. Microsyst. **39**(2), 74–82 (2015)
20. Shabany, M., Patel, D., Gulak, P.: A low-latency low-power QR-decomposition ASIC implementation in 0.13 μm CMOS. IEEE Trans. Circuits Syst. I Regul. Pap. **60**(2), 327–340 (2013)
21. Lin, J.S., Hwang, Y.T., Fang, S.H., Chu, P.H.: Low-complexity high-throughput QR decomposition design for MIMO systems. IEEE Trans. Very Large Scale Integr. Syst. **23**(10), 2342–2346 (2015)
22. Chen, C.M., Lin, C.H., Tsai, P.Y.: Multi-mode sorted QR decomposition for $4 \times 4$ and $8 \times 8$ single-user/multi-user MIMO precoding. In: 2015 IEEE International Symposium on Circuits and Systems (ISCAS), pp. 2980–2983, May 2015
23. Zhang, C., Liu, L., Markovic, D., Owall, V.: A heterogeneous reconfigurable cell array for MIMO signal processing. IEEE Trans. Circuits Syst. I Regul. Pap. **62**(3), 733–742 (2015)

# Simulating and Analyzing the Effect of Timeliness on the Accuracy Rate of Central Path Planning

Dayong Song[1], Yanheng Liu[1], Jian Wang[1(✉)], Shaoqing Xu[2], and Lin Li[1]

[1] College of Computer Science and Technology, Jilin University, Changchun, China
songdy14@mails.jlu.edu.cn, {yhliu,wangjian591}@jlu.edu.cn,
lilynn1116@163.com

[2] Information and Communications Company of Jilin, State Grid, Changchun, China
jilinatm@foxmail.com

**Abstract.** Vehicular networks enable vehicles to realtimely upload states to the cloud-based Traffic Control Center (TCC) that then performs global optimized path planning and returns the planned result to the requester for improving traffic congestion. Since a large number of vehicles simultaneously send the path-planning requests to TCC, the TCC has to consume a non-negligible time delay to solve the multi-objective optimization problem in a highly dynamic graph with restrict to the temporal and spatial preferences. This paper aims to provide an overall assessment of the relation between timeliness and accuracy rate of central path planning. To this end, we view the path-planning delay as a variable and perform extensive simulations to analyze the difference of the accuracy rate, traveling time, and velocity between the planed optimal route and the ideal case without any time delay against various combinations of parameters, e.g., vehicle density, in-degree of destination, total number of intersections, and the distance length from the origin to destination.

**Keywords:** Vehicular networks · Central path planning · Delay

## 1 Introduction

Over the last few years, a substantial increase of vehicle number has seriously affects human lives and causes frequent traffic congestion and accidents, resulting in the low efficiency of transport and the exhaust emissions of pollutants. To address this issue, traffic efficiency improvement is becoming a main concern that scientific research institutions and government look forward to solve. As an important component of Intelligent Transportation Systems (ITS), the path planning system can provide vehicles multiple alternative routes to meet users' various trip preferences, e.g., the shortest distance, the travel-time priority, the gasoline-cost priority, and more others. The development of path planning system has facilitated to improve traffic efficiency and relieve traffic congestion.

Vehicular networks enable sensors to measure a road congestion level for the path planning purpose, and share the current congestion level and vehicles' states-e.g. location, velocity, and even the remaining battery with the Traffic Control Center (TCC) for


M. Huang et al. (Eds.): WICON 2016, LNICST 214, pp. 179–188, 2018.
https://doi.org/10.1007/978-3-319-72998-5_19

the realtime path planning service. As a result, TCC performs global optimized path planning and then feeds the latest planed path back to the vehicles to avoid the on-going congestion. Due to the ubiquitous clouding computing, it is envisioned that every vehicle initiates a path-planning request to the TCC at the origin and follows the decided route towards the destination. Such central path planning is expected to attain a global optimization prospect of traffic efficiency.

In spite of cloud-based TCC, whether or not the timeliness of path planning result can satisfy the users' demand is still not yet clear well. It can be anticipated that a large number of vehicles concurrently issue their navigation queries to TCC at the same time, and accompanying various temporal and spatial priority preferences. TCC has to exhaustively find a feasible global optimization solution for every requester according to the current vehicles' distribution over the map. Regarding such non-trivial workload challenge, though the TCC is equipped by cloud-computing capacity, it has to spend a non-negligible time delay, during which the requester has to stay at the place where it sent request, but the other vehicles are still under movement. This embarrassing situation may cause an inaccurate planned route decision. The inaccuracy extent depends on the time delay duration of path planning decision. If short, the planned route is possibly exactly same to the ideal result that corresponds to without any delay at all, otherwise may result in a completely different route. The total delay of the central path planning system includes the collection time, path planning time, and feedback time. By far, the cloud-based TCC has not been large-scalely deployed, so it is difficult to conduct real testing to explore the effect of time delay on the accuracy of the path planning results. It is necessary to use accurate models and large-scale trace dataset instead of the real testbed to carry out investigation. This paper does not differentiate the collection time, path planning time, and feedback time and treats the total delay as a variable. We employ the map of Cologne city and the mobility traces dataset to investigate the effect of delay on the accuracy rate, traveling time, and velocity against various combinations of parameters, e.g., vehicle density, in-degree of destination, total number of intersections, and the distance length from the origin to destination.

## 2 Related Work

Central path planning needs to process very large number of geospatial data. Cloud computing is now widely viewed as a promising paradigm for establishing future geoprocessing systems [1]. In recent years, some applications have developed prototypes of geospatial on cloud both in academia and in industry. Wang et al. [2] described a prototype for retrieving and indexing geospatial data developed for Google App Engine (GAE). Asavasuthirakul et al. [3] presented a novel methodology, called integrated GNSS (iGNSS) QoS prediction to provide a means for navigation applications to plan according to GNSS positioning quality. Karimi et al. [4] explored the feasibility of using GAE for a module in iGNSS QoS prediction. These studies provide a quality criterion of GNSS positioning for the path planning application.

To reduce the time delay of calculating the path planning results and as far as possible to obtain the optimal path planning results, Hiraishi et al. [5] proposed a dynamic route

finding method based on Time-Constrained Search (TCS) that finds a provably optimal solution within a specified time. Chakraborty et al. [6] proposed a GA based algorithm to find out simultaneously several alternate routes depending on different criterion according to driver's choice. Yousefi and Roghayeh [7] proposed a method that finds the paths with a combination of Divide and Conquer method and Ant Colony algorithm. In these work, the delay is impossible to avoid, so this paper is devoted to discussing the impact of delay on the accuracy rate of the path planning result.

## 3 System Model

Figure 1 demonstrates the workflow of central path planning system. (1) The requesting vehicle collects the current situated location at the origin using the mounted GPS. (2) The requester uploads the collected location information along with the destination coordinate to the TCC. (3) Upon receiving the path planning request, the TCC performs the global optimization path planning according to the current sensed traffic distribution and the requester's trip preference like distance priority and/or time priority. (4) The planned result is feed back to the requester that then follows the target route towards the destination.

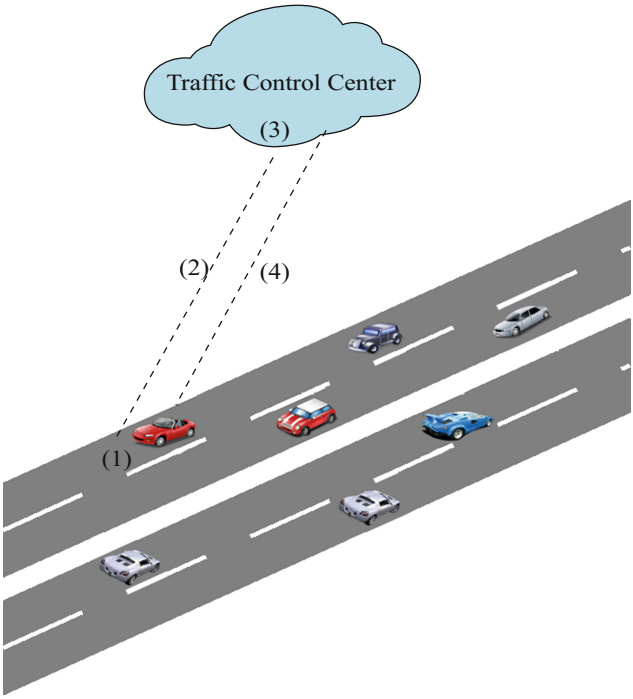


**Fig. 1.** Workflow of central path planning system

The road network can be viewed as a dynamic directional weighted graph $G$ consisting of a set of edges (road segments) $E$ and a set of vertexes (intersections, terminals, etc.) $V$. The weight $w_{ij}(t)$ of edge $e_{ij}$ at time $t$ is expressed by:

$$w_{ij}(t)=\alpha n_{ij}(t) + (1 - \alpha) l_{ij}. \quad (1)$$

where $n_{ij}(t)$ is the density of vehicles on road $e_{ij}$ at time $t$, $l_{ij}$ is the distance length of road $e_{ij}$, and the parameter α is the weight factor. Vehicle density $n_{ij}(t)$ and length $l_{ij}$ are normalized into range [0, 1]. In the simulations, the TCC adopts the Dijkstra algorithm to find the optimal route with the smallest weight sum at the time instant of the TCC receiving the requestor's request. The ideal route is defined as the planned result according to the snapshot of $G$ at the time instant of the requester sending the path planning request, i.e., there is no time delay. If the time delay present, the resulted $n_{ij}(t)$ and $l_{ij}$ may not equal the values at the time when the result is fed back to the requester. Therefore, we focus on the comparison of the optimal route and ideal route through the extensive simulations. We consider that the path planning result is accurate if the optimal and ideal routes are exactly the same, otherwise not.

## 4 Simulation

We employ the map dataset of Cologne from SUMO, which specifies the road net (such as the road origin, end point, cross-connection point and longitude, latitude of each node) of Cologne, and also indicates the vehicle mobility trace. According to the dataset, we can calculate the length $l_{ij}$ of each road segment. We run the dataset in SUMO and then collect the vehicles distribution in unit of seconds, i.e., the location coordinates and speed of all the vehicles are recorded in every second. Vehicle density $n_{ij}(t)$ can be obtained by the vehicles distribution. The weight factor α is set to 0.5 to calculate the weight $w_{ij}(t)$ of each road segment.

Figure 2 shows the effect of time delay on the average accuracy rate of the path planning results. The selected scope of the focused area from the dataset falls into a rectangle with vertex coordinates longitude (6.97, 7.00) and latitude (50.92, 50.95). This area contains 1024 edges and 520 vertexes. If the optimal route is exactly same to the ideal route, the accuracy count is added by 1 accordingly, otherwise not. The accuracy rate is the ratio of accuracy count to the total number of path planning requests. We randomly select 6 vertexes as the origins and 50 vertexes as the destinations from all the 520 vertexes. From Fig. 2, one can observe that the accuracy rate of the path planning results is indeed reduced as the delay increases.

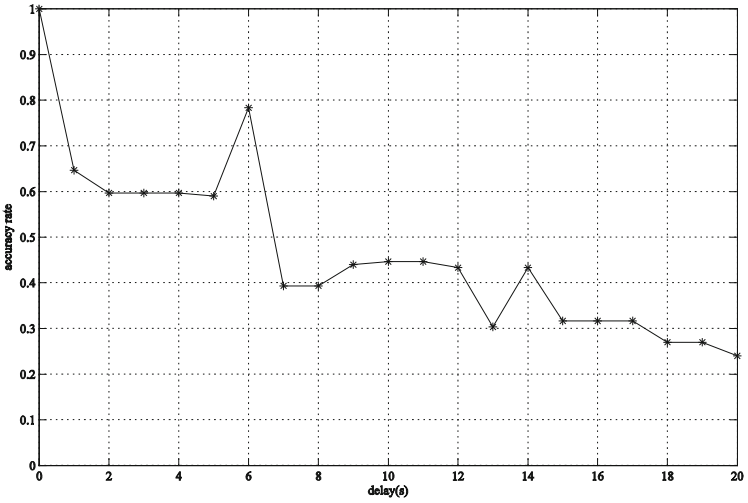


**Fig. 2.** Average accuracy rate of path planning results vs. delay

The vehicle density of the same road segment may be different in different time periods. Figure 3 shows the effect of vehicle density on the accuracy rate of the path planning results against the delay. We use Python to parse the road topology stored in the XML file and manually adjust the vehicle density spanning over three grades, i.e. sparse ($\leq$ 4vehicles/km), normal (5–8vehicles/km), and dense ($\geq$ 9vehicles/km). We still randomly select 6 vertexes as the origins and 50 vertexes as the destinations. From the results, one can learn that the accuracy rate of the path planning results is higher in the normal vehicle density than in the sparse and dense case.

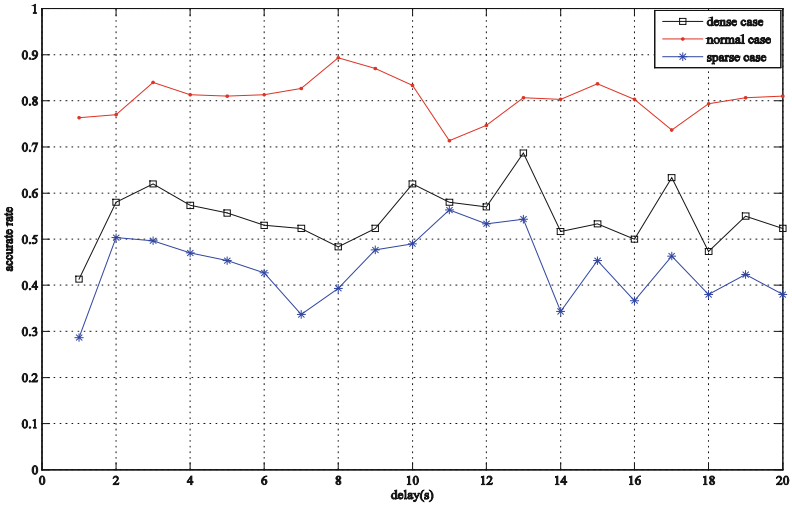


**Fig. 3.** Average accuracy rate of path planning results vs. vehicle density

Figure 4 shows the effect of the distance between the origin and destination on the accuracy rate of path planning results. The scope of the road map is focused on the rectangle with vertex coordinates at longitude (6.93, 6.97) and latitude (50.93, 50.97). We divide the area into nine-sub-area Sudoku (as shown in Fig. 5) and select the origin nodes within longitude (6.93, 6.943) and latitude (50.93, 50.943). The destination nodes of the first group simulation (i.e. the black line and red line) fall into the rectangle with vertexes at longitude [6.943, 6.956] and latitude (50.93, 50.943), and longitude [6.956, 6.97] and latitude (50.93, 50.943), respectively. The destinations of the second group (i.e. the purple line and blue line) are set within the rectangle with coordinates at longitude [6.943, 6.956] and latitude (50.943, 50.956), and longitude [6.956, 6.97] and latitude (50.956, 50.97), respectively. Figure 4 shows that the long travel distance between the origin and destination drops the accuracy rate and even more seriously as the delay increases, such as when the delay is greater than 5 s and 13 s.

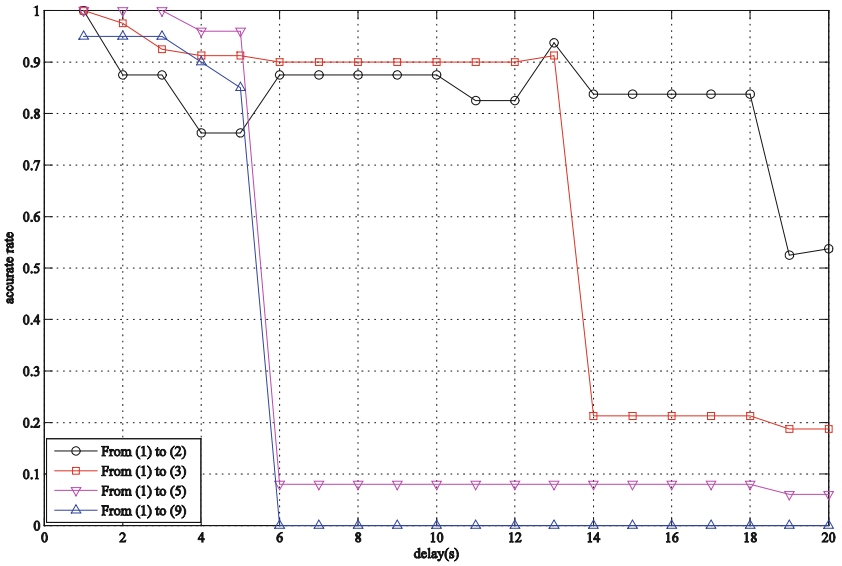


**Fig. 4.** Average accuracy rate of path planning results vs. travel distance

To explore how the destination's in-degree (i.e. the number of roads permitted to enter into the intersection) affects the accuracy rate, we find out some vertexes with in-degree 3 or 4 from Cologne map as the destination set. Vehicles start from the same origin (whatever the in-degree of start point is) towards a randomly selected destination. Figure 6 shows the effect of the destination in-degree on the average accuracy rate of path planning results against the delay, where we can observe that the larger the in-degree of the destination, the lower the accuracy rate.

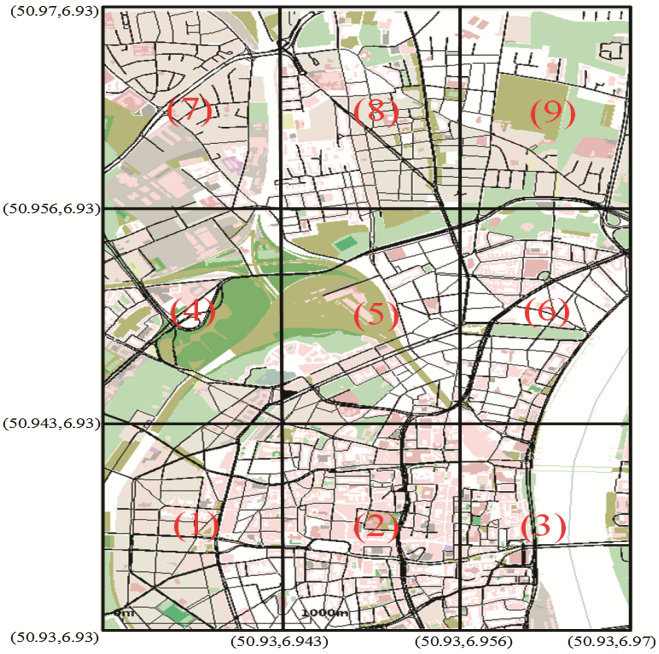


**Fig. 5.** Sudoku of simulation area

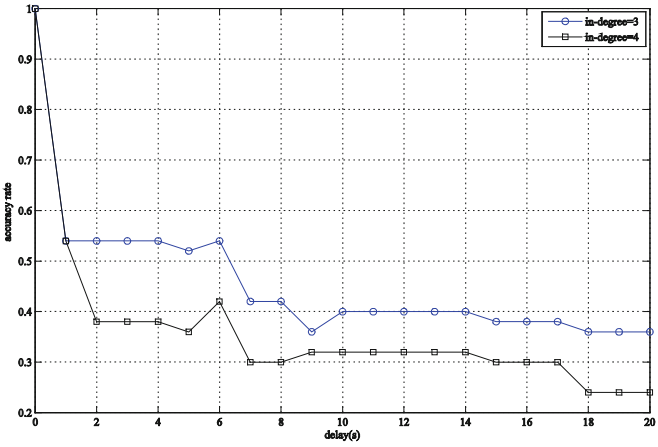


**Fig. 6.** Average accuracy rate of path planning results vs. in-degree of destination

Figure 7 shows the effect of the total number of intersections on the average accuracy rate of path planning results against the delay, where the more the number of intersections, the lower the accuracy rate. We imported the Cologne map into Cytoscape tool and manually removed the intersections on demand but ensured the graph connected, and thus resulting in a controllable intersection number.

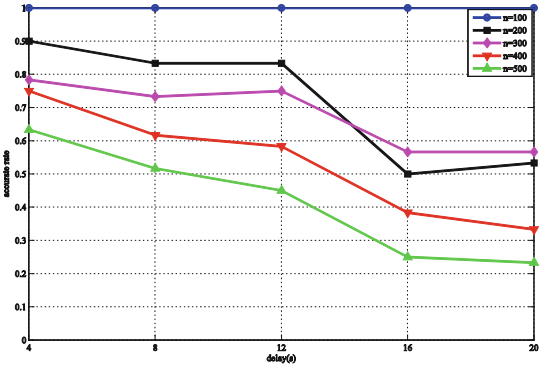


**Fig. 7.** Average accuracy rate of path planning results vs. intersection number

Figure 8 shows the effect of delay on the traveling time. We fixed the origin and destination of vehicles. In the case of considering delay, we calculate the ideal route then import the route into SUMO, and always make vehicles move along the planned route towards the same destination but against the different traffic distributions started at time 4 s, 8 s, 12 s, 16 s and 20 s, respectively, which corresponds to the same elapsed path planning delay. In the case of without delay, we employed the vehicles' distribution snapshot at time 4 s, 8 s, 12 s, 16 s, and 20 s to calculate the path planning results, and also respectively imported these results to SUMO to collect the corresponding traveling time. In Fig. 8, it can be seen that the path planning delay prolongs the average traveling time.

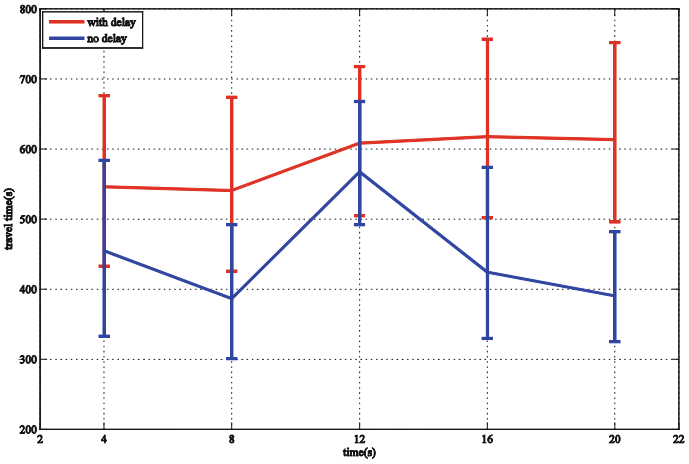


**Fig. 8.** The effect of delay on the travel time

Figure 9 uncovers the effect of delay on the travel velocity. It can be observed that the delay has little impact on the travel velocity. In Fig. 9b, the first vehicle reaching to

the destination is at time 361 s while 406 s in Fig. 9a, which is in accordance to Fig. 8, i.e. the delay poses the negative effect on the average traveling time.

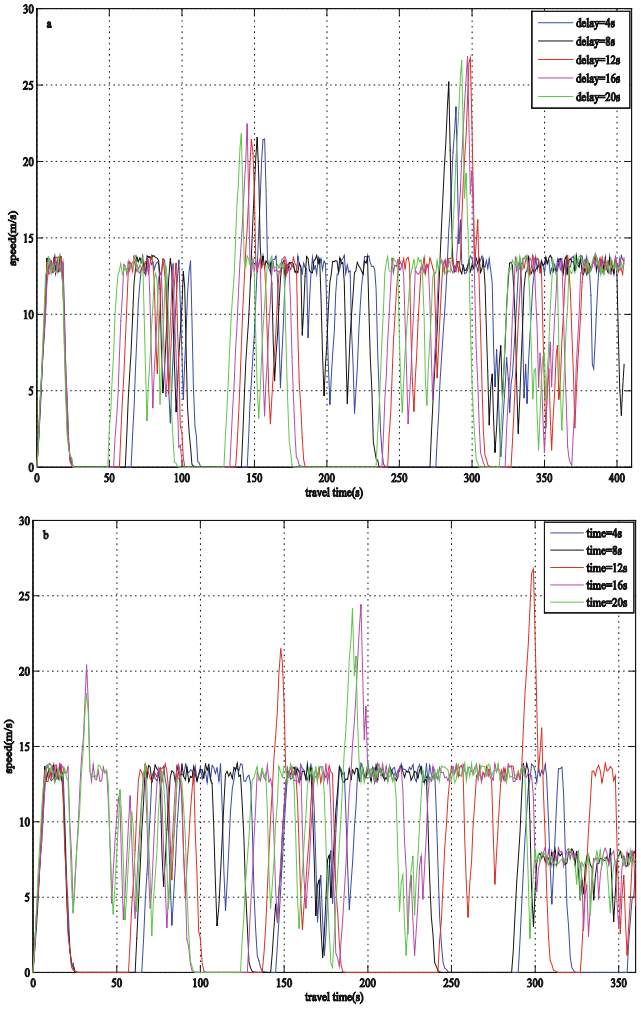


**Fig. 9.** The effect of delay on the travel speed

## 5 Conclusions

This paper investigated the effects of timeliness of the central path planning on the accuracy rate through simulating the global path planning using the dataset of Cologne and SUMO. We viewed the delay as a variable and uncovered the difference between the optimal route and ideal route with respect to the accuracy rate, travel time and velocity against various combinations of parameters, e.g., vehicle density, in-degree of

destination, total number of intersections, and the distance length from the origin to destination. The extensive simulations show that the delay indeed heavily affects the accuracy of path planning results, e.g., the sparse and dense vehicle density affects the accuracy rate more seriously than the normal case, the long distance between the origin and destination drops the accuracy rate, and the accuracy rate is low if the in-degree of the destination is large. The future work will be focused on the modeling of concrete delay generation process.

**Acknowledgments.** This work was supported by National Nature Science Foundation [61373123, 61572229]; International Scholar Exchange Fellowship (ISEF) program of Korea Foundation for Advanced Studies (KFAS); and Jilin Provincial International Cooperation Foundation [20140414008GH, 20150414004GH].

## References

1. Brauner, J., Foerster, T., Schaeffer, B., Baranski, B.: Towards a research agenda for geoprocessing services. In: 12th AGILE International Conference on Geographic Information Science, vol. 1, pp. 1–12. IKG, Leibniz University of Hanover, Hanover, Germany (2009)
2. Wang, Y., Wang, S., Zhou, D.: Retrieving and indexing spatial data in the cloud computing environment. In: Jaatun, M.G., Zhao, G., Rong, C. (eds.) CloudCom 2009. LNCS, vol. 5931, pp. 322–331. Springer, Heidelberg (2009). https://doi.org/10.1007/978-3-642-10665-1_29
3. Asavasuthirakul, D., Karimi, H.A.: Integrated GNSS QoS prediction for navigation services. In: Proceedings of the Sixth ACM SIGSPATIAL International Workshop on Computational Transportation Science, p. 73. ACM (2013)
4. Karimi, H.A., Roongpiboonsopit, D., Wang, H.: Exploring real-time geoprocessing in cloud computing: navigation services case study. Trans. GIS **15**(5), 613–633 (2011)
5. Hiraishi, H., Ohwada, H., Mizoguchi, F.: Intercommunicating car navigation system with dynamic route finding. In: 1999 Proceedings of the IEEE/IEEJ/JSAI International Conference on Intelligent Transportation Systems, pp. 284–289. IEEE (1999)
6. Chakraborty, B., Maeda, T., Chakraborty, G.: Multiobjective route selection for car navigation system using genetic algorithm. In: Proceedings of the 2005 IEEE Mid-Summer Workshop on Soft Computing in Industrial Applications, SMCia 2005, pp. 190–195. IEEE (2005)
7. Yousefi, P., Zamani, R.: The optimal routing of cars in the car navigation system by taking the combination of divide and conquer method and ant colony algorithm into consideration. Int. J. Mach. Learn. Comput. **3**(1), 44 (2013)

# An Optimization of DBN/GPU Speech Recognition on Wireless Network Applications

Weipeng Jing[1,2(✉)], Tao Jiang[1], and Yaqiu Liu[1]

[1] College of Information and Computer Engineering, Northeast Forestry University, Harbin, China
weipeng.jing@outlook.com, taojiang920619@outlook.com, yaqiuLiu@gmail.com
[2] Guangdong Provincial Key Laboratory of Petrochemical Equipment Fault Diagnosis, Maoming, China

**Abstract.** With the development of wireless networks and mobile computing, using speech recognition with wireless networks in mobile terminals to process data has become a new trend in mobile computing and achieved great success. Therefore, how to improve the speed of training speech recognition is still a problem worth studying. Using GPU to accelerate the training of speech recognition based on Deep Belief Network (DBN) has achieved great success, but there exits some problems. Aiming the problems that single GPU can not store huge parameters of DBM at one time and the unreasonable usage of GPU's memory model, we propose a new method in this paper. We divide the weight matrix into blocks, take the connections between visible units and hidden unit as threads and store the weight matrix into shared memory of GPU, establishing a reasonable memory model. Experimental results show that the optimized GPU implementation achieves 223 times and 1.5 times acceleration compared to single CPU and single GPU in Kaldi respectively, which demonstrate that our method can improve the DBN's training speed in mobile computing without GPU memory limitation.

**Keywords:** Wireless networks · Speech recognition · DBN · GPU Parallel computation · Mobile computing

## 1 Introduction

With the development of wireless networks and mobile network, 4G/5G mobile communications have got more and more attention, Internet of things and mobile computing [1] have also achieved great success in practical applications. Under these circumstances, it has been a trend that the speech signals are taken as inputting information, processed and transferred to others in mobile terminals' applications. So how to improve the training speed of speech recognition in mobile terminals with wireless networks has become one of important research topics in mobile computing. The Gauss Mixture Model and Hidden Markov Model (GMM-HMM) is used to make acoustic models in traditional speech recognition methods.


M. Huang et al. (Eds.): WICON 2016, LNICST 214, pp. 189–196, 2018.
https://doi.org/10.1007/978-3-319-72998-5_20

However, this model is a typical shallow learning structure, and its performance is limited under the massive data. Hinton [2] proposes the "depth learning" which points the training of the depth neural network could be completed by "layer-by-layer initialization", which is widely used in the field of speech recognition. Deep Belief Network (DBN), as a typical model of deep learning, can be trained quickly, so it is widely used in speech recognition and has achieved great success [3]. However the continuous increments of speech input signals in mobile terminals lead to spending a large amount of time on DBN's training. Therefore, how to improve the speed of DBN training under the massive data is an urgent problem that needs solving.

GPU has more powerful computing ability than CPU and has been applied into mobile terminals for mobile computing. Paprotski accelerates the speed of RBM's training by Compute Unified Device Architecture (CUDA) and by speeding up RBM's training to further accelerate DBN model's training speed has become a new trend [4]. The RBM is trained by function library of CuBLAS to accelerate in [5], but it is too versatile. Special kernels function is written in [6] to make full use of GPU computing resources, but its implementation is too complex and is not stably. Moreover, there are a large number of parameters in RBM model, which makes it be likely to occur the phenomenon that the single GPU can't store all the parameters one-time.

In summary, considering the problems that single GPU can't store all the parameters one-time and inefficient usage of memory model, in this paper, we propose a new GPU implementation of DBN to accelerate the speed of speech recognition with wireless networks in which we divide the weight matrix into many sub-weight matrixes, select appropriate GPU memory and further establish a reasonable memory model to store the trained parameters.

## 2 DBN Training

A DBN is a probability generation model, which is composed of several Restricted Boltzmann Machine (RBM) layers and a layer of Backpropagation (BP) neural network. The training process of DBN model in speech recognition mainly contains layer-wise greedy unsupervised learning as pre-training and supervised fine-tuning. The advantage of pre-training lies in that it can provide an effective initial training value to the DBN model; the significance of fine-tuning is that it can adjust the whole parameters of DBN which are calculated by pre-training, and gets the optimal value of DBN's parameters.

### 2.1 Pre-training of DBN

We use the Contrastive Divergence (CD) algorithm [7] to make unsupervised training for each layer of RBM to make sure that the training speech data's feature vectors are mapped to the different feature spaces.

A RBM is an energy-based generative model that consists of two layers: a layer of binary visible units and a layer of binary hidden units, with symmetrical connections. Any unit in one layer is connected to all units in the other layer and has no connection with units in the same layer. Since speech observations are sequential and real-valued,

we consider RBM's visible units obey Gaussian distribution and the hidden units obey Bernoulli distribution. Thus the energy of Gaussian-Bernoulli configuration is given by Eq. 1:

$$E(v,h) = \sum_{i=1}^{m} \frac{(v_i - a_i)^2}{2} - \sum_{i=1}^{n} h_j b_j - \sum_{i=1}^{m} \sum_{j=1}^{n} W_{ij} v_i h_j \tag{1}$$

where $v_i \in R^m$ represents the initial input value of speech data's features, $h_j \in R^n$ denotes the output value of speech data's extracted features. $\theta = \{W_{ij}, a_i, b_j\}$ is the parameters of the RBM. Considering RBM's special structure, the probability of $h_j$ given $v_i$ becomes

$$P(h_j = 1|v) = sigm\left(\sum_{i=1}^{m} W_{ij} v_i + b_j\right) \tag{2}$$

where $sigm()$ is the sigmoid function. Similarly given a specific hidden state $h_j$, the probability of $v_i$ given $h_j$ is:

$$P(v_i = 1|h) = sigm\left(\sum_{j=1}^{n} W_{ij} h_j + a_i\right) \tag{3}$$

In order to obtain the value of RBM's $\theta$, we could maximize the training data's likelihood function. So we use a much faster method: CD-k algorithm ($k = 1$) [7]. Here are the following update rules:

$$\Delta W_{ij} = \varepsilon\left(< v_i^{(0)}, h_j^{(0)} >, < v_i^{(k)}, h_j^{(k)} >\right) \tag{4}$$

$$\Delta a_i = \varepsilon\left(< v_i^{(0)} >, < v_i^{(k)} >\right) \tag{5}$$

$$\Delta b_j = \varepsilon\left(< h_j^{(0)} >, < h_j^{(k)} >\right) \tag{6}$$

where $\varepsilon$ is learning rate, $v_i^{(0)}$ represents the initial trained speech data's features, $h_j^{(0)}$ denotes the trained speech data's extracted features. $v_i^{(k)}$ and $h_j^{(k)}$ are the reconstructed trained speech data's features and reconstructed trained speech data's extracted features respectively which are obtained after k iterations of Gibbs sampling.

### 2.2 Fine-Tuning of DBN

We can get the initial value of the entire DBN model after the pre-training is completed. After the pre-training, we can do the progress of fine-tuning using the trained speech data in which each frame is labeled with a target class label. We divide the fine-tuning into two steps. Firstly, the speech data's features extracted from the last layer of RBM are taken as the input values of the BP neural network, and then the output values are

classified by the softmax function. Secondly, use the cross entropy [8] as the loss function and do the calculations with error Backpropagation algorithm, adjusting the parameters of the whole DBN model.

Because it needs a long time for BP algorithm to complete an update of $\theta$, we choose SGD algorithm. After completing the speech features' classification of a mini-batch, we update the $\theta$ directly using the calculated error to accelerate the speed of training DBN.

## 3 GPU Implementation

GPU has successfully applied in to speech recognition based on DBN. However, there are still some problems in using GPU. For example, existing methods usually ignore that the number of RBM's parameters is so large that a single GPU can not store them at one-time. The different type of memory in GPU has different access speed. Therefore, we implement the optimization of RBM's training using single GPU based on the memory model with sliced weight matrix that are from two aspects. Firstly, divide the weight matrix into sub-weight matrixes. Secondly, make full use of shared memory of GPU to establish reasonable memory model.

### 3.1 Division of Weight Matrix

We can improve the training speed of RBM by training the data with size of l (the number of mini-batch [9]), but there still exists a problem that the large size of l will hurt the overall efficiency of learning. So in the training process, the size of l we choose is much smaller than the m, n which are the dimensions of trained speech data's features $v_i \in R^{m \times l}$ and speech data's extracted features $h_j \in R^{n \times l}$ respectively. $v_i$, bias $a_i$, $h_j$ and bias $b_j$ are small so that they can store in the GPU device memory. However, the weight matrix is so large duo to interconnections between any two units, it is likely to occur the phenomenon the weight matrix can not store in GPU device at one-time. So we divided it into many sub-weight matrixes $W_i \in R^{m' \times n}$ where $m' << m$ such that every $W_i$ could be stored in the GPU device memory.

### 3.2 Memory Model Based on Shared Memory with Minimal Transfer

We copy the DBN model's parameters trained from CPU to GPU after having divided the weight matrix into sub-weight matrixes. According Eqs. 2 and 3, we calculate $h_j^0$ and $v_i^k$. When calculating $h_j^0$ with GPU, in order to hide the global memory latency, we need to use threads at a much finer granularity to take full use of the GPU computing resources. Hence, we take the connection $W_{ij} \in W_i$ as the smallest unit of computation which is called thread performing a function that multiples the $v_i$ by its weight. We can make every block represent a unit by this way. In other words, every block can be taken as a determined element of the speech data's extracted features and we can store the $W_i$ in the shared memory to make full use of the shared memory having faster access speed

to compute every thread's value, and sum up them with reduction process. Then, we calculate $h_j^0$.

As for the calculation of $v_i^k$, we also divide the weight matrix into $W_i$ and transferring $W_i$ one by one on demand. However, the transfer of $W_i$ would cost lots of time, we adopt a method that avoids the undesirable memory transfer of $W_i$. Because the calculation of $v_i^k$ and $h_j^0$ use the same $W_i$, we will calculate the $v_i^k$ immediately after the calculation the $v_i^k$. The order that $W_i$ stored in the shared memory (row-major or column) affects the calculation of $h_j^0$ and $v_i^k$.

We use the same method to get the calculation of $h_j^k$. After $h_j^k$ is finished, we also update $W_i$ immediately as the updating $W_i$ needs the corresponding $v_i^k$ and $h_j^k$ according Eq. 4. Also we know that the updating of $W_i$ needs $h_j^k$, $h_j^0$, $v_i^k$, $v_i$ matrices, if we adopt the same method above, the updating of $W_i$ could not be done in a coalesced manner and many blocks are trying to access to the same memory address at the same time, which could potentially lead to memory conflicts. So we propose a new way that each block processes several adjacent connections that require, to some degree, access the same elements of $h_j^k$, $h_j^0$, $v_i^k$, $v_i$ matrices to update $W_i$. We can copy the parameters for updating $W_i$ to the shared memory in each block for each sample, so that all the threads in one block could access them in a coalesced manner to update $W_i$ without memory conflicts.

## 4 Experimental Results and Analysis

We use TIMIT corpus in this paper. In the process of training, we use the method of early-stop [7]. The input data are the 440-dimensional speech features which are spliced by 40-dimensional fMLLR features. In the pre-training of DBN, we refer to the settings of the instance of TIMIT in Kaldi. We use the Intel(R) Xeon(R) CPU E5-2620 v2 @ 2.10 GHz with 128G memory, NVIDIA Teskla K20m with 5G device memory and speech recognition toolkit Kaldi in our experimental environment.

### 4.1 Training Time Spent on RBM

We did experiments to compare the training time spent on one iteration of RBM with the 440 visible units and different hidden units in three different ways. (1) the optimized GPU implementation with 1/4 memory usage and four streams (2) the method used with single GPU in [10] (3) the implementation of Kaldi with single GPU. In the following experiments the optimized GPU implementation is like (1). Figure 1 describes the results.

We can learn that the number of hidden units becomes larger, the cost time becomes much from Fig. 1. At first, the first way spends the most time because it need more time to exchange the weight matrix and streams synchronization. But with the increment of the number of hidden units, the first way costs less time than the others. The reason is that the first way uses reasonable memory model and streams process. The first way achieves acceleration with a maximum time of 1.7 than the third way when the number of hidden units is $2^{13}$.

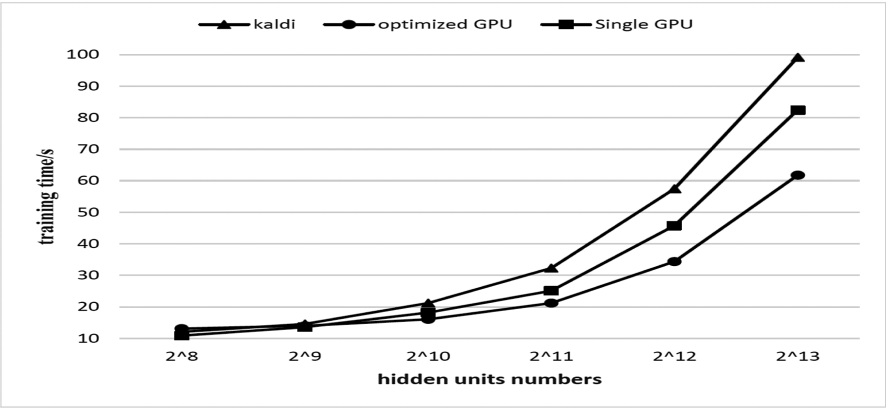


**Fig. 1.** One iteration of RBM's training time

### 4.2 Training Time and Word Error Rate Spent on DBN

We did experiments to compare the time spent on training DBN model using five different ways. (1) the implementation of Kaldi with single CPU (2) single GPU + CUDAC (3) the implementation of Kaldi with single GPU (4) the optimized GPU implementation. Table 1 lists the results.

**Table 1.** Training DBN's time

| Model | Time/h |
|---|---|
| Kaldi with single CPU | 372 |
| Single GPU + CUDAC | 3 |
| Kaldi with single GPU | 2.5 |
| Optimized GPU implementation | 1.67 |

From Table 1, the optimized GPU implementation could greatly reduce the time spent on training DBN model. It obtains accelerations of 1.5 times and 223 times than that using Kaldi with single GPU and single CPU respectively. It confirms that the optimized GPU implementation can achieve a better acceleration effect.

The word right rate is the factor that we must consider. So we did experiments to compare the DBN's word error rate with three different ways. (1) the implementation of Kaldi with single CPU (2) the implementation of Kaldi with single GPU (3) the optimized GPU implementation. Here is the word error rate of DBN model's training.

From Table 2, we know that the optimized GPU implementation could obtain better performance with only 5% performance loss comparing the Kaldi with single CPU. This is acceptable for us. It proves that the optimized GPU implementation could accelerate the training speed of DBN model, and remain a better word right rate.

**Table 2.** Training DBN's word error rate

| Model | Error rate |
|---|---|
| Kaldi with single CPU | 18.6% |
| Kaldi with single GPU | 18.8% |
| Optimized GPU implementation | 19.5% |

## 5 Conclusion

Applying the DBN model into the combination of speech recognition and wireless networks has achieved great success in mobile computing. In this paper, aiming at the problems huge parameters of DBN and unreasonable usage of GPU's memory model, we propose the memory model based on sliced weight matrix that could train large-scale DBN without parameters restriction and make full use of GPU's computing resources, making the GPU in mobile terminals to process more data with wireless networks. Results show that the optimized GPU implementation of DBN in mobile terminals for mobile computing not only can accelerate its training speed with large parameters, but also ensure the accuracy of the results.

**Acknowledgements.** The work described in this paper is supported by Guangdong Provincial Key Laboratory of Petrochemical Equipment Fault Diagnosis, Guangdong University of Petrochemical Technology (GDUPTKLAB201502) and Special Fund for Forest Scientific Research in the Public Welfare (201504307).

## References

1. Chen, W., Dong, S., et al.: Research on man-machine interaction of handheld mobile computing. Comput. Appl. **25**(10), 2219–2223 (2005)
2. Hinton, G.E., Salakhutdinov, R.: Reducing the dimensionality of data with neural networks. Science **313**(5786), 504–507 (2006)
3. Seide, F., Li, G., Yu, D.: Conversational speech transcription using context-dependent deep neural networks. In: 12th Conference of the International Speech Communication Association, Florence, pp. 437–440 (2011)
4. Ly, D.L., Paprotski, V.: Neural networks on GPUs: restricted Boltzmann machines. In: 9th International Conference on Machine Learning and Applications, Washington, pp. 307–312 (2010)
5. Raina, R., Madhavan, A., Ng, A.Y.: Large-scale deep unsupervised learning using graphics processors. In: 26th International Conference on Machine Learning, Montreal, pp. 873–880 (2009)
6. Lopes, N., Ribeiro, B.: Towards adaptive learning with improved convergence of deep belief networks on graphics processing units. Pattern Recogn. **47**(1), 114–127 (2014)
7. Hinton, G.E.: Training products of experts by minimizing contrastive divergence. Neural Comput. **14**(8), 1771–1800 (2002)
8. Li, X., Li, C.: Alternating update layers for DBN-DNN fast training method. Appl. Res. Comput. **33**(3), 843–847 (2016)

9. Zhu, Y., Zhang, Y., Pan, Y.: Large-scale restricted Boltzmann machines on single GPU. In: 2013 IEEE International Conference on Big Data, Santa Clara, pp. 169–174 (2013)
10. Xue, S., Song, Y., et al.: Fast training algorithm for deep neural network using multiple GPUs. J. Tsinghua Univ. (Sci. & Tech.) **53**(6), 745–748 (2013)

# Estimating End-to-End Available Bandwidth for Cyber-Physical Applications in Hybrid Networks

Hui Zhou[1,2], Chunyang Ye[1,2(✉)], Yucong Duan[1,2], Qi Qi[1,2], and Yu Zhang[1,2]

[1] State Key Laboratory of Marine Resource Utilization in the South China Sea, Hainan University, Haikou, China
{zhouhui,cyye,duanyucong,qqi,yuzhang2015}@hainu.edu.cn
[2] College of Information Science and Technology, Hainan University, Renmin Road No. 58, Haidian District, Haikou, China

**Abstract.** Available bandwidth estimation is very important for network operators, users, and bandwidth-sensitive applications. In the last 20 years, various techniques and systems have been proposed to estimate end-to-end available bandwidth. They were mostly tested in simulation or inside small-scale networks, but they can't consistently offer satisfying accuracy over the Internet. An active probing method SOProbe is proposed, and it measures end-to-end available bandwidth from only the installed host. The key idea of SOProbe is to identify the rate range where the available bandwidth resides. To archives this, SOProbe sends probe packets at selected transmission rates, and tries to catch the relationship between probe packets and available bandwidth.

**Keywords:** Active probe · Available bandwidth · Network measurement

## 1 Introduction

Mobile devices like iPhone and Android phones have become hugely popular, and widely used. Mobile Internet devices quickly spread over the world, their processing ability, built-in cameras, sensors, and pervasive cellular connections make them ideal platforms for constructing comprehensive cyber-physical applications. A cyber-physical application is a computer system that receives and responses to data from outside stimuli, and makes decisions that also impact the physical world [14].

Traditional cyber-physical applications include flight avionics, electronic medical devices, power grid control systems, and anything that can be managed by a remote computer through cable or wireless connection [5]. Cyber-physical applications can impact the real world and react to events, they always require strict quality and performance assurance. Mobile devices are equipped with a variety of sensors (such as ambient light sensors, gyroscope, accelerometers, GPS, microphones, and cameras) that cyber-physical applications use to measure environmental digitally. The combination of data from sensors with wireless networks and the growing data process power motivates more and more cyber-physical applications.


M. Huang et al. (Eds.): WICON 2016, LNICST 214, pp. 197–206, 2018.
https://doi.org/10.1007/978-3-319-72998-5_21

Though a lot of work has been done to make the operating environment of mobile devices seem to be like general computer, they are indeed different. A step further, mobile device push more rigid demand on their communicating capacity. First of all, bandwidth is always very spare. Second, cyber-physical systems tend to generate small-size IP packets. Third, short roundtrip time is preferred, thus packet replication, corruption, loss, and retransmission would largely affect the usage.

For many large-scale cyber-physical applications, the design is divided into three steps. First, application runs on mobile devices, e.g., iPhone or Android-based smart phone, connect to WIFI or the Internet through cellular network of ISP. Second, data packets traverse from ISP to server nodes located closed to the mobile devices, these nodes are generally named access servers. Third, a large amount of nodes hosted together to perform data-intensive computation, as well as to visit vast stored data. For load-balance and data replication, there are always many backup nodes spread over different racks, server rooms, or even cities.

Consequently, the performance bottleneck often exist between the second and the third steps. It is often the case that when mobile devices in a city all connect to a network node in another rack, or another server room, or even another city. It becomes crucial for the access servers to be intelligent to choose suitable nodes for performing data-intensive tasks.

This paper presents SOProbe, an original light-weight method that can quickly and precisely measures the end-to-end available bandwidth from the installed nodes. The key point of SOProbe is to identify a very narrow rate range of available bandwidth. As verified by our theoretical method, the dispersion of a long packet array will be enlarged only if the initial transmission rate is higher than available-bw. Therefore, SOProbe sends packet arrays at different initial transmit rates, and catches per-link dispersion of the arrays to estimate the relation between available bandwidth and the initial transmit rates. The efficiency and accuracy of SOProbe have been tested in carefully designed simulations.

This paper is organized as follows. Section 2 introduces the background. Section 3 presents the measurement methodology in details, and Sect. 4 sets up simulations to verify the accuracy and efficiency of SOProbe. Finally, Sect. 5 concludes the paper.

## 2 Related Work

Specifically, the available-bandwidth (available-bw) is defined as the maximum data rate that an end-to-end path can provide to a packet flow, without reducing the rate of the cross-traffic in the path [8]. Quite a few active probe techniques have been proposed. The first technique that tried to estimate available-bw was Cprobe [2]. Cprobe sends short arrays of ICMP echo packets to target host as close as possible, and calculates the obtained throughput from the head and the tail ICMP replies. The basic idea is that the time distance of a lengthy packet array is inversely proportional to available-bw.

However, Dovrolis proved that what the packet arrays catch is the asymptotic dispersion rate (ADR), instead of available-bw [8]. After Cprobe, quite a few methods that relied on both endpoints of a communication path were proposed. Delphi [12], for

example, estimate the volume of background traffic in network paths. However, since Delphi interprets queueing delays of all links as that of the bottleneck, it is not applicable in the presence of hidden bottleneck problem [16]. Because the initial transmit rate is adjusted according to the measurement result of previous probes, SOProbe is able to handle this problem when its bandwidth resolution is smaller than the bandwidth difference of the actual and fake bottleneck links.

A representational end-to-end available-bw estimation tool, i.e. Pathload, was introduced in [7], and was explained in [3]. Pathload doesn't simply report a number; instead, it outputs a rate range where available-bw would reside. In order to reduce the rate range, Pathload transmits packet arrays at different rates and watches their transmit delay at the other end of the path. Parallelly, SOProbe manipulates a rate range by probing a network path with packet arrays sent at selected data rates. But SOProbe is only installed on the source node, and it pay much more attention to the reverse path and router queuing effect.

A lot of techniques have also been presented to measure bandwidth with only the source node. However, these techniques mainly concentrated on measuring capacity, i.e. the physical communication rate of a link or a path, instead of available-bw. For example, pathchar [4], and the tailgating technique [1] measure per-hop link capacity. While Bprobe, nettimer, pathrate, and the PBM techniques catch path capacity [16]. In Parallel, Prasad demonstrated that layer-2 store-and-forward devices can strongly influence these methods [11]. But the layer-2 devices won't affect the accuracy of SOProbe since it relies on dispersion technique, instead of estimating delay.

Hu addressed the problem of bottleneck location and presented Pathneck [6]. Pathneck is based on the founding that background data interleave with probe packet arrays, thus changing the transmission time of packet array. By catching per-hop array transmission time, the location of bottleneck, and the narrowed rate of available-bw, can be inferred. The TTL configuration of packet array in SOProbe is similar to the recursive packet train adopted by Pathneck. However, SOProbe provides more accuracy since it can precisely control the inter-packet gap during estimation.

## 3 SOProbe Measurement Methodology

SOProbe is a single-end method and it uses the link congestion effect [16] in an iterative probing manner. SOProbe is built on the observation that, if a packet array is inserted into a network path at data rate $r_p$ that is higher than available-bw, communication time must be enlarged by some links along the path; if $r_p$ is not higher than available-bw, the communication time keep unchanged. As a result, by catching whether the path expands the packet arrays injected at selected rates, the available-bw can be computed.

The path is a sequence of store-and-forward links [16] that transfer packets from source host $R_0$ to destination host $R_n$ through a set of intermediate routers $R_1, R_2 \ldots R_{n-1}$. Link $L_i$ is the data connection from $R_i$ to $R_{i+1}$. Since, at any time, $L_i$ is either idle or forwarding packets at its capacity rate (maximum speed) $C_i$, its available-bw is defined as the spare bandwidth over a time interval $\tau$:

$$A_i(t, t+\tau) = \frac{1}{\tau}\int_t^{t+\tau} \left(C_i - \lambda_i(t)\right)dt \tag{1}$$

In (1), $A_i(t, t+\tau)$ is the available-bw of $L_i$ in the interval $(t, t+\tau)$, and $\lambda_i$ is the rate of cross-traffic in $L_i$. Particularly, the end-to-end available-bw is the path available-bw, and is also the minimum link available-bw of the path:

$$A(t, t+\tau) = \underset{i=0\ldots n-1}{Min}\left\{A_i(t, t+\tau)\right\} \tag{2}$$

Here, $\tau$ is the time taken by an estimation instance. The link that maintains the minimum link available-bw is the bottleneck link. From a specific instant, the source node sends out an array of $N$ packets to another node along a network path at data rate $r_p$. Every packet is of size $S$ and is equally spaced. Figure 1 shows the array as it traverses on $L_i$. $\Delta_i$ is the transmission time between the first and the last packets, the per-packet dispersion (PPD) in $L_i$ is

$$p_i = \frac{\Delta_i}{N(i)-1}(1 \le i \le n) \tag{3}$$

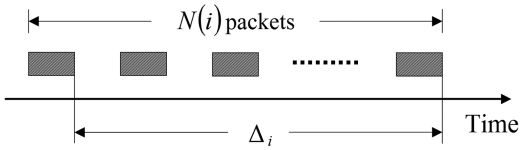


**Fig. 1.** A probing packet train on $L_i$.

Here, $N(i)$ is the number of packets that the array remains when it transmit on $L_i$. Then we have

$$\Delta p_i = p_i - p_{i-1}\,(1 < i \le n) \tag{4}$$

If $n = 1$, the path consists of one link. The path always keeps packet dispersion because PPD on the first link is also the PPD on the last link.

We focus on path effect when $n > 1$. Note that the source node can't send packets at rate higher than $A_i$, i.e. $r_p \le A_1$. As a result, $r_c^1 + r_p \le r_c^1 + A_1 = C_1$. Consequently, $L_1$ transmits all data packets without delay. This means that $r_c^1$ maintains unchanged since background traffic on $L_1$ is not affected by the probe packet array. Additionally, the background data on $L_2$ comes from $L_1$ and somewhere else; $r_c^2$ is unaffected because $r_c^1$ doesn't change and relative path features are regarded as fixed during a measurement instance.

It needs more attention to study how the packet array enters $L_2$ from $L_1$. In Average, in a $p_1$ period, one probe packet moves into $L_2$. Meanwhile, the amount of cross data packets entering $L_2$ is $X_2 = r_c^2 \cdot p_1$. As a result, the amount of packets that $L_2$ receives in one $p_1$ period is $S + X_2$. Since $r_p \le A$, we have $r_p \le A_2$ and

$$S + X_2 = \left(r_p + r_c^2\right) \cdot p_1 \le \left(A_2 + r_c^2\right) \cdot p_1 = C_2 \cdot p_1 \tag{5}$$

Therefore, $L_2$ is able to transmit all the packets from $R_1$ without the need of queue. So the rate of packet array remains $r_p$ as the array enters $L_2$, and $p_2 = p_1$, i.e. $\Delta p_2 = 0$. Meanwhile, the background traffic on both $L_2$ and $L_3$ isn't influenced by the probe packet array. Inductively, this can be proved in the subsequent links. Suppose $n > 2$, $\Delta p_i = 0$ for $i = 2, 3 \cdots k$ $(2 \le k \le n-1)$. The rate of probe array on $L_k$ is $r_p$; $r_c^k$ and $r_c^{k+1}$ are not affected by the probe array.

When the probe packet array moves in $L_{k+1}$ from $L_k$, only one probe packet moves into $L_{k+1}$ in a $p_k$ period. In average, the amount of background traffic goes into $L_{k+1}$ from $R_k$ in that $p_k$ period is $X_{k+1} = r_c^{i+1} \cdot p_k$. As a result, the total network amount that $L_{k+1}$ receives during $p_k$ period is $S + X_{k+1}$. By definition, $r_p \le A \le A_{k+1}$.

$$S + X_{k+1} = \left(r_p + r_c^{k+1}\right) \cdot p_k \le \left(A_{k+1} + r_c^{k+1}\right) \cdot p_k = C_{k+1} \cdot p_k \tag{6}$$

Therefore, all income packets can be delivered out by $L_{k+1}$ without being queued, $\Delta p_{k+1} = 0$ and the rate of probe array on $L_{k+1}$ is still $r_p$. In addition, $r_c^{k+1}$ and $r_c^{k+2}$ remain unchanged. Finally, we conclude that $\forall i \in (1, n]$, $\Delta p_i = 0$.

Because available-bw is the minimum link available-bw of the path and $r_p > A$, there is at least one link whose available-bw is lower than $r_p$. Precisely, a link is named *the first narrow link* if its available-bw is first less than $r_p$. Evidently, $L_1$ can't be the first narrow link since $r_p \le A_1$.

Assume that $L_2$ is the first narrow link, then $r_p > A_2$. As shown above, when the probe packet array moves from $L_1$ to $L_2$, the total amount of traffic that enters $L_2$ in a $p_1$ period is $S + X_2$, so

$$S + X_2 = \left(r_p + r_c^2\right) \cdot p_1 > \left(A_2 + r_c^2\right) \cdot p_1 = C_2 \cdot p_1 \tag{7}$$

This means that $L_2$ must take more time to deliver out the packets it receives in $p_1$. Consequently, internal queue is built up and the transmission time of probe array is enlarged. In average, $L_2$ expands the PPD to be

$$p_2 = \frac{S + X_2}{C_2} > p_1 \tag{8}$$

Therefore, $\Delta p_2 = p_2 - p_1 > 0$.

SOProbe uses binary search algorithm to identify the rate range. Initially, $R_{\min} = 0$ and $R_{\max} = A_1$. Since $r_p \le A_1$, $A_1$ is the maximum probe data rate that the source node can achieve. Suppose that the $n^{th}$ packet array is transmitted at rate $r_p(n)$, and the first probe rate $r_p(1) = A_1/2$.

If $r_p(n) > A$, then $R_{\max} = r_p(n)$
If $r_p(n) \le A$, then $R_{\min} = r_p(n)$

$$r_p(n+1) = \frac{(R_{\min} + R_{\max})}{2}$$

When $R_{\max} - R_{\min} \leq \delta$, the process finishes. Here, $\delta$ is the bandwidth resolution that indicates how small the estimated rate range could be. This process eventually converges to a rate range $[R_{\min}, R_{\max}]$ after probe the target path with $\log_2(A_1/\delta)$ different data rates.

To understand the relation between available-bw and probe data rate, the source node should be able to obtain PPD of its probe packet array. According to the ICMP protocol that is widely used by network infrastructure, we design a probe packet array that would trigger intermediate router replies. In particular, $N$ IP packets of size $S$ are equally spaced by $\Delta P$, and are sent to the destination at rate $r_p$. Obviously, $\Delta P = p_1$. $S$ and $\Delta P$ are carefully selected, and

$$r_p = \frac{S}{\Delta P} \tag{9}$$

Additionally, the time-to-live (TTL) parameters of probe packets are $\{1, 2 \cdots (n-1), n, n, (n-1) \cdots 2, 1\}$. Here, $n$ is the number of links and $N \geq 2{\cdot}n$. Setting TTL parameters in this way makes each intermediate router along the path response two ICMP packets back to the source. When the array moves to the first router ($R_1$), its first and last packets expire because their TTL parameters are 1. Consequently, these two packets are dropped and $R_1$ sends two ICMP packets back to the source [10]. The other probe packets of the train are forwarded to $R_2$ after their TTL are decremented by 1. Every subsequent router along the path repeats the above process (Fig. 2).

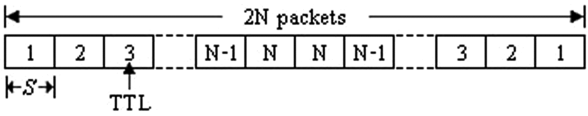


**Fig. 2.** Structure of the probing packet train.

As a result, each intermediate router sends back two ICMP packets. The source measure the interval between two ICMP packets from router $R_i$ to estimate $\Delta_i$, i.e. the dispersion of packet array in the incoming link of that router.

## 4 Simulation Verification

SOProbe have been tested in Network Simulator (NS) [9] - a widely used simulate platform. SOProbe was developed in the agent and application levels of NS. In real networks, it is the intermediate router that counts the TTL field of every incoming IP packet, decrements it and replies with ICMP error if the TTL expires. While in NS, it is the link that checks TTL and will drop the expired packets without any reply. To handle this problem, we implemented an application and attached it to every node except the

source node. This application sends 56-byte ICMP packet back to the source when it receives a probe packet. Therefore, the source directly sends packets to the ICMP application attached to a node if the source wants that node to send back ICMP replies.

Our experiment use a linear topology. In this topology, nodes 0 and 7 are the source and destination, nodes 1–6 are intermediate routers. $C_4$ (the $X$) is configured according to different use cases. All links are duplex; capacities of links are in the unit of bits per second. In addition, every link applies the drop-tail queueing principle. Table 1 lists parameters used in the experiment.

**Table 1.** Parameters used in the simulation

| Parameter | Description |
|---|---|
| $N$ | The number of packets in a train |
| $S$ | The packet size |
| $g$ | The PPD gauge parameter |
| $\delta$ | The bandwidth resolution |
| $\beta$ | The loss gauge parameter, and $\beta = 100\%$ |
| $u_t$ | The utilization of a path |

In experiments, one hop persistent (OHP) background traffic is applied to the path. Precisely, an OHP packet stream comes from four CBR sources, and will move out of the path after one link. Packets of each OHP traffic stream are carefully set as follows: 15% 576 bytes, 20% 1500 bytes, 50% 40 bytes and 15% randomly distributed between 40 and 1500 bytes, similar to the Internet packets measured in [13]. All link usage are equal. Here, $X = 10$ Mbps and the path is 40% utilized indicates that all links are 40% utilized, i.e. the background traffic on each link is {20, 32, 24, 4, 28, 8, 40 Mbps}. Precisely, there are two paths in Fig. 3: the forward path from node 0 to node 7, and the reverse one from node 7 back to node 0. What we are measuring is the forward path available-bw.

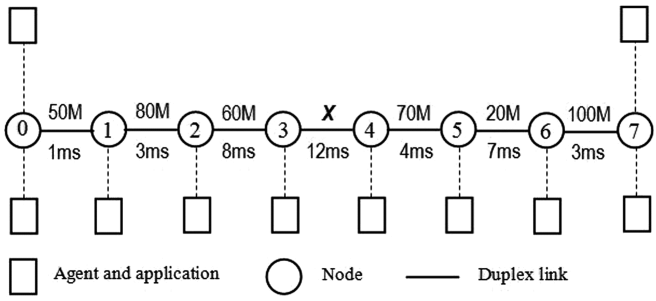


**Fig. 3.** Simulation topology.

We first demonstrate one SOProbe estimation process. Then we test SOProbe with bidirectional background traffic and different bottleneck link positions. The effect of

path features is also studied. After that, we record the convergence time that SOProbe process takes.

$X$ = 10 Mbps, all forward links are 20% usage, then available-bw is 8 Mbps. Figure 4 demonstrates a SOProbe measurement process that finishes after 6 probes. The initial rate range of available-bw is [0, 50 Mbps], and $r_p$ = 25 Mbps. SOProbe catches that $r_p > A$ because it detects PPD expansion. As a result, it shrink the rate range to [0, 25 Mbps] and generates the next probe packet array at 12.5 Mbps. PPD expansion is still there, so SOProbe decreases $r_p$ to 6.25 Mbps and tries again. This time, there isn't a PPD expansion; SOProbe sets the rate range to [6.25, 12.5 Mbps] and probes at 9.375 Mbps. Particularly, at the 6$^{th}$ probe, the range is [7.813, 9.375 Mbps], and $r_p$ = 8.594 Mbps. Once again, a PPD expansion is detected. After this, the range [7.813, 8.594 Mbps] is outputted because it meets the limit of bandwidth resolution ($\delta$ = 1 Mbps in this case).

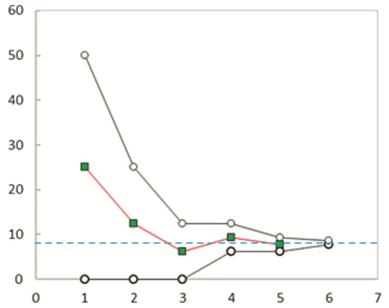


**Fig. 4.** A SOProbe measurement process.

$X$ = 10 Mbps, both forward and reverse paths are 20%, 40%, 60%, and 80% utilized, respectively. Figure 5 reports the rate ranges after performing 50 SOProbe measurements for the designed 16 cases. In the following simulations, SOProbe are executed 50 times for each setting. In particular, "FP $u_t = x\%$" means the forward path is $x\%$ utilized. In the same way, "RP $u_t = x\%$" denotes that every link of the reverse path is $x\%$ utilized.

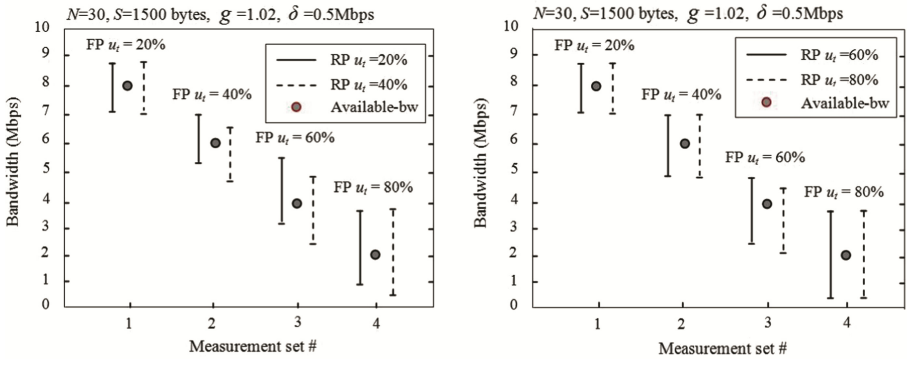


**Fig. 5.** Results under different loaded conditions, link utilization conditions.

The first founding is that background traffic in the forward path mainly determines the measurement accuracy. When the forward path was no more than 40% utilized, SOProbe reports rate ranges where available-bw nicely resides. As the forward path became more and more congested, SOProbe lost the accuracy slowly. Though the outputted range still includes the available-bw when forward path was 80% utilized, the range fluctuates and cover a comparably bigger region.

Another observation is that background traffic in reverse path influences the measurement accuracy lightly. When the forward path is underutilized ($u_t = 20\%$), the estimations are stable no matter how high is the traffic load in the reverse path. When forward path is 40% or 60% utilized, background traffic in the reverse path would affect the measurement. Finally, as the forward path comes to 80% utilized, background traffic in forward path dominates the measurement, and the influence of the reverse path traffic decreased.

The simulation reveals that a lengthy packet array of large network packets would interleave with the existing background traffic. Compared with probe packets (1500 bytes), ICMP packets (56 bytes) returned by nodes 1–7 are affected by background traffic slightly. SOProbe isn't sensitive to the background traffic in reverse path. Meanwhile, SOProbe can accurately estimate the available-bw when the forward path is not much loaded.

In the above experiments, the time taken by one SOProbe measurement highly depends on $N$ and $\delta$. The longer the packet array is, the more time that transmission requires. A smaller resolution parameter $\delta$ often leads to more probe tries. Every packet array is transmitted at a selected rate, different packet size would only result in the space in between packets. Analogously, parameter $g$ would affect the estimation accuracy, but it isn't relative to the number of probes that one estimation takes.

Table 2 shows that, one single SOProbe estimation instance uses nearly 2–3 s. In particular, all high estimation time occurred only when the forward path is overloaded. According to a research founding, the Internet path properties do not change much on the scale of hours [15], SOProbe can measure available-bw in a timely manner.

**Table 2.** Convergence time of SOProbe

| $N$ | $\delta$ (Mbps) | Convergence time (min, mean, max) (seconds) |
|---|---|---|
| 20 | 0.5 | 1.90, 2.02, 2.35 |
| 20 | 1.0 | 1.62, 1.77, 1.96 |
| 30 | 0.5 | 2.52, 2.83, 3.11 |
| 30 | 1.0 | 2.06, 2.40, 2.88 |

## 5 Conclusions

A novel active probe technique, SOProbe, was presented to estimate end-to-end available bandwidth from only the source node. With SOProbe, one can estimate available bandwidth from a single source, this enable smart devices and applications to estimate and select better network paths actively. The key idea of SOProbe and its working

process have been verified in NS simulation with carefully designed topology and comprehensive cross-traffic setting.

**Acknowledgments.** Our work is supported by National Natural Science Foundation of China under grant No. 61379047, 61562019, 61662019, 61662021, the Natural Science Foundation of Hainan Province under grant No. 20156223, the Major Science and Technology Project of Hainan Province under grant No. ZDKJ2016015.

## References

1. Allman, M., Paxson, V.: On estimating end-to-end network path properties. In: Proceedings of ACM SIGCOMM, pp. 263–274 (1999)
2. Carter, R., Crovella, M.: Measuring bottleneck link speed in packet-switched networks. Perform. Eval. **27**(28), 297–318 (1996)
3. Dovrolis, C., Ramanathan, P., Moore, D.: Packet dispersion techniques and a capacity estimation methodology. IEEE/ACM Trans. Netw. **12**, 963–977 (2004)
4. Downey, A.: Using pathchar to estimate internet link characteristics. In: Proceedings of ACM SIGCOMM, pp. 222–233 (1999)
5. Govindan, R., Minei, I., Kallahalla, M., Koley, B., Vahdat, A.: Evolve or die: high-availability design principles drawn from Googles network infrastructure. In: Proceedings of ACM SIGCOMM (2016)
6. Hu, N., Li, L.: Locating internet bottlenecks: algorithms, measurements, and implications. In: Proceedings of ACM SIGCOMM, pp. 41–54 (2004)
7. Jain, M., Dovrolis, C.: Pathload: a measurement tool for end-to-end available bandwidth. In: Proceedings of Passive and Active Measurements Workshop, pp. 14–25 (2002)
8. Jain, M., Dovrolis, C.: End-to-end available bandwidth: measurement methodology, dynamics, and relation with TCP throughput. IEEE/ACM Trans. Netw. **11**(4), 537–549 (2003)
9. Network Simulator. http://www.isi.edu/nsnam/ns/
10. Paxson, V.: End-to-end routing behavior in the internet. IEEE/ACM Trans. Netw. **5**(5), 601–615 (1997)
11. Prasad, R., Dovrolis, C., Mah, B.: The effect of layer-2 store-and-forward devices on per-hop capacity estimation. In: Proceedings of IEEE INFOCOM, pp. 243–254 (2003)
12. Ribeiro, V., Coates, M., Baraniuk, R.: Multifractal cross-traffic estimation. In: Proceedings of ITC Specialist Seminar IP Traffic Measurement, Modeling, and Management (2000)
13. Thompson, K., Miller, G., Wilder, R.: Wide-area internet traffic patterns and characteristics. IEEE Netw. **11**, 10–23 (1997)
14. White, J., Clarke, S., Groba, C., Dougherty, B., Thompson, C., Schmidt, D.: R&D challenges and solutions for mobile cyber-physical applications and supporting internet services. J. Internet Serv. Appl. **1**(1), 45–56 (2010)
15. Zhang, Y., Duffield, N.: On the constancy of Internet path properties. In: Proceedings of ACM (2001)
16. Zhou, H.: Measuring available bandwidth for smart cyber-physical applications. Tsinghua Sci. Technol. **16**, 601–610 (2011)

# Delay Aware Resource Allocation for Device-to-Device Communication Underlaying Cellular Networks

Heli Zhang[1(✉)], Wang Yang[1], Hong Ji[1], Xi Li[1], Victor C. M. Leung[2], and Lichao Yang[1]

[1] Beijing University of Posts and Telecommunications, Beijing, People's Republic of China
zhangheli@bupt.edu.cn
[2] The University of British Columbia, Vancouver, Canada

**Abstract.** Device-to-device (D2D) communications can bring significant performance improvement by allowing direct communications between users. Most of previous work usually focuses on the optimization of throughput, energy efficiency, offloading and so on. However, the delay performance of D2D users is less considered. In this paper, we formulate a resource allocation problem to maximize the system throughput while guarantying the delay performance for each user. The resource allocation is dynamic due to the consideration of both channel state and the queue length information. The optimization problem is a mixed integer non-linear programming problem and the solution space is large. Then in order to solve the problem with low complexity, we introduce particle swarm optimization algorithm to the resource allocation scheme. Various simulation results show that the throughput of the scheme is close to the global optimum and the delay performance for each user is guaranteed.

**Keywords:** Device-to-device communication · Resource allocation
Particle swarm optimization · Delay

## 1 Introduction

To accommodate the increasing traffic in future cellular systems, device-to-device (D2D) communications is a potential technology to achieve higher data rate and consume lower transmit power. Recently, D2D communications underlaying a cellular network infrastructure has been proposed and attracted much attention [1–3]. This hybrid infrastructure can bring several advantages such as higher system throughput, less network congestion and lower power consumption. However, in underlay mode D2D users share the same spectrum resources with regular cellular users. Sophisticated resource allocation for cellular and D2D users needs to be performed to protect cellular users and to achieve improved overall performance.

Much work has been done on resource allocation for D2D communications. Zhang et al. [4] propose a graph-based resource allocation method for cellular networks with underlay D2D communications which accounts for interference and capacity of the network. The simulation results show that the graph-based approach performs close to


M. Huang et al. (Eds.): WICON 2016, LNICST 214, pp. 207–217, 2018.
https://doi.org/10.1007/978-3-319-72998-5_22

the throughput-optimal resource allocation. The author of [5] considers the fair resource allocation problem for device-to-device communications in Orthogonal Frequency Division Multiple Access (OFDMA)-based wireless cellular networks. He proposes a two-phase solution approach where resource allocation for cellular downlink and uplink flows with max-min fairness is performed in the first phase and resource allocation for D2D flows with rate protection for cellular flows is conducted in the second phase. In [6–8], the authors propose simple interference avoidance mechanisms in OFDMA network, which commonly enables D2D users to reuse appropriate resource using resource allocation information of legacy users in control signaling. Marco et al. [9] propose a flexible resource reuse scheme incorporating mode selection and power allocation. It minimizes the overall power consumption, but not maximizes the system throughput. Yu et al. [10] propose to use Han-Kobayashi rate splitting techniques to improve the throughput of D2D communications. Xu et al. in [11] consider the sum-rate optimization in a single cell scenario with underlayed D2D communications. They adopt the iterative combinatorial auction game in their proposed spectrum resource allocation mechanism.

Although much work has been done on resource allocation, the delay factor is ignored. Since many services are real-time and delay-sensitive, for example, voice conversation, video streaming, and interactive gaming, it is important to take delay into account when designing the protocols and algorithms for D2D communications. Wang et al. [12] propose a low complexity practical solution to solve the delay-aware resource allocation problems for D2D communications by exploiting the interference filtering property of CSMA-like MAC protocols. Lei et al. [13] propose an optimization framework on delay-aware resource control with bursty traffic and formulate a general queuing model for performance evaluation and optimization. However, they still fail to pay attention to subchannel allocation with the consideration of delay performance.

In this paper, we study a delay based resource allocation problem for the OFDMA cellular network underplayed with D2D user pairs. The system throughput is maximized while the parameter of transmission delay is set as the constraint in the problem formulation. Considering the proposed problem is a mixed integer non-linear programming problem with high complexity, we present a resource allocation scheme based on particle swarm optimization (PSO). It can provides joint subchannel scheduling and simple power allocation for both cellular users and D2D users.

The remaining of this paper is organized as follows. Section 2 provides the system model considered in this paper and formulations of the optimization problem. In Sect. 3, we briefly introduce the standard particle swarm optimization and describe the PSO-based resource allocation scheme. We provide numerical results in Sect. 4 and draw conclusions in Sect. 5.

## 2 System Model

As is illustrated in Fig. 1, we consider the downlink transmission in an OFDMA single cell network where $K_1$ cellular users and $K_2$ D2D pairs share $N$ subchannels in underlay mode. The set of cellular users and D2D pairs are denoted as $C = \{c_1, c_2, \cdots, c_{K_1}\}$ and $D = \{d_1, d_2, \cdots, d_{K_2}\}$, respectively. Furthermore, we uniformly label cellular

users and D2D pairs with $k = 1, 2, \cdots, K$, where $K$ equals $K_1 + K_2$. Here D2D communications reuse the downlink resources of cellular network. We assume that the BS can get to know all downlink channel states information and thus it can allocate resources between users flexibly.

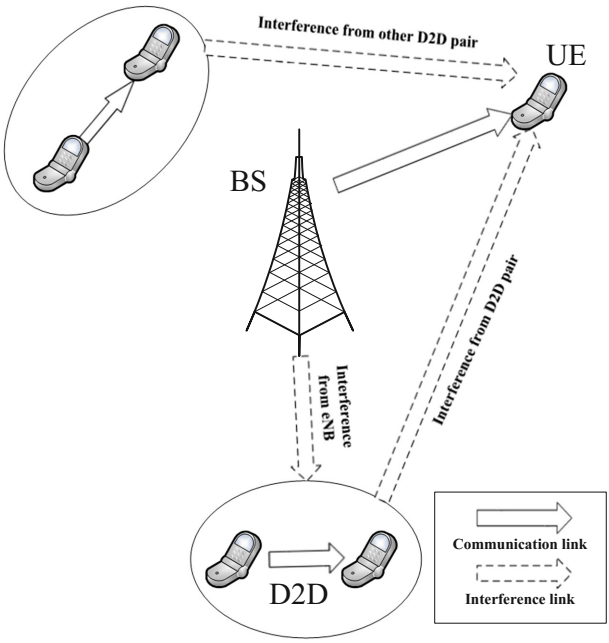


**Fig. 1.** System model

Let $x_k^n$ be a binary variable where $x_k^n = 1$ if subchannel $n$ is allocated for user $k$ and $x_k^n = 0$ otherwise. We assume that the BS has the maximum power budget of $P_{BS}^{\max}$, and meanwhile, the transmit power constraint of D2D users is $P_d^{\max}$. Denoting the transmit power of D2D pair $k$ on subchannel $n$ by $P_k^n$ and the transmission power allocated to cellular user $k$ on subchannel $n$ at the BS by $P_{BS}^n$. $g_{kk}^n$ and $g_{BSk}^n$ respectively represent the channel gain from the transmitter to the receiver of D2D pair $k$ on subchannel $n$ and the channel gain from the BS to cellular user $k$ on subchannel $n$. Then the SINR at cellular user $k$ or the receiver of D2D pair $k$ on subchannel n can be written as:

$$S_k^n = \begin{cases} \dfrac{P_{BS}^n g_{BSk}^n}{I_k^n + \sigma_k^n} \; k \in \mathrm{C} \\ \dfrac{P_k^n g_{kk}^n}{I_k^n + \sigma_k^n} \; k \in D \end{cases} \tag{1}$$

where $\sigma_k^n$ denotes the noise power and $I_k^n$ represents the interference power from other users on subchannel $n$. If a D2D pair occupies a subchannel which is assigned to a

cellular user, it will suffer interference from the BS. Cellular users will be interfered by D2D pairs which sharing the same subchannels with them. In general, channel capacity can be calculated by Shannon formula but can not be achieved in reality. So we use a factor $\Gamma(\Gamma \leq 1)$ represents the gap to the Shannon capacity. The transmission rate of cellular user $k$ or D2D pair $k$ on subchannel $n$ can be expressed as

$$r_k^n = B\log_2(1 + \Gamma S_k^n) \tag{2}$$

where $B$ is the bandwidth of subchannel $n$. For the sake of simplicity, we assume one subchannel only can be assigned to one D2D pair so that there will be no interference among D2D pairs. Let $l_k$ denote the queue length of cellular user $k$ or the transmitter of D2D pair $k$ and the arrival rate of packets is subject to Poisson distribution. Then we can formulate the resource allocation problem as follows:

$$\max \sum_k \sum_n x_k^n r_k^n \tag{3}$$

$$\text{s.t} \sum_{k \in C} x_k^n \leq 1, \forall n \tag{3.a}$$

$$\sum_{k \in D} x_k^n \leq 1, \forall n \tag{3.b}$$

$$x_k^n = \{0, 1\}, \forall n, k \tag{3.c}$$

$$\sum_n \sum_{k \in C} x_k^n P_{BS}^n \leq P_{BS}^{\max} \tag{3.d}$$

$$\sum_n x_k^n P_k^n \leq P_d^{\max}, \forall k \in D \tag{3.e}$$

$$\frac{l_k}{\sum_n x_k^n r_k^n} \leq D_k^{threshold}, \forall k \tag{3.f}$$

Our objective is to maximize the system throughput. Constraints (3.a) and (3.b) ensure that each subchannel can be allocated to at most one cellular user or one D2D pair. Function (3.c) indicates whether subchannel $n$ is allocated to cellular user or D2D pair $k$. Constraints (3.d) and (3.e) restrict the maximum transmission power of BS and the transmitter of D2D pair. Constraints (3.f) describes the delay threshold denoted by $D_k^{threshold}$ for every user. The optimization problem above is a mixed integer non-linear programming problem with a large solution space.

## 3 PSO-Based Resource Allocation Scheme

Particle Swarm Optimization is a stochastic population based optimization algorithm with inherent simplicity and high efficiency, so it has been a popular candidate for solving various complex optimization problems [14]. In basic PSO, the position of each particle represents a potential solution to the optimization problem, and an objective function is defined to evaluate the quality of the solutions. A swarm of S particles move around in a M-dimensional problem search space to look for the global optimum position that produces the best fitness of the objective function. In every iteration, every particle adjusts its velocity to follow the historical personal best position (denoted by $pbest_i$) and global best position (denoted by $gbest$) found so far in order to lead them to the best solution.

The velocity and position of particle $i$ are updated with the following equations:

$$\begin{aligned} v_i^m(t+1) = w \times v_i^m(t) + c_1 \times r_1 \times (pbest_i(t) - x_i^m(t)) \\ + \ c_2 \times r_2 \times (gbest(t) - x_i^m(t)) \end{aligned} \tag{4}$$

$$x_i^m(t+1) = x_i^m(t) + v_i^m(t+1) \tag{5}$$

The parameters, $x_i^m$ and $v_i^m$ represent the position and velocity of particle $i$ where $i = 1, 2, \cdots, S$ and $m = 1, 2, \cdots, M$. $c_1$ and $c_2$ are two positive constant named as learning factors, usually set as $c_1 = c_2 = 2$. $r_1$ and $r_2$ are random variables between $[0, 1]$. $w$ is an inertia weight factor that control the velocity of the particle.

The standard PSO is used to solve an optimization problem in a continuous solution space which is not appropriate for the delay based resource allocation in this paper. Under this context, we propose a PSO-based resource allocation scheme. The main issues are the way to represent particles that can map integer solutions onto continuous space and how to define the fitness function to evaluate the quality of particles with all that constraints.

The problem in Sect. 2 contains two parts including power allocation and subchannel allocation, respectively. To decouple the power allocation and subchannel allocation, we assume that the transmitters of D2D pairs and the BS allocate equal power to the subchannels, which is a simple and practical power allocation policy. Then we can merely consider the subchannel allocation without violate the constraints (3.d) and (3.e). As such, the representation of particles will just deal with indicator $x_k^n$, which has a discrete value. Of course we can use discrete PSO to solve the problem, but it is difficult to design a discrete PSO for such a problem. So we convert the problem into a continuous one.

We use a vector consisting of $2N$ real elements to denote the position of each particle, each element is between 0 and 1. The position of particle represents subchannel allocation for cellular users and D2D pairs. In this paper, we jointly allocate subchannels for cellular users and D2D pairs so that we can jointly optimize them to achieve better system performance than just dynamically allocate subchannels for D2D pairs when cellular users' subchannel allocation is fixed.

Thus there are two elements in the vector correspond to each subchannel. For $N$ subchannels and $S$ particles, the position of particle $i$ can be expressed as $\mathrm{X}_i = (x_i^1, x_i^2, \cdots, x_i^n, \cdots, x_i^N, x_i^{N+1}, x_i^{N+2}, \cdots, x_i^{N+n}, \cdots, x_i^{2N})$, $i = 1, 2, \cdots, S$. The two elements correspond to subchannel n are $x_i^n$ and $x_i^{N+n}$. The index of cellular user and D2D pair who gets subchannel n can be decoded by $x_i^n$ and $x_i^{N+n}$ respectively. To decode the vector, we divide $\mathrm{X}_i$ into two parts evenly, which are $(x_i^1, x_i^2, \cdots, x_i^n, \cdots, x_i^N)$ and $(x_i^{N+1}, x_i^{N+2}, \cdots, x_i^{N+n}, \cdots, x_i^{2N})$. Then the element of each part can be decoded into integers as follows:

$$D(x_i^n) = floor(x_i^n \times (K_1 + 1)),\ x_i^n \in (0, 1) \tag{6}$$

$$D(x_i^{N+n}) = floor(x_i^{N+n} \times (K_2 + 1)) + K_1 + 1,\ x_i^{N+n} \in (0, 1) \tag{7}$$

It is obvious that the values of $D(x_i^n)$ range from 0 to $K_1$ and the values of $D(x_i^{N+n})$ range from $K_1 + 1$ to $K_1 + K_2 + 1$. The values of $D(x_i^n)$ and $D(x_i^{N+n})$ means the index of cellular users and D2D pairs who is allocated subchannel $n$ while 0 and $K_1 + K_2 + 1$ indicate subchannel $n$ isn't allocated to cellular users and D2D pairs respectively.

After finding the way to represent particles and decode it into the result of subchannel allocation, the power allocation problem is solved by the BS and the transmitters of D2D pairs allocate their total power equally among the subchannels assigned to them. All the constraints except (3.f) are satisfied. So the resource allocation problem becomes maximizing the system throughput under constraint (3.f).

To transform a constrained problem into an unconstrained one, we import a penalty function. It is a technique to handle constrained problem by adding a penalty function to the objective function to cancel the constraint. The penalty function we defined can be expressed as:

$$Penalty = \sum_k \left[ \min\left(0, D_k^{threshold} - \frac{l_k}{\sum_n x_k^n r_k^n}\right)\right]^2 \tag{8}$$

Then the fitness function would be:

$$Fitness = \sum_k \sum_n x_k^n r_k^n - P \sum_k \left[ \min\left(0, D_k^{threshold} - \frac{l_k}{\sum_n x_k^n r_k^n}\right)\right]^2 \tag{9}$$

where $P \in R^+$ is a penalty factor. The penalty function is an important aspect to guide the particle to get out of the non-feasible region as soon as possible. As a feasible solution, the penalty function should equal 0 and the answer of fitness function is the solution to the resource allocation problem we proposed.

The PSO-based resource allocation scheme can be describe as follows:

PSO-based resource allocation scheme

**Initialization** Set the particles positions $x_i^m$ and velocities $v_i^m$ with random number between 0 and 1, and $pbest_i$ and $gbest$ with 0, $i = 1, 2, \cdots, S$ and $m = 1, 2, \cdots, 2N$.
**for** each iteration **do**
  **for** each particle **do**
    Update the velocity $v_i^m$ and the position $x_i^m$ according to (4) and (5).
    Decode the position $x_i^m$ of particle into $\mathrm{D}(x_i^m)$ according to (6) and (7).
    Calculate the power on each subchannel $P_k^n$ and $P_{BS}^n$.
    Calculate the fitness function according to (8) and (9).
    Update the personal best position $\mathrm{pbest}_i$ according to the value of fitness function.
  **end for**
  Update the global best position $\mathrm{gbest}$ according to the value of fitness function.
**end for**

## 4 Numerical Result

In this section, simulation results are provided to evaluate the performance of the proposed PSO-based resource allocation scheme. We consider a single cell OFDMA cellular network with a radius of R = 500 m. Cellular users and D2D pairs are distributed uniformly over the cell area, while the number of cellular users is 3 and the number of D2D pairs varies from 2 to 7. The distance-dependent path loss is modeled as $L(d) = 128.1 + 37.6 \log_{10} d$ for the links between BS to users and $L(d) = 148 + 40 \log_{10} d$ for the D2D links, where $d$ is distance in kilometers. The system bandwidth is 3 MHz and it is divided into 15 subchannels with equal bandwidth. The delay threshold of all users is set as $D_k^{threshold}$=100 ms. The transmit power of BS and UE is 36 dBm and 17 dBm respectively. Meanwhile, the noise power spectral density is set to be −174 dBm/Hz. Moreover, the parameters of the PSO algorithm are set as follows. The number of iterations $T = 1000$, the number of particles $S = 20$, two learning factors are set as $c_1 = c_2 = 2$, the inertia weight factor $w$ decreasing linearly from 0.95 to 0.4.

The PSO-based scheme is compared with traverse resource allocation scheme and random resource allocation scheme. The traverse scheme go through every kind of

resource allocation and select the one that can maximize the system throughput while each user's delay threshold is satisfied. The random scheme assign one subchannel to one user randomly until all subchannels are allocated, and it doesn't consider any constraint at all.

In Figs. 2 and 3, we respectively provide the system throughput and the average user delay of three schemes, while the number of D2D pairs increases from 2 to 7 and the distance between D2D transmitter and D2D receiver is set to 50 m. The system throughput of PSO-based scheme is a little lower than the traverse scheme, because the solution of traverse scheme is global optimum for considering every condition and the solution of PSO-based scheme is local optimum when the iteration number is limited. However, the complexity of traverse scheme is much higher than PSO-based scheme. So we sacrifice a little performance on system throughput to dramatically decrease the complexity of the scheme. Our target is to maximize the system throughput, so we already make full use of the system resources no matter what the number of D2D pairs is. Hence as the number of D2D pairs grows, the system throughput just grows a little bit. It is obvious that the system throughput and the average user delay of random scheme vary randomly and its performance is worse than other schemes because it has no mechanism to ensure the system performance.

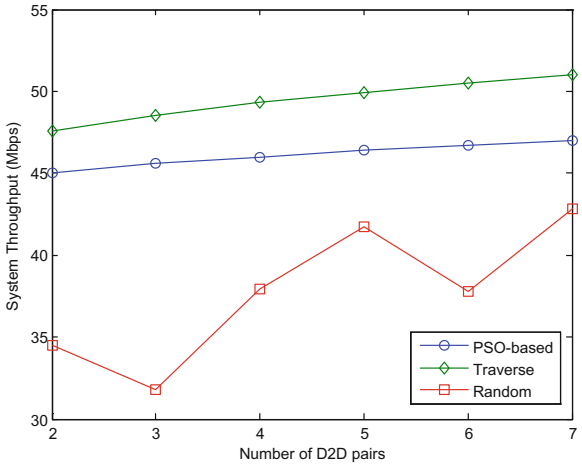


**Fig. 2.** System throughput versus number of D2D pairs

The average user delay of the PSO-based scheme and the traverse scheme are pretty close according to Fig. 3. Moreover, the average user delay increases with the number of D2D pairs because the resource for each user is less than before. There is one thing needs to be clarify. It is possible that not all users are allocated with subchannels while using the random scheme, especially when the number of D2D pairs grows. When a user isn't allocated with subchannels, the throughput would be zero and the delay would be infinite for this user. Then we wouldn't take the user into account when we calculate the system performance.

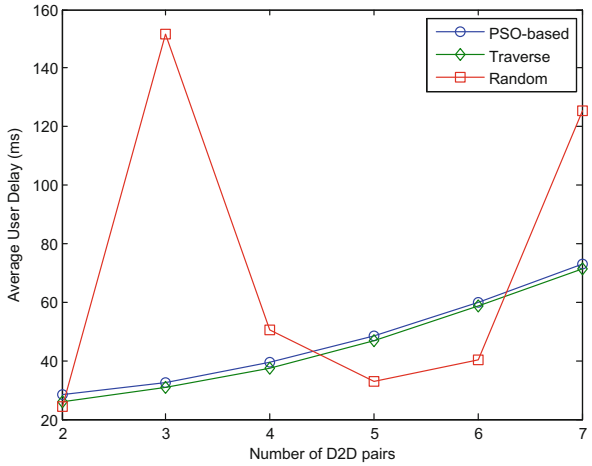


**Fig. 3.** Average user delay versus number of D2D pairs

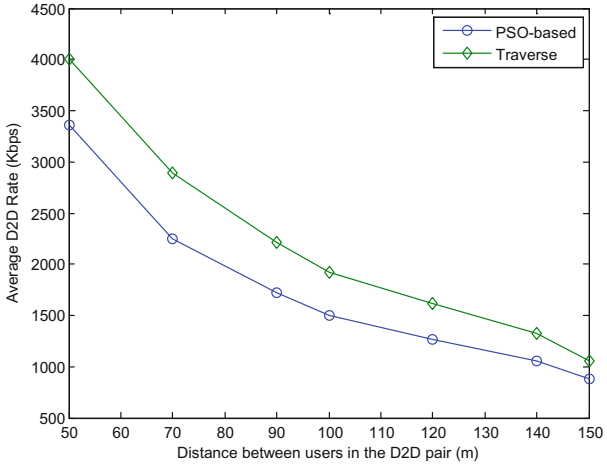


**Fig. 4.** Average D2D rate versus distance

Figures 4 and 5 illustrate the average rate and the average delay of D2D pairs versus the distance between users in the D2D pair, and the number of D2D pairs is set to 3. We don't consider the random scheme here because it has no certain pattern of changing. As the distance between users in the D2D pair grows, the average D2D rate decreases rapidly at first, then it becomes to decrease gently. When the distance is small, the channel condition between D2D users will be the best. In this case, our scheme schedules subchannels to the D2D pairs mostly to maximize the system throughput. However, as the distance between users in the D2D pair is getting larger, the average D2D rate is decreasing since the channel condition is getting worse. On the

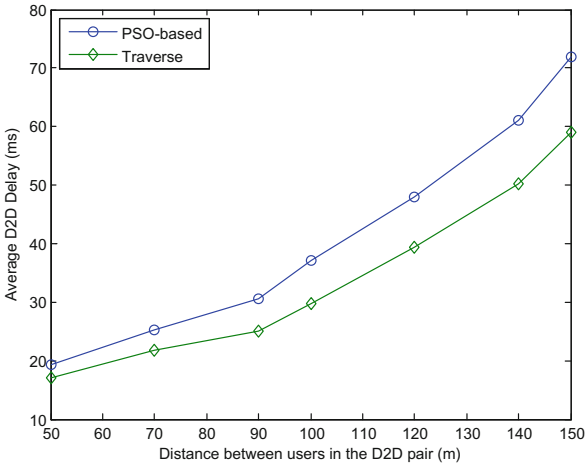


**Fig. 5.** Average D2D delay versus distance

other hand, every user has to satisfy the delay constraint, so the average D2D rate then becomes to decrease gently.

It is obvious that the average delay of D2D pairs increases with the distance. The difference of average delay between the PSO-based scheme and the traverse scheme is getting bigger when the distance grows, because the rate of D2D users is getting smaller.

## 5 Conclusion

In this paper, we develop the PSO-based scheme to maximize the system throughput for D2D communication underlay of cellular networks, which can jointly schedule the subchannels of cellular users and D2D pairs with the constraint of users' delay threshold. This scheme maps resource allocation solutions onto the representation of particles and construct a fitness function while handling constraints with penalty function. Through the simulation results, we have shown that the local optimum we get through the PSO-based scheme with low complexity is close to the global optimum on system performance. The result also show that the performance of D2D communications is highly affected by distance between users in D2D pairs.

## References

1. Lei, L., et al.: Operator controlled device-to-device communications in LTE-advanced networks. IEEE Wirel. Commun. **19**(3), 96–104 (2012)
2. Fodor, G., et al.: Design aspects of network assisted device-to-device communications. IEEE Commun. Mag. **50**(3), 170–177 (2012)

3. Wei, L., et al.: Enable device-to-device communications underlaying cellular networks: challenges and research aspects. IEEE Commun. Mag. **50**(3), 170–177 (2014)
4. Zhang, R., et al.: Interference-aware graph based resource sharing for device-to-device communications underlaying cellular networks. In: 2013 IEEE Wireless Communications and Networking Conference (WCNC), pp. 140–145. IEEE (2013)
5. Le, L.B.: Fair resource allocation for device-to-device communications in wireless cellular networks. In: 2012 IEEE Global Communications Conference (GLOBECOM). IEEE (2012)
6. Kim, H.-S., Na, J.-H., Cho, E.: Resource allocation policy to avoid interference between cellular and D2D Links/and D2D links in mobile networks. In: 2014 International Conference on Information Networking (ICOIN). IEEE (2014)
7. Guo, B., Sun, S., Gao, Q.: Downlink interference management for D2D communication underlying cellular networks. In: 2013 IEEE/CIC International Conference on Communications in China-Workshops (CIC/ICCC). IEEE (2013)
8. Xu, S., Wang, H., Chen, T.: Effective interference cancellation mechanisms for D2D communication in multi-cell cellular networks. In: 2012 IEEE 75th Vehicular Technology Conference (VTC Spring). IEEE (2012)
9. Belleschi, M., Fodor, G., Abrardo, A.: Performance analysis of a distributed resource allocation scheme for D2D communications. In: 2011 IEEE GLOBECOM Workshops (GC Wkshps). IEEE (2011)
10. Yu, C.-H., Tirkkonen, O.: Device-to-device underlay cellular network based on rate splitting. In: 2012 IEEE Wireless Communications and Networking Conference (WCNC). IEEE (2012)
11. Xu, C., et al.: Resource allocation using a reverse iterative combinatorial auction for device-to-device underlay cellular networks. In: 2012 IEEE Global Communications Conference (GLOBECOM). IEEE (2012)
12. Wang, W., Lau, V.K.N.: Delay-aware cross-layer design for device-to-device communications in future cellular systems. IEEE Commun. Mag. **52**(6), 133–139 (2014)
13. Lei, L., et al.: Resource control in network assisted device-to-device communications: solutions and challenges. IEEE Commun. Mag. **52**(6), 108–117 (2014)
14. Tsujimoto, T., et al.: A relationship between network topology and search performance of PSO. In: 2012 IEEE Congress on Evolutionary Computation (CEC). IEEE (2012)

# An Improved Dynamic Clustering Algorithm Based on Uplink Capacity Analysis in Ultra-Dense Network System

Jie Zeng(✉), Qi Zhang, Xin Su, and Liping Rong

Tsinghua National Laboratory for Information Science and Technology,
Research Institute of Information Technology,
Tsinghua University, Beijing, China
zengjie@tsinghua.edu.cn

**Abstract.** The Ultra-Dense Network (UDN) system is considered as a promising technology in the future wireless communication. Different from the existing heterogeneous network, UDN has a smaller cell radius and a new network structure. The core concept of UDN is to deploy the Low Power Base Stations (LPBSs). With denser cells, the interference scenario is even severer in UDN than Long Term Evolution (LTE) heterogeneous network. Clustering cooperation should reduce interference among the cells. In this paper, we firstly derive the total uplink capacity of the whole system. Then we present a novel dynamic clustering algorithm. The objective of this algorithm for densely deployed small cell network is to make a better tradeoff between the system performance and complexity, while overcome the inter-Mobile Station (MS) interference. Simulation results show that our approach yields significant capacity gains when compared with some proposed clustering algorithms.

**Keywords:** Ultra-Dense Network · Uplink capacity
Dynamic clustering algorithm

## 1 Introduction

Fueled by the popularization of smart devices, wireless traffic experienced an exponential growth in recent years. The explosive growth of mobile data traffic these years puts forward high requirements for the bandwidth and performance of coverage and capacity of the 5th generation (5G) networks, such as ultra-high traffic volume density and ultrahigh peak data rate [1]. It is expected [2] that the growth will reach 1000-times by 2020 which is often regarded as the start of the time frame for future generation wireless network. Generally speaking, capacity enhancement can be realized in three ways, i.e. spectrum efficiency improvement, wider bandwidth and cell densification [3]. To deal with this growth rate, the Ultra-Dense Network (UDN) system is considered as a promising technology in the future wireless communication. UDN is viewed as one of the key technologies for 5G [4]. Different from the existing heterogeneous network, UDN has a smaller cell radius and a new network structure. The core concept of UDN is to deploy the Low Power Base Stations (LPBSs). In recent years, UDN attracts many researchers in colleges and workers in industries. Both the industry and academia are


M. Huang et al. (Eds.): WICON 2016, LNICST 214, pp. 218–227, 2018.
https://doi.org/10.1007/978-3-319-72998-5_23

working together, e.g. Mobile and wireless communications Enablers for 2020 Information Society and 5th Generation Non-Orthogonal Waveforms (5GNOW), to meet the capacity demand of the 5G mobile communication systems [2, 5].

With denser cells, the interference scenario is even severer in UDN than Long Term Evolution (LTE) heterogeneous network. This is because the smaller distance between LPBSs. Clustering cooperation should reduce interference among the cells. There have been some researches about cell clustering schemes in UDN. Recently, [6] employs Macro-Diversity-Coordinated Multipoint (MD-CoMP) to deal with the serious inter-Mobile Station (MS) interference and solves the joint optimization problem that is approximated by two sub-problems, i.e. clustering based on load information using game theory and inter-cell resource allocation based graph-coloring algorithms. Thus a Two-Step Joint Clustering and Scheduling (TS-JCS) scheme is proposed in [6]. [7] proposes a graph-based low complexity dynamic clustering algorithm. The key idea in [7] is that dividing the UDN into some clusters under size constraint, the maximum intra-cluster interference and minimum inter-cluster interference. [8] draws attention to the realistic scenario of randomly distributed Femtocell Access Points (FAPs) in heterogeneous networks and proposes a clustering approach combined with an active FAP selection algorithm to boost both spectral and energy efficiency without manual configuration. [9] presents a modified K-means clustering algorithm to maximize the sum throughput and proposes a two stage resource management scheme to solve this problem. Focusing on UDN scenario, [10] gives a definition of cell cluster and designs new synchronization signals. Moreover, a new cell clustering scheme based on the redesigned signals is presented in [10]. [11] proposes a user scheduling algorithm to gauge the performance gain of semi-static clustering and demonstrates the gain of semi-static clustering in the non-asymptotic regime.

This paper aims to make a better tradeoff between the system performance and complexity for uplink transmission with dynamic clustering approach in UDN. In this paper, the following tasks are completed: we firstly derive the total uplink capacity of the whole system. Then we present a novel dynamic clustering algorithm. The objective of this algorithm for densely deployed small cell network is to improve the total uplink capacity, while overcoming the inter-Mobile Station (MS) interference. Simulation results show that our approach yields significant capacity gains when compared with some proposed clustering algorithms.

The remainder of this paper is organized as follows: In Sect. 2, we present the system model of UDN with multi-user environment and derive the total uplink capacity of the whole system. In Sect. 3, some existing clustering algorithms are described and a novel dynamic clustering algorithm is presented. We provide simulation results in Sect. 4. Finally, conclusions are provided in Sect. 5.

The notation adopted in this paper conforms to the following convention. Column vectors are denoted in lowercase boldface: $\boldsymbol{x}$. Matrices are denoted in uppercase boldface: $\boldsymbol{A}$. $\boldsymbol{I_k}$ denotes the identity matrix of size $k \times k$. $(\cdot)^T$ and $(\cdot)^H$ represent the transpose and conjugate transpose matrix respectively. $\det(\boldsymbol{A})$ denotes the determinant of $\boldsymbol{A}$. The operator $E(\cdot)$ denotes expectation.

## 2 System Model

We consider the uplink transmission in UDN with $M$ MSs and $N$ LPBSs. The LPBSs are very dense in UDN, so both MS and LPBS are equipped with a single antenna here. In the UDN system, we assume that LPBS serves the MS which is the nearest to the LPBSs and one MS can be served by several LPBSs. As shown in Fig. 1, MSs uniformly and randomly are distributed in the area and LPBSs are grid-point distribution. Also the number of MSs must be no larger than the number of LPBSs ($M \leq N$). In the following, we will provide the system model of full LPBS cooperation and LPBS clustering scheme.

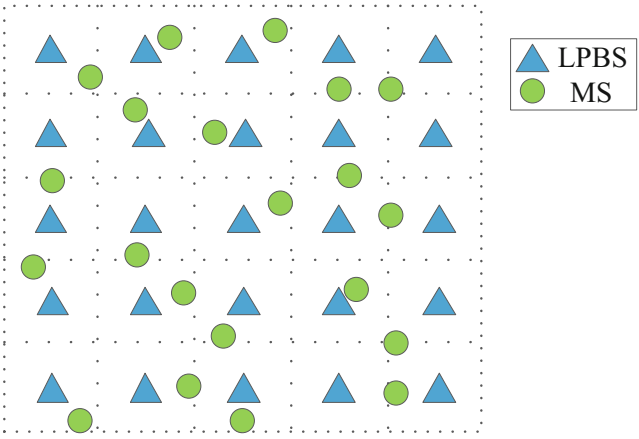


**Fig. 1.** Structure of UDN with twenty-one MSs and twenty-five LPBSs ($M = 21$, $N = 25$). The small triangle and the small circle represent LPBS and MS respectively.

### 2.1 System Model of Multi-user with Full Cooperation

In this subsection, we consider the circumstance that all the LPBSs serve all the MSs, i.e. full cooperation. The transmit symbols of each MS are assumed independent complex Gaussian with variance $P$. We also assume that the channels from LPBSs to MSs are flat fading and spatial-temporally independent. The uplink channel matrix between the MSs and the LPBSs can be expressed as a $N \times M$ matrix,

$$\boldsymbol{H} = [\boldsymbol{h}_1 \boldsymbol{h}_2 \cdots \boldsymbol{h}_M] \tag{1}$$

where $\boldsymbol{h}_m \in \mathbb{C}^{N \times 1}$ is the channel vector between the $m_{th}$ MS and all of the LPBSs. We define that central unit can control and manage the information from different LPBSs. We assume the central unit has full channel state information (CSI), i.e. channel matrix $\boldsymbol{H}$ is known by the central unit. Then, the uplink capacity of the MSs can be denoted as

$$C_{uplink\text{-}capacity} = \log_2[det(\boldsymbol{I}_N + \frac{P}{\sigma^2}\boldsymbol{H}\boldsymbol{H}^H)] \tag{2}$$

Full cooperation is restricted by signaling overhead and real-time processing complexity. So all the $N$ LPBSs need to be divided to some clusters and jointly combine and process the received signals within clusters. In the following, we will give the system model of multi-user with clustering approach.

### 2.2 System Model of Multi-user with Clustering Approach of the LPBSs

We can define the set of all the LPBSs of the system as $\mathcal{A}$, and the set of all the MSs served by these LPBSs as $\mathcal{U}$. Through a clustering algorithm, we could acquire $\mathcal{R}$, the set of all disjoint clusters which are subset of $\mathcal{A}$. In consideration of signaling overhead and real-time processing complexity, we assume that at most $K$ LPBSs cooperation is affordable for the system. So the $\mathcal{R}$ is between $\frac{N}{K}$ and $N$, and $\mathcal{R}$ needs to be an integer. These clusters are mapped to some groups of MSs. So $\mathcal{U}$ is correspondingly clustered to $\mathcal{L}$, the set of all disjoint groups which are subset of $\mathcal{U}$, where $|\mathcal{R}| = |\mathcal{L}|$.

Let $\mathcal{V}(\mathcal{V} \in \mathcal{R})$ be a given LPBS cluster. $\mathcal{V}$ is mapped to a MS cluster $\mathcal{T}(\mathcal{T} \in \mathcal{L})$, i.e. $\mathcal{V} \to \mathcal{T}$. The LPBSs of $\mathcal{V}$ serve the MSs of $\mathcal{T}$. We define the uplink channel matrix as $\boldsymbol{H}(\mathcal{V}, \mathcal{T})$. Transmitted symbols vector by $\mathcal{T}$ is denoted as $\mathbf{s}(\mathcal{T})$. Transmit symbols are assumed independent complex Gaussian random variable with unit variance, i.e. $E[\boldsymbol{s}(\mathcal{T})\boldsymbol{s}(\mathcal{T})^H] = \boldsymbol{I}_{|\mathcal{T}|}$. Received signals vector by $\mathcal{V}$ is denoted as $\boldsymbol{y}(\mathcal{V})$. $\boldsymbol{n}(\mathcal{V})$ represents the additive white Gaussian noise, and $E[\boldsymbol{n}(\mathcal{V})\boldsymbol{n}(\mathcal{V})^H] = \sigma^2\boldsymbol{I}_{|\mathcal{V}|}$. In our analysis, the transmit symbols of each MS are assumed independent complex Gaussian with variance $P$. So the power allocation matrix of $\mathcal{T}$ is $\boldsymbol{A}(\mathcal{T}) = \sqrt{P} \times \boldsymbol{I}_{|\mathcal{T}|}$. Let us denote the received signals of the LPBS cluster $\mathcal{V}$

$$\boldsymbol{y}(\mathcal{V}) = \boldsymbol{H}(\mathcal{V}, \mathcal{T})\boldsymbol{A}(\mathcal{T})\boldsymbol{s}(\mathcal{T}) + \sum_{\mathcal{Q} \in \mathcal{L}, \mathcal{Q} \notin \mathcal{T}} \boldsymbol{H}(\mathcal{V}, \mathcal{Q})\boldsymbol{A}(\mathcal{Q})\boldsymbol{s}(\mathcal{Q}) + \boldsymbol{n}(\mathcal{V}) \tag{3}$$

where $\sum_{\mathcal{Q} \in \mathcal{L}, \mathcal{Q} \notin \mathcal{T}} \boldsymbol{H}(\mathcal{V}, \mathcal{Q})\boldsymbol{A}(\mathcal{Q})\boldsymbol{s}(\mathcal{Q})$ represents the inter-cluster interference from MSs which are not included in $\mathcal{T}$.

From the above, we can derive the uplink capacity of the LPBS cluster $\mathcal{V}$ as

$$C(\mathcal{V}) = \log_2 \left[ \frac{\det\left(\frac{P}{\sigma^2}\boldsymbol{H}(\mathcal{V}, \mathcal{T})\boldsymbol{H}(\mathcal{V}, \mathcal{T})^H + \frac{P}{\sigma^2} \sum_{\mathcal{Q} \in \mathcal{L}, \mathcal{Q} \notin \mathcal{T}} \boldsymbol{H}(\mathcal{V}, \mathcal{Q})\boldsymbol{H}(\mathcal{V}, \mathcal{Q})^H + \boldsymbol{I}_{|\mathcal{V}|}\right)}{\det\left(\frac{P}{\sigma^2} \sum_{\mathcal{Q} \in \mathcal{L}, \mathcal{Q} \notin \mathcal{T}} \boldsymbol{H}(\mathcal{V}, \mathcal{Q})\boldsymbol{H}(\mathcal{V}, \mathcal{Q})^H + \boldsymbol{I}_{|\mathcal{V}|}\right)} \right] \tag{4}$$

The total uplink capacity of the whole system is represented by

$$C_{total} = \sum_{\mathcal{V} \in \mathcal{R}} C(\mathcal{V}) \tag{5}$$

## 3 Clustering Algorithm

In this section, we provide three kinds of LPBS clustering algorithms which we divide many LPBSs into small group in order to reduce the complexity and the energy consumption of signal processing in UDN systems. Our objective is to design a methodology to avoid severe inter-MS interference and improve the total capacity of the system.

In the uplink of UDN system, system performance is mainly limited by the inter-MS interference, especially when some MSs are near to each other. Cooperation of LPBSs could benefit from inter-MS interference cancellation. By clustering, a better tradeoff between the cooperation benefit and joint processing complexity can be obtained. It is reasonable especially when the number of LPBS is large.

### 3.1 Static Clustering Algorithm

In this algorithm, the cluster size and the cluster scheme are fixed. The idea of the static clustering algorithm is that usually the interference between the MSs served by the neighbor LPBSs is severe. Then the LPBSs are clustered according to their locations and never changed in time. This algorithm is very simple but short of flexibility. But not all of the MSs served by the neighbor LPBSs cause severe interference. So static cooperation brings little benefit with some clusters. On the other hand, since cooperation clusters are static, this algorithm can ignore the interference between the MSs served by the nonadjacent LPBSs, and this will introduce severe inter-cluster interference.

### 3.2 Semi-dynamic Clustering Algorithm

This algorithm specifies the size of the cluster, however, the cluster scheme changes dynamically. For any one of these LPBSs, we use order searching scheme to find the cooperation partner based on interference to signal power ratio and form a cluster. This algorithm is more flexible than static clustering algorithm. However, the fixed cluster size may block some better cluster schemes and degrade the system performance.

### 3.3 Dynamic Clustering Algorithm

In this subsection, we propose a novel dynamic clustering algorithm which can improve the total system capacity. In this algorithm, the size of the cluster and the cluster scheme are changing. But considering the signaling overhead and real-time processing complexity, we assume that the size of the cluster keeps less than $K$, i.e. at most $K$ LPBSs cooperation is affordable for the system. Every LPBS serves its nearest MS. So, in one LPBS cluster $\mathcal{V}$, the LPBSs' nearest MSs are regarded as the MS cluster $\mathcal{T}$, i.e. $\mathcal{V}$ is mapped to the MS cluster $\mathcal{T}$. This cluster scheme is formed based on a

pre-defined Signal-Interference Matrix (SIM). The dynamic clustering algorithm is summarized as follows:

(1) Map the each LPBS to their nearest MS. The LPBSs which serve the same MS forms a cluster. If one LPBS only serve one MS, the LPBS is a single cluster. Then the initial cluster set $\mathcal{R}_0$ is obtained. $M$ MSs are correspondingly clustered to $\mathcal{L}_0$. We can know the initial size of the cluster, i.e. $|\mathcal{R}_0| = |\mathcal{L}_0| = M$.

(2) Define a SIM as

$$SIM = \begin{bmatrix} I_{11} & I_{12} & \cdots & I_{1M} \\ I_{21} & I_{22} & \cdots & I_{2M} \\ \vdots & \vdots & \ddots & \vdots \\ I_{N1} & I_{N2} & \cdots & I_{NM} \end{bmatrix} \tag{6}$$

where $I_{im} = P \times \left|\hat{h}_{im}\right|^2$. $\hat{h}_{im}$ is a parameter of the channel from the $i_{th}$ LPBS to the $m_{th}$ MS. $\hat{h}_{im}$ could be the instantaneous CSI, large-scale CSI, or path loss. For each row, taking the maximum of $I_{im}(1 \le m \le M)$ as the signal, we use $S_{ik^i}(1 \le k^i \le M)$ to represent the maximum of $I_{im}(1 \le m \le M)$. So we know the $k^i_{th}$ MS is served by the $i_{th}$ LPBS, i.e. the $k^i_{th}$ MS is the nearest MS to the $i_{th}$ LPBS.

(3) Each LPBS updates the cluster scheme based on the order of its signal component $S_{ik^i}(1 \le k^i \le M)$, from large to small. The update order based on the signal component is more benefit for the MSs with better channel condition. That is because they have more potential of achieving higher channel capacity. After the $g_{th}$, $\mathcal{R}_{g-1}$ becomes $\mathcal{R}_g$, $g \in \{1, 2, \ldots, N\}$. And the final cluster scheme will be $\mathcal{R}_N$, correspondingly $\mathcal{L}_0$ becomes $\mathcal{L}_N$. The update obeys the follow rules:

   (a) Find out the biggest interference component $I_{im}$ of current LPBS $i$, $m \in \{1, 2, \ldots (k^i - 1), (k^i + 1), \ldots M\}$.

   (b) Define a parameter $\delta$ called threshold. If $\frac{I_{im}}{S_{ik^i}} < \delta$ or $\frac{I_{im}}{\sigma^2} < \delta$, consider the interference to current LPBS is small enough to ignore, and keep the current cluster scheme. If $\frac{I_{im}}{S_{ik^i}} \ge \delta$ and $\frac{I_{im}}{\sigma^2} \ge \delta$, combine the cluster of $i_{th}$ LPBS and the LPBS cluster serving the $m_{th}$ MS. In this algorithm, we try to put the MSs which cause the strongest interference to each other in one cluster, to take more advantages of cooperation. And the parameter of threshold provides the possibility of simple non-cooperation processing for some MSs which are unnecessary to cooperate with others. These characteristics make this algorithm could realize dynamic adjusting according to the channel condition of the MSs.

   (c) If the number of LPBSs in the new cluster after the combing does not exceed the maximum $K$, then go to the next updating step. Otherwise, the cluster scheme does not change, then also go to the next updating step.

## 4 Simulation Results and Analysis

For simplicity, as show in Fig. 1 a grid-point model is considered in our paper. The LPBSs are deployed in grid, and each of them is equipped with one omnidirectional antenna. The location of MSs follow random distribution in the cell. The length of the cell is 35 m, and the minimum distance between MS and LPBS is 10 m. The channel vector between the $m_{th}$ MS and $i_{th}$ LPBS is $\hat{h}_{im} = \sqrt{\beta_{im}}\gamma_{im}$, where $\sqrt{\beta_{im}}$ represents the large-scale fading which consist of path-loss and shadow fading. $\gamma_{im}$ represents the small fading and $\gamma_{im} \in CN(0, 1)$.

In Fig. 2, the average uplink capacity per LPBS versus the size of cluster in static cluster cooperation and semi-static and is given. With the increasing of the size of the cluster, the average uplink capacity per LPBS is increasing. But the big and constant size of the cluster will cause the signaling overhead and real-time processing complexity.

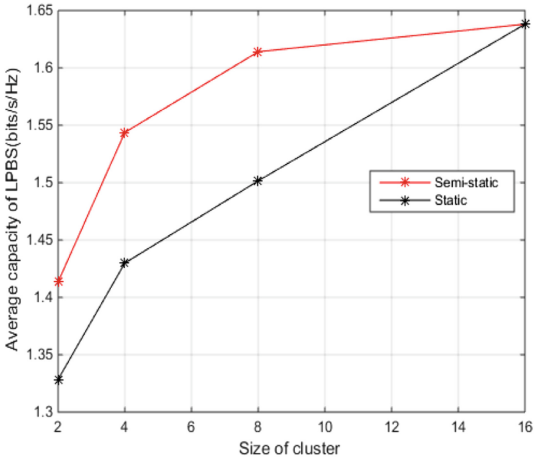


**Fig. 2.** Average uplink capacity per LPBS versus the number of cooperate LPBSs in static cluster and semi-static cluster cooperation.

In Fig. 3, the average uplink capacity per LPBS versus the threshold in dynamic cluster cooperation is given. With the increasing of the threshold $\delta$, the average uplink capacity per LPBS is decreasing. With the threshold increasing, the users which originally belongs to a certain LPBS became an interfere user of other LPBS. Thus the useful signals turn into interference. In UDN, the density and mobility of UE is very high, it is important to adjust the threshold of each LPBS dynamically. The dynamic clustering method can change the threshold according to the real-time SINR or the quality of UE, it can ensure the high quality of service (QoS) of UE and keep the computational complexity in an acceptable level.

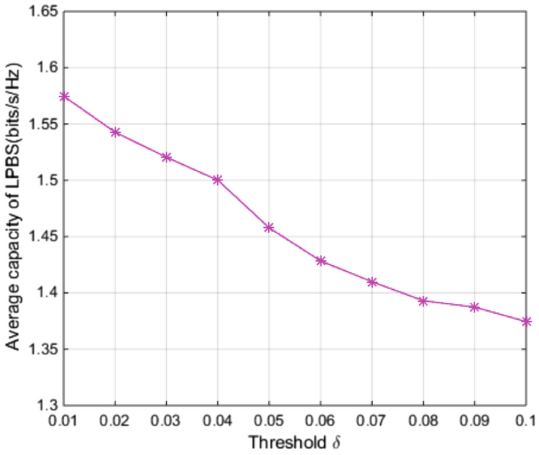


**Fig. 3.** Average uplink capacity per LPBS versus the threshold $\delta$ in dynamic cluster cooperation.

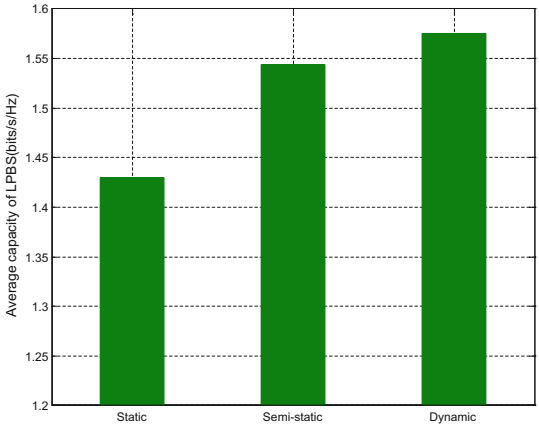


**Fig. 4.** The comparison of these three kinds of schemes

Figure 4 is the comparison of these three kinds of schemes, in order to a better comparison between the three methods, we choose the appropriate parameters based on the simulation parameters in three cases. We set the cluster size is 4 in the static way and choose 4 LPBS for cooperation in semi-dynamic way. In the dynamic clustering method, we select threshold as 0.02. It can be seen that under the static way, the average uplink capacity is much smaller than other two ways. This is because that the static way just removes the strong interference, but it cannot manage the interference effectively to all users. As to the semi-dynamic way, because of the use of direct collaboration between LPBSs, the interference within the cluster can be completely eliminated. However, the collaboration between LPBSs will cause an extra cost to ensure the information interaction. By using dynamic clustering method, the threshold

can be decreased when the number of UE become large and vice versa. It can get a better balance between the interference and computational complexity.

## 5 Conclusions

In the uplink of UDN, there exits severe interference among LPBSs because of the densely deployed small cell. Cluster cooperation is a promising solution. However, the challenge is the additional signaling overhead and real-time processing complexity. In this paper, we derive the total uplink capacity of the whole system, and we present a novel dynamic clustering algorithm to make a better tradeoff between the system performance and complexity. This algorithm also provides flexibility to use the CSI according to capability of the system. We compare this algorithm with proposed static clustering algorithm and semi-dynamic clustering algorithm. The simulation results prove this algorithm leads to significant capacity gains.

**Acknowledgments.** This work was supported by the China's 863 Project (No. 2015AA01A706), the National S&T Major Project (No. 2014ZX03004003), Science and Technology Program of Beijing (No. D161100001016002), State Key Laboratory of Wireless Mobile Communications, China Academy of Telecommunications Technology (CATT), and by Beijing Samsung Telecom R&D Center.

## References

1. 5G Whitepaper, FuTURE Forum 5G SIG (2015)
2. Popovski, P., Braun, Y., Mayer, H.-P'., Fertl, P.: Requirements and KPIs for 5G mobile and wireless system, Technical report (2014). https://www.metis2020.com
3. Peng, H., Xiao, Y., Ruyue, Y.N., Yifei, Y.: Ultra dense network: challenges, enabling technologies and new trends. IEEE Commun. Mag. **13**(2), 30–40 (2016)
4. Boccardi, F., Heath, R.W., Lozano, A., Marzetta, T.L., Popovski, P.: Five disruptive technology directions for 5G. IEEE Commun. Mag. **52**(2), 74–80 (2014)
5. Aspar, S., Wunder, G.: 5G Cellular communications scenarios and system requirements. https://www.5gnow.eu
6. Liu, L., Garcia, V., Tian, L., Pan, Z., Shi, J.: Joint clustering and inter-cell resource allocation for CoMP in ultra dense cellular networks. In: IEEE International Conference on Communications (ICC), pp. 2560–2564 (2015)
7. Siyi, C., Chengwen, X., Zesong, F., Hualei, W., Zhengang, P.: Dynamic clustering algorithm design for ultra dense small cell networks in 5G. In: 10th International Conference on Communications and Networking in China (ChinaCom), pp. 836–840 (2015)
8. Ye, Y., Zhang, H., Xiong, X., Liu, Y.: Dynamic min-cut clustering for energy savings in ultra-dense networks. In: 2015 IEEE 82nd Vehicular Technology Conference (VTC Fall), pp. 1–5 (2015)
9. Wei, R., Wang, Y., Zhang, Y.: A two-stage cluster-based resource management scheme in ultra-dense networks. In: 2014 IEEE/CIC International Conference on Communications in China (ICCC), pp. 738–742 (2014)

10. Sisi, Z., Hui, Z., Xiaoyue, H., Wenxiu, Z.: A new cell search scheme based on cell-clustering for UDN. In: 11th International Conference on Wireless Communications, Networking and Mobile Computing (WiCOM), pp. 1–5 (2015)
11. Khan, T.A., Xinchen, Z., Heath, R.W.: A stochastic geometry approach to analyzing cellular networks with semi-static clustering. In: 2015 IEEE Global Communications Conference (GLOBECOM), pp. 1–6 (2015)

# Wideband Spectrum Sensing by Multi-step Sample Autocorrelation Detection

Lu Chen, Xiaoqin Wu, and Yong Bai(✉)

State Key Lab of Marine Resource Utilization in South China Sea, College of Information Science and Technology, Hainan University, 58 Renmin Avenue, Haikou 570228, Hainan, China
bai@hainu.edu.cn

**Abstract.** Wideband spectrum sensing capability by using multi-step energy detection has been enabled in GNU Radio software radio platform. To improve the detection performance, we propose a novel approach of wideband spectrum sensing by multi-step sample autocorrelation detection. We first describe the principle of signal sample autocorrelation detection, then we present our proposed multi-step sample autocorrelation detection procedure for wideband spectrum sensing. The proposed procedure is simulated by using MATLAB, and the simulation results demonstrate that our proposal can achieve required detection performance by setting proper decision threshold.

**Keywords:** Spectrum sensing · Energy detection
Sample autocorrelation detection · GNU Radio

## 1 Introduction

The scarcity of suitable radio spectrum resource becomes ever more pressing with increasing demand on wireless applications and services. The existing command-and-control spectrum management that relies on static allocation results in low spectrum utilization [1]. To address the spectrum scarcity problem, cognitive radio that can sense idle spectrum and perform dynamic spectrum access has been considered to be a promising technology. The existing spectrum sensing techniques include energy detection [2, 3]; matched-filtering detection [4]; cyclo-stationary detection [5] and eigenvalue detection [6]. Among them, energy detection is a signal source detection algorithm which has the advantage of simplicity. However, the performance of energy detection is vulnerable to noise uncertainty [7]. To overcome the shortcoming of energy detection, the authors in [8] proposed a covariance absolute value (CAV) algorithm, where the diagonal and off-diagonal elements in the statistical covariance matrix of the received signal are compared to determine the presence of primary user (PU). In [9], the authors discussed the CAV detection results in Rayleigh fading channel under low signal-noise-ratio (SNR). In practical GNU Radio software radio platform, the spectrum sensing by using multi-step energy detection in frequency domain can be supported [10–12].

To further improve the detection performance of spectrum sensing, we propose a wideband spectrum sensing by multi-step sample autocorrelation detection considering that the sample autocorrelation detection is robust to the noise uncertainty. We first


M. Huang et al. (Eds.): WICON 2016, LNICST 214, pp. 228–239, 2018.
https://doi.org/10.1007/978-3-319-72998-5_24

describe the principle of signal sample autocorrelation detection, then we present our proposed multi-step sample autocorrelation detection procedure. By simulating the procedure using MATLAB, we obtain the detection performance (e.g., detection probability and false alarm probability) in one-step narrowband spectrum sensing, and we discuss the factors influencing the detection performance in one-step spectrum sensing, i.e., the decision threshold, SNR, sensing time, number of available samples, and the smoothing factor. The simulation results demonstrate that our proposal can achieve required detection performance by setting proper detection threshold. Due to the signals can be detected without the knowledge of the noise power, the sample autocorrelation detection is robust to the noise uncertainty.

The remainder of the paper is organized as follows: The principle of signal sample autocorrelation detection is presented in Sect. 2. Section 3 describes our proposed multi-step frequency domain sample autocorrelation detection procedure. Section 4 presents the simulations and discussions. Section 5 draws the conclusions.

## 2 The Principle of Signal Sample Autocorrelation Detection

A signal detector is to find the test statistic of the received signal and compare it with a predefined threshold for deciding whether the signal exists or not. The signal detection can be formulated as a binary hypotheses testing problem as follows.

$$H_0 : y(n) = \eta(n), \quad n = 1, 2, 3, \cdots, N \tag{1}$$

$$H_1 : y(n) = h(x(n)) + \eta(n), \quad n = 1, 2, 3, \cdots, N \tag{2}$$

where, $H_0$ and $H_1$ represent the hypothesis "primary signal absent" and the hypothesis "primary signal present", respectively; $x(n)$ denotes $n$th sample of the primary signal to be detected; $\eta(n)$ is $n$th sample of noise process; $y(n)$ denotes $n$th sample of the received signal; $N$ is the total number of samples collected during the sensing time $T$; $h(\cdot)$ denotes the channel fading process.

### 2.1 Theoretical Analysis for Sample Autocorrelation Detection

When sample autocorrelation detection is performed in time-domain, the signal $x(t)$ is transmitted through a radio channel and passed through a bandpass filter (BPF) with bandwidth $W$; then the filtered signals is sampled and the sample autocorrelation matrix is calculated. Next, the ratio of its diagonal and off-diagonal elements is treated as the test statistic and is compared to the predefined threshold.

From the discrete sampling sequences of $y(t)$, we choose a suitable smoothing factor $L$ and define the following vectors,

$$\hat{y}(n) = [y(n) \quad [Y(n-1)] \quad \cdots \quad y(n-L+1)]^T \tag{3}$$

Where $n = 0, 1, \ldots, N-1, [\cdot]^T$ stands for matrix transpose.

The autocorrelation matrix of the received signal is defined as follows,

$$R_y = E[\hat{y}(n)\hat{y}^T(n)] \tag{4}$$

In this paper, we calculate and estimate the sample autocorrelation matrix by limited number of $y(n)$. In practice, we can only approximate such a matrix when using limited signal samples. Let us define the sample autocorrelation of the received signals as

$$\lambda(l) = \frac{1}{N_s}\sum_{m=0}^{N_s-1} y(m)y(m-l), \quad l = 0, 1, \cdots, L-1 \tag{5}$$

Where $N_s$ is the number of available samples. In fact, signal autocorrelation matrix $R_y$ can be approximated by the sample autocorrelation matrix $R_y(N_s)$ and we defined as

$$R_y \approx R_y(N_s) = \begin{pmatrix} \lambda(0) & \lambda(1) & \cdots & \lambda(L-1) \\ \lambda(1) & \lambda(0) & \cdots & \lambda(L-2) \\ \vdots & \vdots & \vdots & \vdots \\ \lambda(L-1) & \lambda(L-2) & \cdots & \lambda(0) \end{pmatrix} \tag{6}$$

Note that the sample covariance matrix is symmetric and Toeplitz. Obviously, if there is no signal and $N_s$ is big enough, the off-diagonal elements of $R_y(N_s)$ are all zeros. If there is signal and the signal samples are correlated, $R_y(N_s)$ will be almost surely not a diagonal matrix. Let $r_{ij}$ be the elements of the matrix $R_y(N_s)$ and we define

$$T_{all} = \frac{1}{L}\sum_{i=1}^{L}\sum_{j=1}^{L}\left|r_{ij}\right| \tag{7}$$

$$T_{diag} = \frac{1}{L}\sum_{i=1}^{L}\left|r_{ii}\right| \tag{8}$$

Then, the test statistic of the detector is given by

$$Ratio = T_{all} \Big/ T_{diag} \tag{9}$$

and it is compared with a predefined threshold $\gamma$ for hypothesis testing. Therefore, this method can be described as follows: if $Ratio > \gamma$, signal is decided to be present; otherwise, signal is decided to be absent. The signal sample autocorrelation detection does not need the information about PU signal, noise and channel, it is robust to noise uncertainty compared with the energy detection.

### 2.2 Threshold Determination

For signal detection, selecting an appropriate detection threshold is the key to improve the detection performance of the algorithm. The authors in [13] derived the threshold

based on the minimum error probability criterion and pointed out that reducing the total error probability can improve the detection performance. In this paper, we select an appropriate threshold based on the false alarm probability and the detection probability.

The detection threshold can generally be determined based on the Newman-Pearson criterion, to obtain the relationship between the false alarm probability and detection threshold.

In [8], the relation between the detection threshold and false alarm probability under the hypothesis $H_0$ is given as follows,

$$\gamma = \frac{1 + (L-1)\sqrt{\frac{2}{\pi \cdot N_s}}}{1 - Q^{-1}(P_{fa}) \cdot \sqrt{2/N_s}} \tag{10}$$

Where the function $Q(\cdot)$ is as follows $Q(a) = \int_a^{\infty} \sqrt{\frac{1}{2\pi}} \cdot e^{\frac{-x^2}{2}} dx$, and $Q(a) = 1 - Q(-a)$, $Q^{-1}(\cdot)$ represents its inverse function.

The threshold is set in order to achieve a specified probability of false alarm according to the Newman-Pearson criterion. However, the prerequisite for (10) is that the transformed signal is not filtered by a band-pass filter. In our simulation, the received signal is filtered by a narrow band-pass filter, (10) is no longer applicable to our problem. We proposed a novel approach to the determination of the threshold through the experimental and simulation method by considering both the requirements of detection probability and false alarm probability.

In the IEEE 802.22 draft standard [14], where $P_{fa} = 0.01$–$0.1$, $P_d = 0.9$–$1.0$. We obtain an appropriate threshold in a certain detection performance ($P_d > 0.95$ and $P_{fa} < 0.05$). In Sect. 4, we will give a detailed description of how to obtain the appropriate threshold through the experimental and simulation approach.

## 3 Wideband Spectrum Sensing Procedure by Multi-step Sample Autocorrelation Detection

Wideband spectrum detection by using multi-step energy detection in frequency domain has been enable in the GNU Radio package. When the spectrum to be detected is larger than the maximum detection bandwidth in the default settings of USRP, it cannot sense the whole spectrum in one step. For instance, when the A/D sampling rate (adc_rate) is set to 64 MBbytes/s and the extraction rate (decim) is 16, the maximum detection bandwidth of USRP is adc_rate/decim = 4 MHz.

Since energy detection is affected by noise power, we present an approach of wideband spectrum sensing by multi-step sample autocorrelation detection as shown in Fig. 1.

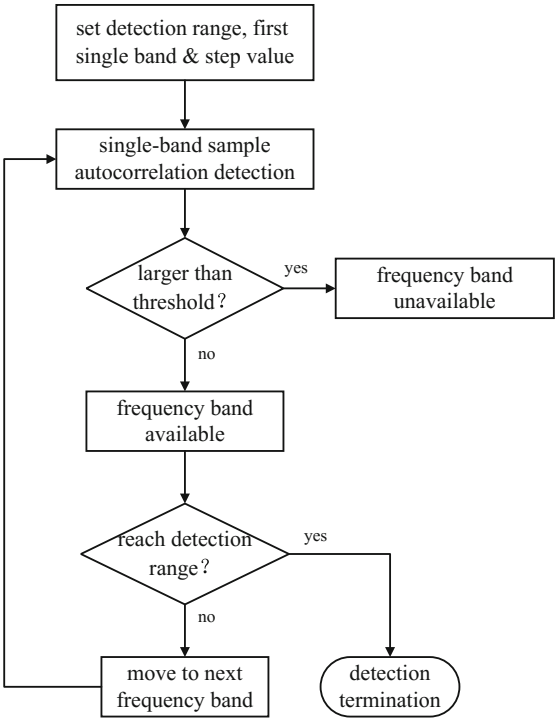


**Fig. 1.** The procedure of wideband spectrum sensing by multi-step sample autocorrelation detection.

In the multi-step sample autocorrelation detection, the equipment first sets up the spectrum range to be sensed, first single band, and step value; then the RF board of USRP changes the central frequency step-by-step, and single-band sample autocorrelation detection is performed for a narrow range of frequency in one step. In each step, it compares the calculated test statistic based on sample autocorrelation with a predefined threshold and determines whether the primary users exists or not. Such a procedure is continued until the whole spectrum range is reached.

It is worth pointing out the frequency step value has influence on the detection bandwidth resolution and the detection time. The smaller the step value, the higher the frequency band resolution is, but the detection time is longer and the complexity of the detection is increased. On the contrary, when using a larger step value, the detection speed is faster, but the frequency band resolution is lower.

## 4 Simulations and Discussions

We simulate the multi-step sample autocorrelation detection procedure for wideband spectrum sensing by using MATLAB.

Firstly, a wideband signal is generated by modulating a baseband signal. The baseband signal has sinc waveform with 2 MHz bandwidth and BPSK modulation. The symbol duration of the baseband signal is set to 0.5 μs. Then, the baseband signal is modulated onto two carriers at 5 MHz and 15 MHz respectively. The signal's occupied spectrum is within 4–6 MHz and 14–16 MHz with such parameters. The whole spectrum range to be sensed is assumed to be 20 MHz. The sampling frequency is set to be 40 MHz. The one-step size for spectrum sensing is set to be 200 kHz. The received signal is obtained by adding white Gaussian noise to the modulated signal. At different SNRs, we change the signal power while keeping the noise power to be 1 at each sampling point. The one-step spectrum sensing at 200 kHz narrowband is implemented by a 200 kHz bandpass filter with 500-order Kaiser window. The multi-step wideband spectrum sensing is realized by adjusting the central frequency of the 200 kHz bandpass filter step by step until the whole 20 MHz spectrum is sensed. In each step, the calculated test statistic in (9) is compared with a threshold for signal detection. At each 200 kHz narrowband, the number of sensed BPSK symbols is set to 2000 (i.e., $N = 2000$); the number of available samples is set to be 20000 (i.e., $Ns = 20000$).

Figure 2 shows the detection probability $P_d$ versus the test statistic when the smoothing factor $L$ is 15 to 20. At $L = 15$, the required decision threshold $\gamma$ is 9.0 and 9.5 to satisfy $P_d \geq 0.95$ at SNR $= -5$ dB and 5 dB respectively; At $L = 20$, the required decision threshold $\gamma$ is 10.5 and 11.5 to satisfy $P_d \geq 0.95$ at SNR $= -5$ dB and 5 dB respectively.

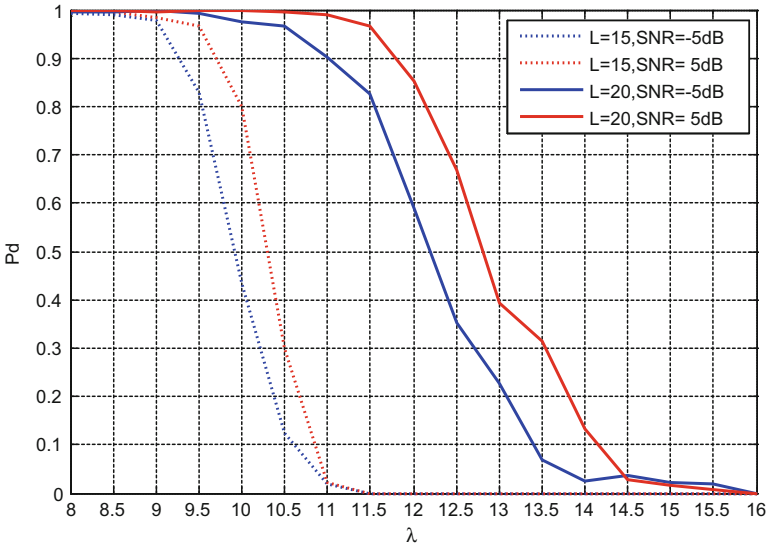


**Fig. 2.** Detection probability versus test statistic with different $L$

Figure 3 shows the false-alarm probability $P_f$ versus the test statistic when $L$ is 15 and 20. It can be seen that, at $L = 15$, $\gamma$ increases from 6.4 to 6.7 when the SNR $= -5$ dB

and 5 dB to satisfy $P_f \leq 0.05$; At $L = 20$, $\gamma$ increases from 8.0 to 8.6 when the SNR $= -5$ dB and 5 dB.

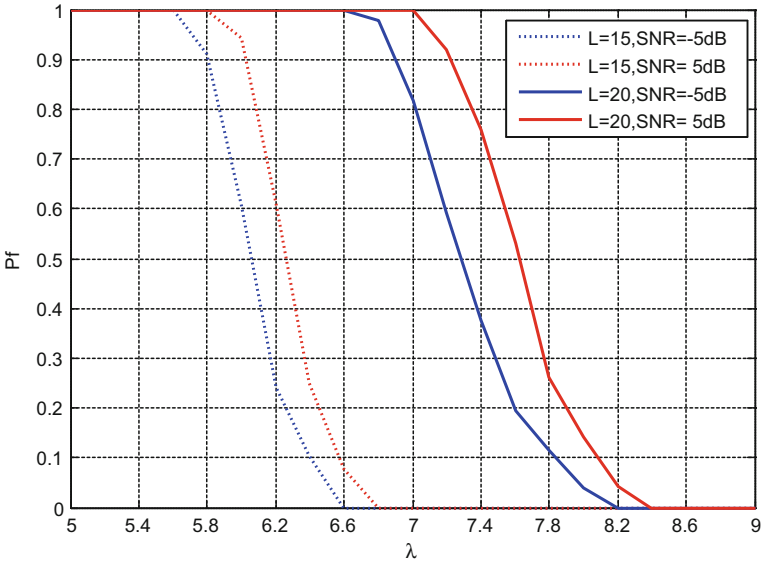


**Fig. 3.** False-alarm probability versus test statistic with different $L$

From Figs. 2 and 3, it also can be seen that the decision threshold $\gamma$ influences the performance of false-alarm probability and detection probability. In addition, at the same smoothing factor, the decision threshold to satisfy a certain false-alarm probability and detection probability is loosely affected by the SNR. Hence the sample autocorrelation detection is robust to the noise uncertainty. Meanwhile, the decision threshold increases with the increases of the smoothing factor $L$ to achieve the same detection probability.

The decision threshold for the sample autocorrelation detection in one-step 200 kHz band can be determined from the simulation results of Figs. 2 and 3.

When $L$ is 15 and SNR is $-5$ dB, the decision threshold $\gamma$ should be less than 8.5 to satisfy $P_d \geq 0.95$. Furthermore, $\gamma$ should be greater than 6.6 to satisfy $P_f \leq 0.05$. Therefore, a value between 6.6 and 8.5 can be chosen as the decision threshold in one-step spectrum sensing for the case that $L = 15$ and SNR $= -5$ dB.

When $L$ is 20 and SNR is $-5$ dB, $\gamma$ should be less than 10.5 to satisfy $P_d \geq 0.95$. Furthermore, $\gamma$ should be greater than 8.2 to satisfy $P_f \leq 0.05$. Therefore, a value between 8.2 and 10.5 can be chosen as the decision threshold in one-step spectrum sensing for the case that $L = 20$ and SNR $= -5$ dB.

When $L$ is 20 and SNR is 5 dB, $\gamma$ should be less than 10.6 to satisfy $P_d \geq 0.95$. Furthermore, $\gamma$ should be greater than 8.4 to satisfy $P_f \leq 0.05$. Therefore, a value between 8.4 and 10.6 can be chosen as the decision threshold in one-step spectrum sensing for the case that $L = 20$ and SNR $= 5$ dB.

Figure 4 shows the test statistic of the detector in 100 steps for 20 MHz spectrum sensing by multi-step sample autocorrelation detection for the case that $L = 15$ and SNR $= -5$ dB. $\gamma$ is chosen to be 7.8 in one-step spectrum sensing for such a case. It can be seen from Fig. 4 that the test statistic of the detector is continuously larger than 7.8 from the 21th to the 30th 200 kHz steps, and from the 71th to the 80th 200 kHz steps. Therefore, the occupied spectrum can be decided to be from 4.0 MHz to 6.0 MHz and from 14.0 MHz to 16.0 MHz, and the idle spectrum is the spectrum range except 4.0 MHz to 6.0 MHz and 14.0 MHz to 16.0 MHz in the 20 MHz.

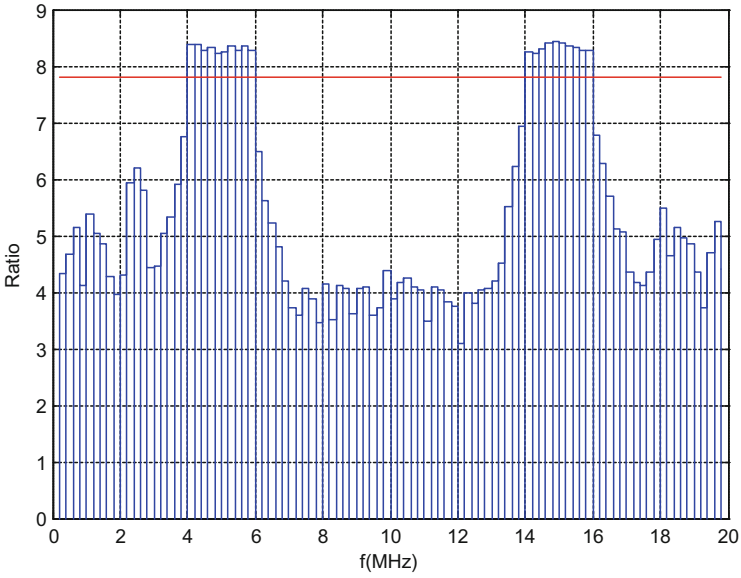


**Fig. 4.** Detected test statistic in 100 steps for 20 MHz spectrum sensing ($SNR = -5$ dB, $L = 15$)

Figure 5 shows the test statistic of the detector in 100 steps for 20 MHz spectrum sensing by multi-step sample autocorrelation detection for the case that SNR $= -5$ dB and $L = 20$. $\gamma$ is chosen to be 9.0 in one-step spectrum sensing for such a case. It can be seen that from Fig. 5 the test statistic is continuously larger than 9.0 from the 21th to the 30th 200 kHz steps, and from the 71th to the 80th 200 kHz steps. Therefore, the idle spectrum is the spectrum range except 4.0 MHz to 6.0 MHz and 14.0 MHz to 6.0 MHz in the 20 MHz.

Figure 6 shows the test statistic of the detector in 100 steps for 20 MHz spectrum sensing by multi-step sample autocorrelation detection for the case that $L = 20$ and SNR $= 5$ dB. $\gamma$ is chosen to be 9.0 in one-step spectrum sensing for such a case. It can be seen that from Fig. 5 the test statistic is continuously larger than 9.0 from the 21th to the 30th 200 kHz steps, and from the 71th to the 80th 200 kHz steps. Therefore, the idle spectrum is the spectrum range except 4.0 MHz to 6.0 MHz and 14.0 MHz to 6.0 MHz in the 20 MHz.

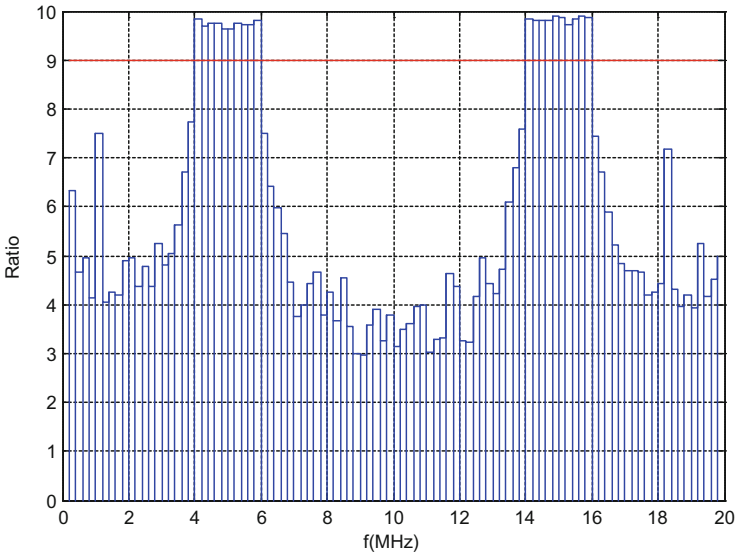


**Fig. 5.** Detected test statistic in 100 steps for 20 MHz spectrum sensing ($SNR = -5$ dB, $L = 20$)

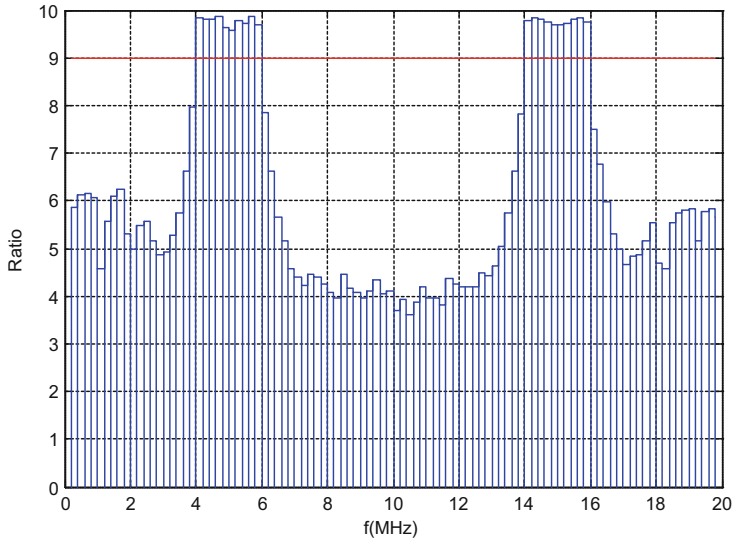


**Fig. 6.** Detected test statistic in 100 steps for 20 MHz spectrum sensing ($SNR = 5$ dB, $L = 20$)

From (5) – the equation of the sample autocorrelation, it can be seen that the sample autocorrelation matrix is mainly determined by two factors, $N_s$ and $L$. At the same $N_s$, the detection probability is increasing. Obviously with the increase of the smoothing factor, the complexity of the algorithm increases in a certain extent. In practice, we can choose a relatively small smoothing factor if it can meet the detection performance.

To investigate the impact of the number of available samples $N_s$ on the detection probability, we simulate $P_d$ versus the test statistic when $N_s$ is 20000 and 40000, respectively. Figure 7 shows that the $\gamma$ increases from 10.6 to 11.5 with $N_s$ increases from 20000 to 40000 to satisfy $P_d \geq 0.95$.

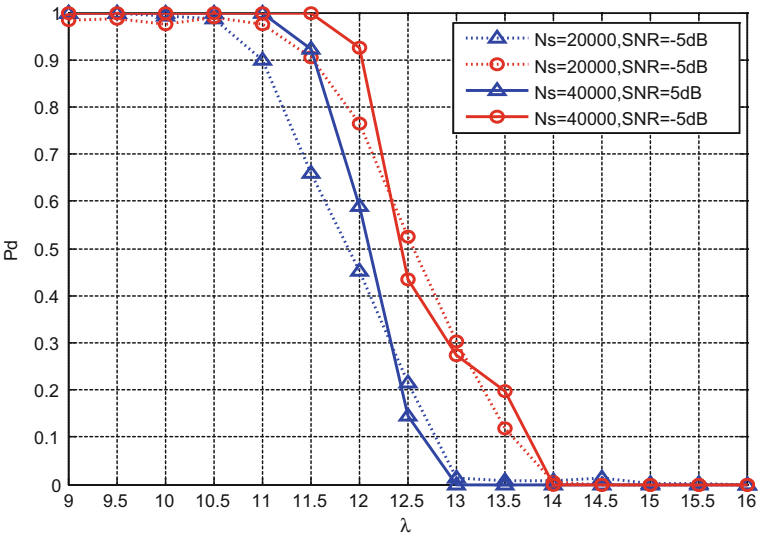


**Fig. 7.** Detection probability versus t with different $N_s$ ($L = 15$)

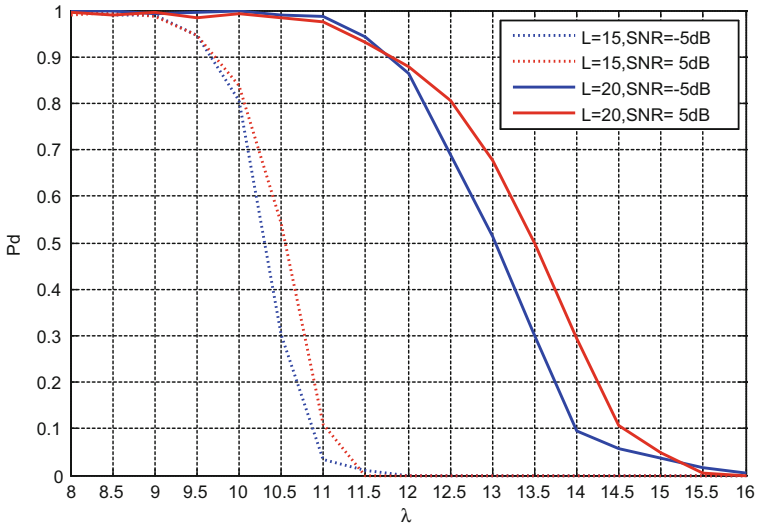


**Fig. 8.** Detection probability versus test statistic with different $L$

Next, we evaluate the sensing performance with different sensing time. The number samples at each 200 kHz narrowband is set to 3000 (i.e., $N = 3000$) instead of 2000. Figure 8 shows $P_d$ versus $\gamma$ for $N = 3000$ when $L$ is 15 and 20, respectively. $\gamma$ increases from 9.5 to 11.5 when $L$ increases from 15 to 20 to satisfy $P_d \geq 0.95$; Comparing Fig. 2 for the case $N = 2000$, $\gamma$ needs to be increased to satisfy $P_d \geq 0.95$. Figure 9 shows $P_f$ versus $\gamma$ for $N = 3000$ when $L$ is 15 and 20, respectively. It can be seen that, to satisfy $p_f \leq 0.05$ at the same SNR, $\gamma$ increases from 7.4 to 9.3. Comparing Fig. 3 for the case $N = 2000$, $\gamma$ needs to be increased to satisfy $p_f \leq 0.05$.

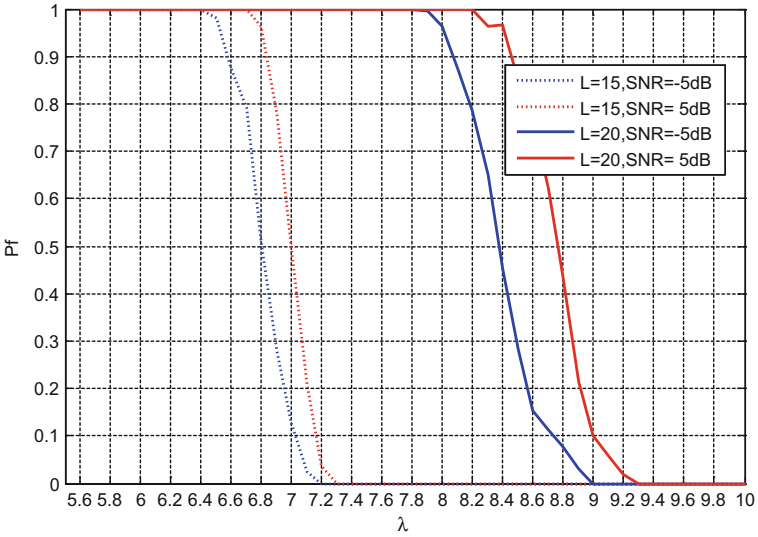


**Fig. 9.** False-alarm probability versus test statistic with different $L$

## 5 Conclusions

When a sensing device cannot sense the spectrum range in one step because the whole spectrum to be sensed is wider than the one-step detection bandwidth, the software radio platform (like GNU Radio) employs multi-step energy detection in frequency domain to fulfill the sensing task. Considering that the sample autocorrelation detection is robust to the noise uncertainty, we proposed a novel approach of wideband spectrum sensing by employing the sample autocorrelation detection instead of energy detection in the multiple sensing steps. In the one-step narrowband spectrum sensing, the test statistic of the received signal is calculated based on the sample autocorrelation and it is compared with a predefined threshold to decide whether the signal exists or not. By simulating our proposed procedure, we obtained the achieved detection probability and false alarm probability of spectrum sensing in one-step spectrum sensing. From the simulation results, we examined the factors (SNR, sensing time, the number of available samples and the smoothing factor) that influence the decision threshold. In the performance evaluation, the decision threshold is determined considering both the requirements

of detection probability and false alarm probability. Due to the fact that the sample autocorrelation detection can work without the knowledge of noise power, our proposal provides a more robust approach for wideband spectrum sensing than the multi-step energy detection.

**Acknowledgments.** This paper was supported by the National Natural Science Foundation of China (Grant No. 61561017 and Grant No. 61261024), National Science & Technology Pillar Program (Grant No. 2014BAD10B04), and Hainan Province Major Science & Technology Project (Grant No. ZDKJ2016015).

## References

1. Mitolal, J., Maguire, G.Q.: Cognitive radio: making software radios more personal. IEEE Pers. Commun. **6**, 13–18 (1999)
2. Cabric, D., Mishra, S.M., Brodersen, R.W.: Implementation issues in spectrum sensing for cognitive radios. In: Proceedings of the Thirty-Eighth Asilomar Conference, pp. 772–776. IEEE Press, New York (2004)
3. Tandra, R., Sahai, A.: Fundamental limits on detection in low SNR under noise uncertainty. In: Proceedings of Wireless Communication, pp. 464–469. IEEE Press, New York (2005)
4. Cabric, D., Tkachenko, A., Brodersen, R.W.: Spectrum sensing measurements of pilot, energy, and collaborative detection. In: Proceedings of Military Communications Conference (MILCOM), pp. 1–7. IEEE Press, New York (2006)
5. Gardner, W.A.: Exploitation of spectral redundancy in cyclostationary signals. IEEE Signal Process. Mag. **8**, 14–36 (1991)
6. Zeng, Y.H., Liang, Y.-C.: Eigenvalue based spectrum sensing algorithms for cognitive radio. IEEE Trans. Commun. **57**, 1784–1793 (2009)
7. Digham, F.F., Alouini, M.-S., Simon, M.K.: On the energy detection of unknown signals over fading channels. In: IEEE International Conference on Communication, pp. 3575–3579. IEEE Press, New York (2003)
8. Zeng, Y.H., Liang, Y.-C.: Spectrum-sensing algorithms for cognitive radio based on statistical covariances. IEEE Trans. Veh. Technol. **58**, 1804–1815 (2009)
9. Li, B., Chen, Y.B., Dong, G.F.: Spectrum sensing based on signal sample autocorrelation in Rayleigh Fading channel. In: 7th International Conference on Wireless Communications, Networking and Mobile Computing, pp. 1–4. IEEE Press, New York (2011)
10. Quan, Z., Cui, S., Sayed, A.H., et al.: Optimal multiband joint detection for spectrum sensing in cognitive radio networks. IEEE Trans. Signal Process. **57**, 1128–1140 (2009)
11. Sarijari, M.A., Marwanto, A., Fisal, N., Yusof, S.K.S., et al.: Energy detection sensing based on GNU radio and USRP: an analysis study. In: IEEE 9th Malaysia International Conference on Communications (MICC), pp. 338–342. IEEE Press, New York (2009)
12. Shun, Y.D., Xiao, Q.W., Yong, B.: Wideband spectrum sensing by multistep frequency domain energy detection in GNU radio. WSEAS Trans. Commun. **15**, 168–175 (2016)
13. Liu, Y., Zeng, C., Wang, H., et al.: Energy detection threshold optimization for cooperative spectrum sensing. In: Advanced Computer Control (ICACC), pp. 566–570. IEEE Press, New York (2010)
14. IEEE: IEEE 802.22 Working Group on Wireless Regional Area Networks [EB/OL]. http://www.ieee802.org/22/. 12 Jan 2011

# Noncoherent Joint Multiple Symbol Differential Detection and Channel Decoding in Massive MIMO System

Jing Feng[1(✉)], Hui Gao[1], Taotao Wang[2], Tiejun Lv[1], and Weibin Guo[3]

[1] Beijing University of Posts and Telecommunications, Beijing, China
fengjing@bupt.edu.cn
[2] The Chinese University of Hong Kong, Sha Tin, Hong Kong
[3] Shenzhen Institute of Radio Testing and Technology, Shenzhen, China

**Abstract.** A noncoherent joint multiple symbol differential detection (MSDD) and channel decoding framework is proposed for massive multiple-input multiple-output (M-MIMO) system. The proposed framework bears the potential to solve the high channel estimation overhead for conventional coherent M-MIMO systems. Employing the autocorrelation receiver (AcR) and the belief propagation (BP) message passing algorithm, the proposed soft-input soft-output (SISO) MSDD can be easily integrated with advanced channel coding. Simulation results show that the BER performance can be significantly improved within a few iterations of the proposed scheme.

**Keywords:** MSDD · Massive MIMO · SISO · BP

## 1 Introduction

Massive multiple-input multiple-output (M-MIMO) system has attracted much attention recently. Equipped with the massive antenna arrays, M-MIMO system can achieve very high spectral efficiency and energy efficiency [1–3]. One of the challenges of coherent M-MIMO is the acquisition of channel state information (CSI). As the number of antennas at the base station grows large, the system overhead and the complexity associated with channel estimation will become too high and unaffordable. When considering low-complexity and low-overhead M-MIMO system, some noncoherent transmission schemes may be more favorable.

One of the typical noncoherent detectors is the differential detection (DD) with the autocorrelation receiver (AcR). Noting the performance of the simple DD may suffer from noise enhancement, multiple symbol differential detection (MSDD) is proposed to suppress the noise in the reference signals [4]. MSDD

This work was supported by the National Natural Science Foundation of China under Grants 61401041, 61271188 and 61671072, and by the Meteorological Information and Signal Processing Key Laboratory of Sichuan Higher Education (QXXCSYS201601).


M. Huang et al. (Eds.): WICON 2016, LNICST 214, pp. 240–249, 2018.
https://doi.org/10.1007/978-3-319-72998-5_25

jointly detects multiple consecutive symbols, and it has been shown to achieve comparable performance of the coherent counterpart in many interesting scenarios [5–7]. In particular, the authors of [8] introduce the MSDD to M-MIMO system by noting the similarity between channel responses of the impulse radio ultra-wide band (IR-UWB) system [9] and the single-user M-MIMO system. Recently, MSDD has been combined with advanced channel coding techniques to further improve the system performance for IR-UWB [10], which is built upon an novel soft-input soft-output (SISO) framework. Regarding the M-MIMO system, the hard-output decision metric in [8] is not suitable for SISO channel decoding [11]. To this end, a soft-output decision metric and a corresponding SISO framework is needed to further improve the performance of [8].

In this paper, we propose a SISO framework jointly employing MSDD and channel decoding for single user M-MIMO system. The proposed framework does not need any knowledge of CSI, which reduces the system overhead and the intensive computational cost of acquiring CSI. In particular, we develop the SISO MSDD scheme by belief propagation (BP) message passing on a factor graph [12]. Since BP algorithm is also employed by advanced channel codes, such as LDPC decoding, we unify the treatment for SISO MSDD and LDPC channel decoding with a single factor graph and simple message flow scheduling. To be more specific, the soft outputs of SISO MSDD are considered as the inputs of the channel decoding, and the soft outputs of channel decoding are fed back to SISO MSDD, which turns conventional soft-output MSDD into an iterative manner. We also propose a simple blind method to estimate a key parameter needed for detection. Simulations show the good performance of estimated parameter in detection and that the bit error rate (BER) performance of the system can be significantly enhanced by a few iterations with our proposed scheme.

## 2 System Model

We consider the *uplink* transmission scenario, where a signal-antenna user transmit to a $N_R$-antenna base station, and $N_R$ is very large. In each discrete time $k$, the user transmits a symbol $b_k$ drawn from an $M$-ary PSK constellation.

$$\mathbf{r}_k = \mathbf{h}_k b_k + \mathbf{n}_k, \tag{1}$$

where the channel vector is denoted as $\mathbf{h}_k = [h_{k,1}, h_{k,2}, ..., h_{k,N_R}]^T$ and the noise vector is denoted as $\mathbf{n}_k = [n_{k,1}, n_{k,2}, ..., n_{k,N_R}]^T$. We consider a rich scattering environment, so the channel coefficient $h_{k,m}$ from the user to the $m$-th receive antenna and the i.i.d. AWGN components are modeled as a zero-mean circularly-symmetric complex Gaussian random variables, i.e., $h_{k,m} \sim \mathcal{CN}(0, \sigma_h^2)$ and $n_{k,m} \sim \mathcal{CN}(0, \sigma_n^2)$, which are independent over receive antennas. We consider quasi-static channel, i.e., the channel coefficients remain stationary for a sufficient long transmission [8]. Therefore, the time subscript $k$ of the channel vector $\mathbf{h}_k$ in (1) is omitted for simplicity hereafter.

## 3 Noncoherent Detection in Massive MIMO System

### 3.1 Noncoherent Autocorrelation Receiver

The performance of nonherent DD receiver can be improved by MSDD [4]. The differential encoding is needed at the transmitter and 2-DPSK is used to facilitate the noncoherent detection. To avoid explicit CSI, the detector is built on the autocorrelation receiver (AcR) which calculates the correlations between received differential signal vectors. Each transmission burst consists of $K$ data symbols $[a_1, a_2, ...., a_K]$, i.e., $(K+1)$ DPSK modulated differential symbols $[b_0, b_1, ..., b_K]$. Correspondingly, the received differential signal vectors during the whole transmission burst can be stacked into a matrix $R = [\mathbf{r}_0, \mathbf{r}_1, \mathbf{r}_2, ..., \mathbf{r}_K]^T$. In MSDD, $R$ is divided into $S = K/M$ blocks, where $M$ is the block size. The $s$-th block, $s = 1, ..., S$, includes $M$ data symbol vectors. The length of the observation window of the $s$-th block is $M+1$ and the window slides down $M$ differential signal vectors after they have been processed jointly, as shown in Fig. 1. The adjacent observation windows overlap one differential signal vector, and different blocks are processed independently.

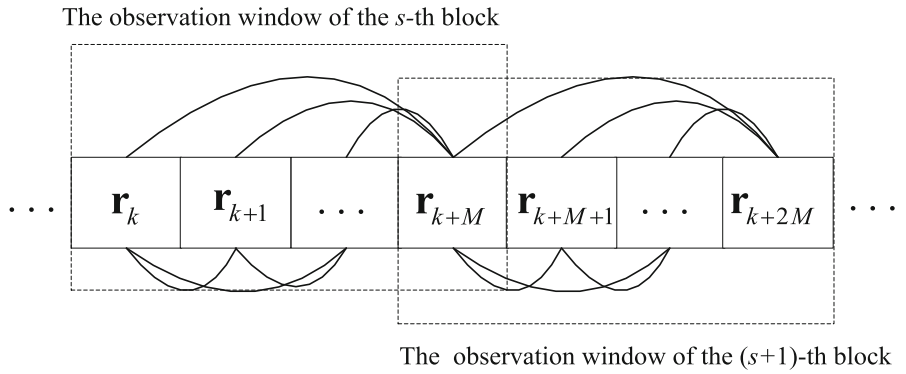


**Fig. 1.** The illustration of the observation window of the $s$-th and the $(s+1)$-th block. The solid lines denote the correlation operation between the received differential signal vectors in a block.

Using the result of differential modulation $b_k^* b_l = (\prod_{z=l+1}^{k} a_z)$, we drive the correlation operation between the $k$-th and the $l$-th received differential signal vectors in the $s$-th block. So the correlation coefficient is calculated as

$$\begin{aligned} z_{k,l} &= \mathbf{r}_k^{\mathrm{H}} \mathbf{r}_l \\ &= ||\mathbf{h}||^2 \cdot b_k^* b_l + n_{k,l}, \\ &= E_g \cdot (\prod_{z=l+1}^{k} a_z) + n_{k,l}, \end{aligned} \tag{2}$$

$$n_{k,l} = b_k^* \cdot \mathbf{h}^{\mathrm{H}}\mathbf{n}_l + \mathbf{n}_k^{\mathrm{H}}\mathbf{h} \cdot b_l + \mathbf{n}_k^{\mathrm{H}}\mathbf{n}_l. \tag{3}$$

We stack all $z_{k,l}$ of the $s$-th block into a vector $\mathbf{z}_s = [z_{k,l}]$, $k = (s-1)M + 1, ..., sM$, $l = (s-1)M, ..., k-1$, which contains $M(M+1)/2$ correlation coefficients. $||\cdot||$ denotes 2-norm of a vector, and $E_g = \|\mathbf{h}\|^2$ represents the captured energy of the signal vector, whose estimation is discussed in Sect. 4.

### 3.2 Multiple Symbol Differential Detection

With the knowledge of $\mathbf{z}_s$, [8] adopts the hard-output decision based on maximum-likelihood estimate of the symbols in $s$-th block jointly, and the MSDD decision metric is

$$\mathbf{b}_s = \underset{\bar{\mathbf{b}}_s \in \{\pm 1\}^{M+1}, \bar{b}_0 = 1}{\arg\max} \bar{\mathbf{b}}_s \mathbf{Z}_s \bar{\mathbf{b}}_s^{\mathrm{H}}, \tag{4}$$

where the diagonal weighting matrix $\mathbf{Z}_s = \mathbf{diag}(\mathbf{z}_s)$ and $\bar{\mathbf{b}}_s \in \{\pm 1\}^{M+1}$ represents the differential candidate symbols.

## 4 Noncoherent Joint Detection and Channel Decoding in Massive MIMO System

In order to further improve the system performance, we incorporate the channel codes. The decoding of powerful channel codes, such as LDPC and Turbo code, relies on soft-outputs of detector to realize iterative algorithm within channel decoding [11]. Obviously, the hard-output decision metric in [8] is not suitable for iterative decoding, so a new soft-output decision metric for the massive MIMO system is needed to study. In this section, we firstly investigate a new soft-output decision metric, and then propose the joint MSDD and channel decoding framework which enables novel additional iterative processing as shown in Fig. 2.

### 4.1 The Soft-Output Decision Metric for SISO MSDD

In order to enable the iterative algorithm, we need to calculate the probability distribution of correlation coefficient $z_{k,l}$.

**Theorem 1.** *For massive MIMO system with AcR, the correlation coefficient $z_{k,l}$ can be approximated as a Gaussian random variable with the mean $\mu = (\prod_{z=l+1}^{k} a_z) \cdot E_g$ and the variance $\sigma^2 = 2E_g \cdot \sigma_n^2 + N_R \cdot \sigma_n^4$:*

$$p(z_{k,l}|\mathbf{x}_s) = \frac{1}{\pi\sigma^2} \exp\left[-\frac{1}{\sigma^2}|z_{k,l} - \mu|^2\right], \tag{5}$$

*where $\mathbf{x}_s = [a_{(s-1)M+1}, a_{(s-2)M+2}, ..., a_{sM}]^T$ is the candidate data symbols in the $s$-th block.*

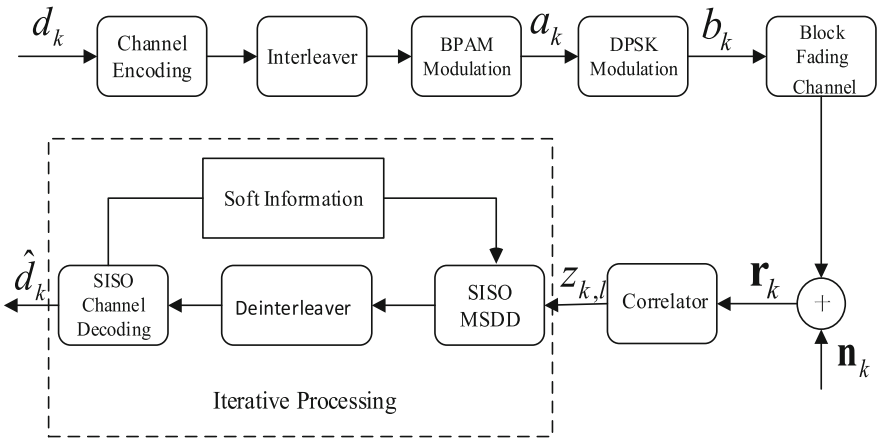


**Fig. 2.** The block diagram of noncoherent joint MSDD and channel decoding in massive MIMO system.

*Proof.* It is noted that the noise component $n_{k,l}$ in (3) contains two linear terms and a noise-by-noise product term. Given the assumed channel model, clearly the first and second term are Gaussian random variables, and the third one can be decomposed into a sum of $N_R$ independent random variables. According to the central limit theorem, the third noise term can be approximated as a Gaussian random variable with zero mean and the variance $N_R \cdot \sigma_n^4$. The approximation is very good when $N_R$ is large in massive MIMO scenario. For DPSK, $|b_k| = 1$. The conditional variance of $n_{k,l}$ is

$$\begin{aligned} Var\left[n_{k,l} \mid \mathbf{h}\right] &= Var\left[b_k^* \cdot \mathbf{h}^{\mathrm{H}}\mathbf{n}_l \mid \mathbf{h}\right] + Var\left[\mathbf{n}_k^{\mathrm{H}}\mathbf{h}{\cdot}b_l \mid \mathbf{h}\right] \\ &\quad + Var\left[\mathbf{n}_k^{\mathrm{H}}\mathbf{n}_l \mid \mathbf{h}\right] \\ &= 2E_g \cdot \sigma_n^2 + N_R \cdot \sigma_n^4 . \end{aligned}$$

So $Var\left[z_{k,l} \mid \mathbf{h}\right] = Var\left[n_{k,l} \mid \mathbf{h}\right] = 2E_g \cdot \sigma_n^2 + N_R \cdot \sigma_n^4$, and the mean $E\left[z_{k,l} \mid \mathbf{h}\right] = E_g \cdot (\prod_{z=l+1}^{k} a_z)$.

Given the observation $\mathbf{z}_s$, the SISO MSDD scheme aims to calculate the *a posteriori* probability (APP) of data symbol $a_k$:

$$p(a_k|\mathbf{z}_s) \propto \sum_{\mathbf{x}_s:\sim a_k} p(\mathbf{z}_s|\mathbf{x}_s)p(\mathbf{x}_s), \tag{6}$$

for $k = (s-1)M+1, ..., sM$, $s = 1, 2, ..., S$, and the notation $\sum_{\mathbf{x}_s:\sim a_k}$ means the summation over all data symbols in $\mathbf{x}_s$ except $a_k$.

### 4.2 Parameter Estimation

It can be concluded from (2) that the correlation coefficient depends on the data symbols and the captured energy $E_g$. To obtain the knowledge of the parameter $E_g$, our receiver employs an energy estimation method

$$\hat{E}_g = \frac{1}{J}\sum_{s=1}^{S}\sum_{k=(s-1)M+1}^{sM}\sum_{l=(s-1)M}^{k-1}|z_{k,l}|\,, \tag{7}$$

where $J$ is the number of the elements in the set of the correlation coefficients $\{\mathbf{z}_s|s=1,2,...,S\}$. In total $J = SM(M+1)/2$. With the estimation $\hat{E}_g$, we substitute it into the signal model (2). We compare the performances of the perfect $E_g$ and the estimated $\hat{E}_g$ in our proposed algorithm in the simulation.

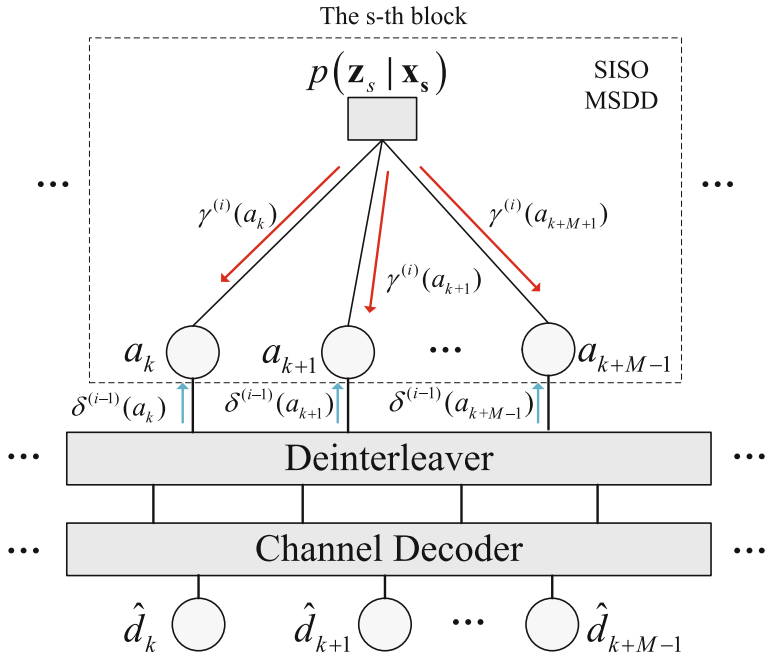


**Fig. 3.** The factor graph of joint MSDD and channel decoding with the block size $M$. $a_k$ is the data symbol. $\hat{d}_k$ is the decoding result of the information bit $d_k$. The red arrows denote extrinsic information from SISO MSDD to the channel decoder in the $i$-th iteration, and the blue arrows denote the extrinsic information from the channel decoder to SISO MSDD in the $(i-1)$-th iteration. (Color figure online)

### 4.3 Joint MSDD and Channel Decoding Framework

In this subsection, we propose a SISO MSDD scheme using BP message passing algorithm. For the calculation of (6), we apply a factor graph to represent the probabilistic model of the system. Then the BP massages can pass on the factor graph. To realize this, we factorize the global probability function $p(\mathbf{z}_s|\mathbf{x}_s)p(\mathbf{x}_s)$ in (6) into many small local functions. Firstly, the channel evidence information function $p(\mathbf{z}_s|\mathbf{x_s})$, or channel transition probability, is obtained by the Gaussian approximation on the discrete noise components according to the Theorem 1

$$p(\mathbf{z}_s|\mathbf{x_s}) = \prod_{l=(s-1)M+1}^{sM} \prod_{k=(s-1)M}^{l-1} p(z_{k,l}|\mathbf{x}_s)$$
$$\propto \prod_{l=(s-1)M+1}^{sM} \prod_{k=(s-1)M}^{l-1}$$
$$\exp(-\frac{1}{\sigma^2}|z_{k,l} - (\prod_{z=l+1}^{k} a_z) \cdot \hat{E}_g|^2). \tag{8}$$

Then we factorize $p(\mathbf{x}_s)$, though in coded system, data symbols can be seen approximately independent by interleaving operation, so

$$p(\mathbf{x}_s) = \prod_{k=(s-1)M+1}^{sM} p(a_k). \tag{9}$$

Substituting (8), (9) into (6) leads to

$$\gamma(a_k) \propto \sum_{\mathbf{x}_s:\sim a_k} p(\mathbf{z}_s|\mathbf{x}_s) \prod_{((l\epsilon I_s)\cap(l\neq k))} \delta(a_l). \tag{10}$$

$I_s = \{(s-1)M+1, ..., sM\}$, and $\gamma(a_k)$ and $\delta(a_l)$ denote the APP and the *priori* information of $a_k$, respectively.

According to (10), we can now calculate $p(a_k|\mathbf{z}_s)$ using a BP message passing algorithm for all $a_k$. Figure 3 shows the framework for joint MSDD and channel decoding. The framework can be divided into two parts: the upper one in dash line box illustrates the SISO MSDD processing in one of the blocks of the size $M$; the under one shows the processing of deinterleaver and channel decoder. The massages exchanged between the MSDD and the channel decoding are known as extrinsic information. The total length of data symbols of a transmission burst are divided into $S$ blocks, they are processed simultaneously.

The algorithm of joint MSDD and channel decoding is briefly described as follows:

- *Initialization*: Since no extrinsic information from channel decoder, the *priori* information $\delta^{(0)}(a_l)$ is assumed equiprobable.
- *Step*1: For the $s$-th block in the $i$-th iteration as shown in the Fig. 3, with the knowledge of $p(\mathbf{z}_s|\mathbf{x_s})$ and the *priori* information $\delta^{(i-1)}(a_l)$, compute $\gamma^{(i)}(a_k)$ in the probability domain using (10). $\gamma^{(i)}(a_k)$ is new APP of data symbol $a_l$, which is considered as the extrinsic information from MSDD and sent into channel decoder.
- *Step 2*: The extrinsic information $\gamma^{(i)}(a_k)$ run several rounds of within the channel decoder, and the channel decoder updates $\delta^{(i-1)}(a_l)$. Updated $\delta^{(i-1)}(a_l)$ is new *priori* information of data symbol $a_l$, which is treated as the extrinsic information from channel decoder and sent into MSDD.
- *Step 3*: Steps 1 and 2 are repeated after a certain number of iterations, and the final channel decoding results of information bits are obtained as results.

## 5 Simulation Results

The performance of the proposed scheme is validated by numerical simulations. There is an uniform linear array with $N_R = 100$ antennas at the receiver. Block fading channel changes after a transmission burst of the length $K = 300$, and the results is averaged over 10000 channel realizations. The signal-to-noise (SNR) is defined as $E_s/\sigma_n^2$. $E_s$ is the transmitted energy per PSK symbol. The LDPC code [13] with coding rate $R = 1/2$ and 10 iterations within the LDPC channel decoder is applied.

Figure 4 presents the BER comparisons of the coded MSDD with different number of iterations between detection and decoding. The block size is $M = 3$, using estimated $\hat{E}_g$. It is clear to see that the BER performance of coded MSDD scheme outperforms the uncoded one with enormous gains by iterative processing with powerful channel code. When the iteration between MSDD and channel decoding is one, the SISO MSDD degrades to the soft-output MSDD since no extrinsic information from LDPC decoding is sent into MSDD, which is the case of MSDD in [8] that we modify with channel encoding. In addition, it is also shown that six iterations brings about 0.5 dB gain compared to single iteration. The gain benefits from that more accurate *priori* information of data symbols is sent into MSDD and more accurate *posteriori* information of data symbols is sent into decoder, at the cost of extra iterations between SISO MSDD and SISO

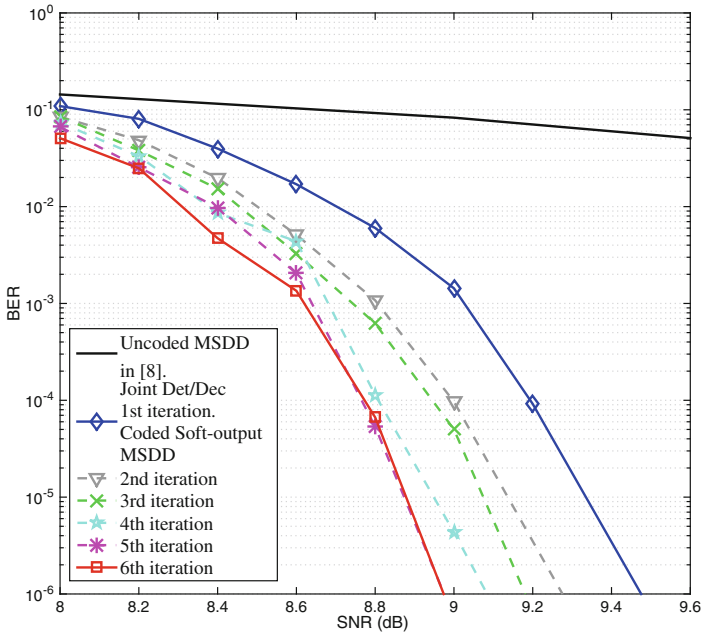


**Fig. 4.** BER comparisons of the coded MSDD with different number of iterations between detection and decoding. Block size $M = 3$.

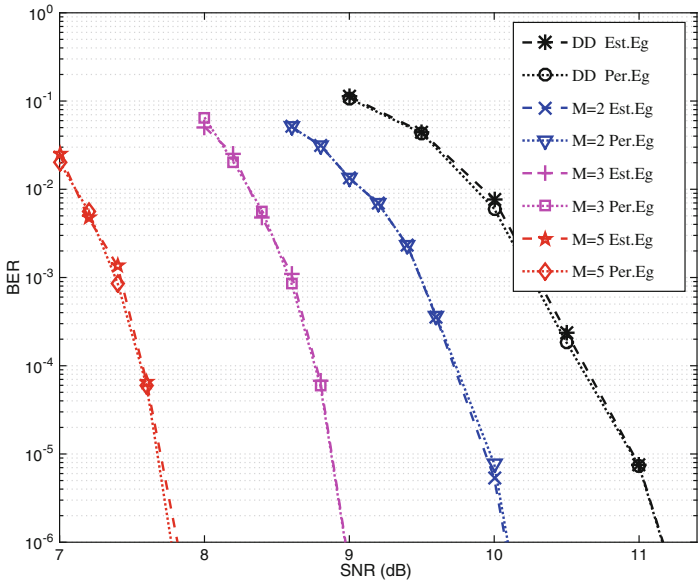


**Fig. 5.** The BER comparisons of the coded MSDD with different block size.

channel decoder. Moreover, the BER result of five iterations is near to that of six iterations, which denotes six iterations between SISO MSDD and SISO LDPC decoder can reach converged error performance.

Figure 5 depicts the BER comparisons of the coded MSDD with different block size. We can observe that when the block size increases, the BER performance is also improved (1.1, 2.3, 3.5 dB at the BER of $10^{-6}$ for $M = 2, 3, 5$). It also shows the impact of the estimated $\hat{E}_g$ on the BER performance. One can see that the estimated $\hat{E}_g$ almost has the same performance as that of the perfect $E_g$, which inspires us that we proposed straightforward way of energy estimation is sufficient for the implementation of our algorithm.

## 6 Conclusions

In this paper, we propose a noncoherent joint MSDD and channel decoding framework in M-MIMO system with BP message passing algorithm. We have integrated BP for SISO MSDD and BP for channel decoding under the massage passing framework, which enables MSDD for computing the *posteriori* of the data symbols with updated information from channel decoder. Simulations indicate that the proposed joint detection and decoding scheme has significantly improved the performance over the hard-output and the soft-output MSDD, with the price of extra iterations between detector and channel decoder. A noncoherent joint MSDD and channel decoding framework adapted for multi-user in massive MIMO system shall be for future work.

## References


1. Rusek, F., Persson, D., Lau, B.K., Larsson, E., Marzetta, T., Edfors, O., Tufvesson, F.: Scaling up MIMO: Opportunities and challenges with very large arrays. IEEE Signal Process. Mag. **30**(1), 40–60 (2013)
2. Marzetta, T.: Noncooperative cellular wireless with unlimited numbers of base station antennas. IEEE Trans. Wirel. Commun. **9**(11), 3590–3600 (2010)
3. Lu, L., Li, G., Swindlehurst, A., Ashikhmin, A., Zhang, R.: An overview of massive MIMO: Benefits and challenges. IEEE J. Sel. Topics Signal Process. **8**(5), 742–758 (2014)
4. Divsalar, D., Simon, M.K.: Multiple-symbol differential detection of MPSK. IEEE Trans. Commun. **38**(3), 300–308 (1990)
5. Lottici, V., Tian, Z.: Multiple symbol differential detection for UWB communications. IEEE Trans. Wirel. Commun. 7(5) (2008)
6. Wang, C., Gao, H., Lv, T.: Soft-input soft-output multiple symbol detection for ultra-wideband systems. KSII Trans. Internet Inf. Syst. **9**(7), 2614–2632 (2015)
7. Wang, T., Lv, T., Gao, H., Lu, Y.: BER analysis of decision-feedback multiple-symbol detection in noncoherent MIMO ultrawideband systems. IEEE Trans. Veh. Technol. **62**(9), 4684–4690 (2013)
8. Schenk, A., Fischer, R.F.H.: Noncoherent detection in massive MIMO systems. In: Proceedings of the International ITG/IEEE Workshop on Smart Antennas, pp. 1–8, March 2013
9. Witrisal, K., Leus, G., Janssen, G., Pausini, M., Troesch, F., Zasowski, T., Romme, J.: Noncoherent ultra-wideband systems. IEEE Signal Process. Mag. **26**(4), 48–66 (2009)
10. Zhou, Q., Ma, X.: Soft-input soft-output multiple symbol differential detection for UWB communications. IEEE Commun. Lett. **16**(8), 1296–1299 (2012)
11. Wiberg, N., Loeliger, H.-A., Kotter, R.: Codes and iterative decoding on general graphs. Eur. Trans. Telecommun. **6**(5), 513–525 (1995)
12. Kschischang, F.R., Frey, B.J., Loeliger, H.-A.: Factor graphs and the sum-product algorithm. IEEE Trans. Inf. Theory **47**(2), 498–519 (2001)
13. MacKay, D.: Good error-correcting codes based on very sparse matrices. IEEE Trans. Inf. Theory **45**(2), 399–431 (1999)

# Downlink PDMA in the Heterogeneous Network

Jie Zeng(✉), Xiaofeng Lin, Liping Rong, and Xin Su

Tsinghua National Laboratory for Information Science and Technology, Research Institute of Information Technology, Tsinghua University, Beijing, China
zengjie@tsinghua.edu.cn

**Abstract.** Non-orthogonal multiple access (NOMA) is considered as a promising multiple access technology, which could satisfy various incremental requirements of the coming fifth generation (5G) mobile communication system. As a novel NOMA scheme based on the joint design of the transmitter and receiver, pattern division multiple access (PDMA) could enhance spectrum efficiency significantly, compared to traditional orthogonal multiple access (OMA) schemes. In this paper, a particular pattern design of downlink PDMA in heterogeneous network is proposed. In overlapping deployment scenario of macro cells and small cells, the downlink signals are transmitted with a novel spatial and power domain superposition pattern. The user pairing and spatial/power allocation schemes are therefore proposed optimizing the pattern design. Analysis and simulation results illuminate the pattern design of downlink PDMA could enhance the spectrum efficiency obviously.

**Keywords:** Heterogeneous network · Non-orthogonal multiple access
Pattern division multiple access · Superposition

## 1 Introduction

Radio access technologies (RATs) for mobile communications are typically characterized by multiple access (MA) schemes. MA allows multiple users to access and share the resources simultaneously. From 1G to 4G, MA techniques vary accompanying with the evolution of wireless communication systems, including frequency-division multiple access (FDMA), time-division multiple access (TDMA), code-division multiple access (CDMA), and orthogonal frequency-division multiple access (OFDMA). In orthogonal multiple access (OMA) schemes, different users are allocated with radio resources which are orthogonal in either the time, frequency, or code domain to avoid or alleviate inter-user interference. The above-mentioned MA schemes are all OMA schemes. With simple single-user detection, OMA can achieve good system-level throughput performance in packet-domain services. However, due to the orthogonal resource allocation mechanisms that OMA schemes take, the maximum number of supported users is strictly limited by the finite resources. Besides, it is known that OMA cannot always achieve the sum rate of multiple user wireless communication systems.


M. Huang et al. (Eds.): WICON 2016, LNICST 214, pp. 250–260, 2018.
https://doi.org/10.1007/978-3-319-72998-5_26

It is anticipated that explosive data traffic increase will happen in 5G era. Besides, 5G needs to support massive connectivity of users, due to new traffic types and data services are emerging, notably machine-to-machine communications to support concepts such as the smart grid, smart homes and cities, and e-health. In order to guarantee the sustainability of the 3rd Generation Partnership Project (3GPP) RATs over the coming Release 14 and onward, new solutions that are competent to meet prospective challenges must be investigated [1]. Different from conventional OMA schemes, non-orthogonal multiple access (NOMA) can support much more users via non-orthogonal resource allocation. NOMA is expected to be adopted to increase system throughput and accommodate massive connectivity. From the perspective of information theory, NOMA outperforms orthogonal multiple access and it is optimal in the sense of achieving the capacity region of the downlink channel. Successive interference cancellation (SIC) is commonly used in the process of the multi-user signal separation on the receiver side [2, 3]. With the robust performance gain, NOMA scheme could be utilized widely in practical deployment [4].

Pattern division multiple access (PDMA), is novel NOMA scheme evolving from SIC amenable multiple access (SAMA), and it is based on the joint design of the transmitter and receiver to optimize of multi-user communication system. Non-orthogonal pattern is utilized to distinguish different users at the transmitter, and SIC is adopted to achieve the quasi optimal multi-user detection at the receiver. A pattern design of PDMA is presented in this paper to satisfy the downlink channel. In overlapped deployment scenario of macro cells and small cells, the paired users are superposed in the same resource blocks and with appropriate power allocation. Simulation results show that both the average and edge throughput have been greatly improved.

The rest of this paper is organized as follows: Sect. 2 describes the system model of downlink PDMA in the heterogeneous network. Section 3 presents the method of user pairing, the spatial superposition scheme and the power allocation scheme of PDMA. Section 4 introduces the detail simulation model and throughput performance. Finally, Sect. 5 concludes the paper.

## 2 System Model

In this paper, an overlapped deployment of macro cells and small cells is considered as is shown in Fig. 1. Without loss of generality, only one sector of a macro cell is shown. Small cells are randomly distributed in every sector in the form of clusters to provide hotspot coverage. Users are randomly distributed in macro cells and small cells. The users are divided into two kinds: the hotspot users and common users. Hotspot users are distributed in small cells. Hotspot users are also divided into two kinds: the users distributed in the coverage of small cell and the users in the coverage of small cell cluster but not in the coverage of small cells. Macro base station (BS) and small cell BS could be scheduled uniformly. All users are assumed static when we introduce the spatial domain and power domain allocation scheme.

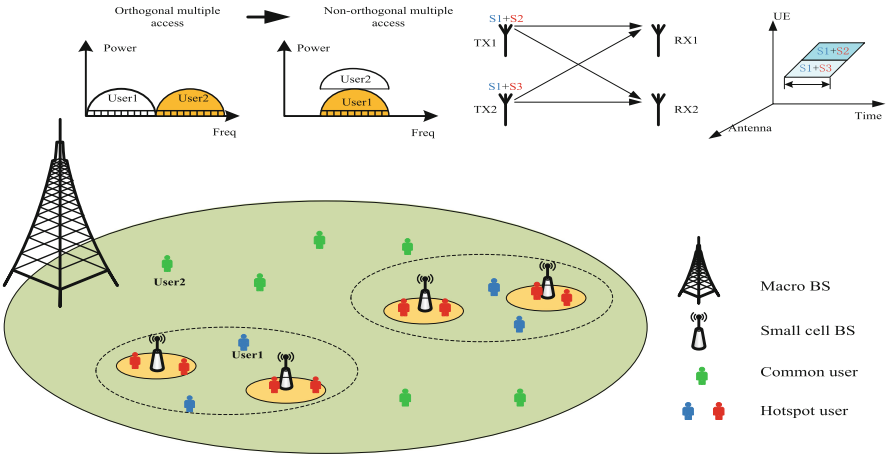


**Fig. 1.** A overlapped deployment of macro cells and small cells

The basic thought of PDMA is utilizing non-orthogonality of the signal pattern based on power domain, space domain and code domain (jointly or separately) to distinguish signals of different users. And non-orthogonal signals can be separated and detected by SIC receivers effectively. The non-orthogonal transmission on the time-frequency domain realizes the enhancement of spectrum efficiency [5, 6].

The basic principle of PDMA is improving resource utilization through the equivalent diversity. According to the theory of V-BLAST system [7], the equivalent diversity of the *i*th interference cancellation stage is

$$N_{div} = N_R - N_T + i \tag{1}$$

where $N_R$ denotes the receive diversity and $N_T$ denotes the transmit diversity. The signal processing from transmitter to receiver is shown in Fig. 2.

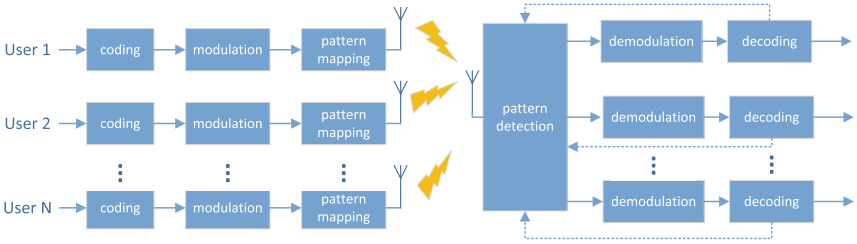


**Fig. 2.** Signal processing in communication system with PDMA

Multi-user information theory points out that the sum capacity of NOMA scheme could be close to the theoretical limit. The main study point of this paper is applying

the PDMA of spatial and power domain to transmitter design in the heterogeneous network. The contents consist the allocation of power, the joint optimization of time-frequency resources combined with power and multiple user clustering. In the power domain PDMA model, User 1 and User 2 are defined as cell-edge user and central user respectively. Different from the orthogonal condition, User 1 and User 2 which are allocated different power in the same frequency band. The spectrum resources are saved in this way with the growth of the corresponding gain. An example is present in Fig. 1 to compare non-orthogonal with orthogonal multi-user access in the power domain. It is assumed that User 1 is the user in the edge small cell cluster and is served by macro BS, and User 2 will be selected from macro BS correspondingly. Macro BS will allocate different transmitted power to User 1 and User 2. If User 1 is served by small cell, the principle is the same. The optimization of spatial resource is also presented in Fig. 1. The data streams are transmitted by the superposed spatial domain.

In the downlink, SIC process is adopted to get the signal of every user. The order of decoding is mainly decided by the decreasing channel gain normalized by noise and inter-cell interference power. Based on the order, it is assumed that any user can correctly decode the signals of any other user which has the prior decoding order before the corresponding user. In this way, the user with higher channel gain could remove the inter-user interference from the user which has the lower channel gain. Assuming successful decoding and no error propagation, every receiver could get the signal accurately.

## 3 PDMA Transmitter Pattern Design

### 3.1 User Pairing Strategy

The main research object studied in this paper is the users of the small cell clusters. Cell-edge users and central users are selected by the user pairing strategy. At the initial stage of the system, users access BS according to the reference signal received power (RSRP). Users select their served BS by the formula:

$$BS_{serving}(b) = \underset{b}{argmax}\{SINR_{u,b}\} \tag{2}$$

where $b$ denotes the BS and $u$ denotes the user. Every user selects the served BS according to the polling mechanism. After the selection of BS, the users in the coverage area of small cell cluster which are not in the coverage radius of the small cell are regarded as the cell-edge users. The cell-edge user is called $U_{edge}$ for short. The SIC scheme could separate the mixed signal for the discriminating power allocation. So every cell-edge user will match a central user. The central user is called $U_{central}$ for short. According to the served BS of $U_{edge}$, the next step is to decide the pairing user to $U_{edge}$. Because $U_{edge}$ in the small cell cluster but not in the coverage of the small cell, the served BS has two: macro BS and small cell BS. If the served BS of $U_{edge}$ is macro

BS, $U_{central}$ will be chosen from the users served by the macro BS. The selection criteria is shown as follows:

$$\begin{aligned} U_{central} &= \underset{m^* \in Mue, m \in Mue,}{argmax} \left\{ \alpha_{m^*,m} \right\} \\ \alpha_{m^*,m} &= \left\| |h_{m^*}|^2 / N_{0,m^*} - |h_m|^2 / N_{0,m} \right\| \end{aligned} \tag{3}$$

where $m^*$ denotes the $U_{edge}$ and $m$ denote the user served by macro BS. $m^*$ and $m$ are in the set of *Mue* which is the set of users served by macro BS. $|h_{m^*}|^2 \Big/ N_{0,m^*}$ and $|h_m|^2 / N_{0,m}$ express the channel gain respectively. $\alpha_{m^*,m}$ denotes the difference value of the two channel gain.

If the served BS of $U_{edge}$ is small cell BS, $U_{central}$ will be chosen from the users served by the small cell BS. The selection criteria is shown as follows:

$$\begin{aligned} U_{central} &= \underset{m^* \in Sue, m \in Sue,}{argmax} \left\{ \alpha_{m^*,m} \right\} \\ \alpha_{m^*,m} &= \left\| |h_{m^*}|^2 / N_{0,m^*} - |h_m|^2 / N_{0,m} \right\| \end{aligned} \tag{4}$$

where $m^*$ denotes the $U_{edge}$ and $m$ denote the user served by small cell BS. $m^*$ and $m$ are in the set of *Sue* which is the set of users served by small cell BS. $|h_{m*}|^2 / N_{0,m*}$ and $|h_m|^2 / N_{0,m}$ express the channel gain respectively. $\alpha_{m*,m}$ denotes the difference value of the two channel gain.

After the user pairing strategy, every $U_{edge}$ will have a corresponding $U_{central}$. Every $U_{central}$ may have more than one $U_{edge}$.

### 3.2 Spatial Domain Enhancement of PDMA

The users in the same group could use the same resources through the design of the pattern in the spatial domain, as shown in Fig. 3(b). In traditional OMA schemes, user 1 sends symbol S1 through antenna TX1, while user 2 sends symbol S2, symbol S3 through antenna TX1, antenna TX2 respectively. However, the performance of the system is poor even SIC receivers are utilized, that TX1 sends S1, S2 simultaneously. In PDMA scheme, simple spatial coding is expected to be adopted. As shown in Fig. 3(b), TX1 sends S1 + S2, while TX2 sends S1 + S3. Thus, S1, S2 and S3 have identical equivalent diversity. The performance of the system can be satisfied by utilizing SIC receivers, for that the data streams on the superposed spatial domain could be separated by the SIC level demodulation. The structure of the spatial pattern is designed as follows:

$$H_{s,2\times 3} = \begin{pmatrix} 1 & 1 & 0 \\ 1 & 0 & 1 \end{pmatrix} \tag{5}$$

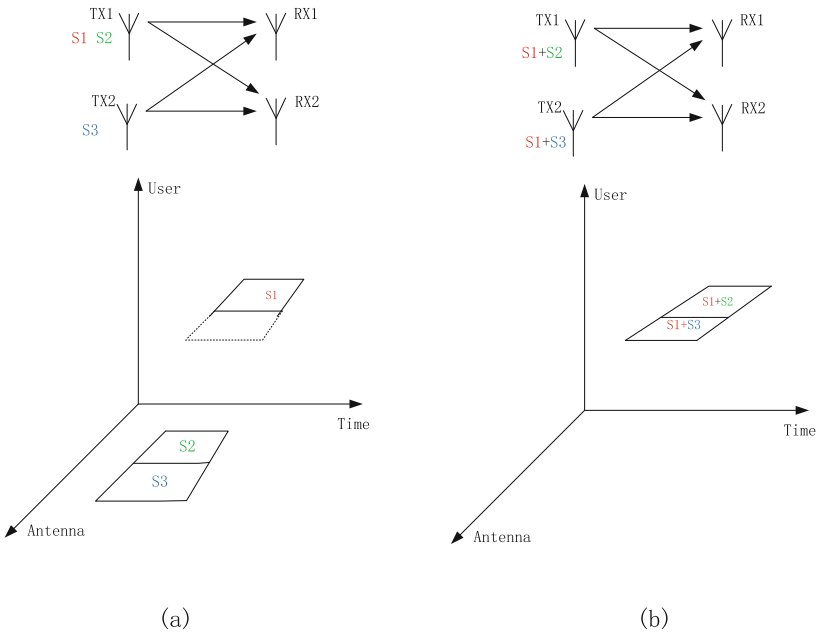


**Fig. 3.** Illustration of spatial domain scheme with PDMA

### 3.3 Power Allocation Enhancement of PDMA

The power allocation considers every group of users. It is assumed that the total transmit power $P_b(i_b(k))$ indicates the index of the users. At every sub carrier of bandwidth $b$ is a total of the coded modulation symbols, $d_b(i_b(k))$, of the $i_b(k)$-th user. So the sum signal $x_b$ is superposed as follows:

$$x_b = \sum_{k=1}^{M_b} \sqrt{P_b(i_b(k))} d_b(i_b(k)) \tag{6}$$

where $E\left[\left|d_b(i_b(k))\right|^2\right] = 1$ and $P_b(i_b(k))$ is the allocated transmit power to the user $i_b(k)$ at bandwidth $b$ and $\sum_{k=1}^{M_b} P_b(i_b(k)) = P$. The $N_r$ dimensional received signal vector of user $i_b(k)$ at every sub carrier of bandwidth $b$, $Y_b(i_b(k))$, is represented by

$$\begin{aligned} Y_b(i_b(k)) &= H_{ch}(i_b(k)) * H_s x_b + N_b(i_b(k)) \\ &= H(i_b(k)) x_b + N_b(i_b(k)) \end{aligned} \tag{7}$$

where $H_{ch}(i_b(k))$ is the $N_r$ -dimensional channel coefficient vector of user $i_b(k)$. $H_{ch}(i_b(k))$ consists of distance dependent loss, shadowing loss and instantaneous fading coefficients. $N_b(i_b(k))$ is the $N_r$ -dimensional noise plus inter-cell interference. And $*$means the element-wise product. Let $H = H_{ch} * H_s$.

Assuming that the receiver treats inter-cell interference as white noise, at the receiver maximal ratio combining is applied to $Y_b(i_b(k))$ as follows:

$$\begin{aligned}\tilde{Y}_b(i_b(k)) &= H^H(i_b(k))Y_b(i_b(k))/||H|| \\ &= \sqrt{G_b(i_b(k))}x_b + n_b(i_b(k))\end{aligned} \tag{8}$$

where $G_b(i_b(k)) = \|H(i_b(k))\|^2$ is the combining gain after maximal ratio combining and $n_b(i_b(k)) = H(i_b(k))N_b(i_b(k))/||H_b||$ is the noise plus inter-cell interference after maximal ratio combining. The average power of $n_b(i_b(k))$ is presented as $N_{0,b}(i_b(k)) = E[|n_b(i_b(k))|]^2$. So the $\tilde{Y}_b(i_b(k))$ could be expressed as:

$$\tilde{Y}_b(i_b(k)) = \sqrt{G_b(i_b(k))}\sum_{k=1}^{M_b}\sqrt{P_b(i_b(k))}d_b(i_b(k)) + n_b(i_b(k)) \tag{9}$$

In downlink of the system, the SIC process is implemented at the user receiver. The optimal order for decoding is in the order of decreasing channel gain normalized by noise and inter-cell interference power. It is assumed that any user could correctly decode the signals of other users whose decoding order comes before the corresponding user. Take 3 users for example, User 1, User 2 are the cell-edge users and User 3 is the central user. User 1 and user 3 form user pair 1, while user 2 and user 3 form user pair 2, as illustrated in Fig. 4. Assuming successful decoding and no error propagation, the throughput of User $i$, $Thr_i$ is represented as

$$Thr_1 = log_2\left(1 + \frac{P_1|h_1|^2}{P_3|h_1|^2 + N_{0,1}}\right) \tag{10}$$

$$Thr_2 = log_2\left(1 + \frac{P_2|h_2|^2}{P_3|h_2|^2 + N_{0,2}}\right) \tag{11}$$

$$Thr_3 = log_2\left(1 + \frac{P_3|h_3|^2}{N_{0,3}}\right) \tag{12}$$

So to get the value of $P_i$, the sum throughput $Thr$ of User $i$ will be maximized. The expression is shown as follows:

$$Thr = max(Thr_1 + Thr_2 + Thr_3) \tag{13}$$

From (10), (11), (12), it could be seen that power allocation for each user greatly affects the user throughput performance and thus the modulation and coding scheme used for data transmission of each user. So the overall cell throughput, cell-edge throughput, and user fairness are closely related to the power allocation scheme adopted. The exact value of $P_i$ will be got with solving the maximum value of $Thr$.

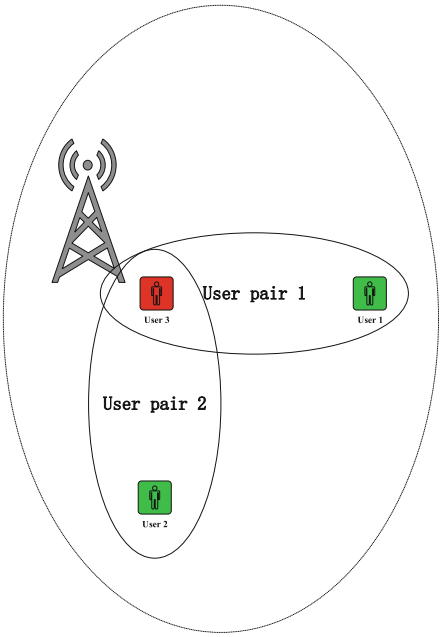


**Fig. 4.** Illustration of 3 users scenario.

# 4 Simulation and Analysis

## 4.1 Simulation Assumptions

We model a heterogeneous cellular network with 19 macro BSs. According to the 3GPP standards [8, 9], macro BS is located in the center of the three hexagonal sectors. The inter-site distance is 500 m. Macro BSs equip with three directional antennas with each antenna covering one sector. In our simulation, there is one small cell cluster randomly distributed in every sector for hotspot deployment. The radius of the small cell cluster is 70 m. There are 4 small cells in every cluster. The small cell BS is located in the center of the small cell. The radius of the small cell is 50 m. The transmitting and receiving antennas are all isotropic antenna in the small cell BSs and users.

Users are dropped randomly with uniform distribution. There are two types of users: common users and hotspot users. Hotspot users are distributed in the coverage area of small cell. Common users are distributed in macro cell. The specific parameters are shown in Table 1.

All the users are stationary, so the total number in each sector remains constant during the simulation.

**Table 1.** Simulation parameters

| Parameter | Statistical characterization |
|---|---|
| *LTE network model* | |
| Cell layout | 19 sites/57 sectors |
| Tx power for macro BS | 46 dBm |
| Tx power for small cell BS | 30 dBm |
| Number of cluster per sector | 1 |
| Number of small cell per sector | 4 |
| Inter-site distance | 500 m |
| Cluster radius | 70 m |
| Small cell radius | 50 m |
| Carrier frequency | 2 GHz |
| Pathloss model for macro | 128.1 + 37.6log(R), R in Kms |
| Pathloss model for small cell | 140.3 + 36.7log(R), R in Kms |
| Shadowing standard deviation | 8 dB |
| Shadowing correlation distance | 50 m |
| Thermal noise density | −174 dBm/Hz |
| *User model* | |
| Total number of users | 60 |
| Hotspot users ratio | 2/3 |
| Antenna gain | 0 dBi |

### 4.2 Results and Analysis

According to the system level simulation model, we evaluate the system performance of the power allocation scheme with PDMA in power domain. We simulate two representative scenarios for comparison. The scenarios are set as follows:

1. Based on the system model presented in Sect. 2, the system adopts OMA as a comparison scheme. Equal transmission power is allocated to each user.
2. Based on the system model presented in Sect. 2, the signals are transmitted from BS according to the pattern design scheme with PDMA.

The main discriminant standard of system performance is the throughput of the users. So we count user throughput of each scenarios. The cumulative distribution function (CDF) of the user throughput is plotted. Assuming there is one small cell cluster in every sector, the result is shown in Fig. 5.

From the distribution of the user throughput, it is clearly that the pattern design scheme with PDMA really improves the user throughput by more than 20%, more users could get a higher throughput based on the spatial and power domain overlapped transmission. By this way, the total throughput of the system can also be improved correspondingly.

PDMA is more appropriate for multi-user scenarios compared to OMA. With the number of users increasing, pattern design scheme with PDMA will gain more advantages by utilizing non-orthogonal power allocation scheme. From this point of

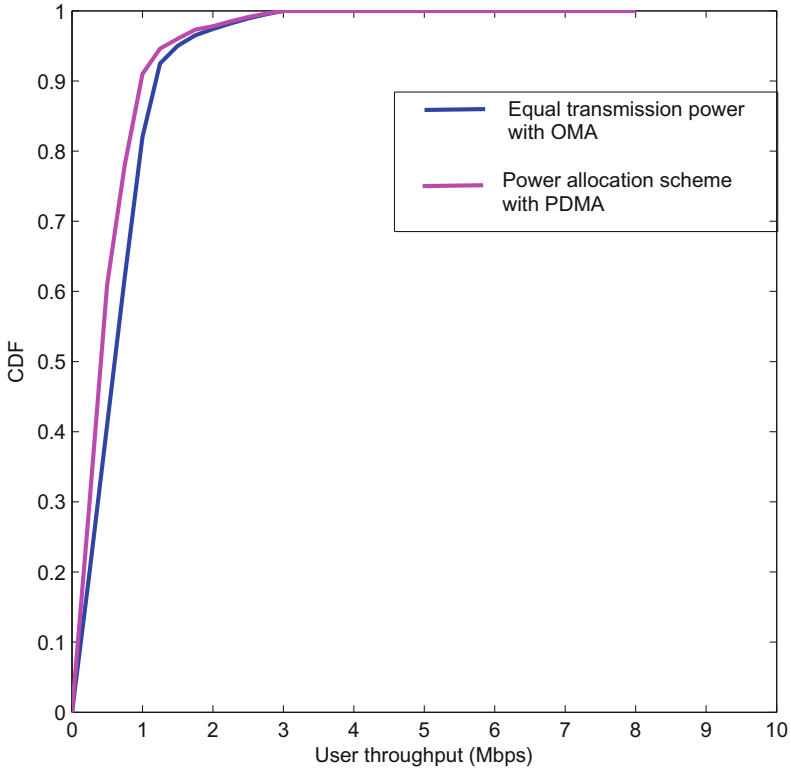


**Fig. 5.** CDF of users' throughput

view, the pattern design scheme with PDMA is suitable for the dense users distribution case. Moreover, our proposed pattern design scheme with PDMA is of low complexity, which means that it is feasible and cost-effective in practical scenarios.

## 5 Conclusion

In this paper, we reviewed the multiple access schemes of cellular mobile communications. In the context of 5G, the requirements of further increasing system throughput and supporting massive connectivity prompt the research on NOMA. Some merits of NOMA schemes were listed in this paper. PDMA which is based on the joint-design of the transmitter and receiver could enhance spectrum efficiency and system throughput. The spatial and power domain superposition was considered. In overlapped deployment scenario of macro cells and small cells, the pairing users in the same cluster were superposed in the same resource blocks and allocated with different power. The signals were transmitted with spatial and power domain superposition. The simulation results shed light on the pattern design scheme with PDMA in the heterogeneous network. The CDF of our proposed scheme is superior to that for OMA, and it means that our

proposed scheme could enhance the system throughput and have an effect on the following research.

**Acknowledgements.** This work was supported by the China's 863 Project (No. 2015AA01A709), the National S&T Major Project (No. 2014ZX03004003), Science and Technology Program of Beijing (No. D161100001016002), S&T Cooperation Projects (No. 2015DFT10160B), State Key Laboratory of Wireless Mobile Communications, China Academy of Telecommunications Technology (CATT), and Beijing Samsung Telecom R&D Center.

## References

1. Andrews, J., Buzzi, S., Choi, W., Hanly, S., Lozano, A., Soong, A., Zhang, J.: What will 5G be? arXiv preprint arXiv:1405.2957 (2014)
2. Otao, N., Kishiyama, Y., Higuchi, K.: Performance of non-orthogonal access with SIC in cellular downlink using proportional fair-based resource allocation. In: 2012 International Symposium on Wireless Communication Systems (ISWCS), pp. 476–480. IEEE (2012)
3. Benjebbour, A., Li, A., Saito, Y., Kishiyama, Y., Harada, A., Nakamura, T.: System-level performance of downlink noma for future LTE enhancements. In: 2013 IEEE Globecom Workshops (GC), pp. 66–70. IEEE (2013)
4. Al-Imari, M., Xiao, P., Imran, M.A., Tafazolli, R.: Uplink non-orthogonal multiple access for 5G wireless networks. In: 11th International Symposium on Wireless Communications Systems (ISWCS), pp. 781–785. IEEE (2014)
5. Dai, X., Chen, S., Sun, S., Kang, S., Wang, Y., Shen, Z., Xu, J.: Successive interference cancelation amenable multiple access (SAMA) for future wireless communications. In: 2014 IEEE International Conference on Communication Systems (ICCS), pp. 222–226. IEEE (2014)
6. Myneni, S., Misra, S., Xue, G.: SAMA: serverless anonymous mutual authentication for low-cost RFID tags. In: 2011 IEEE International Conference on Communications (ICC), pp. 1–5. IEEE (2011)
7. Truhachev, D.: Universal multiple access via spatially coupling data transmission. In: 2013 IEEE International Symposium on Information Theory Proceedings (ISIT), pp. 1884–1888. IEEE (2013)
8. G. TR36.814: Further Advancements for E-UTRA Physical Layer Aspects v.9.0.0 (2010)
9. G. TR36.872: Small cell enhancements for E-UTRA and E-UTRAN - Physical layer aspects v.12.1.0 (2013)

# Internet of Things

# Edge Caching to Deliver Mobile Content in Vehicular Ad Hoc Networks

Zhou Su(✉), Qichao Xu, and Yilong Hui

School of Mechatronic Engineering and Automation, Shanghai University, Shanghai 20072, China
zhousu@ieee.org

**Abstract.** Vehicular ad hoc networks (VANETs), which can provide drivers with convenience and entertainment services, have attracted attentions from both academia and industry. In the VANETs, caching contents at the edge of road-side units (RSUs) can facilitate the timely content delivery to driving-through vehicles when requested. However, as both the scale of network and the number of content keep increasing, due to the limited cache capacity, how to selectively keep the replicas in the cache in VANETs becomes a challenging issue. In this paper, to resolve the above issue, we firstly make an analysis on the edge caching based on content access, vehicle velocity and road traffic. Then, we propose a cost model to decide whether and where to obtain the caching replica of content when the moving vehicle requests for it. In addition, we prove the efficiency of our proposed scheme with intensive simulation experiments.

**Keywords:** Vehicular ad hoc networks · Dynamic content · Caching

## 1 Introduction

Vehicular ad hoc networks (VANETs) [1–3] have become a promising filed as diverse multimedia communication services can be provided for drivers during driving. Currently, both the inter-vehicle content delivery and roadside-to-vehicle content delivery have already been applied to daily life with a great deal of market potential [4–10]. In VANETs, road-side units (RSUs) and on-board units (OBUs) are two important elements for content delivery. RSUs are a group of fixed peers, which are placed along the side of roads to provide moving vehicles with wireless communications within their coverage areas. OBUs are moving vehicles with wireless equipments, by which the OBUs may request content during moving. With OBUs and RSUs, VANETs can be formed where each vehicle can communicate with other vehicles and can also access backbone networks through RSUs.

Compared with RSUs, OBUs always have limited storage capacity and unstable connection. Therefore it becomes necessary to store several replicas of the original content on the edge of a group of RSUs. When an OBU requests for content, if the replica of this content is available in the cache of its connecting RSU, the requested content can be provided directly from the RSU to this moving vehicle directly. Otherwise, the OBU needs to contact other OBUs or other


M. Huang et al. (Eds.): WICON 2016, LNICST 214, pp. 263–271, 2018.
https://doi.org/10.1007/978-3-319-72998-5_27

far RSUs connected by wired network to fetch the content, resulting in an extra user delay.

However, due to the limited caching capacity of RSU, with the increasing scale of various content delivered in the VANETs, it is impossible to keep caching the replicas of all content in RSUs. When the cache of an RSU exceeds its capacity limit, some replica must be removed to make room for the newly coming content. Then, when a future request from an OBU rises for this removed replica, as it is not available in its connecting RSU, the OBU will wait for more time to get it from other sites. Therefore, how to determine the replicas to be cached in the RSUs becomes a new challenge.

Vehicular content caching is different from the conventional caching [11,12]. On one hand, as the content requester in VCNs is a moving vehicle, the requested content needs to be delivered to a moving peer, instead of a static content requester in the conventional caching scenario. On the other hand, when a moving vehicle needs to get a content, there may be multiple options including getting content from other moving vehicles or from the connected RSU, while the conventional caching is just to fetch the requested content from its server. Therefore, in this paper an edge caching scheme is studied by fully exploring the features of vehicles and utilizing both the infrastructure and infrastructureless vehicle-to-vehicle communication modes.

The remainder of the paper is organized as follows. Section 2 reviews the related work. Section 3 presents the system model. Section 4 presents the analysis of caching for vehicular content request and delivery. Section 5 evaluates the performance of the proposal using extensive simulations and Sect. 6 closes the paper with concluding remarks.

## 2 Related Work

There are multiple works on VANETs. A swarming protocol for ad hoc wireless network is proposed in [13] by using a gossip mechanism and a piece-selection strategy, where the content can be delivered and shared in a peer-to-peer pattern among vehicles. Cabernet [14] is developed to deliver vehicular contents among moving peers using WiFi access points during the time of driving. [15] develops a content search mechanism (i.e., find out the location where the particular content is stored) based on the analysis of social cluster relations. To search for the desired content, the query can be efficiently sent out by considering the parameters such as bandwidth and lifetime. [16] presents an information sharing method which can maximize the spread of information queries among vehicles, and reduce the useless queries and duplicated replies at the same time.

Mobile content dissemination is studied with variable sensitivity levels and lengths of delay in an opportunistic RSU-aided network [17], where the storage of RSU is analyzed with different sizes allocated by a heuristic algorithm. A design of distributed content services in peer-to-peer based vehicular networks is presented [18]. The proposed scheme can improve users' satisfaction and achieve fairness through opportunistic transmissions and the media-aware content distribution. [19] propose to explore the parked vehicles to help with

vehicular content distribution. [20] develops a coalitional graph game for modeling the cooperation where OBUs can be organized into coalitions to coordinate transmissions autonomously. It allows different OBUs to exchange and complement content when some content is lost during delivery.

In the least recently used (LRU), the content which is the least recently accessed by users would be removed from the cache, when the near-capacity cache needs to accommodate the newly coming content. In the least frequently used (LFU), the content which is the least frequently accessed would be removed. The main problem of LRU is that the caching is determined only by the interval between two requests, where the characteristics of content are not well considered, while in LFU, content which was frequently accessed in a past period may remain in the cache for a long time even it has lost its popularity and has not been requested by the user recently.

## 3 System Model

Each RSU $r_i$ $(i = 1, \ldots, I)$ is placed in different locations of the network. Within the coverage area of $r_i$, there are several roads and the $j$-th $(j = 1, \ldots, J)$ road in $r_i$'s coverage area is denoted by $l_{i,j}$. Let $c_{i,j}$ denote the length of road $l_{i,j}$, and let $u_{i,j}$ denote the number of lanes of road $l_{i,j}$. For road $l_{i,j}$, there could be multiple moving vehicles where $o_{i,j,k}$ denotes the $k$-th moving vehicle on road $l_{i,j}$. For the vehicles moving on road $l_{i,j}$, the velocity of vehicle $o_{i,j,k}$ is denoted by $v_{i,j,k}$. The velocity of different vehicles is divided into $N$ discrete levels by $ls_n$ $(n = 1, \ldots, N)$,

$$ls_n \in [\min(v_{i,j,k}), \max(v_{i,j,k})]. \tag{1}$$

The arrival rate of moving vehicles at each level of velocity is defined by $ra_n$ $(n = 1, \ldots, N)$, where

$$RA = \sum_{n=1}^{N} ra_n. \tag{2}$$

According to [21], the occurrence probability of each velocity level is obtained by $p_{ra_n}$ $(n = 1, \ldots, N)$, where

$$p_{ra_n} = \frac{ra_n}{RA}. \tag{3}$$

For communications between moving vehicle $o_{i,j,k}$ and its connected RSU $r_i$, the coverage area of $r_i$ is divided into several zones according to the transmission rate of vehicles to the RSU. As indicated in [22] and the references therein, with different distances to RSUs, vehicles would suffer from different channel impairments and transmit at different data rate. In zone $u$ $(u = 1, \ldots, U)$, the transmission rate $bw^u_{r_i,o_{i,j,k}}$ between moving vehicle $o_{i,j,k}$ and its connected RSU $r_i$ is determined by the zone model, in which different mobility zone within the coverage area of RSU has different transmission rate.

The arrival of content requests from moving vehicles follows a Poison process. Let $\lambda_{i,j,k}$ denote vehicle $o_{i,j,k}$'s request rate. Let $Q$ denote the total number of content which can be requested. For the $q$-th ($q = 1, \ldots, Q$) content, its data size is defined by $s_q$. The original content is stored in the content server which is connected to RSUs by wire connections. The RSUs can only store replicas of certain content due to a limited caching capacity. Considering that some content may be requested more frequently than others, content in VANETs is modeled to have different popularity. The popularity of content follows a Zipf distribution [12]. The probability that content $q$ is requested is given by

$$p_q = \frac{\left[\sum_{q=1}^{Q} \frac{1}{e_q^{\tau}}\right]^{-1}}{e_q^{\tau}}, \tag{4}$$

where $\tau$ is the parameter of the Zipf distribution, and the ranking of request times of content $q$ is denoted by $e_q$.

## 4 Caching Analysis for Content Distribution

When a given moving vehicle $o_{i,j,k}$ requests content $q$, if the replica of content $q$ is available in its connected RSU $r_i$, the RSU $r_i$ sends the replica of content $q$ directly to the moving vehicle $o_{i,j,k}$. Otherwise, to obtain the requested content $q$ there are two options for $o_{i,j,k}$. One is to contact other moving vehicles which have the replica of content $q$. The other is to let $r_i$ contact other nearby RSUs for fetching the content. In this section, we give the analysis of both options.

For a given $o_{i,j,k}$, the number of moving vehicles that $o_{i,j,k}$ can connect is given by [21],

$$cv_{i,j,k} = \frac{1}{e^{-\sum_n \frac{ra_n}{ls_n} TR_{i,j,k}}}, \tag{5}$$

where $TR_{i,j,k}$ is the fixed transmission range of $o_{i,j,k}$. Define $o_{i,j,z}$ ($z = 1, \ldots, cv_{i,j,k}$) as the moving vehicles which $o_{i,j,k}$ is able to connect to within its fixed transmission range. We define the probability that a request arises from a given moving vehicle $o_{i,j,k}$ within the coverage of its connected RSU as $w_{i,j,k}$. Let $t_i$ be the total number of requests for content where these requests are from all moving vehicles in the coverage area of $r_i$ within a past watching period $\Delta t$. During the past watching period $\Delta t$, the number of requests from this moving vehicle can be obtained by

$$\sum_i \sum_j t_i \cdot w_{i,j,z}. \tag{6}$$

If there has been a request from $o_{i,j,z}$ for content $q$, as the vehicle keeps the content after obtaining it, $o_{i,j,z}$ can be a candidate to provide content $q$.

Define $rep_{z,q}$ as follows.

$$rep_{z,q} = \begin{cases} 1, & \sum_i \sum_j t_i \cdot w_{i,j,z} \cdot p_q \geq 1; \\ 0, & \sum_i \sum_j t_i \cdot w_{i,j,z} \cdot p_q < 1. \end{cases} \tag{7}$$

The transmission rate of $o_{i,j,z}$ is

$$bw_{o_{i,j,k},o_{i,j,z}} \cdot \log_2 \left( 1 + \frac{po_{o_{i,j,k}}}{bw_{o_{i,j,k},o_{i,j,z}} \cdot N_0 + \sum_{i=1}^{cv_{i,j,k}} if_i} \right) \tag{8}$$

where $bw_{o_{i,j,k},o_{i,j,z}}$ denotes the bandwidth between $o_{i,j,k}$ and $o_{i,j,z}$. $po_{o_{i,j,k}}$ is the received signal power of $o_{i,j,k}$ while $if_i$ is defined as the interference experienced at receiver from other transmitters. Thus, the delay to obtain content $q$ from $o_{i,j,z}$ is

$$del_{o_{i,j,k},o_{i,j,z}} = \frac{s_q}{bw_{o_{i,j,k},o_{i,j,z}} \cdot \log_2 \left( 1 + \frac{po_{o_{i,j,k}}}{bw_{o_{i,j,k},o_{i,j,z}} \cdot N_0 + \sum_{i=1}^{cv_{i,j,k}} if_i} \right)}. \tag{9}$$

If the above delay is smaller than the possible connection time $cd_{o_{i,j,k}}$ between $o_{i,j,z}$ and $o_{i,j,k}$, this moving vehicle can be a candidate for obtaining content.

$$con_{z,q} = \begin{cases} 1, & del_{o_{i,j,k},o_{i,j,z}} \leq cd_{o_{i,j,k}}; \\ 0, & del_{o_{i,j,k},o_{i,j,z}} > cd_{o_{i,j,k}}. \end{cases} \tag{10}$$

From [21], the possible connection time $cd_{o_{i,j,k}}$ between $o_{i,j,z}$ and $o_{i,j,k}$ can be obtained by

$$cd_{o_{i,j,k}} = \frac{1 - e^{-\sum_n \frac{ra_n}{ls_n} TR_{i,j,k}}}{\sum_n \frac{ra_n}{ls_n} \cdot e^{-\sum_n \frac{ra_n}{ls_n} TR_{i,j,k}}}. \tag{11}$$

Then, we can calculate the average delay to obtain content $q$ from other vehicles by

$$\frac{1}{cv'_{i,j,k}} \sum_{z=1}^{cv_{i,j,k}} rep_{z,q} \cdot con_{z,q} \cdot del_{o_{i,j,k},o_{i,j,z}}, \tag{12}$$

where $cv'_{i,j,k}$ is the total number of $o_{i,j,z}$ which satisfies both $con_{z,q} = 1$ and $rep_{z,q} = 1$.

If the moving vehicle $o_{i,j,k}$ obtains the requested content $q$ from other fixed RSUs, when its connected RSU $r_i$ does not have the replica of content $q$, $r_i$ needs to fetch this content from a nearby wired connected RSU $r_m$

$(m = 1, \ldots, M \ \& \ m \neq i)$ which has the replica of content $q$. And, after obtaining content $q$, $r_i$ sends content $q$ to the moving vehicle $o_{i,j,k}$.

For a given $r_m$, the delay to obtain content $q$ from it to $r_i$ can be obtained by

$$del_{r_i,r_m} = \frac{s_q}{bw_{r_i,r_m}} \cdot d_{r_i,r_m}, \tag{13}$$

where the shortest distance (hop count) away from $r_m$ to $r_i$ is defined by $d_{r_i,r_m}$, and the average bandwidth (per hop) during the path from $r_m$ to $r_i$ is denoted by $bw_{r_i,r_m}$.

Based on the zone model [22], the delay during the delivery from $r_i$ to $o_{i,j,k}$ within the $u$-th zone becomes

$$del^u_{r_i,o_{i,j,k}} = \frac{s^u_q}{bw^u_{r_i,o_{i,j,k}}}. \tag{14}$$

If $\sum_{\varepsilon=1}^{u+1} s^\varepsilon_q > s_q$, we can know that all of the bytes of content $q$ can be transmitted from $r_i$ to $o_{i,j,k}$ and we have

$$del^{u+1}_{r_i,o_{i,j,k}} = \frac{s_q - \sum_{\varepsilon=1}^{u} s^\varepsilon_q}{bw^{u+1}_{r_i,o_{i,j,k}}}. \tag{15}$$

Thus, the total delay to transmit content $q$ from $r_i$ to $o_{i,j,k}$ is

$$\sum_{\varepsilon=1}^{u+1} del^\varepsilon_{r_i,o_{i,j,k}}. \tag{16}$$

In addition, the total delay when $r_i$ fetches a replica of content $q$ from $r_m$ and then sends to $o_{i,j,k}$ can be obtained by

$$del_{r_i,r_m} + \sum_{\varepsilon=1}^{u+1} del^\varepsilon_{r_i,o_{i,j,k}}. \tag{17}$$

If RSU $r_m$ has a replica of the requested content $q$ and this replica can be delivered to the moving vehicle $o_{i,j,k}$ within the connection time between this moving vehicle and its connected RSU $r_i$, RSU $r_m$ can be a candidate for content delivery. Define $con_{k,q,i,j,m}$ and $rep_{m,q}$ to show the candidate for providing the replica of content $q$ as follows.

$$con_{k,q,i,j,m} = \begin{cases} 1, & del_{r_i,r_m} + \sum_{\varepsilon=1}^{u+1} del^\varepsilon_{r_i,o_{i,j,k}} \leq g_{r_i,o_{i,j,k}}; \\ 0, & del_{r_i,r_m} + \sum_{\varepsilon=1}^{u+1} del^\varepsilon_{r_i,o_{i,j,k}} > g_{r_i,o_{i,j,k}}. \end{cases} \tag{18}$$

$$rep_{m,q} = \begin{cases} 1, & cp_{m,q} \geq 1; \\ 0, & cp_{m,q} < 1. \end{cases} \tag{19}$$

In the above equations, if $con_{k,q,i,j,m} = 1$ and $rep_{m,q} = 1$, RSU $r_m$ is determined as a candidate for content delivery.

Then, we can obtain the average delay to obtain content $q$ from RSU $r_m$ after the moving vehicle $o_{i,j,k}$ sending the request to RSU $r_i$ by

$$\frac{1}{M'} \sum_{m=1}^{M} rep_{m,q} \cdot con_{k,q,i,j,m} \cdot (del_{r_i,r_m} + \sum_{\varepsilon=1}^{u+1} del^{\varepsilon}_{r_i,o_{i,j,k}}), \tag{20}$$

where $M'$ is the number of $r_m$ which satisfies both $con_{k,q,i,j,m} = 1$ and $rep_{m,q} = 1$.

If the following inequality holds,

$$\begin{aligned} &\frac{1}{cv'_{i,j,k}} \sum_{z=1}^{cv_{i,j,k}} rep_{z,q} \cdot con_{z,q} \cdot del_{o_{i,j,k},o_{i,j,z}} \\ &< \frac{1}{M'} \sum_{m=1}^{M} rep_{m,q} \cdot con_{k,q,i,j,m} \cdot (del_{r_i,r_m} + \sum_{\varepsilon=1}^{u+1} del^{\varepsilon}_{r_i,o_{i,j,k}}), \end{aligned} \tag{21}$$

content $q$ is delivered from moving vehicles. Otherwise, content $q$ is provided by the replica on the edge of RSUs.

## 5 Simulation Results

Using the scenario in [23], simulation involves 100 vehicles moving on a linear highway, where the velocities of vehicles are uniformly distributed in the range [70 km/h, 130 km/h]. The communication range of a vehicle is 300 m. Each content is divided into 100 pieces of equal size which is 2 MBytes. A content is downloaded successfully when all the pieces are collected. The probability that a content is requested follows the Zipf distribution where contents have different popularity. Here, the parameter of Zipf distribution is set to be 0.8 [12]. The cache size of RSUs is 0.15, i.e. 15% of the total content can be cached in an RSU (due to limited cache capacity) [21]. The transmission rate between moving vehicles and fixed RSUs is determined based on the zone model [22].

Figure 1 shows the relative delay compared with the delay to fetch the requested content by using the Random scheme, where the total number of requests is varied from 1000 to 9000. It can be seen that the proposed algorithm can achieve the lowest relative delay. The reason is as follows: in our proposal, the edge caching among several RSUs is analyzed, where the RSUs can also provide the requested content. Therefore, different from other conventional algorithms, when the vehicle requests for the replica of the content, the caching replicas on the edge of RSUs may provide this content cooperatively with other vehicles based on the constraints of transmission time. Then, the requested content need not to be fetched from its content server so that the delay can be reduced.

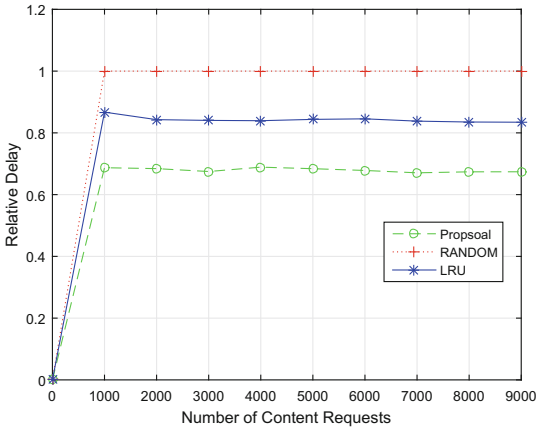


**Fig. 1.** Relative delay of different algorithms when the number of content requests is increased.

## 6 Conclusion

In this paper, a cooperative scheme for edge caching has been proposed for VANETs to provide multimedia content delivery services. Based on the properties of vehicle velocity, road traffic and content popularity, the edge caching has been analyzed. Besides, a cost model has been proposed to compare the cost to fetch the requested content from a moving vehicle or other RSUs. Furthermore, simulation results clearly demonstrated the performance improvement with the proposed algorithm. There are several works to be done as further researches. Security issue related to the replicas of cache will be considered.

## References

1. Liu, N., Liu, M., Chen, G., Cao, J.: The sharing at roadside: vehicular content distribution using parked vehicles. In: Proceedings of IEEE INFOCOM, Orlando, FL, USA (2012)
2. Lu, N., Luan, T.H., Wang, M., Shen, X., Bai, F.: Capacity and delay analysis for social-proximity urban vehicular networks. In: Proceedings of IEEE INFOCOM, Orlando, FL, USA (2012)
3. Farradyne, P.: Vehicle infrastructure integration (vii)-architecture and functional requirements. Draft Version, vol. 1 (2005)
4. Liu, Z., Dong, M., Gu, B., Zhang, C., Ji, Y., Tanaka, Y.: Fast-start video delivery in future internet architectures with intra-domain caching. Mob. Netw. Appl. **22**, 98–112 (2016). ACM/Springer
5. Wu, C., Ohzahata, S., Ji, Y., Kato, T.: How to utilize inter-flow network coding in vanets: a backbone based approach. IEEE Trans. Intell. Transport. Syst. **17**(8), 2223–2237 (2016)
6. Jiang, F., Liu, Z., Kanchana, T., Li, Z., Ji, Y., Seneviratne, A.: Transfetch: a viewing behavior driven video distribution framework in public transport. In: Proceedings of IEEE LCN (2016)

7. Wu, C., Ji, Y., Liu, F., Ohzahata, S., Kato, T.: Towards practical and intelligent routing in vehicular ad hoc networks. IEEE Trans. Veh. Technol. **64**(12), 1–17 (2015)
8. Xu, Q., Su, Z., Guo, S.: A game theoretical incentive scheme for relay selection services in mobile social networks. IEEE Trans. Veh. Technol. **65**(8), 6692–6702 (2016)
9. Su, Z., Xu, Q., Fei, M., Dong, M.: Game theoretic resource allocation in media cloud with mobile social users. IEEE Trans. Multimed. **18**(8), 1650–1660 (2016)
10. Su, Z., Hui, Y., Guo, S.: D2D-based content delivery with parked vehicles in vehicular social networks. IEEE Wirel. Commun. **23**(4), 90–95 (2016)
11. Aioffi, W.M., Mateus, G.R., de Almeida, J.M., Loureiro, A.A.F.: Dynamic content distribution for mobile enterprise networks. IEEE J. Sel. Areas Commun. **23**(10), 2022–2031 (2005)
12. Breslau, L., Cao, P., Fan, L., Phillips, G., Shenker, S.: Web caching and Zipf-like distributions: evidence and implications. In: Proceedings of IEEE INFOCOM, New York, NY, USA (1999)
13. Nandan, A., Das, S., Pau, G., Gerla, M., Sanadidi, M.: Co-operative downloading in vehicular ad-hoc wireless networks. In: Proceedings of IEEE/IFIP WONS, St. Moritz, Switzerland (2005)
14. Eriksson, J., Balakrishnan, H., Madden, S.: Cabernet: vehicular content delivery using wifi. In: Proceedings of ACM MobiCom, San Francisco, CA, USA (2008)
15. Lin, S.-H., Hu, J.-Y., Chou, C.-F., Chang, C., Hung, C.-C.: A novel social cluster-based P2P framework for integrating vanets with the internet. In: Proceedings of IEEE WCNC, Budapest, Hungary (2009)
16. Fiore, M., Casetti, C., Chiasserini, C.-F., Garetto, M.: Analysis and simulation of a content delivery application for vehicular wireless networks. Perform. Eval. **64**(5), 444–463 (2007)
17. Li, Y., Zhu, X., Jin, D., Wu, D.: Multiple content dissemination in roadside unit aided vehicular opportunistic networks. IEEE Trans. Veh. Technol. **63**(8), 3947–3956 (2014)
18. Zhou, L., Zhang, Y., Song, K., Jing, W., Vasilakos, A.V.: Distributed media services in P2P-based vehicular networks. IEEE Trans. Veh. Technol. **60**(2), 692–703 (2011)
19. Malandrino, F., Casetti, C., Chiasserini, C.-F., Sommer, C., Dressler, F.: The role of parked cars in content downloading for vehicular networks. IEEE Trans. Veh. Technol. **63**(9), 4606–4617 (2014)
20. Wang, T., Song, L., Han, Z.: Coalitional graph games for popular content distribution in cognitive radio vanets. IEEE Trans. Veh. Technol. **62**(8), 4010–4019 (2013)
21. Yousefi, S., Altman, E., El-Azouzi, R., Fathy, M.: Analytical model for connectivity in vehicular ad hoc networks. IEEE Trans. Veh. Technol. **57**(6), 3341–3356 (2008)
22. Luan, T.H., Ling, X., Shen, X.: MAC in motion: impact of mobility on the MAC of drive-thru internet. IEEE Trans. Mobile Comput. **11**(2), 305–319 (2012)
23. Luan, T., Shen, X., Bai, F., Sun, L.: Feel bored? Join verse! Engineering vehicular proximity social network. IEEE Trans. Veh. Technol. **64**(3), 1120–1131 (2015)

# Enhanced IoT Data Acquisition in Information Centric Networks

Lijun Dong(✉)

Futurewei Technologies Inc., 10180 Telesis Court, Suite 220,
San Diego, CA 92121, USA
lijun.dong@huawei.com

**Abstract.** The new characteristics of IoT (Internet of Things) data and clients' IoT data retrieval require the ICN infrastructure to be more intelligent and advanced capabilities. This paper proposes enhanced in-network functionalities of ICN routers, which are smart in-network caching, context-aware forwarding. The paper illustrates the proposed enhanced in-network capabilities of ICN routers to enable the efficient IoT data acquisition. The simulation shows the significant performance improvement with different network settings.

**Keywords:** Information centric networks · In-network capabilities
Internet of Things · Data acquisition

## 1 Introduction

Information-Centric Networking (ICN) [1] has emerged as a promising candidate for the architecture of the future Internet as well as the future Internet of Things (IoT) [2]. ICN integrates name-based routing and in-network caching as fundamentals of the network infrastructure. The NDN architecture [4] is one of the most influential ICN architectures in the community. A NDN router maintains three data structures: the Forwarding Information Base (FIB) that associates the content names to the forwarding face(s) towards the producer(s), the Pending Interest Table (PIT) that records the incoming faces where the interests came from and have not replied by producer, the Content Store (CS) that caches content from a producer when it is forwarded to the requesters.

IoT Data [5] has some unique characteristics. One of them is that IoT data is normally measured in time series, thus associated with time context information. Both historic and fresh data may be needed by the client. On the other hand, IoT data may vary greatly in sizes and is normally associated with the location context information.

In general, IoT data may be associate different kinds of context information. Context [3] is defined as any information that can be used to characterize the situation of an entity. An entity is a person, place, or object that is considered relevant to the interaction between a user and an application, including the user and applications themselves.

Clients' IoT data acquisition usually requires that the data satisfies certain conditions on associated context information, such as time, size and location requirements.


M. Huang et al. (Eds.): WICON 2016, LNICST 214, pp. 272–278, 2018.
https://doi.org/10.1007/978-3-319-72998-5_28

A typical client's request would look like: I want the traffic video at time 3:30 PM today on route 56 exit 3; I want the temperature of today in 92121.

Currently, the NDN routers only provide the basic functions of in-network caching, name based message forwarding. The NDN routers lack the context-awareness capability for data acquisition. Due to unawareness of the context information, a NDN router may not be able to make the correct decisions on choosing the forwarding face if there are multiple producers for the requested data. The network bandwidth could be wasted on the message or data transmission that is not needed by the client. Therefore, it is extremely important to enable enhanced context-awareness capability for content acquisition by NDN primitives and protocols. This paper proposes the new capability of context aware forwarding and smart in-network caching for the NDN routers.

## 2 Enhanced IoT Data Acquisition

The paper proposes that the enhanced in-network capabilities can be incorporated into the NDN routers.

- Smart In-Network Caching: a NDN router can cache the information that is forwarded by itself. It is proposed that the information could be in different kinds of categories, such as an interest message for data retrieval and subscription, semantics information of a resource, data discovery result, etc., other than just named content/data resource. The caching criteria could be different for different categories of information. Each NDN router can make independent decisions or collaborate with neighboring routers on deciding whether to cache the information being routed through.
- Context Aware Forwarding: a NDN router can forward a content acquisition request based on the specified context requirements. The context information may also be piggybacked in data message and recorded by the NDN router when the data message is being forwarded. As a result, the context information is associated with the IoT data stored in the CS, the forwarding entries maintained in the FIB, as well as the pending interests in the PIT. When an interest is received by a NDN router, it needs to match not just the content name in the request, but also the context requirement incorporated in the interest message. If it finds an exact match of the data in the CS with the same name and the same context information, then the data is returned to the client. Otherwise, the interest is either added in the PIT along with the context requirement, or aggregated in the existing entry in the PIT with the same requested data name. If the interest is totally new to the PIT (a new entry is added in the PIT), then the interest message is forwarded to the other NDN router based on the FIB. The context aware forwarding capability enabled in the FIB will try to match the contextual requirement in the interest message with the context associated the forwarding faces for the same requested data name. The most matched face is used to forward the interest message to the next NDN router until it reaches a producer that can provide the IoT data.

In the following, we use the examples shown in Fig. 1 to illustrate how context-aware content acquisition is supported in the ICN networks (e.g. by NDN routers).

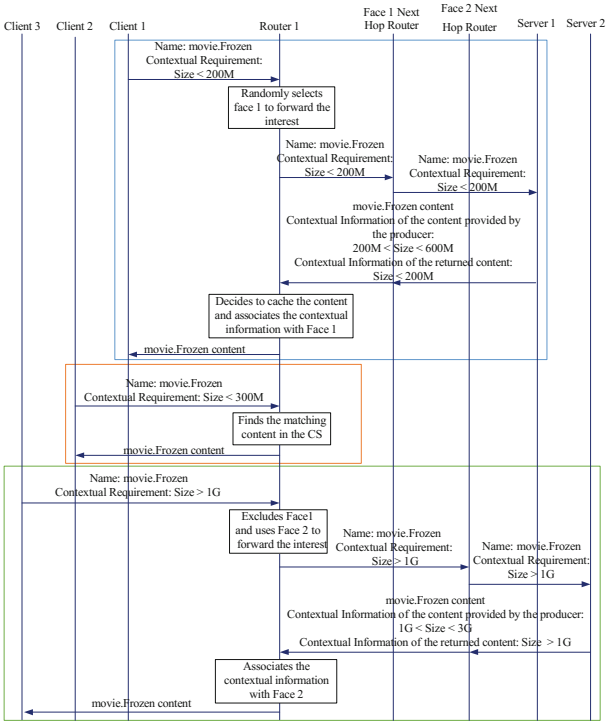


**Fig. 1.** Exemplary message flow of context-aware content requests

The client 1 sends an interest with the content name (i.e. movie.Frozen) and contextual requirement (i.e. Size < 200 M) to the attached router 1. The FIB for the prefix movie.Frozen exists in the router 1, which has two forwarding faces, i.e. 1 and 2. The forwarding faces are not associated with any context information yet. The router 1 can randomly selects one of the faces to forward the interest to limit the overhead in propagating the interest message. In the example, the face 1 is chosen. The face 1 next hop router then forwards the interest to one of the producers, i.e. the server 1. The server 1 processes the interest request, extracts the content name and the contextual requirement. The server 1 finds that it can provide the content data with matching contextual information. The server 1 replies with the content data, and piggybacks the contextual information of the content that can be provided by itself (i.e. 200 M < Size < 600 M, which indicates all the sizes that the Server 1 is able to provide for the content movie.Frozen), as well as the original contextual requirement of the returned content (i.e. Size < 200 M). The content is forwarded via the reverse path to the router 1. The router 1 returns the content to the client 1. The router 1 decides to cache the content based on the local caching criteria. The cached content has contextual

information of "Size < 200 M". The router 1 associates the piggybacked contextual information to the forwarding face 1. It indicates that through the face 1, the content movie.Frozen with the contextual information of "200 M < Size < 600 M" can be returned.

The client 2 sends an interest with the content name (i.e. movie.Frozen) and contextual requirement (i.e. Size < 300 M) to the attached router 1. The router 1 finds a local cached copy which satisfies the contextual requirement, and returns to the client 2. The interest is dropped at the router 1.

The client 3 sends an interest with the content name (i.e. movie.Frozen) and contextual requirement (i.e. Size > 1G) to the attached router 1. The router 1 is able to exclude the face 1 since its associated contextual information opposes to the required one. The router 1 is contextual aware in making the decision to forward the interest to the face 2. The face 2 next hop router then forwards the interest to one of the producers, i.e. the server 2. The server 2 processes the interest request, extracts the content name and the contextual requirement. The server 2 finds that it can provide the content data with matching contextual information. The server 2 replies with the content data, and piggybacks the contextual information of the content that can be provided by itself (i.e. 1G < Size < 3G, which indicates all the sizes that the Server 2 is able to provide for the content movie.Frozen), as well as the original contextual requirement of the returned content (i.e. Size > 1G).

The content is forwarded via the reverse path to the router 1. The router 1 returns the content to the client 2. The router 1 decides not to cache the content due to limited storage. The router 1 associates the piggybacked contextual information to the forwarding face 2. It indicates that through the face 2, the content movie.Frozen with the contextual information of "1G < Size < 3G" can be returned.

## 3 Performance Evaluation

In this section, we evaluate the performance of the mechanisms proposed in the previous sections. The event-driven simulator simulates and compares the proposed context-aware solution versus the random selection and round-robin selection of forwarding faces for content request with contextual requirement. In the random selection approach, each ICN router receiving an interest always randomly selects a forwarding face in the FIB corresponding to the requested content name, if there are multiple ones. In the round robin approach, each ICN router receiving an interest always forwards it to the faces in a round-robin manner.

The metric evaluated is "success rate per sent interest", which quantifies the average successful ratio for the client receiving the content which satisfies the contextual requirements, among all interest messages sent during the simulation.

In the first set of simulations, we vary the network connectivity, which is defined as the probability that two nodes in the network connecting to each other. The total number of nodes in the network is 180. The total number of interests in the workload is 10000. The total number of content in the network is 1000. The maximum number of contexts per content is 5.

Figure 2 includes two figures on the success ratio per sent interest with network connectivity varies from 0.2 to 0.6: (a) Without retransmission. The option adopted is that after an interest fails, the interest is dropped by the client without retransmission. For random selection and round robin mechanisms, the success ratios are similar, which are around 60%. It indicates that when an ICN router chooses a forwarding face from multiple faces either randomly or in a round-robin manner, it can't guarantee that the interest reaches the accurate content provider satisfying the contextual requirements. However, with proposed context-aware solution, with contextual information associated and recorded in the FIB, the ICN router can make the right decision in choosing the forwarding face towards the accurate content provider. After the FIBs in ICN routers are stable, the success ratio per sent interest of the proposed context-aware solution can stay as 100%. (b) With retransmission to ensure successful content retrieval. The option adopted is that after an interest fails, the interest is resent by the client until it reaches the maximum retry number. The maximum retry number is set to be large enough to ensure that every interest would be eventually replied with a content satisfying the contextual requirements. With the number of successful interests to be fixed (i.e. the number of the interests in the workload), the success ratio per sent interest performance in Fig. 2(b) indicates that the round robin mechanism has better chance over the random selection mechanism to reach the accurate content provider with retransmission. When the network connectivity increases, the number of hops between two nodes in the network (i.e. between the client and the content provider) is smaller, while the number of forwarding faces for a content in an ICN router may be larger. Those two factors result in the success ratio per sent interest to be constant when network connectivity varies in both option (a) and (b).

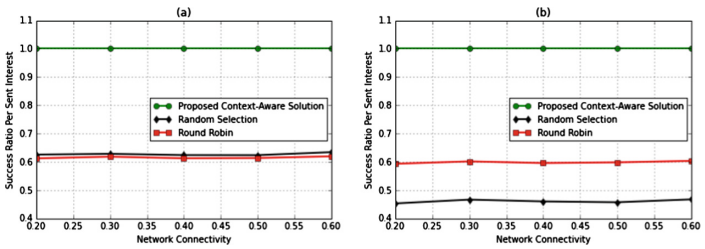


**Fig. 2.** Success ratio per sent interest vs. network connectivity

In the second set of simulations, we vary the parameter of context variety per content, which is defined as the maximum number of associated contexts for each-content. The number of associated contexts for each content is set up randomly between 1 to this parameter. We assume that there is one and only one content server to provide a content with one context, which suggests that the number of content provider for each content is same as the number of the content's associated contexts. The total number of nodes in the network is 180. The network connectivity is 0.3. The total number of interests in the workload is 10000. The total number of content in the network is 1000.

Figure 3 includes two figures on the success ratio per sent interest with context variety per content changes from 2 to 8: (a) Without retransmission. The random selection and round robin mechanisms show almost the same performance in success ratio per sent interest. When the context variety per content increases, the success ration per sent interest for both mechanisms decreases from 100% to 55%, while the proposed context aware solution maintains the 100% successful ratio per sent interest when the FIBs in ICN routers are stable. (b) With retransmission to ensure successful content retrieval. The round robin mechanism performs slightly better than random selection mechanism, but both still follow the same performance decreasing trend with the increment of the context variety per content. The proposed context aware solution again maintains 100% success ratio per sent interest, which means every request in the workload is satisfied with the accurate content after every single interest message is sent out.

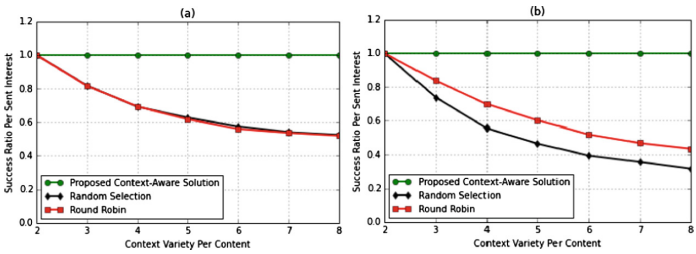


**Fig. 3.** Success ratio per sent interest vs. context variety per content

## 4 Conclusion

In IoT applications/use cases, the content acquisition requests from clients often involve the contextual requirements. Only such contextual requirements are satisfied by the returned content, the content retrieval request can be considered successful. In the paper, we proposed the enhanced in-network capabilities to support IoT data acquisition in the ICN infrastructure. We performed thorough simulations to evaluate the performance of the proposed context-aware solution compared to the two existing mechanisms: random selection and round robin. The results verified the substantial performance improvement of the proposed solution with very little network overhead.

## References

1. Xylomenos, G., Ververidis, C.N., Siris, V.A., Fotiou, N., Tsilopoulos, C., Vasilakos, X., Katsaros, K.V., Polyzos, G.C.: A survey of information-centric networking research. IEEE Commun. Surv. Tutor. **16**(2), 1024–1049 (2014)
2. Baccelli, E., Mehlis, C., Hahm, O., Schmidt, T., Wahlisch, M.: Information centric networking in the IoT: experiments with NDN in the wild. In: ACM ICN (2014)

3. NDN: The Named Data Networking Project. http://www.named-data.net/
4. Dey, A.K.: Understanding and using context. Pers. Ubiquit. Comput. J. **5**, 4–7 (2001)
5. Zhang, Y., Raychadhuri, D., Grieco, L., Baccelli, E., Burke, J., Ravindran, R., Wang, G., Lindren, A., Ahlgren, B., Schelen, O.: Requirements and challenges for IoT over ICN. https://datatracker.ietf.org/doc/draft-zhang-icnrg-icniot-requirements/

# Horizontal Slicing Clustering Based Movement Detection Method for IoTs

Xiaoyu Li[1], Xiaoling Wu[2,3,4(✉)], Daoping Huang[1], and Lei Shu[5]

[1] South China University of Technology, Guangzhou, China
[2] Guangdong University of Technology, Guangzhou, China
[3] Guangzhou Institute of Advanced Technology, Chinese Academy of Sciences, Guangzhou, China
xl.wu@giat.ac.cn
[4] Shenzhen Institutes of Advanced Technology, Chinese Academy of Sciences, Shenzhen, China
[5] Guangdong University of Petrochemical Technology, Maoming, China

**Abstract.** Movement detection in Internet of Things (IoTs) has been widely used in many fields, such as valuables monitoring, safety protection and empty-nesters care. Monitoring by videos, GPS and ultrasonic is the most common method to address the movement detection in IoTs. However, these efforts are circumscribed because they need the support of the special equipment, such as cameras, infrared equipment and ultrasonic facilities. It is significant to detect the movement in IoTs systems without additional equipment and ensure its high detection precision. Therefore, in this paper we derive an innovative method called Horizontal Slicing Clustering (HSC) to detect the movement in the IoTs. Received Signal Strength Indicator (RSSI) data are the network parameters which are utilized in this method. The simulation results show their effectiveness in movement detection.

**Keywords:** Internet of things (IoTs) · Movement detection
Horizontal slicing clustering (HSC)
Received signal strength indicator (RSSI)

## 1 Introduction

IoTs is the network of physical objects, vehicles, buildings and other items embedded with electronics, software, sensors, and network connectivity that enables these objects to collect and exchange data [1]. The main supports of IoTs are telecommunication technology, internet technology, electronic technology and information processing technology. IoTs have been applied in various social core departments with the rapid development. In these departments, movement detection is a very valuable topic. In factories, movement detection can achieve the monitoring of valuable instruments and equipment; in hospitals, medical workers can employ movement detection technology to care patients. At present, the movement detection technology has a wide range of research. Many researchers have accomplished movement detection through the Video [2], GPS [3], red line [4], ultra sound wave [5], RF [6] and so on. Although many


M. Huang et al. (Eds.): WICON 2016, LNICST 214, pp. 279–287, 2018.
https://doi.org/10.1007/978-3-319-72998-5_29

movement detection systems have been proposed, few of them can be used in daily living setting because of the limitation of relevant equipment. The expected result is to achieve movement detection without additional equipment. So devices-free methods for movement detection have attracted a lot of attention. The projects about passive means for movement detection have been given [7, 8]. In current devices-free efforts, CSI data are chosen as a better choice compared with RSSI data because the former are more stable than the latter. Current studies about RSSI data based methods are unable to obtain good efforts because of their fluctuation. However, CSI can only be collected from few wireless devices, so its application is very circumscribed. Thus, a high-precision and widely applicable movement detection method for IoTs system is needed. In this paper, Horizontal Slicing Clustering (HSC) method is proposed to determine whether movement exists in the working environment of IoTs. We apply this method to analyze the RSSI data which can be collected from any wireless devices of IoTs. Analyzing the feature of the RSSI data through HSC method when the IoTs system is working, then we can judge the actual status of the working environment.

## 2 Related Work

### 2.1 RSSI

RSSI data are used as major metrics in this paper. RSSI data are frequently used in IoTs to indicate the strength of communication signals between wireless devices. The distance between antennas will influence the RSSI value directly [9]. In [9], RSSI is defined as follows:

$$RSSI = 10 \cdot \log \frac{P_{RX}}{P_{\mathrm{Re}f}} \tag{1}$$

where PRef is typically taken as 1 mW and PRx is the remaining power of the wave at the receiver. RSSI is relatively stable if there are no movement or other changes in the environment. RSSI data can get influences from a number of factors such as reflection from objects, electromagnetic fields, diffraction, and other multipath effects [10]. Because of these effects, the movement in the environment is an important factor which can influence the RSSI data. It has been proved that the movement of human will affect the propagation of wireless signals [11, 12]. When someone moves around the communicating environment, the reflection, diffraction and other factors will be changed, so the feature of RSSI data will be different. Thus, we can determine the movement by the respective feature of different RSSI data. One of the desirable reasons that we select RSSI data in this paper is that the indicators can be collected easily from any wireless devices in IoTs when they communicating with others.

Obviously, it is very difficult to determine the movement only by the original RSSI data because they might overlap each other. In this paper, we use HSC method to deal with the indistinguishable RSSI data and get the differentiable HSC curves. Hence, detecting the movement in the environment where the IoTs system is deployed. Moreover, using only RSSI data to realize movement detection is challengeable

because RSSI data can be affected by other factors such as the interferences from the noise. In order to improve the effectiveness of the analysis, adaptability and robustness of algorithm are needed.

### 2.2 Mathematical Morphology

In this paper, an innovative method called Horizontal Slicing Clustering (HSC) is presented to detect the movement in the communicating environment. In order to establish the detection method, we use tools taken from Mathematical Morphology (MM). MM is based on set theory, lattice theory, topology, and random functions [13] and it is most commonly used for digital image processing. Meanwhile, it can be employed as well on graphs, surface meshes, solids, and many other spatial structures [14]. [15, 16] introduced the application of MM to deal with the clustering of functional data. MM operators extract the relevant structures of the set under study by probing it with another set of a known shape called structuring element (SE) [17]. The SE can be any kind of shape that researchers are interested in. Erosion, dilation, opening and closing are four basic operations in MM. The erosion of the binary image A by the structuring element B is defined by:

$$A\Theta B = \left\{x \,|\, (B)_x \subseteq A\right\} \tag{2}$$

Where x is a vector and (B)x is defined as:

$$(B)_x = \{b + x \,|\, b \in B\} \tag{3}$$

The dilation of A by B is given by the expression:

$$A \oplus B = \left\{x \,|\, \left[(B)_x \cap A\right] \neq \phi\right\} \tag{4}$$

The opening of A by B is obtained by the erosion of A by B, followed by dilation of the resulting image by B:

$$A \circ B = (A\Theta B) \oplus B \tag{5}$$

The closing of A by B is obtained by the dilation of A by B, followed by erosion of the resulting structure by B:

$$A \bullet B = (A \oplus B)\Theta B \tag{6}$$

## 3 Horizontal Slicing Clustering

In this section, detailed explanation of Horizontal Slicing Clustering (HSC) method is presented. The inspiration of HSC algorithm is from mathematical morphology. An HSC function is a process of slicing. Slicing is a Mathematical Morphology

(MM) based operation. The key point of HSC method is slicing the original signals with different size of the Structuring Elements (SE) and clustering the sliced results. Sliced results are generated by successively dilating or eroding the target image by increasing the size of SE. In this paper, we take the unit square as the original SE because RSSI data are integers. The increasing speed of the SE is 1 at each time. In order to analyze the RSSI data through HSC method, the RSSI data collected by receivers will be transformed to step function. So we can get the RSSI data based step curve in two-dimension. The horizontal axis shows the simulation time and the vertical axis represents the signal strength. We call the step curve as RSSI curve. By using incremental SE to slice the RSSI curve horizontally, the different structures of RSSI curve can be separated. By clustering the sliced results, we can get the proportional distribution of the different structures from the RSSI curve. Main steps of HSC function are as follows:

Step(a): Calculating the total areas of the original RSSI curve S0.
Step(b): Setting the unit square as basic SE.
Step(c): Using current SE to slice the RSSI curve. If there are peaks match the size of current SE, counting the total sliced areas Y(n) and removing these sliced area from RSSI curve. If no peak matches the current SE, regarding the Y(n) as 0.
Step(d): Calculating the ratio between the summation of all sliced areas so far and the S0 and we can get HSC(i). We call the summation of all the sliced areas so far as Section Score (SS).
Step(e): Adding one unit of the SE horizontally to enlarge it and repeat steps (c) and (d) until all the areas of the RSSI curve are sliced.

The HSC(i) is defined as:

$$HSC(\mathrm{i}) = \frac{SS(\mathrm{i})}{S_0} \tag{7}$$

Where SS(i) is defined as:

$$SS(\mathrm{i}) = \sum_{n=1}^{i} Y(n) \tag{8}$$

In Fig. 1, an example of HSC function is illustrated. A random signal was generated by Matlab, where S(x) = [0, 0, 2, 3, 4, 7, 4, 5, 9, 8, 5, 4, 3, 3, 2, 0]. Figure 1(a) is the step function of the random signal. Applying HSC algorithm and we can get the HSC curve, as shown in Fig. 1(b). In this paper, we employ HSC algorithm to extract the structural feature of RSSI data to determine whether there is movement in the environment. For more detail of HSC method, we generate Table 1. Sliced areas Y(n) are generated by Mathematical Morphology (MM) based slicing. After all the areas have been sliced by incremental SE, we gather the information together and calculate their Section Score(SS). Then we can get HSC by dividing SS(i) to the total area. In our experiment, we use this HSC method to process the RSSI data of wireless nodes when they communicating in different situations.

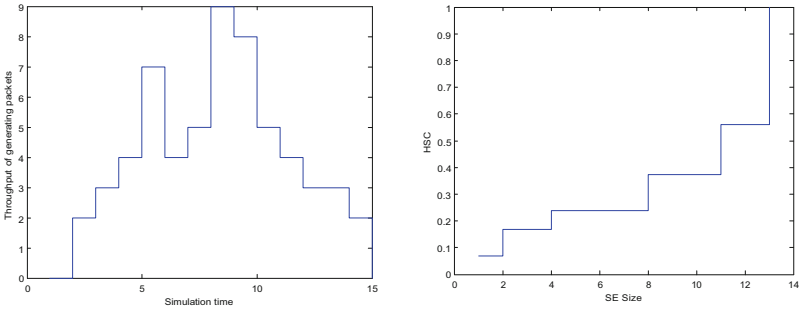


(a) Stepwise function of the random signal (b) HSC function of the random signal

**Fig. 1.** Illustrative example of HSC function

**Table 1.** Illustrative example of HSC.

| SE size | Matched numbers | Sliced areas | Section score | HSC |
|---|---|---|---|---|
| 1 | 4 | 4 | 4 | 4/59 |
| 2 | 3 | 6 | 10 | 10/59 |
| 3 | 0 | 0 | 10 | 10/59 |
| 4 | 1 | 4 | 14 | 14/59 |
| 5 | 0 | 0 | 14 | 14/59 |
| 6 | 0 | 0 | 14 | 14/59 |
| 7 | 0 | 0 | 14 | 14/59 |
| 8 | 1 | 8 | 22 | 22/59 |
| 9 | 0 | 0 | 22 | 22/59 |
| 10 | 0 | 0 | 22 | 22/59 |
| 11 | 1 | 11 | 33 | 33/59 |
| 12 | 0 | 0 | 33 | 33/59 |
| 13 | 2 | 26 | 59 | 59/59 |

## 4 Experimental Details

In IoTs system, transmitters broadcast wireless signals, meanwhile, receivers in the similar system collect the data. We name the transmitters as Access Points (APs) and receivers as Monitoring Points (MPs) hereafter. The APs can be typically access points, such as routers which can transmit wireless signals. And the MPs could be any existing wireless devices in living setting, such as smartphones and smartbands. In our experiment, we used a router and three smartphones which were the most universal devices in daily living setting as the experimental equipment. The router was employed as AP and the smartphones were used as MP and named MP (1), MP (2), MP (3) respectively. The operating system of the smartphones was Android. Android system is a kind of open source operating system based on Linux. The system was running in 2.4 GHz. We opened the wireless hotspot function of the router so it could build a

small communicating system as a kernel. Many interested activities often happened in several seconds, so we increased the sample rate to 10 packets per second in order to capture the changes of the signals by the short time activities. There were two scenarios in dormitory and students' park respectively in our experiment. Through the results generated from different environments, we could verify the environmental adaptability of our algorithm.

The topologies of the nodes in the experiments can be seen in Fig. 2. In the first scenario, we collected RSSI data from two cases separately. In case one there was no movement in the dormitory and in case two an experimenter opened the door and moved around the dormitory. The AP was deployed in the center of the dormitory and the MPs was deployed around the AP. In the second scenario, we deployed a small IoTs system in the students' park and the RSSI data were collected by the MPs again. There were also two situations in the second scenario in which the first was that the system was deployed at night when the environment was quiet and there was no movement there, and the second was collecting RSSI data at twelve o'clock when students came home from school and the students' park was busy. The AP was deployed in the center of students' park and the MPs was also around the AP. Each MP recorded 2000 successive data points in each scenario, half of which were collected from the dynamic environment and the other half were from the static situation.

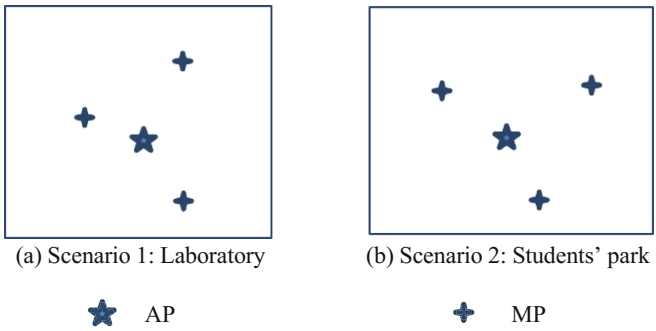


**Fig. 2.** Topologies of IoTs

## 5 Result Analysis

The primary motivation is detecting movement in the communicating environment without additional equipment. In our experiment, by comparing the HSC curves of RSSI data collected by the smartphones in different situations, we can successfully and clearly differentiate their feature through HSC curves, which makes it possible to determine whether there is movement in the environment. Figure 3 shows HSC curves in different situations. We gathered the HSC function of RSSI data received by MP (1), MP (2) and MP (3) when the status of environment is different. The green curves show the static situation and the reds represent the dynamic status. It is very clear to observe that the HSC curves have been successfully differentiated into two different clusters in

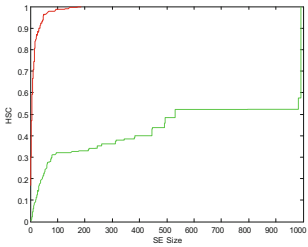


Scenario 1: Dormitory

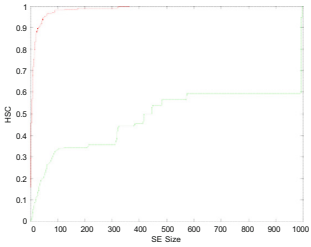


Scenario 2: Student' park

(a) HSC Function of Received RSSI of MP (1)

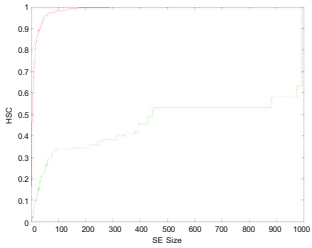


Scenario 1: Dormitory

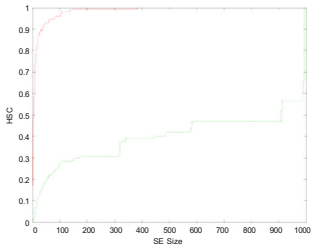


Scenario 2: Student' park

(b) HSC Function of Received RSSI of MP (2)

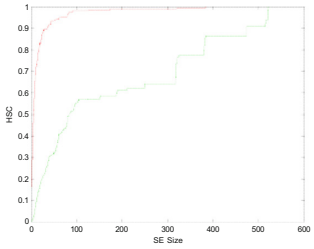


Scenario 1: Dormitory

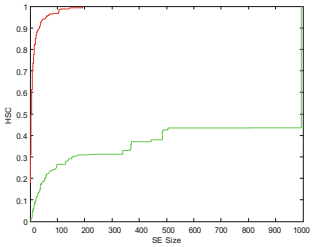


Scenario 2: Student' park

(c) HSC Function of Received RSSI of MP (3)

**Fig. 3.** HSC results of RSSI

each scenario. The shapes of HSC curves are dissimilar when the IoTs system communicates in different situations, which makes it possible to determine whether there is movement by briefly observing and analyzing the shapes of HSC curves.

Assume an IoTs system which works in a static condition. At a certain moment, the movement suddenly appears in the environment. Then the HSC curves of RSSI data will change and be different. By differentiable HSC curves, the communication condition can be determined. From the results of two different scenarios, the environmental adaptability of HSC method can be shown.

## 6 Conclusion

In this paper, a practical problem in IoTs is presented, which is how to determine the movement in the environment of IoTs without additional equipment. HSC method is presented to solve this problem. The detailed explanation of HSC method is presented in this paper. Finally, our experiment results indicate that the HSC method can translate the indistinguishable RSSI data into the differentiable HSC curves and have some ability of environmental adaptability. Hence, movement in the communicating environment can be effectively determined.

**Acknowledgments.** This work is supported by the 2014 Natural Science Foundation of Guangdong Province under Grant 2014A030313685, the 2014 Pearl River Science and Technology Nova Program of Guangzhou under Grant 2014J2200023, Guangdong High-Tech Development Fund No. 2013B010401035, 2013 top Level Talents Project in "Sailing Plan" of Guangdong Province, National Natural Science Foundation of China (Grant No. 61401107), and 2014 Guangdong Province Outstanding Young Professor Project (No. Yq014116).

## References

1. Matern, D., Condurache, A., Mertins, A.: Automated intrusion detection for video surveillance using conditional random fields. In: International Conference on Machine Vision Application, pp. 298–301 (2013)
2. Kichun, J.: Interacting multiple model filter-based sensor fusion of GPS with in-vehicle sensors for real-time vehicle positioning. IEEE Trans. Intell. Transp. Syst. **13**(1), 329–343 (2012)
3. Want, R., Hopper, A., Falcao, V., et al.: The active badge location system. ACM Trans. Inf. Syst. **10**(1), 91–102 (1992)
4. Priyantha, N.B., Chakraborty, A., Balakrishnan, H.: The cricket location-support system. In: Proceedings of the 6th Annual International Conference on Mobile Computing and Networking, pp. 32–43 (2000)
5. Ye, H., Ektesabi, M.: RF indoor intrusion detection system. Lecture Notes in Engineering and Computer Science. DOAJ (2008)
6. Selvabala, V., Ganesh, A.B.: Implementation of wireless sensor network based human fall detection system. Procedia Eng. **30**, 767–773 (2012)
7. Xiao, J., Wu, K., Yi, Y., Wang, L., Ni, L.M.: FIMD: Fine-grained device-free motion detection. In: IEEE 18th International Conference on Parallel and Distributed Systems (ICPADS), pp. 229–235 (2012)
8. Zhang, Z., Lu, Z., Saakian, V., Qin, X., Chen, Q., Zheng, L.-R.: Item-level indoor localization with passive UHF RFID based on tag interaction analysis. IEEE Trans. Ind. Electron. **61**(4), 2122–2135 (2014)
9. Grossmann, R., Blumenthal, J., Golatowski, F., Timmermann, D.: Localization in zigbee-based sensor networks. In: Proceedings of the 1st European ZigBee Developers Conference, Munchen, Germany (2007)
10. Zhang, D., Ma, J., Chen, Q., Ni, L.M.: An RF-based system for tracking transceiver-free objects. In: 2007 Fifth Annual IEEE International Conference on Pervasive Computing and Communications, PerCom 2007, pp. 135–144. IEEE (2007)

11. Youssef, M., Mah, M., Agrawala, A.: Challenges: device-free passive localization for wireless environments. In: Proceedings of the 13th Annual ACM International Conference on Mobile Computing and Networking, pp. 222–229 (2007)
12. Serra, J.: Image Analysis and Mathematical Morphology. Academic Press, London (1982)
13. Soille, P.: Morphological Image Analysis: Principles and Applications. Springer, Berlin (2003)
14. Ayala, G., Gaston, M., Leon, T., Mallor, F.: Measuring dissimilarity between curves by means of their granulometric size distributions. In: Functional and Operatorial Statistics. Contributions to Statistics, pp. 35–41 (2008)
15. Leon, T., Ayala, G., Gaston, M., Mallor, F.: Using mathematical morphology for unsupervised classification of functional data. J. Statist. Comput. Simul. **81**(8), 1001–1016 (2011)
16. Gaston, M., Leon, T., Mallor, F., Ramirez, L.: A morphological clustering method for daily solar radiation curves. J. Solar Energy **85**, 1824–1836 (2011)

# Using Wireless Vibration Sensors to Study the Impact of Fouling on Fluid-Conveying Pipelines

Pengfei Wen[1], Jianfeng Huang[1(✉)], Yuanfang Chen[1], and Lei Shu[1,2]

[1] Guangdong Provincial Key Lab of Petrochemical Equipment Fault Diagnosis, Guangdong University of Petrochemical Technology, Maoming 525000, China
pengfei_wen@outlook.com, jianfeng.huang@outlook.com, {yuanfang_chen,lei.shu}@ieee.org
[2] School of Engineering, University of Lincoln, Lincoln, UK

**Abstract.** This paper analyzes the vibration signals on the surface of the fluid-conveying pipelines so as to monitor the state of pipelines, and study the impact of fouling on these pipelines. Wireless acceleration sensors are deployed on pipelines' surfaces to detect the vibration signals under different states. According to the real data from the test experiments, a model is implemented in ANSYS. On this basis, extensive simulation is conducted. The simulation results compare with real test data to verify the efficiency of the model.

**Keywords:** Vibration signals · Fluid-conveying pipelines
Fouling impact · Wireless acceleration sensors

## 1 Research Problem

Heat exchanger is a kind of important equipment in petrochemical plants. For the continuous production of industrial enterprises, the safe and stable operation of heat exchanger is of great importance. When using industrial circulating water as the cooling medium for heat exchangers, sediment and dirt are easily produced. When the heat exchanger is in operation, proper vibration will help reduce dirt and severe dirt will reduce heat exchange efficiency. In order to maintain the original efficiency, the speed need to be increased, which will increase the vibration of heat exchanger. According to statistics, the damage of nearly thirty percent heat exchanger is caused by the vibration of the tube bundle.

At present, the structure, heat transfer performance and heat transfer parameters of heat exchange tubes are simulated and studied by some researchers by means of ANSYS and CFX [9]. However, the research results of fault vibration characteristics of the heat exchanger through the commercial simulation software is quite less, because it involves the fluidic and structural two-way coupling, the heat exchanger structure is very complex, resulting in the difficulty of calculation of finite element analysis [2]. Many scholars have done a lot of research on the on-line monitoring and fault diagnosis of heat exchanger [7,10]. However, their


M. Huang et al. (Eds.): WICON 2016, LNICST 214, pp. 288–292, 2018.
https://doi.org/10.1007/978-3-319-72998-5_30

studies are limited by many factors, e.g., temperature, pressure, petrochemical material flow, and have many disadvantages, e.g. inefficient management, unreliable data, and high labor cost. Considering that petrochemical plants are lacking effective online monitoring system to conduct fault diagnosis for heat exchangers [5,6], this paper aims at proposing a novel method to solve this problem.

## 2 Solution

A heat transfer tube is one of the basic parts of a circulating water heat exchanger for conveying and controlling liquid or gas. Normally, the tubes of pipe - shell circulating water heat exchange are straight, and the pipes between the two baffles are simply supported single span beams. In order to analyze the blockage of the pipeline, this paper uses a two-way coupling separation model. Through the study of different plugging levels of the model, the law of pipe vibration caused by pipe blockage is determined. The simulation results were as show in Fig. 1. After that, the simulation results compare with real test data which collected by wireless acceleration sensors [3,4], to verify the efficiency of the model. In this paper, the fouling of heat exchanger pipeline was discussed and a new diagnostic method is put forward.

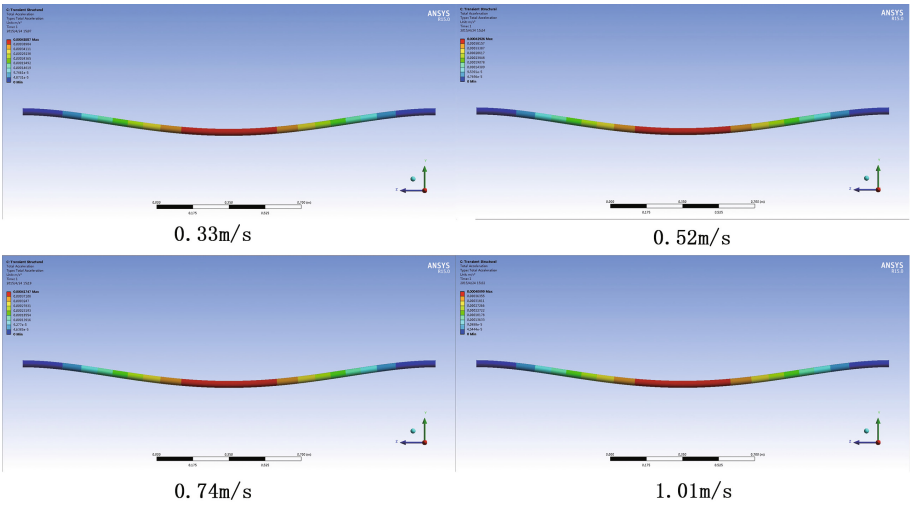


**Fig. 1.** Through constructing the finite element model of fluid - conveying pipe with different levels of pollution, this paper analyzes the four different degree of clogging (0%, 20%, 40%, and 60% fouling) under the influence of flow speed, direction, and load on pipe wall, wall displacement, the fluid domain of accelerated speed fluid conveying pipeline. It is found that fluid flow velocity and direction varied with the fouling position. In addition, wall load, wall displacement and accelerated speed increased with increasing degree of clogging. Therefore, the pollution of flow pipeline has an effect on the vibration of pipes.

## 3 Experiment

From the turbulence model, the normal fluid transportation pipeline model is established by means of ANSYS and CFX. The paper studies the vibration of the pipeline under different ow velocity through the study of the pipeline vibration by ANSYS and CFX. On this basis, the pipeline model of with different blockage levels is established, and the vibration of the pipeline is studied on the premise of the same ow velocity [1,8].

In order to verify whether it is feasible and correct to establish the finite element model of fluid transportation pipeline using ANSYS and CFX, this paper presents an experimental analysis of an experimental model under a given working condition. In this paper, two different diameters of pipeline are used to simulate the vibration produced by the fluid with different inlet velocities. Many high precision wireless sensors are installed at the same data observation point, and computer simulation is carried out to collect vibration signals simultaneously. The experimental facilities were as shown in Fig. 2.

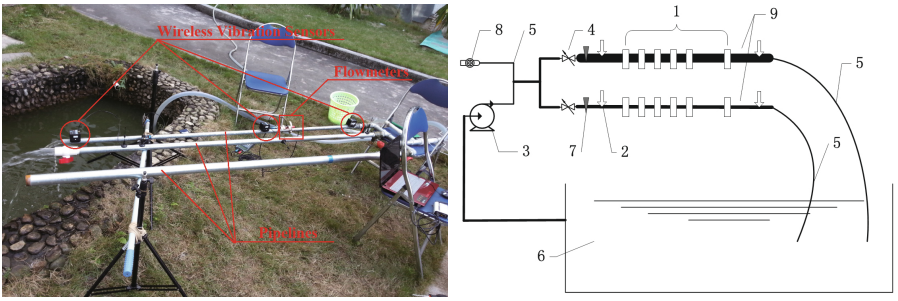


(a) Main components of experimental equipment

(b) Schematic diagram of real test

**Fig. 2.** 1-wireless vibration sensors, 2-flow meters, 3-pumb, 4-water valve, 5-flexible pipeline, 6-pool, 7-press instrument, 8-tap water inlet, 9-pipelines.

## 4 Conclusion and Open Issues

The experimental study was carried out in two different fluid - convey pipes. As shown in Fig. 3, through comparing the simulation model with the real test data of the non-fouling fluid-conveying pipeline in the same working condition, the validity of the simulation model is proved.

The finite element model of fluid-conveying pipeline under fluid-solid coupled interaction was established by ANSYS finite element analysis method. On the basis of this model, finite element analysis is carried out in the pipeline of different velocity and degree of clogging. In addition, a series of pipeline vibration experiments were performed under the same normal conditions. The results

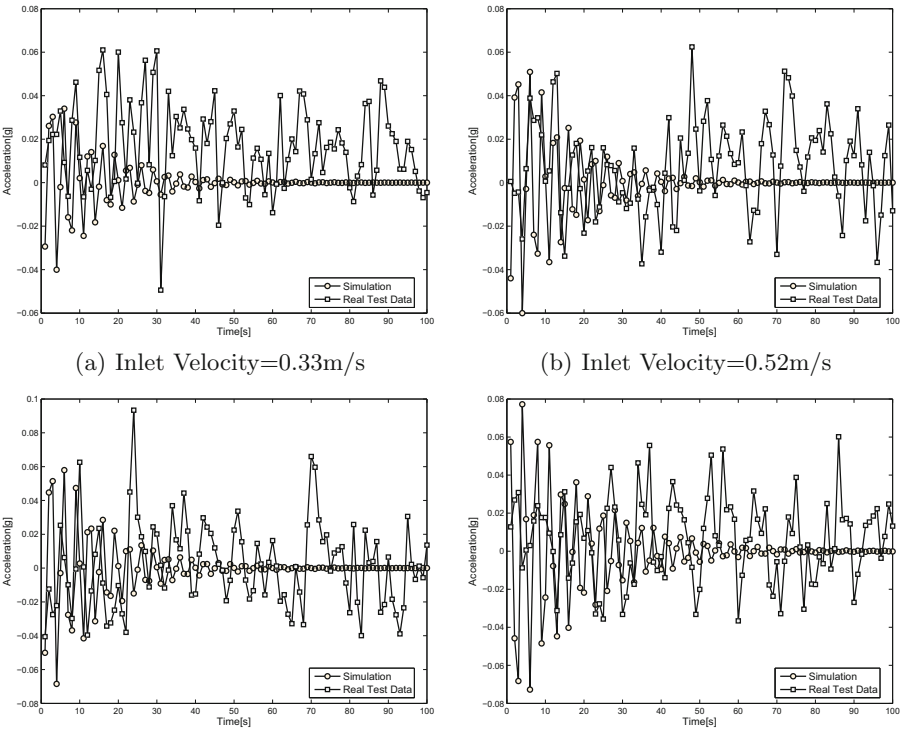


(a) Inlet Velocity=0.33m/s (b) Inlet Velocity=0.52m/s

(c) Inlet Velocity=0.74m/s (d) Inlet Velocity=1.01m/s

**Fig. 3.** Taking the vibration data of the pipeline (DN20) center as an example, the data of the finite element analysis and the actual experiment are basically similar, and the speed is 0.52 or 0.74 m/s. The acceleration speed data is 0.33 m/s. In the same orders of magnitude, the maximal acceleration speed of ANSYS simulation increases with the increase of inlet velocity.

show that the simulation data is basically consistent with the actual test data, only a small amount of data does not match.

### 4.1 Open Research Issues as Future Work

1. Vibration test experiments have been conducted with non-fouling fluid-conveying pipelines, but without fouling pipelines. Designing such fouling pipelines to make test experiments is still an open issue.
2. Vibration signals generated by other running equipment will affect the signal collection on the target equipment. Distinguishing the signals which collected from pipelines and other equipment in highly noisy environment is still an open issue.

**Acknowledgment.** This work is supported by National Natural Science Foundation of China (No. 61401107), International and Hong Kong, Macao & Taiwan collaborative

innovation platform and major international cooperation projects of colleges in Guangdong Province (No. 2015KGJHZ026), The Natural Science Foundation of Guangdong Province (No. 2016A030307029), the Open Fund of Maoming Study and Development Center of Petrochemical Corrosion and Safety Engineering (No. 201509A01), the Open Fund of Guangdong Provincial Key Laboratory of Petrochemical Equipment Fault Diagnosis (No. GDUPTLAB201605), Guangdong University of Petrochemical Technology through Internal Project 2012RC106. Jianfeng Huang is corresponding author.

## References

1. Da Silva, J.J., Lima, A.M.N., Neff, F.H., da Rocha Neto, J.S.: Non-invasive fast detection of internal fouling layers in tubes and ducts by acoustic vibration analysis. IEEE Trans. Instrum. Meas. **58**(1), 108–114 (2009)
2. Huang, J., Chen, G., Shu, L., Wang, S., Zhang, Y.: An experimental study of clogging fault diagnosis in heat exchangers based on vibration signals. IEEE Access **4**, 1800–1809 (2016)
3. Huang, J., Chen, G., Shu, L., Zhang, Q., Wu, X.: WSNs-based mechanical equipment state monitoring and fault diagnosis in China. Int. J. Distrib. Sens. Netw. **2015**(4), 1–14 (2015)
4. Korkua, S.K., Lee, W.J.: Wireless sensor network for performance monitoring of electrical machine. In: North American Power Symposium, pp. 1–5 (2009)
5. Lin, R., Wang, Z., Sun, Y.: Wireless sensor networks solutions for real time monitoring of nuclear power plant. In: Fifth World Congress on Intelligent Control and Automation, 2004, WCICA 2004, vol. 4, pp. 3663–3667 (2004)
6. Lu, B., Gungor, V.C.: Online and remote motor energy monitoring and fault diagnostics using wireless sensor networks. IEEE Trans. Industr. Electron. **56**(11), 4651–4659 (2009)
7. Pang, M., Shu, L., Lu, J., Zhu, X., Rodrigues, J.: A case study: monitoring heat exchanger based on vibration sensors and nondestructive testing technique. In: 2013 8th International ICST Conference on Communications and Networking in China (CHINACOM), pp. 511–516. IEEE (2013)
8. Silva, J., Queiroz, I., Lima, A., Neff, F., Neto, J.R.: Vibration analysis for fouling detection using hammer impact test and finite element simulation. In: Instrumentation and Measurement Technology Conference Proceedings, 2008, IMTC 2008, pp. 636–640. IEEE (2008)
9. Tiwari, A.K., Ghosh, P., Sarkar, J., Dahiya, H., Parekh, J.: Numerical investigation of heat transfer and fluid flow in plate heat exchanger using nanofluids. Int. J. Therm. Sci. **85**, 93–103 (2014)
10. Zhu, X., Shu, L., Zhang, H., Zheng, A., Han, G.: Preliminary exploration: fault diagnosis of the circulating-water heat exchangers based on sound sensor and nondestructive testing technique. In: 2013 8th International ICST Conference on Communications and Networking in China (CHINACOM), pp. 488–492. IEEE (2013)

# Poster and Demo

# Research on Spectrum Detection Technology in Cognitive Radio

Xiaoyu Tang(✉) and Baodan Chen

College of Information Science and Technology, Hainan University,
58 Renmin Avenue, Haikou 570228, Hainan, China
tang71320@sina.com

**Abstract.** The shortage of spectrum resources has hindered the development of the new wireless multimedia technology. Cognitive radio (CR) technology can successfully deal with the growing demand and scarcity of the wireless spectrum. Through this technology the unlicensed users can use the underutilized spectrum without any harmful interference to the licensed users. The spectrum sensing problem is one of the most challenging issues in cognitive radio systems to detect the available frequency bands. This paper introduces the spectrum sensing technology of cognitive radio and summarizes the result of simulation experiment based on GNU Radio and hardware platform.

**Keywords:** Cognitive radio · Spectrum sensing · GNU Radio
Hardware platform

## 1 Introduction

In recent years, wireless technology has entered a prosperous period of a rapid development. The increasing of wireless user and the emerging wireless multimedia applications are leading to an insatiable demand for radio spectrum. But the shortage of spectrum resources has hindered the development of them. So people put forward the initial hypothesis of CR technology. CR is formally defined by FCC as a radio that can change its transmitter parameters based on interaction with the environment in which it operates.

This paper reviews the research status of the simulation experiment of spectrum sensing technology of cognitive radio technology and GNU Radio hardware platform based on the development and more about ideas and put forward a new measurement method is helpful. Section 2 of this paper introduces the spectrum detection technology. In Sect. 3, we have described the simulation experiment and the results of the spectrum detection technology based on GNU Radio in the hardware platform. Then Sect. 4 summaries prospect of the spectrum detection technology of CR.

## 2 Spectrum Detection

In CR systems, when unlicensed users use the band allocated to licensed users for communication should not interfere with the communication of licensed users. So spectrum detection is one of the key technologies for CR system to detect the spectrum


M. Huang et al. (Eds.): WICON 2016, LNICST 214, pp. 295–298, 2018.
https://doi.org/10.1007/978-3-319-72998-5_31

environment efficiently and reliably. Generally, spectrum sensing technology can be roughly divided into transmitter detection, cooperative detection and interference detection. Transmitter detection techniques used to identify licensed users by detect the weak signal from the licensed users' transmitter. In general, detection problem is analyzed as a binary hypothesis model, defined as (1):

$$x(t) = \begin{cases} n(t) & H_0 \\ hs(t) + n(t) & H_1 \end{cases} \tag{1}$$

where x(t) is the signal received by CR during observation window T, n(t) represents the additive white Gaussian noise (AWGN) with mean 0 and variance σ2, s(t) represents the transmitted signal from primary user which is to be detected and h is the channel gain. This is a classic binary signal detection problem in which CR has to decide between two hypotheses, H0 and H1. H0 corresponds to the absence of primary signal in scanned frequency band while H1 indicates that the spectrum is occupied.

## 3 Simulation of Hardware Platform Based on Energy Detection

### 3.1 Energy Detection

Energy detection is the common way for the detection of unknown primary signals in spectrum sensing for its low computational and implementation complexities. Energy detection judges the energy accumulation in a certain frequency band. If the detected energy is higher than the threshold, it is considered that there is the licensed users' signal. If the threshold is lower than the threshold, it is considered that there is only the noise. The principle of energy detection is that the energy of the signal plus noise must be greater than the energy of the existence of the noise. In addition, it is more generic as receivers do not need any knowledge on the primary users' signal [1]. It is the optimal detector when the secondary user cannot gather sufficient information about the primary user signal [2]. Here is the formula (2):

$$E\left\{(s(t)+n(t))^2\right\} = E\left\{s^2(t)\right\} + E\left\{n^2(t)\right\} > E\left\{n^2(t)\right\} \tag{2}$$

In this formula the signal and noise are independent of each other, and the noise is zero mean value. According to the time and frequency domain energy detection can be divided into two types. In this paper we use frequency domain energy detector. Frequency domain energy detection model is shown in Fig. 1:


**Fig. 1.** The modle of frequency domain energy detection.

### 3.2 GNU Radio and Hardware Platform

GNU Radio is an open source software radio project launched by Blossom Eric. It is a tool that can serve the users around the world to study and create a software defined radio system. When connecting the RF hardware, the composition of Radio GNU is easy to form a software radio software platform, which is used to carry out the simulation experiment of sending and receiving data.

### 3.3 Experiment Simulation

We use Hack RF ONE as the experimental platform whose frequency range is 10 MHz–6 GHz. In the frequency range of the receiver, the energy detection can be carried out for any frequency band. TVWS is our measurement band. By measuring the occupancy of this frequency band and analyzing the usage of the frequency band, we can get the simulation results. In the simulation experiment the first thing is setting the center frequency and sampling bandwidth. We set the sensing range 698–806 MHz and 2 MHz as the sampling bandwidth. FFT is 256. The hardware platform will collect and save the signal data. By stepping into the tuning, we can get a wide range of signal spectrum data. Finally, using these data, we draw the corresponding spectrum. Figure 2 is the spectrum sensing data graph under simulation environment. Figure 3 is the spectrum occupancy map in this frequency band.

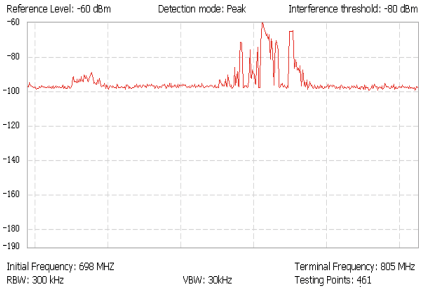


**Fig. 2.** Spectrum sensing data graph

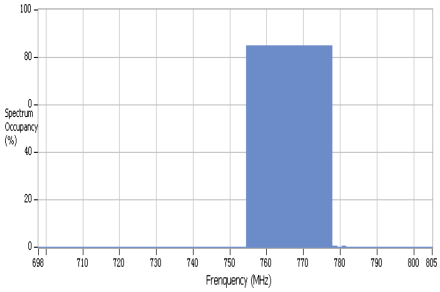


**Fig. 3.** Spectrum occupancy map

We can clearly see that the occupancy rate of 755–780 MHz band is higher. The result is similar with the spectrum analyzer. It can be known that the simulation of hardware platform based on energy detection can accurately detect the main user signal. And the complexity is low, the accuracy is high. In summary, after spectrum sensing, we can have a better understanding of the use of the current spectrum, and then through the opportunity spectrum access, improving the use efficiency of the spectrum.

## 4 Conclusion

Cognitive radio technology is the key to solve the shortage of spectrum resources effective method, spectrum detection technology as one of the key technologies of cognitive radio, is the basis of theory research of cognitive radio technology, is a kind of cognitive radio to the premise of practical application. In this paper, the simulation experiment is carried out by GNU Radio and hardware platform. We can come to the conclusion that the prospect of CR is very attractive, but it is not mature at present. In the future, we should do a deeper research on the theory of spectrum sensing algorithm which focused more on implementation-friendly, low-complexity sensing algorithms that are robust enough to provide required sensing performance with demanded reliability in minimum time.

**Acknowledgments.** This paper was supported by the Hainan province key laboratory and Engineering Technology Research Center Construction Project (Grant No. gczx2014004).

## References

1. Omer, A.E.: Review of spectrum sensing techniques in Cognitive Radio networks. In: International Conference on Computing (2015)
2. Garhwal, A., Bhattacharya, P.P.: A survey on dynamic spectrum access techniques for cognitive radio. Int. J. Next Gener. Netw. (IJNGN) **3**(4), 15–32 (2011)

# Video Quality Assessment by Decoupling Distortions on Primary Visual Information

Yang Li[1], Xu Wang[1], Feng Li[1], Qingrui Guo[1], Qiang Fan[2], Qiwei Peng[2], Wang Luo[2(✉)], Min Feng[2], Yuan Xia[2], and Shaowei Liu[2]

[1] State Grid Xinjiang Electric Power Science Research Institute, Nanjing 210003, China
[2] NARI Group Corporation (State Grid Electric Power Research Institute), Nanjing 210003, China
luowang@sgepri.sgcc.com.cn

**Abstract.** Video quality assessment (VQA) aims to evaluate the video quality consistently with the human perception. In most of existing VQA metrics, additive noises and losses of primary visual information (PVI) are decoupled and evaluated separately for quality assessment. However, PVI losses always include different types of distortions such that PVI distortions are not evaluated well enough. In this paper, a novel full-reference video quality metric is developed by decoupling PVI distortions into two classes: compression distortions and transmission distortions. First, video denoising method is adopted to decompose an input video into two portions, the portion of additive noises and the PVI portion. Then, maximal distortion regions searching (MDRS) algorithm is designed to decompose PVI losses into transmission distortions and compression distortions. Finally, the three distortions are evaluated separately and combined to compute the overall quality score. Experimental results on LIVE database show the effectiveness of the proposed VQA metric.

**Keywords:** Video quality assessment · Human visual system
Transmission distortion · Decoupling distortion

## 1 Introduction

Full Reference (FR) video quality assessment (VQA) metrics refer to algorithms that evaluate qualities of distorted videos with available reference videos. The goal is to evaluate the quality consistently well with human visual system (HVS). Signal-to-noise ratio (SNR) and peak SNR (PSNR) are the most widely used FR quality metrics. These indices are simple to calculate and convenient to be adopted. But they show poor consistency with subjective evaluations [1, 2].

Recently, the area of FR metrics has attracted a lot of attention [3–8]. Structure similarity index (SSIM) [3] was presented as a metric using structural information. To account for human perception of motion information, proper temporal weighting schemes [4, 5] were proposed based on SSIM. Temporal distortions were also considered in VQA metrics during the recent years. A motion-based video integrity


M. Huang et al. (Eds.): WICON 2016, LNICST 214, pp. 299–307, 2018.
https://doi.org/10.1007/978-3-319-72998-5_32

evaluation (MOVIE) index [6] was proposed to define the temporal distortion as the differences between the filter responses along computed motion trajectories. Spatio-temporal structural information was designed to evaluate the video perceptual quality [7]. Both the spatial edge features and temporal motion characteristics [9, 10] were accounted for with the structural features in the localized space-time regions. Different types of distortions cause different degradations. A decoupling based metric [8] were proposed by decomposing distortions into additive noises and distortions on primary visual information (PVI). The overall score was computed by combining evaluations of the two portions.

PVI distortions can be mainly classified into two types: compression distortions (e.g., Ringing, Blocking artifacts) and transmission distortions (e.g., Packet loss). However, these two types of distortions are with different characteristics. Compression distortions are content-dependent distortions. Structural similarity based metrics can perform well on this type of distortion. Transmission distortions which are introduced by packet loss are content-independent distortions. Large and distinct distortion regions randomly appear in video frames. Structural similarity based metrics, such as gradient similarity based metrics [7] can not represent transmission distortions accurately enough, especially when they occur in the original flat regions.

In this letter, a novel video quality metric is developed by decoupling PVI distortions. Video distortions are firstly decomposed into additive noises and PVI distortions using denoising method. Then, PVI distortions are classified into two typical classes: compression distortions and transmission distortions. After evaluating each type of distortions with rational metric, we combine the three evaluated results to compute the overall quality score. Experimental results on LIVE database show the effectiveness of the proposed VQA metric.

## 2 Proposed Method

We first give a brief overview of our approach before going into detail in subsequent sections. The flowchart of the proposed model is shown in Fig. 1. The reference video ($V_r$) and the test video ($V_t$) are firstly decomposed into additive noises ($A_r$ and $A_t$) and

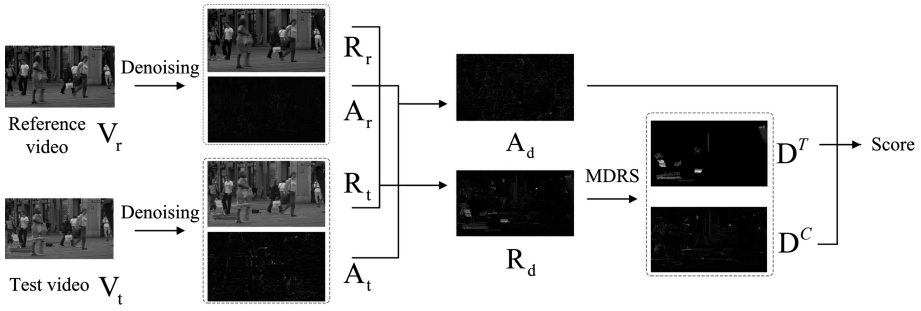


**Fig. 1.** Flowchart of the proposed model. $V_r$ ($V_t$) is the reference (test) video, $A_r$ ($A_t$) and $R_r$ ($R_t$) are the additive noises and reconstructed portions of $V_r$ ($V_t$), respectively. $D^T$ and $D^C$ are the portions of transmission distortions and compression distortions, respectively.

PVI portions ($R_r$ and $R_t$) by using video denoising method. Then, PVI distortions ($R_d$, the difference between $R_r$ and $R_t$) are classified into compression distortions ($D^C$) and transmission distortions ($D^T$), respectively. Different metrics are adopted to measure the degradations of each type, respectively. Finally, a combining scheme is used to generate the overall perceptual quality score of the test video.

### 2.1 Decoupling Distortions

**Algorithm 1 :** Maximal Distortion Regions Search (MDRS)

**Input:** The distortion of denoised video $D$.
**Initialization:** region number: $K$, difference threshold: $T$, window size: $ws$, area threshold: $S$

$OutIndex = cell(1, K)$;
$[W, H] = size(R_d)$; $M = zeros(W, H)$;
**for** $r = 1 : 4 : W$ **do**
  **for** $c = 1 : 4 : H$ **do**
    **if** $(length(find(R_d(r : r + 3, c : c + 3) > T)) == 16)$ **then**
      $M(r : r + 3, c : c + 3) = 1$;
    **end if**
  **end for**
**end for**
**for** $i = 1 \rightarrow K$ **do**
  $Idx = find\_max\_conn\_regions(M)$; $M(Idx) = 0$;
  **if** $length(Idx) > S$ **then**
    $OutIndex(i) = Idx$;
  **end if**
**end for**
**Output:** $OutIndex$;

The reference video and test video are firstly decomposed into additive noise portions and PVI portions via a video denoising method, called VBM3D [11]. A sparse 3D transform-domain collaborative filtering is used in VBM3D. This method performs good restoration on videos with additive noises. The differences between the additive noise portions of the reference video and test video are used to evaluate the additive distortions. This type of distortion may cause uncomfortable sensation. The differences between the PVI portions of the reference video and test video are called PVI distortions.

In order to represent the degradations more accurately, PVI distortions are decomposed into compression distortions and transmission distortions using a method, called Maximal distortion regions searching (MDRS). Compared to ringings and blocky artifacts which were introduced by compression, transmission errors always generate large areas of distortions. Furthermore, the strengths of these distortions are always large in local regions. That is, the regions with large area and distinct distortions tend to be with transmission errors. The goal of MDRS is to detect $k$ maximal regions with transmission distortions, such that $k < K$, where $K$ is the preset maximal number of regions. The PVI distortions $R_d$ are the inputs. The outputs are the locations of the k

regions. Details of MDRS are shown in Algorithm 1. (1) To achieve the constraint that distortions in local regions are large, the PVI distortion ($R_d$) is split into 4 × 4 non-overlapping blocks. For each block, if all the absolute values of the differences are larger than the preset threshold $T$, flags in the corresponding block of $M$ are set to 1. Otherwise, flags are set to 0. (2) The $k$ maximal regions will be searched out by finding the maximal 1−connected regions in $M$. Areas of regions that are bigger than the preset threshold $S$ are considered to be regions with transmission distortions. The other regions are with compression distortions. In this letter, $K$, $S$, and $T$ are set to 8, 32, and 12, respectively, from our empirical study.

### 2.2 Additive Distortion Evaluation

Since MSE presents a good match with additive noises [8], MSE is adopted to evaluate the degradations of the additive noises as follows

$$S_A = S(A_r, A_t) = 1 - \log_{10}(1 + MSE(A_r, A_t))/\log_{10}(255^2), \tag{1}$$

where $A_r$ and $A_t$ are the additive portions of the reference video and test video, respectively; $MSE(A_r, A_t)$ is the mean squared error between $A_r$ and $A_t$.

### 2.3 Transmission Distortion Evaluation

Transmission distortions are always introduced by packet losses. They are susceptible to the strength and area of the distortion regions. Therefore, transmission distortions are evaluated as follows

$$S_T(D^T) = \frac{C_1 - log_{10}\left(S \cdot T + \sum_{i=1}^{k} L_i \cdot S_i^2\right)}{C_1 - log_{10}(S \cdot T)}, \tag{2}$$

where $D^T$ is the transmission distortion detected by MDRS method; $Li$, ($i$ = 1, 2..$k$) is the mean absolute values of the $i^{th}$ maximal distortion region; $Si$, ($i$ = 1, 2..$k$) is the area of the $i^{th}$ maximal distortion region; $k$ is the region number; $C_1 = log_{10}(255 \cdot W^2 \cdot H^2)$, $W$ and $H$ are the image width and height, respectively; $S$ and $T$ are the preset area and difference thresholds used in MDRS. Similar with (1), the denominator is a normalization factor. Adding $S \cdot T$ is to avoid big leap occuring between the scores with and without transmission errors.

### 2.4 Compression Distortion Evaluation

Compression distortions mainly include degradations such as blurrings, blocking artifacts, and ringings. These degradations can be represented well by structural similarity based metrics, such as SSIM, edge gradient similarities. In this work, gradient similarities in spatial and temporal domain are computed to evaluate the compression

distortions. For each pixel, spatio-temporal gradient vector g = ($g_x$, $g_y$, $g_t$) is computed with Sobel filters along $x$, $y$ and $t$ directions, respectively. The Sobel Kernel for t direction is a 3 × 3 × 3 matrix [7]. To balance the effect of temporal and spatial gradients, they are divided by the sum of positive filter coefficients, respectively.

Since human attention mainly allocated to the salient regions, salient pixels are selected to evaluate the degradations of compression distortions. A pixel is considered to be a salient pixel if its spatio-temporal gradient magnitude is above the certain threshold $\zeta$ in either original video or distorted video [7]. The similarities between pixels can be computed as

$$S_p(x_r, x_t) = \left(\frac{2\|\mathrm{g}^r\|\|\mathrm{g}^t\| + C_2}{(\mathrm{g}^r)^2 + (\mathrm{g}^t)^2 + C_2}\right)^{\alpha} \cdot \left(\frac{\mathrm{g}^r \cdot \mathrm{g}^t + C_2}{\|\mathrm{g}^r\|\|\mathrm{g}^t\| + C_2}\right)^{\beta}, \tag{3}$$

where $C_2$ is the small constant to avoid the denominator being zero and is set as $C_2 = 0.03 \times 255^2$ [3]; $\mathrm{g}^r$ and $\mathrm{g}^t$ are the spatio-temporal gradient vectors of pixels $x_r$ and $x_t$ in the reference and test frames, respectively. In (3), the first term represents the similarity of magnitudes between $\mathrm{g}^r$ and $\mathrm{g}^t$; the second term represents the similarity of directions between $\mathrm{g}^r$ and $\mathrm{g}^t$. $\alpha$ and $\beta$ are the relative importance of the two terms. A big value of $\alpha$ highlights the importance of vector magnitude. In this letter, $\alpha$ is set to 2 and $\beta$ is set to 1.

Furthermore, HVS is highly sensitive to blocking artifacts. To measure the degradation of blocky artifacts, spatial gradient $\mathrm{g}^b = \left(g_x^b, g_y^b\right)$ similarities of down-sampled images are evaluated. The reference frame and test frame are down-sampled with rate 8 in both the vertical and horizontal directions. Blocking artifacts are evaluated as

$$S_b(b_r, b_t) = \left(\frac{2\left\|\mathrm{g}^{br}\right\|\left\|\mathrm{g}^{bt}\right\| + C_2}{\left(\mathrm{g}^{br}\right)^2 + \left(\mathrm{g}^{bt}\right)^2 + C_2}\right)^{\alpha} \cdot \left(\frac{\mathrm{g}^{br} \cdot \mathrm{g}^{bt} + C_2}{\|\mathrm{g}^{br}\|\|\mathrm{g}^{bt}\| + C_2}\right)^{\beta}, \tag{4}$$

where $b_r$ and $b_t$ are the pixels in the downsampled frames, i.e., mean values of 8 × 8 non-overlapped blocks of the reference and test frames, respectively. $\mathrm{g}^{br}$ and $\mathrm{g}^{bt}$ are spatial gradient vectors of $b_r$ and $b_t$, respectively. $\alpha$ and $\beta$ are set to the same values as in (4).

Some image regions have no apparent edge but are still with structural characteristics. Structural similarity [3] is adopted to evaluate the degradations on spatial structural information as

$$S_s(x_r, x_t) = \frac{2\sigma_{x_r, x_t} + C_2}{\sigma_{x_r}^2 \sigma_{x_t}^2 + C_2}, \tag{5}$$

where $S(x_r, x_t)$ is the structural similarity between blocks centered at pixels $x_r$ and $x_t$. The block size is set to 11 × 11.

Combine pixel similarities, blocking artifacts, and structural similarities, compression distortion are deduced as

$$S_C = \underset{x_r \in Z}{\text{Avg}}\left(\sum \left(S_p(x_r, x_t) S_s(x_r, x_t) S_b(b_r, b_t)\right)\right). \tag{6}$$

where $b_r$ ($b_t$) is the corresponding down-sampled value of the block in which pixel $x_r$ ($x_t$) located; $Z$ is the set of salient pixels which are degraded with compression distortions; Avg(·) is to calculate the average similarity of $Z$.

### 2.5 Overall Perceptual Quality

Distortion of different types will co-determine the perceptual quality of each frame. To evaluate the distortions on PVI, (2) and (6) are used to compute the perceptual quality score. Furthermore, the weights of the two evaluation parts are related to the noise energy level of the two portions. The similarities of additive distortions can reflect that of the compression distortions to some extent. Therefore, (1) are used to adjust the relative importance of the two portions. Finally, we combine the evaluation of the three portions, (1), (2), and (6). For each frame, the similarity can be computed as

$$S_F(V_r, V_t) = S_T^{S_A} \cdot S_C^{1-S_A} \tag{7}$$

Finally, all of the frame scores are averaged to give a final video quality index.

## 3 Experimental Results

In this section, the effectiveness of the proposed perceptual VQA metric is demonstrated. The LIVE subjective quality video database [12] is used to evaluate the performance of the proposed VQA metric. The LIVE database consists of 10 768 × 432p reference videos and 150 distortion videos. Subjective scores (DMOS) were recorded for all test sequences. The types of distortion comprised of MPEG-2 compression, H.264 compression, and simulated transmission of H.264 compressed bit-streams through error-prone IP networks and error-prone wireless networks. To detect the salient pixels, $\zeta$ is set to 300 through exhaustive experiments. For comparison, results with state-of-the-art VQA metrics are reported. The comparison metrics include PSNR, SW-SSIM [4], MC-SSIM [5], MOVIE [6], STSI [7], VQM [13], and Picture Quality Analyzer. Parts of the results are quoted from [7]. Pearson correlation coefficient (PCC) and Spearman rank order correlation coefficient (SROCC) are used as performance indicators.

The mapping function chosen for regression for each of the metrics is

$$f(x) = \frac{\beta_1 - \beta_2}{1 + exp\left(-\frac{x-\beta_3}{\beta_4}\right)} + \beta_2. \tag{8}$$

where $\{\beta_1, \beta_2, \beta_3, \beta_4\}$ are the fitting parameters.

Table 1 shows the PCC and SROCC on the LIVE video quality database. It can be seen that the proposed metric significantly outperforms other metrics according to the two indicators. The PSNR performs especially poorly on this database. It shows that the conventional pixel based models are incapable to represent perceptual video quality.

**Table 1.** Performance comparison on the live database

| Methods | Pearson CC | Spearman CC |
|---|---|---|
| VQM | 0.702 | 0.723 |
| MOVIE | 0.786 | 0.810 |
| STSI | 0.779 | 0.778 |
| SW-SSIM | 0.585 | 0.596 |
| MC-SSIM | 0.679 | 0.698 |
| PSNR | 0.368 | 0.404 |
| PQR (by PQA500) | 0.695 | 0.712 |
| DMOS (by PQA500) | 0.695 | 0.711 |
| Proposed | 0.816 | 0.809 |

**Table 2.** Spearman CC Scores of VQA metrics on each kind of distortion in live database

| Methods | Wireless | IP | H.264 | MPEG2 |
|---|---|---|---|---|
| PSNR | 0.4675 | 0.4108 | 0.4385 | 0.3856 |
| VQM | 0.7325 | 0.6480 | 0.6459 | 0.7860 |
| STSI | 0.7544 | 0.8072 | 0.8298 | 0.6624 |
| SW-SSIM | 0.5867 | 0.5587 | 0.7206 | 0.6270 |
| PQR (by PQA500) | 0.6464 | 0.7300 | 0.7455 | 0.6456 |
| DMOS (by PQA500) | 0.6426 | 0.7295 | 0.7427 | 0.6445 |
| Proposed | 0.7786 | 0.8069 | 0.8792 | 0.7023 |

In Table 1, it also can be seen that the proposed VQA metric performs significantly better than the SSIM based metrics such as SW-SSIM (PCC increment: 0.23), and MC-SSIM (PCC increment: 0.14). The reason is that the proposed decoupling based method can detect different types of distortions and evaluate each type with the rational measure. Furthermore, the proposed method performs better than the spatio-temporal gradient similarity based method, STSI (Pearson CC increases by 0.04). This can be attributed to that gradient similarity based method cannot represent transmission errors accurately enough. Since transmission distortions are always flat regions without apparent edges, gradient similarity based methods cannot detect these distortions well enough, especially when transmission distortions occur in the original flat regions.

Table 2 shows the PCC on the four kinds of distortions in LIVE database. It demonstrates that the proposed metric performs the best on three kinds of distortions (Wireless, IP, and H.264). For MPEG2 distortion, even though it is not better than VQM metric, it performs significantly better than all the other metrics (SROCC

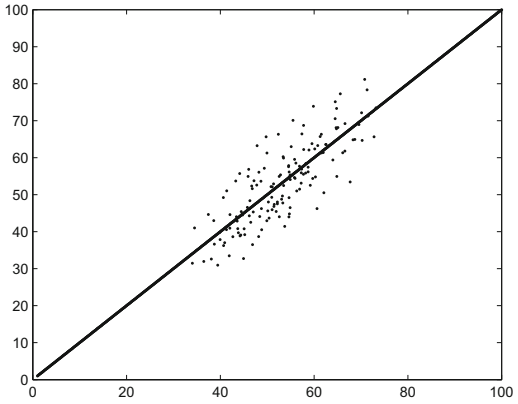


**Fig. 2.** Comparison between scatter plots of the proposed VQA.

increment: at least 0.04). The proposed metric is rather robust to various types of video distortions.

Figure 2 shows the scatter plots of the DMOS against the objective score by the proposed VQA metric on the LIVE database. It can be seen that the proposed metric performs well on videos from low quality to high quality.

## 4 Conclusion

In this letter, a VQA metric by decoupling PVI distortions has been proposed. Besides decoupling videos into additive noises and PVI, PVI distortions are decomposed into compression distortions and transmission distortions in order to evaluate PVI distortions more accurately. Considering the different properties of the decomposed portions, we separately evaluate their quality degradations with rational metrics. Experimental results demonstrate the effectiveness of the proposed metric.

## References

1. Wang, Z., Bovik, A.: A universal image quality index. IEEE Signal Process. Lett. **9**(3), 81–84 (2002)
2. Zhang, X., Feng, X., Wang, W., Xue, W.: Edge strength similarity for image quality assessment. IEEE Signal Process. Lett. **20**(4), 319–322 (2013)
3. Wang, Z., Bovik, A., Sheikh, H., Simoncelli, E.: Image quality assessment: from error visibility to structural similarity. IEEE Trans. Image Process. **13**(4), 600–612 (2004)
4. Wang, Z., Li, Q.: Video quality assessment using a statistical model of human visual speed perception. J. Opt. Soc. Am. A **24**(12), B61–B69 (2007)
5. Moorthy, A., Bovik, A.: Efficient video quality assessment along temporal trajectories. IEEE Trans. Circuits Syst. Video Technol. **20**(11), 1653–1658 (2010)
6. Seshadrinathan, K., Bovik, A.: Motion tuned spatio-temporal quality assessment of natural videos. IEEE Trans. Image Process. **19**(2), 335–350 (2010)

7. Wang, Y., Jiang, T., Ma, S., Gao, W.: Novel spatio-temporal structural information based video quality metric. IEEE Trans. Circuits Syst. Video Technol. **22**(7), 989–998 (2012)
8. Wu, J., Lin, W., Shi, G., Liu, A.: Perceptual quality metric with internal generative mechanism. IEEE Trans. Image Process. **22**(1), 43–54 (2013)
9. Xiong, J., Li, H., Wu, Q., Meng, F.: A fast HEVC inter CU selection method based on pyramid motion divergence. IEEE Trans. Multimedia **16**(2), 559–564 (2014)
10. Xiong, J., Li, H., Meng, F., Zhu, S., Wu, Q., Zeng, B.: MRF-based fast HEVC inter CU decision with the variance of absolute differences. IEEE Trans. Multimedia **16**(8), 2141–2153 (2014)
11. Dabov, K., Foi, A., Egiazarian, K.: Video denoising by sparse 3D transform-domain collaborative filtering. In: Proceedings of European Signal Processing Conference, EUSIPCO 2007, Poznan, Poland, September 2007
12. Seshadrinathan, K., Soundararajan, R., Bovik, A., Cormack, L.: Study of subjective and objective quality assessment of video. IEEE Trans. Image Process. **19**(6), 1427–1441 (2010)
13. Pinson, M., Wolf, S.: A new standardized method for objectively measuring video quality. IEEE Trans. Broadcasting **50**(3), 312–322 (2004)

# Faster-Than-Nyquist Transmission in SC-FDE System over Frequency Selective Channel with One Equalizer

Zhifeng Wang and Yong Bai(✉)

State Key Lab of Marine Resource Utilization in South China Sea, College of Information Science and Technology, Hainan University, 58 Renmin Ave., Haikou 570228, Hainan, China
bai@hainu.edu.cn

**Abstract.** When the Faster-than-Nyquis (FTN) signal transmits in the Single Carrier Frequency-Domain Equalization (SC-FDE) system over the multipath frequency selective channel, the Inter-Symbol Interferences (ISIs) will be induced by both FTN signaling and multipath channel. In this paper, we investigate the method to combat the induced ISIs together with one equalizer at the receiver. The simulation results demonstrate that acceptable BER system performance can be achieved with our proposed transceiver.

**Keywords:** Faster-than-Nyquist (FTN) · SC-FDE · Unique Word Inter-Symbol-Interference (ISI)

## 1 Introduction

The concept of FTN signaling was discovered by Mazo in 1970 [1]. He proved that increasing the rate of data transmitted of signal by 25% more than Nyquist rate in the AWGN channel, the minimum Euclidean distance does not reduce and the performance of transmission does not degrade [2].

In wireless communications, the transmitted signals normally go through multipath channel before reaching the receiver. Both FTN signaling and multipath frequency selective channel can induce ISIs in the transmission. To combat the both ISIs, Sygiura proposed a frequency-domain equalization (FDE) receiver structure in [3], which can operate in the context of FTN signaling transmission. Furthermore, an FTN transceiver without guard interval in the transmitter was used overlap FDE in [4] and demonstrated that the scheme can achieve higher transmission rate than that Nyquist without performance degradation.

In this paper, we investigate the FTN transmission in the SC-FDE system over the multipath frequency selective channel. The main contribution of this paper is that we propose a low-complexity receiver with one equalizer to combat the two induced ISIs together. The simulation results demonstrate that acceptable BER system performance can be achieved with our proposed transceiver.


M. Huang et al. (Eds.): WICON 2016, LNICST 214, pp. 308–311, 2018.
https://doi.org/10.1007/978-3-319-72998-5_33

## 2 System Model

At the transmitter, the information bits are mapped to data symbols after modulation. Then the modulated data appended with a UW (Unique Word) to form a data block, passing through a FTN-shaping filter to get the FTN signal with transmission interval $\tau T_s$. The length of UW is set to be longer than the length of ISIs induced by both FTN signaling and multipath channel to eliminate inter-block interference (IBI). After that the SC-FDE blocks transmitted though the mobile radio channel. A multipath frequency selective channel with additive white Gaussian noise is considered in this paper. The receiver first removes the UW of the received signals, and utilizes the pilot for channel and FTN estimation. Then one MMSE equalizer in the frequency domain is applied on the received signals to combat the induced ISIs by FTN signaling and frequency selective channel. Finally, the equalized signals are demodulated to recover the original data (Fig. 1).

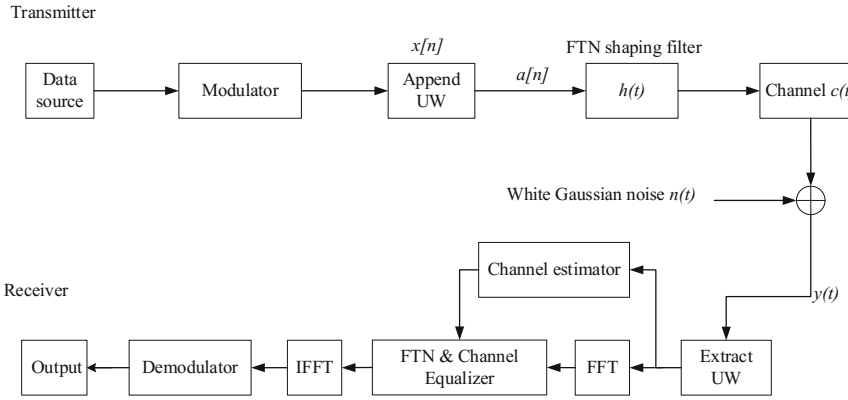


**Fig. 1.** System model of FTN transmission in SC-FDE system with one equalizer.

## 3 Simulation and Discussion

In this section we simulate the FTN transmission for SC-FDE system over multipath frequency selective channel. In the considered SC-FDE system, one transmitted frame is 1024 samples with 768 data symbols and 256 UW samples. The Zadoff-Chu sequences are used as the UW for channel estimation. For channel equalization at the SC-FDE receiver, the MMSE scheme is used. The symbol sampling rate is 1/τ10 M samples per second. In this simulation, we utilize the 3rd generation partnership project (3GPP) Pedestrian A channel with 4 dominant taps.

Figure 2 shows the BER (Bit Error Rate) performance of the SC-FDE system at different FTN rates using the designed frame structure under AWGN channel and multi-path channel.

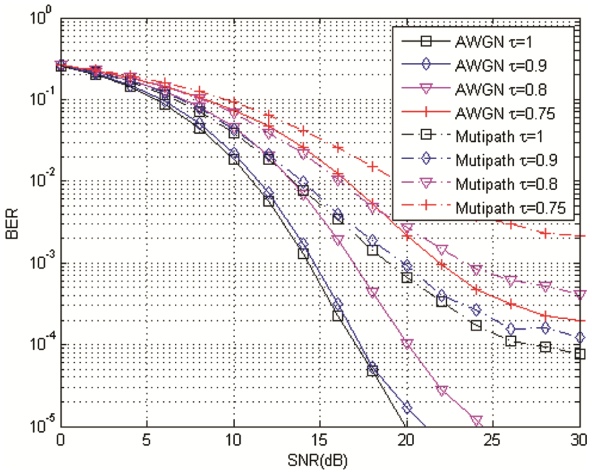


**Fig. 2.** BER performance of FTN transmission for SC-FDE with frame structure

We firstly compare the BER performance of FTNs transmission in AWGN channel with different value of $\tau$. It can be observed that the BER perfomance of system becomes worse when decreasing the value of $\tau$. In case of $\tau = 1$ and $\tau = 0.9$, the system error rate is up to $10^{-4}$ at SNR = 16 dB; for $\tau = 0.8$ SNR needs to be 20 dB to reach the same BER; when $\tau = 0.75$, the error rate is higher at high SNR.

Under the multipath channel, the ISIs are induced by both non-orthogonal FTN transmitter and multipath frequency selective channel, and we can see that at $\tau = 0.9$ and $\tau = 0.8$, the system BER can be almost up to $10^{-4}$ at SNR = 30 dB, which performs an acceptable for the information transmision; When $\tau = 0.75$, the BER performance can be only close to $10^{-3}$ at high SNR. In this case we need to consider the error correcting codes for improving the BER performance.

## 4 Conclusion

When combining FTN signaling with SC-FDE system over frequency selective channel, the FTN signaling and multipath frequency selective channel can both induce ISIs in the received signals. It is a promising approach these ISIs can be combatted by properly designed transceiver structure. With our designed frame structure using UW sequence, we can adopt one MMSE equalizer to combat both ISIs at the receiver. Such a low complexity transceiver can provide acceptable BER performance in a range of FTN signaling rate. The error correcting codes can be considered for further achieving better BER performance in certain SNR regime.

**Acknowledgments.** This paper was supported by the National Natural Science Foundation of China (Grant No. 61561017 and Grant No. 61261024), National Science & Technology Pillar Program (Grant No. 2014BAD10B04), and Hainan Province Major Science & Technology Project (Grant No. ZDKJ2016015).

## References

1. Mazo, J.E.: Faster-than-Nyquist signaling. Bell Syst. Tech. J. **54**(8), 1451–1462 (1975)
2. Mazo, J.E., Landau, H.: On the minimum distance problem for faster-than-Nyquist signaling. IEEE Trans. Inf. Theor. **34**(6), 1420–2427 (1988)
3. Sugiura, S.: Frequency-domain equalization of faster-than-Nyquist signaling. IEEE Wirel. Commun. Lett. **2**(5), 555–558 (2013)
4. Fukumoto, H., Hayashi, K.: Overlap frequency domain equalization for faster-than-Nyquist signaling. Mathematics **4**, 1211–1218 (2015)

# An Ensemble Method Based on SVC and Euclidean Distance for Classification Binary Imbalanced Data

Lei Zhao[1], Lei Wang[1,2], and Guan Gui[1(✉)]

[1] Key Lab of Broadband Wireless Communication and Sensor Network Technology, Nanjing University of Posts and Telecommunications, Nanjing, China
guiguan@njupt.edu.cn

[2] National Mobile Communications Research Laboratory, Southeast University, Nanjing, China

**Abstract.** In recent years, ensemble methods have been widely applied to classify binary imbalanced data. Traditional ensemble rules have manifested performance in dealing with imbalanced data. However, shortage appears that only the results of base classifiers is considered, while these traditional ensemble rules ignore the Euclidean distance between the new data and train data as well as the relations of majority and minority classes in the train data. So we proposed a novel ensemble rule which take Support Vector Classification (SVC) as base classifier. Moreover, the distance between the new data and train data and relations of majority classes and minority classes are taken into account to overcome conventional drawbacks. Simulation results are provided to confirm that the proposed method has better performance than existing ensemble methods.

**Keywords:** Binary imbalanced data · SVC · Euclidean distance Ensemble rule

## 1 Introduction

In recent years, due to the importance of imbalanced data in civilian and government applications, such as facial age estimation [1], speech recognition [2] and governmental decision-making support systems [3], imbalanced problems have been developed tremendously. So, researchers have shown greater interest on this crucial area.

The current research in imbalanced problems focuses more on binary imbalanced data, where data set is sorted into majority classes and minority classes. From Fig. 1(a) and (b), we can see the difference between binary imbalanced data and balanced data. Conventional binary imbalanced data classification methods mainly appear in data level and algorithm level. In data level, the main idea is to transform the imbalanced data into balanced data by increasing data or reducing data, such as synthetic minority over sampling technique (SMOTE) which increases minority classes by using k-nearest neighbors (KNN) algorithm. In contrast, while the main idea in algorithm level is to improve algorithm such


M. Huang et al. (Eds.): WICON 2016, LNICST 214, pp. 312–320, 2018.
https://doi.org/10.1007/978-3-319-72998-5_34

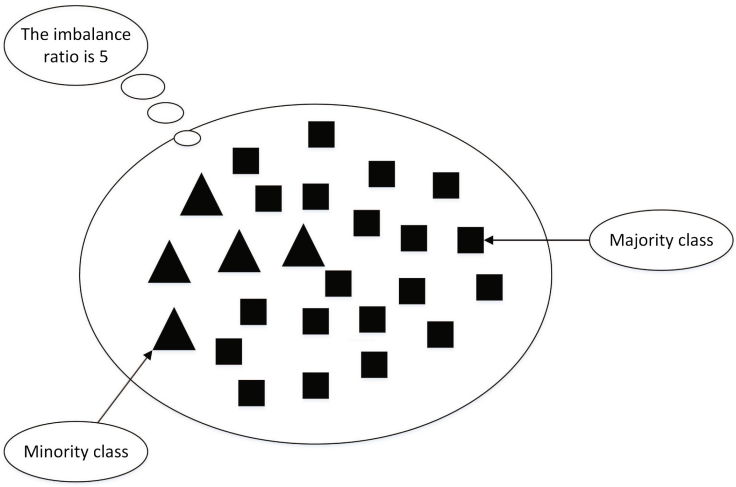


(a) An example of binary imbalanced data, where majority class is 25 and minority one is 5.

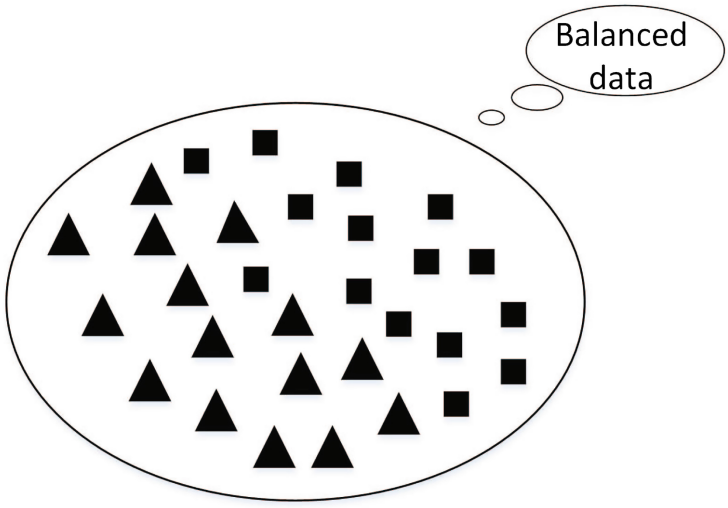


(b) An example of binary balanced data, where majority data is equal to minority one.

**Fig. 1.** A figure illustration of imbalanced data (a) and balanced data (b).

as ensemble learning methods [4], and cost-sensitive analysis. But these methods mentioned above share a collaborative shortage that they ignore the Euclidean distance of the new data and train data, and the number of majority and minority classes which gather around the new data.

To overcome above problems, we proposed a novel ensemble method which take Support Vector Classification (SVC) as base classifier and take the distance

between the new data and train data into account. In our method, KNN is taken as a filter to wipe out some majority classes whose Euclidean distance close to minority classes; then SVC is employed as the base classifier to classify the obtained balanced data; finally, we use our proposed ensemble rule to combine the classification results obtained by base classifiers. Our ensemble method is innovative while not only takes the relationships between majority classes and minority classes in train data but also that of new data and train data into account. The numerical analysis indicates that our ensemble method has an obvious improvement compared with four traditional ensemble rules including Max rule, Min rule, Product rule, and Sum rule [5]. At the same time, we also compare proposed method with another ensemble method (Splitbal + MaxDistance) [6], where the area under curve (AUC) is validated to be enhanced in comparison.

The rest of this paper is organized as follows: Sect. 2 introduces the related work; Sect. 3 presents our proposed method; Sect. 4 reports the experimental procedure, describes the detailed experimental setup and analyzes the corresponding results; finally, in Sect. 5 we summarize the study and draw the conclusion.

## 2 Related Work

Over past decades, the binary imbalanced problem has always been a difficult problem in data mining. So far, many methods have been proposed for handling binary imbalanced problem. Traditional binary imbalanced data classification methods mainly include data level and algorithm level [3]. In algorithm level, methods modify existing classification algorithms for adapting them to binary class imbalanced problem, while in data level methods aim to turn the imbalanced data into balanced data. Our method belongs to algorithm level. Next, we will introduce the present situation in algorithm level.

At present, the algorithm level methods include ensemble learning [5], cost-sensitive learning [7] and recognition-based learning [3]. (1) Ensemble learning is used to reduce the variance and bias by integrating the results of many classification algorithms on imbalanced data. Representatively, boosting uses the iterative method to focus on the samples as classified error, so it can obtain a good performance on imbalance problem. (2) Cost-sensitive learning approaches obtain the lowest classification error by adjusting the class misclassification cost. (3) Recognition based learning, RIPPER [6] and auto association provide the discrimination model created on the examples of the target class alone. They have been certified to be effective in dealing with complicated binary imbalanced data in high dimension.

However, these algorithms have collaborative drawbacks that they all ignore the Euclidean distance of the new data and train data as well as the relations of majority and minority classes in the train data. Our method solve both two problems mentioned above simultaneously by adding the Euclidean distance of the new data and train data and the number of majority and minority classes which gather at the new data into the final classification results.

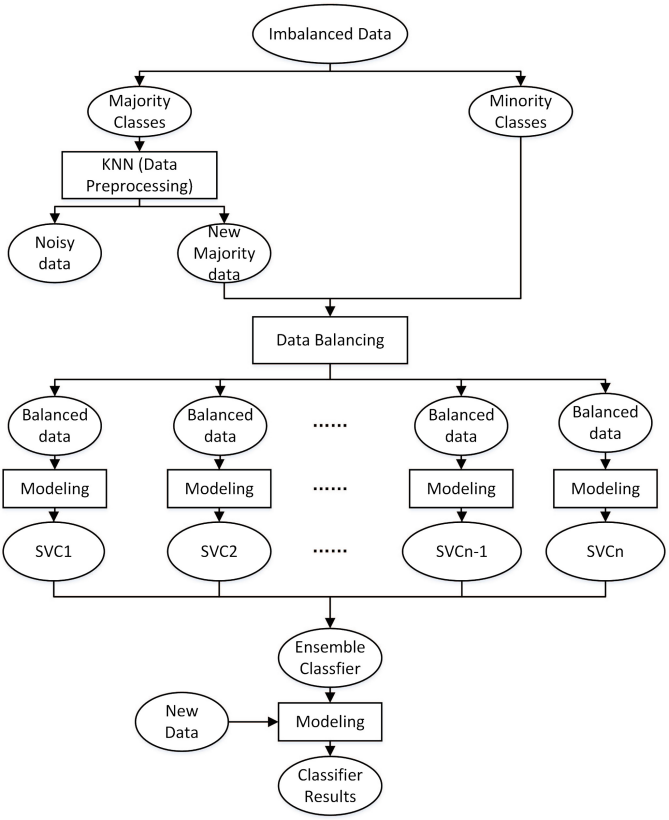


**Fig. 2.** Framework of our proposed method for handing binary imbalanced data

**Table 1.** The strategy for traditional rules

| Year | World population |
|---|---|
| Max | $R_1 = argmax_{1 \le i \le k} P_{i1}, R_2 = argmax_{1 \le i \le k} P_{i2}$ |
| Min | $R_1 = argmin_{1 \le i \le k} P_{i1}, R_2 = argmin_{1 \le i \le k} P_{i2}$ |
| Product | $R_1 = \prod_{i=1}^{k} P^{i1}, R_2 = \prod_{i=1}^{k} P^{i2}$ |
| Sum | $R_1 = \sum_{i=1}^{k} P^{i1}, R_2 = \sum_{i=1}^{k} P^{i2}$ |

**Table 2.** The strategy for MaxDistance rule

| Rule | Strategy |
|---|---|
| MaxDistance | $R_1 = argmax_{1 \le i \le k} \frac{P_{i1}}{D_{i1}+1}, R_2 = argmax_{1 \le i \le k} \frac{P_{i2}}{D_{i2}+1}$ |

## 3 Our Proposed Method

Our proposed method includes four parts: Data Preprocessing, Data Balancing, Modeling, and Classifying. Figure 2 shows the whole process. In our method, we first perform the Data Preprocessing based on KNN; then we divide the majority classes obtained from Data Preprocessing into several sets and each set has the same amount with minority classes; next we use the balanced data set to create the base classifiers with SVC; finally, we use our ensemble rule to combine the results of each base classifiers. In the subsequent, we will introduce the Data Preprocessing and Classifying.

### 3.1 Data Preprocessing

In this part, we innovatively use KNN as a method of data preprocessing. First of all, we divided train set into majority classes and minority classes. Secondly, we set majority classes as test set, if majority data is classified as minority classes, we judge that such majority data is close to minority data in space and can be stricken out. The reason is that these removed data will influence the classify results if the distances of new data and train data is taken into consideration.

### 3.2 Classifying

After Modeling, we can obtain several results from each base classifier which based on SVC. Next, we use our ensemble rule to combine these classification results. We make some assumptions as following: assume that there are K SVC classifiers and every data set has two labels, $C_1$ and $C_2$. For the $i$th SVC classifier $(1 \leq i \leq k)$, it classifies the new data as $C_1$ with the probability $P_{i1}$, and classifies the new data as $C_2$ with the probability $P_{i2}$. In the final classification results, $R_1$ and $R_2$ represent the class $C_1$ and $C_2$, respectively. In [5], four ensemble rules are described, and the details are shown in Table 1. In our ensemble rule, $D_{ij}(1 \leq i \leq k, 1 \leq j \leq 2)$ represents the average distance between new data and the data with class label $C_j$ in train set, and $K_n$ represents the k closest data around new data using KNN. Moreover, $b$ represents the number of data which belongs to minority classes in the k data. The details of our ensemble rule are shown in Table 3. Table 2 shows another ensemble rule Splital + MaxDistance which comes from [6].

From Table 3 we can see that the rule $R_2 = \frac{average(P_{i2})}{D_{i2}} \times (1 + \frac{b}{K_n})$ has a weight of $(1 + \frac{b}{K_n})$. The reason is that the number of majority classes is less than that of majority classes, and such fact will mislead the classification results

**Table 3.** The strategy for proposed ensemble rule

| Rule | Strategy |
|---|---|
| Proposed ensemble rule | $R_1 = \frac{average(P_{i1})}{D_{i1}}, R_2 = \frac{average(P_{i2})}{D_{i2}} \times (1 + \frac{b}{K_n})$ |

**Table 4.** Statistic summary of the 38 highly imbalanced data sets in experimental study

| ID | Data set | ATT | Ins | Mi | IR | ID | Data set | Att | Ins | Mi | IR |
|---|---|---|---|---|---|---|---|---|---|---|---|
| 1 | yeast3 | 9 | 1484 | 163 | 8.10 | 20 | led7digit | 8 | 443 | 37 | 10.97 |
| 2 | ecoli3 | 8 | 336 | 35 | 8.60 | 21 | ecoli01vs5 | 7 | 240 | 20 | 11.00 |
| 3 | yeast2vs4 | 9 | 514 | 51 | 9.08 | 22 | glass06vs5 | 10 | 108 | 9 | 11.00 |
| 4 | ecoli067vs35 | 8 | 222 | 22 | 9.09 | 23 | glass0146vs2 | 10 | 205 | 17 | 11.06 |
| 5 | ecoli0234vs5 | 8 | 202 | 20 | 9.10 | 24 | glass2 | 10 | 214 | 17 | 11.59 |
| 6 | glass015vs2 | 10 | 172 | 17 | 9.12 | 25 | ecoli0147vs56 | 7 | 332 | 25 | 12.28 |
| 7 | yeast0359vs78 | 9 | 506 | 50 | 9.12 | 26 | ecoli0146vs5 | 7 | 280 | 20 | 13.00 |
| 8 | yeast0256vs3789 | 9 | 1004 | 99 | 9.14 | 27 | shuttlec0vsc4 | 10 | 1829 | 123 | 13.87 |
| 9 | yeast02579vs368 | 9 | 1004 | 99 | 9.14 | 28 | yeast1vs7 | 8 | 459 | 30 | 14.30 |
| 10 | ecoli046vs5 | 7 | 203 | 20 | 9.15 | 29 | glass4 | 10 | 214 | 13 | 15.46 |
| 11 | yeast1289vs7 | 9 | 947 | 30 | 30.57 | 30 | ecoli4 | 8 | 336 | 20 | 15.80 |
| 12 | ecoli0267vs35 | 8 | 224 | 22 | 9.18 | 31 | pageblocks13vs4 | 11 | 472 | 28 | 15.86 |
| 13 | glass04vs5 | 10 | 92 | 9 | 9.22 | 32 | glass016vs5 | 10 | 184 | 9 | 19.44 |
| 14 | ecoli0346vs5 | 8 | 205 | 20 | 9.25 | 33 | glass5 | 10 | 214 | 9 | 22.78 |
| 15 | ecoli0347vs56 | 8 | 257 | 25 | 9.28 | 34 | yeast2vs8 | 9 | 482 | 20 | 23.10 |
| 16 | yeast05679vs4 | 9 | 528 | 51 | 9.35 | 35 | yeast4 | 9 | 1484 | 51 | 28.10 |
| 17 | vowel0 | 14 | 988 | 90 | 9.98 | 36 | yeast5 | 9 | 1484 | 44 | 32.73 |
| 18 | ecoli067vs5 | 7 | 220 | 20 | 10.00 | 37 | ecoli0137vs26 | 8 | 281 | 7 | 39.14 |
| 19 | glass016vs2 | 10 | 192 | 17 | 10.29 | 38 | yeast6 | 9 | 1484 | 35 | 41.40 |

**Table 5.** The AUC of our ensemble method and the SMD method with 38 data sets

| ID | Data set | SMD | SVC-KNN | ID | Data set | SMD | SVC-KNN |
|---|---|---|---|---|---|---|---|
| 1 | yeast3 | 0.8648 | **0.9346** | 20 | led7digit | 0.9599 | **0.9600** |
| 2 | ecoli3 | 0.9206 | **0.9329** | 21 | ecoli01vs5 | **0.9505** | 0.9453 |
| 3 | yeast2vs4 | 0.8441 | **0.9227** | 22 | glass06vs5 | 0.9548 | **0.9789** |
| 4 | ecoli067vs35 | **0.8923** | 0.8597 | 23 | glass0146vs2 | 0.7630 | **0.8162** |
| 5 | ecoli0234vs5 | 0.9383 | **0.9419** | 24 | glass2 | 0.7851 | **0.8104** |
| 6 | glass015vs2 | 0.7272 | **0.7978** | 25 | ecoli0147vs56 | 0.9242 | **0.9245** |
| 7 | yeast0359vs78 | 0.6999 | **0.7512** | 26 | ecoli0146vs5 | **0.9520** | 0.9475 |
| 8 | yeast0256vs3789 | 0.7875 | **0.8107** | 27 | shuttlec0vsc4 | 1.0000 | 1.0000 |
| 9 | yeast02579vs368 | 0.9169 | **0.9210** | 28 | yeast1vs7 | 0.6158 | **0.8006** |
| 10 | ecoli046vs5 | **0.9607** | 0.9523 | 29 | glass4 | **0.9659** | 0.9413 |
| 11 | yeast1289vs7 | 0.5761 | **0.7375** | 30 | ecoli4 | 0.8692 | **0.9867** |
| 12 | ecoli0267vs35 | **0.8891** | 0.8523 | 31 | pageblocks13vs4 | 0.9135 | **0.9627** |
| 13 | glass04vs5 | **0.9667** | 0.9633 | 32 | glass016vs5 | **0.9529** | 0.9324 |
| 14 | ecoli0346vs5 | **0.9500** | 0.9444 | 33 | glass5 | **0.9325** | 0.9125 |
| 15 | ecoli0347vs56 | **0.9390** | 0.9323 | 34 | yeast2vs8 | 0.7547 | **0.7765** |
| 16 | yeast05679vs4 | 0.7870 | **0.8478** | 35 | yeast4 | 0.8341 | **0.8704** |
| 17 | vowel0 | 0.9996 | **0.9999** | 36 | yeast5 | 0.9516 | **0.9865** |
| 18 | ecoli067vs5 | **0.9410** | 0.9250 | 37 | ecoli0137vs26 | **0.9768** | 0.9620 |
| 19 | glass016vs2 | 0.7401 | **0.8113** | 38 | yeast6 | 0.8236 | **0.9246** |
| | **Average** | **SMD: 0.8742** | | **SVC-KNN: 0.9020** | | | |

tending to majority classes, so we add a weight into to balance the imbalance ratio. Finally, the final classification result $R_1$ and $R_2$ are obtained with the ensemble rules in Tables 1 and 2, if $R_1 \geq R_2$, the new data is seen as $C_1$,

otherwise $C_2$. In our experiments, we set $K_n$ as 5, for the specific reasons, please see the fourth section.

## 4 Simulation Study

### 4.1 Data Sets

In our paper, we have adopted several binary imbalanced data sets which come from Keel data set repository [8]. The attributes of these data sets are shown in Table 4. Including imbalance radio (IR), total attributes (ATT), total instances, and the number of minority (positive) class instances. For more details of the adopted data sets, please referred to the following cite http://sci2s.ugr.es/keel/imbalanced.php.

In experiments, we used the 5 fold cross validation strategy, furthermore, we set SVC as our basic algorithm. Otherwise, we select AUC [9] as our performance evaluation, because of its superiority to G-mean and F-measure [10] in performance evaluation.

### 4.2 Experimental Design

Our works in this paper consists of three investigations. The first investigation is to test which value of is better in. The second investigation is to compare our method with Splital + MaxDistance when the basic algorithm is SVC. The third investigation is to make a compare of our ensemble rule with traditional ensemble rules including Max rule, Min rule, Product rule, and Sum rule.

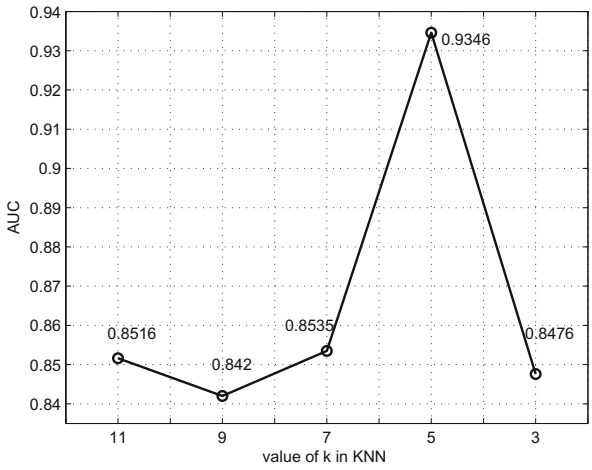


**Fig. 3.** The results while $K_n$ take different values

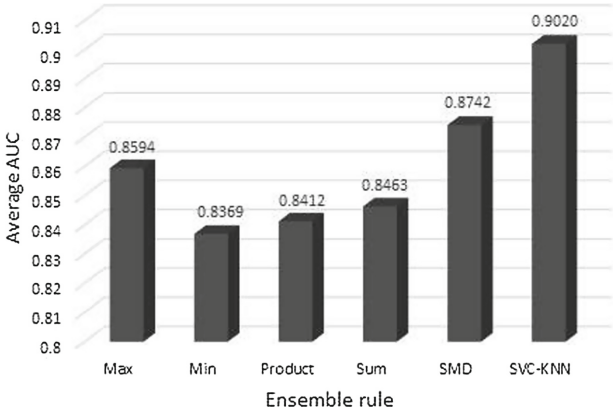


**Fig. 4.** The average AUC of different ensemble rule with 38 data sets

Investigation 1: We use the data set yeast3 to test the AUC value of our ensemble methods when takes different values (under the situation that its value must be odd). The experiment results are shown in Fig. 3. From the Fig. 3, we can figure out that our method could get best performance when $K_n$ is set to 5.

Investigation 2: In this part, we make a compare of our method with the method Splital + MaxDistance (SMD) and the results are shown in Table 5. From Table 5, we can see that our method has a better performance and there is 2.78% increase than another ensemble method. Moreover, the deep color represent the better performance at each data set.

Investigation 3: For the four traditional ensemble rules, we obtained its average AUC value while SVC is set as basic algorithm with 38 imbalanced data sets. From Fig. 4 we can see that our method (SVC-KNN) acquired the best performance and SMD ranked second.

## 5 Conclusion

An ensemble method based on SVC and Euclidean distance for classification of binary imbalanced data has been shown in this paper. Different from the existing methods, our proposed ensemble method is innovative while not only takes the connections between majority classes and minority classes in train data but also that of new data and train data into account.

In this paper, we can learn that our proposed method has a visible improvement compared with existing methods while dealing with binary imbalanced data set. But there some problems need to be solved, such as whether our proposed ensemble rule suit to other basic algorithms (Naive Bayes, Random Forest, and so on). So further research on this area is expected in the future.

**Acknowledgment.** This work was sponsored by National Natural Science Foundation of China (61271240, 61671253); The Priority Academic Development Program

of Jiangsu Higher Education Institutions, China; the Major Projects of the Natural Science Foundation of the Jiangsu Higher Education Institutions (16KJA510004); The Open Research Fund of National Mobile Communications Research Laboratory, Southeast University (2016D01); The Open Research Fund of Key Lab of Broadband Wireless Communication and Sensor Network Technology (NUPT), Ministry of Education (NYKL201509).

## References

1. Castillo, M.D.D., Serrano, J.I.: A multi strategy approach for digital text categorization. ACM SIGKDD Explor. Newsl. **6**(1), 15–32 (2004)
2. An, A., Cercone, N., Huang, X.: A case study for learning from imbalanced data sets. In: Stroulia, E., Matwin, S. (eds.) AI 2001. LNCS (LNAI), vol. 2056, pp. 1–15. Springer, Heidelberg (2001). https://doi.org/10.1007/3-540-45153-6_1
3. He, H., Garcia, E.A.: Learning from imbalanced data. IEEE Trans. Knowl. Data Eng. **21**(9), 1263–1284 (2009)
4. Sun, Z., Song, Q., Zhu, X.: Using coding-based ensemble learning to improve software defect prediction. IEEE Trans. Syst. Man Cybern. Part C **42**(6), 1806–1817 (2012)
5. Kittler, J., Hatef, M., Duin, R.P., Matas, J.: On combining classifiers. IEEE Trans. Pattern Anal. Mach. Intell. **20**(3), 226–239 (1998)
6. Sun, Z., Song, Q., Zhu, X., et al.: A novel ensemble method for classifying imbalanced data. Pattern Recogn. **48**(5), 1623–1637 (2015)
7. Zheng, J.: Cost-sensitive boosting neural networks for software defect prediction. Expert Syst. Appl. **37**(6), 4537–4543 (2010)
8. Alcal, J., Fernndez, A., Luengo, J., Derrac, J., Garca, S., Snchez, L.: KEEL data-mining software tool: data set repository, integration of algorithms and experimental analysis framework. J. Multiple-Valued Logic Soft Comput. **17**(2), 255–287 (2011)
9. Huang, J., Ling, C.X.: Using AUC and accuracy in evaluating learning algorithms. IEEE Trans. Knowl. Data Eng. **17**(3), 299–310 (2005)
10. He, H., Ma, Y.: Imbalanced Learning: Foundations, Algorithms, and Applications. Wiley, Hoboken (2013)

# Author Index


Bai, Yong 109, 139, 228, 308

Cai, Mengfei 61
Cao, Lu 109
Chen, Baodan 295
Chen, Lirui 164
Chen, Lu 228
Chen, Yuanfang 36, 288
Choudhury, Nikumani 10

Ding, Wanmeng 70, 80
Dong, Lijun 272
Dong, Qinghe 61
Duan, Yucong 197

Fan, Qiang 299
Fang, Jiabao 51
Fang, Shaofeng 121, 149
Feng, Jing 240
Feng, Min 299
Fischione, Carlo 101

Gao, Hui 240
Gong, Yi 3
Gui, Guan 312
Guo, Qingrui 299
Guo, Weibin 240
Guo, Yi 51

Han, Yugui 109
He, Qian 61
He, Qingsu 121
Hou, Xinjing 121, 149
Hu, Xing 164
Hu, Zhuhua 109
Huang, Daoping 279
Huang, Jianfeng 288
Hui, Yilong 263

Ji, Hong 207
Jiang, Tao 189
Jiang, Xiaolin 101
Jing, Weipeng 189

Leung, Victor C. M. 207
Li, Feng 299
Li, Gaolei 91
Li, Jianhua 91
Li, Lei 3
Li, Lin 179
Li, Wenjing 121
Li, Xi 207
Li, Xiaoyu 279
Li, Yang 299
Liao, Xiao 121
Lin, Xiaofeng 250
Liu, Bei 155
Liu, Cang 164
Liu, Fang 121, 149
Liu, Hanlin 70, 80
Liu, Lintao 80
Liu, Peng 61
Liu, Shaowei 299
Liu, Yanheng 179
Liu, Yaqiu 189
Liu, Yuanan 121, 149
Lu, Yuliang 70, 80
Luo, Wang 299
Lv, Tiejun 240

Matam, Rakesh 10
Mehmood, Amjad 21
Mukherjee, Mithun 10, 36

Ou, Qinghai 121, 149

Pang, Zhibo 101
Peng, Qiwei 299

Qi, Qi 197

Ran, Xiaoman 36
Rong, Liping 131, 218, 250

Shokri-Ghadikolaei, Hossein 101
Shu, Lei 10, 21, 36, 279, 288
Song, Dayong 179

Su, Xin 131, 155, 218, 250
Su, Zhou 263
Sun, Zhihong 36

Tang, Chuan 164
Tang, Xiaoyu 295
Tong, Minglei 139

Wan, Song 70, 80
Wang, Jian 179
Wang, Jing 155
Wang, Jun 27
Wang, Lei 312
Wang, Taotao 240
Wang, Xu 299
Wang, Yu 164
Wang, Yue 27
Wang, Zhenxing 51
Wang, Zhifeng 308
Wen, Pengfei 288
Wu, Jun 91
Wu, Xiaoling 279
Wu, Xiaoqin 228
Wu, Yang 91
Wu, Yuntao 36

Xia, Yuan 299
Xiang, Suncheng 164
Xing, Zuocheng 164
Xu, Jinsong 164
Xu, Qichao 263
Xu, Shaoqing 179
Xu, Xibin 155

Yan, Li 21
Yan, Xuehu 70, 80
Yang, Lichao 207
Yang, Wang 207
Ye, Chunyang 197
Yuan, Luechao 164

Zeng, Jie 131, 155, 218, 250
Zeng, Lingkang 121
Zhang, Heli 207
Zhang, Liancheng 51
Zhang, Qi 131, 218
Zhang, Yang 164
Zhang, Yu 21, 197
Zhang, Zeyu 21
Zhao, Chengcheng 91
Zhao, Junhui 3
Zhao, Lei 312
Zhao, Wangfeng 164
Zhao, Yaochi 109
Zhou, Hui 197